Regulated cell death in the pathogenesis of renal ciliopathies

INAUGURAL-DISSERTATION

zur

Erlangung des Doktorgrades

der Mathematisch-Naturwissenschaftlichen Fakultät

der Universität zu Köln

vorgelegt von

Emilia Kieckhöfer

aus Aachen

Köln 2024

Berichterstatter (Gutachter):

Prof. Dr. Bernhard Schermer

Prof. Dr. Kay Hofmann

Prof. Dr. Matthias Hammerschmidt

Tag der mündlichen Prüfung: 21.05.2024

I. Abstract

The primary cilium is an evolutionary conserved sensory organelle present on most mammalian cell types. In the kidney, cilia project from the apical surface of tubular epithelial cells. Defects in the structure or function of primary cilia lead to ciliopathies, such as autosomal dominant and recessive Polycystic Kidney Disease (ADPKD/ARPKD), and several genetic syndromes, including Nephronophthisis (NPH), Joubert Syndrome (JBTS) or Bardet-Biedl Syndrome (BBS). These syndromes display overlapping symptoms in different organs and tissues, such as retinopathy, polydactyly, neuronal developmental disorders or obesity, and commonly exhibit development of (poly-)cystic kidney disease. The cystic kidney disease observed in NPH and NPH-related ciliopathies (NPH-RC), such as JBTS or BBS, develops during childhood and adolescence and is accompanied by a massive loss of epithelial cells, as well as inflammation and interstitial fibrosis. This thesis, therefore, follows the hypothesis that regulated cell death (RCD) pathways play a role in the pathogenesis of the kidney phenotype in NPH and NPH-RC, and investigates the bidirectional interconnection between RCD and the primary cilium, as well as the role of RCD in NPH/NPH-RC.

In the first part, we studied how loss of primary cilia would affect the RCD response in murine inner medullary collecting duct cells. This revealed increased expression of the necroptosis key regulator receptor-interacting protein kinase 3 (RIPK3) in cells lacking primary cilia, and increased phosphorylation of the mixed lineage kinase domain-like pseudokinase (MLKL) suggesting elevated necroptosis. In summary, cells lacking primary cilia were prone to undergo necroptosis upon induction of cell death, which was not observed in ciliated cells. This resulted in the first conclusion that the absence of primary cilia increases susceptibility to necroptotic cell death. Conversely, the presence of cilia to some extent may offer protection against necroptosis.

In the second part, we aimed to understand the contribution of RCD pathways to the pathogenesis of cystic kidney disease in the well-established *Nphp9/Nek8^{jck}* mouse model, in which a point mutation in the *Nphp9/Nek8^{jck}* gene leads to a severe and early on-set cystic kidney disease. Crossing this mouse with a conventional knockout of Ripk3 led to an amelioration of cystic kidney disease and kidney function. Notably, this double knockout led to an upregulation of key pyroptotic regulators such as the NLR family pyrin domain containing 3 (NLRP3), Caspase-11 or Gasdermin D (GSDMD). Consistently, the deletion of GsdmD a key regulator of pyroptosis in the *Nphp9/Nek8^{jck}* mouse model also improved the phenotype and function of the kidney. In summary, the *in vivo* data demonstrate that necroptosis, and to a certain extent pyroptosis and the inflammasome, contribute to the loss of kidney function in the studied ciliopathy model.

In the third part of this thesis, we present a mouse model in which the deletion of the *Bbs* gene, *Bbs8*, results in the development of a kidney phenotype, in particular, tubule cystic kidney

disease. Our data support the hypothesis that in the kidneys of the *Bbs8* deficient mice pyroptosis and fibrosis is expressed, without the regulation of necroptosis. Mechanistically, loss of BBS8 resulted in increased expression and activity of the histone deacetylase 2 (HDAC2), which in turn destabilized ciliary microtubules by deacetylation of acetylated alpha-tubulin. In conclusion, the primary cilium exhibits a protective function to prevent RCD, particularly necroptosis and pyroptosis, and both pathways contribute to cystic kidney disease. Future work will have to address to what extent RIPK3 and GSDMD might serve as potential therapeutic targets in NPH or NPH-RC.

II. Zusammenfassung

Das primäre Zilium ist ein evolutionär konserviertes sensorisches Organell, dass bei den meisten Säugetierzelltypen vorhanden ist. In der Niere bilden sich Zilien von der apikalen Oberfläche der Epithelzellen des Nierentubulus aus. Defekte in dieser Struktur oder Störungen der Funktion führen zu Ziliopathien, wie zu autosomal-dominanten und -rezessiven polyzystischen Nierenerkrankung (ADPKD/ARPKD), sowie verschiedenen weiteren genetischen Syndromen, wie zum Beispiel Nephronophthisis (NPH), das Joubert-Syndrom (JBTS) oder das Bardet-Biedl-Syndrom (BBS). Diese Syndrome können überlappende Symptome in diversen Organen und Geweben aufweisen, wie Retinopathie, Polydaktylie, neuronale Entwicklungsstörungen oder Fettleibigkeit. Die Entwicklung einer (poly-) zystischen Nierenerkrankung zeigt sich in diesen regulär als konstante Manifestation. Die zystische Nierenerkrankung, die bei NPH und NPH-verwandten Ziliopathien (NPH-RC) wie bei JBTS oder BBS beobachtet wird, entwickelt sich im Kindes- und Jugendalter und wird von einem massiven Verlust von Epithelzellen der Niere sowie von Entzündungen und interstitieller Fibrose begleitet. Diese Arbeit geht daher von der Hypothese aus, dass regulierter Zelltod (RCD) eine Rolle bei der Entstehung des Nierenphänotyps in NPH und NPH-RC spielt, und untersucht die bidirektionale Verbindung zwischen RCD und dem primären Zilium, sowie die Rolle von RCD in NPH/NPH-RC.

Im ersten Teil dieser Thesis wurde untersucht, wie sich der Verlust der primären Zilien auf die RCD-Reaktion in Zellen des inneren medullären Sammelkanals der Niere in der Maus auswirkt. Dabei zeigte sich eine erhöhte Expression von Nekroptose-Schlüsselregulatoren, wie unter anderem von Receptor-interacting protein kinase 3 (RIPK3), sowie eine erhöhte Phosphorylierung der Mixed lineage kinase domain-like pseudokinase (MLKL). Zusammenfassend zeigen Zellen ohne primäre Zilien eine erhöhte Neigung zu Nekroptose nach Induktion von Zelltod, welches in zilierten Zellen nicht beobachtet werden konnte. Hierdurch ließ sich feststellen, dass das Vorhandensein von primären Zilien bis zu einem gewissen Grad Nekroptose verhindert.

Darüber hinaus war das Ziel die Rolle von RCD-Signalwege, sowie deren Beitrag zur Pathogenese der Zystennierenerkrankung zu untersuchen. Hierzu wurde das etablierte Mausmodell *Nphp9*/*Nek8*^{jck} verwendet, welches durch eine Punktmutation in diesem Gen zu einer schweren und früh einsetzenden Zystennierenerkrankung führt. Die Kreuzung dieser Maus mit einem herkömmlichen *Ripk3* Knockout Model führte zu einer Verbesserung der zystischen Nierenerkrankung, sowie der Nierenfunktion. Bemerkenswert war, dass der doppelte Knockout zu einer Hochregulierung von pyroptotischen Schlüsselregulatoren, wie NLR family pyrin domain containing 3 (NLRP3), Caspase-11 oder Gasdermin D (GSDMD) führte. Dem einhergehend verbesserte der zusätzliche Verlust von GsdmD in der *Nphp9*/*Nek8*^{jck} Maus ebenfalls den Phänotyp und die Funktion der Niere.

Zusammenfassend zeigen die *in vivo* Daten, dass Nekroptose, sowie zum Teil Pyroptose und das Inflammasom, zum Verlust der Nierenfunktion im untersuchten Ziliopathie-Modell beitrugen.

Final konnten wir zeigen, dass die Deletion des *Bbs*-Gens *Bbs8* zur Entwicklung einem tubulären zystischen Nierenphänotyps führt, unter dem potentiellen Einfluss von Pyroptose. Darüber hinaus führte mechanistisch gesehen der Verlust von *Bbs8* zu einer erhöhten Expression und Aktivität der Histondeacetylase 2 (HDAC2). Hierbei destabilisiert HDAC2 die primären Zilien durch Deacetylierung von Alpha-Tubulin. Zusammenfassend zeigt sich, dass das primäre Zilium eine Schutzfunktion besitzt, um RCD, insbesondere Nekroptose und Pyroptose, zu verhindern, und dass beide RCD-Wege akut zur zystischen Nierenerkrankung beitragen. Aus diesem Grund sollten sich künftige Arbeiten mit der Frage befassen, inwieweit RIPK3 und GSDMD als potenzielle therapeutische Ziele bei NPH und anderen NPH-RC dienen könnten.

III. Table of content

I. ABSTRACT I

II. ZUSAMMENFASSUNG III

III. TABLE OF CONTENT V

IV. LIST OF FIGURES VIII

V. LIST OF TABLES VIII

VI. ABBREVIATIONS IX

VII. ABBREVIATIONS OF CHEMICAL COMPOUNDS XIII

VIII. ABBREVIATIONS OF UNITS XIV

IX. ABBREVIATIONS OF METHODS XV

1. INTRODUCTION 1

1.1 Primary cilium **1**
1.1.1 Ciliary dynamics 3
1.1.2 Ciliary signalling pathways 5
1.1.3 Ciliopathies 7

1.2 Renal ciliopathies **9**
1.2.1 Autosomal dominant polycystic kidney disease 10
1.2.2 Nephronophthisis 11
1.2.3 NPH-related ciliopathies 12

1.3 Regulated cell death and related signalling pathways **14**
1.3.1 Apoptosis 16
1.3.2 Necroptosis 17
1.3.3 Ferroptosis 18
1.3.4 Pyroptosis 18
1.3.5 NF-κB 19
1.3.6 Autophagy 19

1.4 Regulated cell death in acute kidney injury **21**

1.5 Regulated cell death in chronic kidney disease **24**

1.6 Thesis Aims **26**

2. MATERIAL AND METHODS 27

2.1 Material 27
2.1.1 Chemicals and reagents 27
2.1.2 Assays and Kits 31
2.1.3 Enzymes 32
2.1.4 Buffers and solutions 33
2.1.4 Oligonucleotides 38
2.1.5 Antibodies 40
2.1.6 Cell lines 42
2.1.7 Plasmids 42
2.1.8 Consumables 43
2.1.9 Equipment 45
2.1.10 Software and online tools 48

2.2 Methods 50
2.2.1 Bacterial culture 50
2.2.1.1 Cloning PCR 50
2.2.1.2 Agarose gel electrophoresis 51
2.2.1.3 Restriction enzyme digestion 51
2.2.1.4 Transformation and isolation of plasmid 52
2.2.1.5 Sanger sequencing 53
2.2.2 Mammalian cell culture 54
2.2.2.1 Culture of immortalized cell lines 54
2.2.2.2 Passaging, counting, freezing and thawing of immortalized cells 54
2.2.2.3 Treatment of mIMCD3 cells 54
2.2.2.4 Live-cell imaging 55
2.2.2.5 Neutral red assay 55
2.2.2.6 Immunofluorescence staining 55
2.2.2.7 Transfection of HEK293T cells 56
2.2.2.8 Co-Immunoprecipitation 56
2.2.3 Mouse work 57
2.2.3.1 Mouse holding and mouse lines 57
2.2.3.2 DNA extraction from mouse tissue via HotSHOT 57
2.2.3.3 Genotyping PCR 57
2.2.3.4 Sample collection 58
2.2.3.5 Staining of renal tissue 58
2.2.3.5.1 Periodic-Acid Schiff staining 58
2.2.3.5.2 Masson Trichrome Staining 58
2.2.3.5.3 TUNEL staining 59
2.2.3.5.4 Immunostaining 59
2.2.3.6 Cyst index analysis 59
2.2.3.7 Cytokine assay 60
2.2.3.8 Single-nuclei sequencing 60
2.2.4 RNA isolation and cDNA transcription 61
2.2.5 Quantitative real-time Polymerase Chain Reaction (qPCR) 61
2.2.6 Sample and tissue lysis for immune blotting 61
2.2.6.1 BCA assay 61
2.2.6.2 SDS polyacrylamide gel electrophoresis 62
2.2.6.3 Chemiluminescent western blot 62
2.2.6.4 Fluorescent western blot 62
2.2.7 Proteomics and phosphoproteomics 63
2.2.7.1 Stage-tip 63
2.2.7.2 Proteome analysis 63
2.2.7.3 Phosphoproteome analysis 64
2.2.8 Raw data deposition 65

2.2.9 Statistics 65

3. RESULTS 66

3.1 Chapter 1 - Primary cilia suppress Ripk3-mediated necroptosis 67

3.2 Chapter 2 - Deletion of *Ripk3* or *GsdmD* improves cystic kidney disease in *Nek8^{jck}* mice 91

3.3 Chapter 3 - Loss of Bbs8 leads to cystic kidney disease in mice and affects tubulin acetylation through HDAC2 120

4. DISCUSSION 153

4.1 Primary cilia as a modulator for regulated cell death 153

4.2 Ciliopathy mutations and complete loss of cilia in RCD regulation 155

4.3 Extrarenal manifestations and systemic inflammatory signalling in ciliopathies: lessons from the BBS8 mice 157

4.4 Inflammation in kidney disease as part of the phenotype in ciliopathies 160

4.5 The impact of Necroptosis in CKD 161

4.6 Cyst formation in distal tubules and loss of epithelial cells 164

4.7 RCD as a therapeutic target in renal ciliopathies 166

5. CONCLUSION 169

X. LIST OF PUBLICATIONS XVI

Publications in Academic Journals XVI
Preprint publications in academic journals XVI

Publications in International Academic Conferences XVI
Oral presentation XVI
Poster presentation XVII

Presentations and posters in the framework of the SFB1403 XVII
Oral presentation XVII
Poster presentation XVII

XI. ERKLÄRUNG XVIII

XII. ACKNOWLEDGMENT XIX

XIII. REFERENCES XX

XIV. SUPPLEMENTS LI

IV. List of figures

Figures of the result section are not listed and can be found in the individual chapters (manuscripts).

Figure 1 **The primary cilium.** 2
Figure 2 **Ciliary dynamics** 5
Figure 3 **The kidney** 10
Figure 4 **Regulated cell death and correspondent level of inflammation.**. 15

Supplementary Figure 1 **Bbs8 knockout mice do not develop cystic liver but fatty liver disease.** LI
Supplementary Figure 2 **Vector map of Flag-tagged human BBS8.** LII

V. List of tables

Table 1 **Ciliopathies and their phenotypes** 8
Table 2 **Chemicals and reagents used** 27
Table 3 **List of all kits used** 31
Table 4 **Enzymes for bacteria culture**. 32
Table 5 **Compositions of buffers or other solutions** 33
Table 6 **Cloning primer set with MluI/ Not1 modification** 38
Table 7 **Sanger sequencing primer.** 38
Table 8 **Polymerase chain reaction (qPCR) oligonucleotides** 38
Table 9 **Oligonucleotides used for mouse genotyping** 39
Table 10 **List of primary antibodies**. 40
Table 11 **List of secondary antibodies** 41
Table 12 **Cell lines used for experiments.**. 42
Table 13 **Plasmids used for overexpression in HEK293T cells** 42
Table 14 **List of consumables used** 43
Table 15 **List of appliances used** 45
Table 16 **List of all used software** 48
Table 17 **List of all used online tools** 49
Table 18 **Cloning reaction mix** 50
Table 19 **Components for amplification of insert.** 51
Table 20 **Digestion mix.** 52
Table 21 **Ligation mix.** 52
Table 22 **Raw data deposition**. 65

VI. Abbreviations

5HTR6	5-hydroxytryptamine receptor 6
ACD	Accidental cell death
ADPKD	Autosomal-dominant polycystic kidney disease
AIF	Apoptosis inducing factor
AKI	Acute kidney injury
ALMS	Alström syndrome
Apaf-1	Apoptotic protease activating factor-1
ARL13B	ADP-ribosylation factor-like 13B
ARPKD	Autosomal-recessive polycystic kidney disease
ASC	apoptosis-associated speck-like protein containing a CARD
Asp	Aspartic acid
ATG	Autophagy-related proteins
AurA	Aurora A
BAK	BCL2 antagonist/killer 1
BAX	BCL2 associated X
BB	Basal body complex
BBS	Bardet-Biedl syndrome
BBS8	Bardet-Biedl syndrome protein 8
CAD	Caspase-activated deoxyribonuclease
Casp	Caspase
CCL-20	CC-chemokine-ligand-20
cDNA	complementary DNA
c-Flip	cellular FLICE inhibitor protein
Chr.	Chromosome
cIAP1	Cellular inhibitor of apoptosis 1
cIAP2	Cellular inhibitor of apoptosis 2
CK2	casein kinase 2
Ckc	Ciliated kidney cells
CKD	Chronic kidney disease
Clu	Clusterin
CP	Ciliary pocket
CRP	C-reactive protein
DAMPs	Damage-associated molecular patterns
Dcdc2a	Doublecortin domain containing 2
DFNA5	Non-syndromic hearing impairment protein 5
Dhh	Desert-Hh
DISC	death-inducing signalling complex
DNA	Deoxyribonucleic acid
dNTP	Deoxyribonucleotide triphosphate
E.coli	Escherichia coli
EB1	small microtubule (MT)-binding protein
ESRF	End stage renal failure
EVC	Ellis van Crefeld syndrom

FA	Folic acid
FADD	Fas-associated death domain
FAS	Fatty acid synthetase
FC	Fibrocystin
fl	floxed
FN	Fibronectin
FZD	Frizzled
gDNA	Genomic DNA
Gli	Glioma-associated oncogene transcription factors
Glis2 (Nphp7)	GLIS Family Zinc Finger 2
GO	Gene ontology
GOBP	Gene ontology biological processes
GOCC	Gene ontology cellular compartments
GOMF	Gene ontology molecular functions
GPCRs	G-protein coupled receptors
GPX4	Glutathione peroxidase 4
GSDMD	Gasdermin D
GSH	Glutathione
GSK-3β	Glycogen synthase kinase beta
H+L	Heavy and light chain
HDAC2	Histone deacetylase 2
HDAC6	Histone deacetylase 6
HEF1	human enhancer of filamentation 1
HEK293T	Human embryonic kidney cells
Hh	Hedgehog
Hprt1	Hypoxanthine Phosphoribosyltransferase 1
IAP	Inhibitors of apoptosis proteins
IFNγ	Interferon-γ
IFT	Intraflagellar transport
IFT-A	Intraflagellar transport A complex
IFT-B	Intraflagellar transport B complex
IgG	Immunoglobulin G
Ihh	Indian-Hh
IL-1	Interleukin 1
IL-18	Interleukin 18
IL-1β	Interleukin 1β
IL-6	Interleukin 6
INVS/Nphp2	Inversin
iPSCs	Inducible pluripotent stem cells
IRI	Ischemia-reperfusion injuries
IκB	IkappaB kinase
JATD	Jeune syndrome
JBTS	Joubert syndrome
Jck	Juvenile cystic kidney
KEGG	Kyoto Encyclopedia of Genes and Genomes
Kif3a	Kinesin family member 3A

KISS1R	Kisspeptin 1 receptor
KO	Knockout
Ksp:Cre	Cadherin 16 promoter driven Cre recombinase
LAMP2	Lysosome-associated membrane protein 2
LC3	Microtubule-associated protein 1A/1B-light chain 3
Lcn2	Lipocalin 2
LEF	Lymphoid enhancer factor
LOV1	Location of vulva’
LPS	Lipopolysaccharide
MAPK	Mitogen-activated protein kinases
MCHR1	Melanin-concentrating hormone receptor 1
mIMCD3	Murine Inner medullary collecting duct
MKS	Meckel-Gruber syndrome
MLKL	Mixed-lineage kinase domain-like protein
MT	Microtubules
MTOC	Microtubule-organization centre
mTOR	Mechanistic target of rapamycin kinase
NAPDH	Glyceraldehyde-3-phosphate dehydrogenase
Nckc	Non-ciliated kidney cells
Nek8/Nphp9	NIMA Related Kinase 8
NF-κB	Nuclear factor 'kappa-light-chain-enhancer' of activated B-cells
NF-κB 1/p50	nuclear factor NF-kappa-B p50 subunit
NF-κB 2/p65	nuclear factor NF-kappa-B p65 subunit
NLRP3	NLR family pyrin domain containing 3
NLRs	nucleotide-binding oligomerization domain (NOD) -like receptors
NOD	nucleotide-binding oligomerization domain
Non-PCD	Non-programmed cell death
NPH	Nephronophthisis
NPHP	Nephronophthisis proteins
NPH-RC	NPH-related ciliopathies
OFD	Oro-facial-digital syndrome
OPTN	Optineurin
p	Phospho
P0	Postnatal day 0/ at birth
P100	Postnatal day 100
PAMPs	Pathogen-associated molecular pattern
PCD	Programmed cell death
PCM	Pericentriolar material
PDGF	Platelet-derived growth factor
PDGFR	Platelet-derived growth factor receptor
PKD	Polycystic kidney disease
Pkd1	Polycystin-1
PKD1L1	Polycystin-1-like protein
Pkd2	Polycystin-2
PKHD1	Hepatic disease 1
PLK1	Polo-like kinase 1

PTCH	Patched
RCD	Regulated cell death
RelA	V-Rel avian reticuloendotheliosis viral oncogene homolog A
RHD	Receptor homology domain
RIPK1	Receptor Interacting Serine/Threonine Kinase 1
RIPK3	Receptor Interacting Serine/Threonine Kinase 3
RNA	Ribonucleic acid
ROS	Reactive oxygen species
RP1	Retinitis pigmentosa 1
RPE	Retinal pigment epithelium
SAA	Serum amyloid A
SAP	Serum amyloid P
Sdccag8 (Nphp10)	Serologically defined colon cancer antigen 8
Ser	Serine
Shh	Sonic-Hh
SLSN	Senior-Løken syndrome
SMO	Smoothened
SNx	Subtotal nephrectomy
Spp1	Secreted phosphoprotein 1
SQSTM1/p62	Sequestosom 1
SSTR3	somatostatin receptor 3
STAT3	Signal transducer and activator of transcription 3
TAZ	PDZ-binding motif
TCF	T-cell factor
tg	Transgenic
TGF	Transforming Growth Factor
TGF-β	TGF-beta
Thr	Threonine
tKO	Transgenic knockout
TLR	Toll-like receptors
TNF	Tumour necrosis factor
$TNFR_1$	TNF receptor 1
TNFα	TNF-alpha
TRADD	TNF receptor-associated death domain
TRAF	receptor-associated factors
Tsc1	Tuberous sclerosis 1
Tsc2	Tuberous sclerosis 2
TZ	Transition zone
URECS	Urine derived kidney epithelial cells
UUO	Unilateral ureteral obstruction
VHL	von Hippel-Lindau
w/o	Without
Wnt	Wingless
Wnt5a	Wnt family member 5A
XIAP	X-linked inhibitor of apoptosis
YAP	Yes-associated protein

γH2AX	phosphorylated histone H2A variant H2AX

VII. Abbreviations of chemical compounds

APS	Ammonium peroxydisulfate
BCA	Bicinchoninic acid
Biri	Birinapant
BSA	Bovine serum albumin
CAA	Chloroacetamide
$CaCl_2$	Calcium chloride
CHX	Cycloheximide
CO_2	Carbon dioxide
DAPI	4',6-diamidino-2-phenylindole
ddH_2O	Double distilled water
DMEM	Dulbecco's modified eagle medium
DMEM-F12	Dulbecco's Modified Eagle Medium/Nutrient Mixture F-12 Ham
DMSO	Dimethyl sulfoxide
DTT	Dithiothreitol
ECL	Enhanced chemiluminescence
EDTA	Ethylenediaminetetraacetic acid
Em	Emricasan
EtOH	Ethanol
FA	Folic acid
FBS	Fetal bovine serum
H_2O	Water
H_2O_2	Hydrogen peroxide
HCl	Hydrogen chloride
HEBS	HEPES-buffered saline
HEPES	4-(2-hydroxyethyl)-1-piperazineethanesulfonic acid
HRP	Horseradish peroxidase
KCl	Potassium chloride
LB Medium	Lysogeny broth
LPS	Lipopolysaccharide
LTL	Lotus tetragonolobus lectin
MtOH	Methanol
N_2	Nitrogen
Na_2HPO_4	Disodium hydrogen phosphate
$Na_3C_6H_5O_7$	Trisodium citrate
Na_3VO_4	Sodium orthovanadate
$Na_4P_2O_7$	Tetrasodium pyrophosphate
NaCl	Sodium chloride
Na-DOC	Sodium deoycholate
NaF	Sodium fluoride
NaOH	Sodium hydroxide
NDS	Normal donkey serum

Nec-1	Necrostatin-1
Nec-1s	Necrostatin-1 stable
PAA	Polyacrylamide
PAS	Periodic acid–schiff
PBS	Phosphate buffered saline
PBSTx-100	PBS + Triton X-100
PFA	Paraformaldehyde
PMSF	Phenylmethylsulfonyl fluoride
PPI	Phosphatase-protease-inhibitor
Pst	Penicillin-streptomycin
RIPA	Radioimmunoprecipitation assay
SDS	Sodium dodecyl sulfate
SOC	Super optimal broth medium
TAE	Tris-acetate-EDTA
TBS	Tris buffered saline
TEMED	N,N,N´,N´-tetramethylethylenediamine
Tris	Tris(hydroxymethyl)aminomethane
Tris-HCL	Tris hydrochloride

VIII. Abbreviations of units

% (v/v)	Volume concentration
% (w/v)	Mass concentration
°C	Degrees celsius
FDR	False discovery rate
g, mg, µg, ng	gram, milligram, microgram, nanogram
h, min, sec, ms	hours, minutes, seconds, milliseconds
kbp, bp	Kilo base pair, base pair
kDa, Da	kilo Dalton, dalton
l, ml, µl	liter, milliliter, microliter
LFQ	Label-free quantification
M, mM, µM, nM	molar, millimolar, micromolar, nanomolar
mA	Milliampere
p-value	Probability value
rpm	rounds per minute
RT	Room temperature
SD	Standard deviation
Tm	Melting temperature
U	Units
V	Volt

IX. Abbreviations of methods

co-IP	Co-Immunoprecipitation
ELISA	Enzyme-linked Immunosorbent Assay
FACS	Fluorescence activated cell sorting
IF	Immunofluorescence
PCR	Polymerase chain reaction
PP	Phosphoproteome
qPCR	Quantitative real time polymerase chain reaction
RNA-seq	RNA sequencing
scRNA-seq	Single cell RNA sequencing
SDS-PAGE	SDS polyacrylamide gel electrophoresis
snRNA-seq	Single nuclear RNA sequencing
snRNA-seq	Single nucleus RNA sequencing
TUNEL	TdT-mediated dUTP nick end labelling
WP	whole proteome

1. Introduction

Ciliopathies are rare genetic disorders which, collectively, affect millions of patients worldwide. These disorders frequently involve multiple organs and tissues, with the kidneys being commonly affected e.g. chronic kidney disease (CKD). However, the role of cilia in the development and maintenance of kidney architecture and function is not fully understood. Therefore, it is important to investigate renal ciliary functions, especially as defects can cause cystic kidney diseases. One potential process underlying CKD and the accompanied loss of tubules and inflammation could be regulated cell death (RCD). RCD comprises a network of interconnecting pathways, like apoptosis, necroptosis and pyroptosis. Taken together, it is crucial to understand how the cilium influences these processes of cell death in the context of CKD. This could lead to novel strategies to protect renal cells from damage and cell death, improve regenerative responses, and ultimately ameliorate the devastating consequences of renal disease. Unravelling the intricate mechanisms not only expands our fundamental understanding of renal ciliopathies, RCD and the primary cilium, but also provides tangible benefits to patients worldwide, offering hope and new opportunities in the field of medicine and renal disease.

1.1 Primary cilium

The primary cilium is a highly specialized microtubule-based sensory organelle which extends from the apical surface of most mammalian cells, including fibroblasts and neurons [1,2]. This evolutionarily conserved structure was first discovered in 1675 [3,4]. However, it took almost 200 years until they were observed in the kidney for the first time, and eventually the term 'cilium' was introduced in reference to its microscopic, hair-like structure [5,6]. As another century passed, primary cilia (dys)function was found to be linked to human diseases [7,8]. At the same time, the term ‘cilium’ was more specifically differentiated, distinguishing single unfrequented immotile ‘primary’ cilia from multiple ‘motile’ cilia [9].

The architecture of the primary cilium consists of the axoneme, the basal body complex (BB) and the transition zone (TZ) (**Fig. 1 A**)**.** The shaft of the cilium (axoneme) contains nine outer doublets of microtubules (MT) arranged as a ring, lacking a central MT pair (9+0), which is covered by a ciliary membrane [10]. Recently, cryo-electron tomography of primary cilia on resin-embedded MDCK-II cells, discovered that the arrangement of “9+0” can be found only at the very base of the primary cilium before resolving towards unstructured small MT-binding protein (EB1)-decorated microtubules and actin filaments [11]. The TZ is situated between the BB and the axoneme, and acts as a highly specialized gatekeeper, controlling the entry and exit of proteins in and out of the axoneme [12]. This zone is characterized by the Y-shaped linkers, attaching the outer doublets to the ciliary membrane [13]. In some cell types, in proximity to the primary cilium, there are two membrane invaginations at the same height as the TZ, so-called ciliary pockets (CP). These CP are rich in budded clathrin and connect the periciliary

to the ciliary membrane [14,15], linking the primary cilium to the actin cytoskeleton [16,17]. The function of the CP is thought to be to be equal to the function of '*flagella* pockets' within endo- and exocytosis and vesicular-trafficking activity [15]. However, the appearance of the CP has been postulated as a consequence of two distinct pathways of primary ciliogenesis dependent on the proximity of the centrosome to the plasma membrane [17,18]. Although they are found with a low frequency in mouse-derived inner medullary collecting duct cells (mIMDC3) [15], polarized renal epithelial cells like Madin-Darby canine kidney cells do not have a CP [19,20]. It is clear that the CP is organized differently in different cell types [21]; for this reason, little is known regarding the mechanism and the occurrence of these pit-like structures. The BB anchors the cilium to the cell and consists of a mother and a daughter centriole surrounded by pericentriolar material (PCM) [22]. This complex is required to assemble and disassemble the primary cilium. The distal appendages are required for the mother centriole to attach preciliary vesicles during ciliogenesis [23]. The subdistal appendages anchor the BB to the MT network and regulate the position of the primary cilium [24].

Overall, the primary cilium is a complex structure with a highly specified and highly dynamic protein composition. Besides the evolutionary conserved fundamental role in development and tissue homeostasis, this organelle can be found in almost all cells, influencing novel and tissue-specific functions [25,26]. Disruption of the machinery caused by pathogenic variants of ciliary proteins leads to defects and subsequently to disease patterns in different organs and tissues.

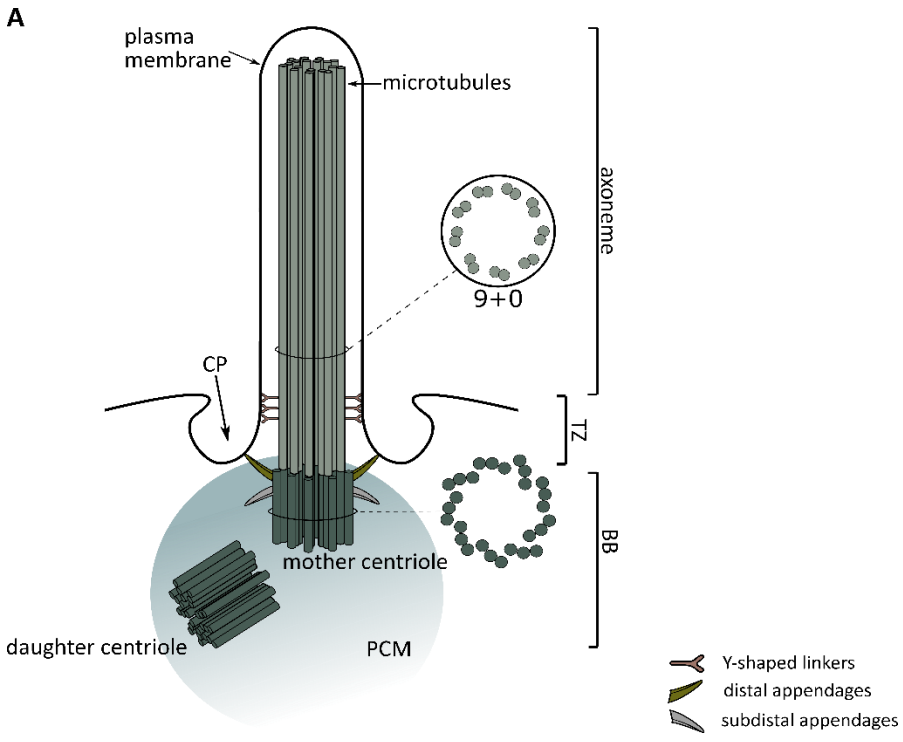

Figure 1 ***The primary cilium. A.*** *Schematic overview of the 9+0 primary cilium. PCM: Pericentriolar material; TZ: Transition zone; BB: Basal body complex; CP: Ciliary pocket.*

1.1.1 Ciliary dynamics

Primary cilia have one feature which is unique among organelles: they periodically appear and disappear during the cell cycle. This process of ciliogenesis is directly connected to mitosis and, therefore, proliferation. The assembly of the primary cilium occurs in the late G_1 phase (**Fig. 2 A**), when the BB migrates towards the plasma membrane [27]. This is inducible *in vitro* by serum starvation, through which cells uniformly synchronize [28]. After docking to the actin-rich cortex, the outgrowth of axonemal microtubules is induced. The assembly and length of the cilium are controlled by multiple cilium-associated disease genes e.g. tuberous sclerosis 1 (*Tsc1*), *Tsc2* [29,30], *Retinitis pigmentosa* 1 (*RP1*) [31] or the nephronophthisis-related protein nephrocystin 4 (NPHP4) [32,33], but mainly through intraflagellar transport (IFT). IFT transports signalling molecules to and along the primary cilium since no translation occurs in the ciliary compartment [34]. Thereby, the bi-directional movement is organized by IFT-A, IFT-B (intrinsically divided into IFT-B1 and IFT-B2) and the BBSome complex [35,36]. Each IFT complex is composed of multiple proteins polymerised into functional trains responsible for transporting cargo along microtubule tracks within the cilium. The transport is initiated by the autopolymerisation of the IFT-B complexes which act as the binding platform for IFT-A, dynein-1b, and, finally, kinesin-2 [37]. During anterograde transport, the IFT complex is transported via kinesin into the cilium and along the axoneme to the tip [38]. Before entering, structural or signalling cargos are transported to the base of the cilium through the BBSome complex and then attach to the IFT train [39]. At the tip of the cilium, the IFT complex undergoes conformational changes into the retrograde train and, through dynein-1b, it is transported back to the ciliary base, carrying a new selection of cargos [40]. Intermediate-resolution cryo-electron tomography revealed that each of the 20 IFT proteins has its own specific and fundamental role [38], which substantiates that a disturbance leads to an imbalance and consequently to disease. One example is IFT88, an IFT-B1 complex protein whose C terminus is required for the docking to the C terminus of IFT144 in IFT-A [41]. When mutated, the tethering between IFT-B and IFT-A becomes loose and the machinery does not work properly resulting in aberrant primary cilium assembly. In this case, IFT88 dysfunction triggers downstream polycystic kidney disease (PKD) [8]. Other cilia-related genes prevent cilia assembly upon dysfunction, e.g. *kinesin family member 3a (Kif3a)* [31,42]. Kif3a deletion is also known to induce PKD, besides other symptoms [43,44], by inhibiting renal ciliogenesis, as it is important for the anterograde transport mediated by kinesin-II, the heterotrimeric protein composed of two motor subunits (KIF3A and KIF3B) [45]. Hence, disruptions in the assembly of primary cilia prevent ciliary signalling and support cell proliferation.

Primary cilium function is also significantly dependent on ciliary length. The length is determined by disassembly-proteins, which are regulated by their own signal transduction pathways [46–48]. Disassembly has been observed in a biphasic manner: the first wave after growth factor

stimulation (G_0/G_1-S transition), and the second phase right before mitotic onset [49]. Within this process, the primary cilium length decreases, which is tightly regulated by Aurora kinase A (AURA) and polo-like kinase 1 (PLK1) activity, after the cells re-enter the cell cycle from G_0/G_1 [50]. Two main proteins have been described as regulators of AURA: Pitchfork [51], a protein associated with the basal body; and human enhancer of filamentation 1 (HEF1) [52], a scaffolding protein. AURA and PLK1 synergistically activate histone deacetylase 6 (HDAC6), which functions as an α-tubulin deacetylase [52,53]. This enzymatic activity facilitates the deacetylation of ciliary microtubules during the intricate process of ciliary disassembly [54] (**Fig. 2 B**). Another regulator of AURA is the histone deacetylase 2 (HDAC2), whereby inactivation of HDAC2 leads to a decrease of AURA expression and, therefore, elongation of the primary cilium [55]. This cascade is under the control of the casein kinase 2 (CK2) [56]. However, other proteins are also involved in the disassembly process, for example, von Hippel-Lindau (VHL), and glycogen synthase kinase beta (GSK-3β) [57]. Consequently, defects in cilium disassembly have been reported to cause imbalanced ciliary signalling, axoneme elongation and to suppress re-entry into the cell cycle.

Primary cilia function as dynamic organelles, perpetually undergoing assembly and disassembly processes. This process of is significantly regulated by the ciliary function as a cell cycle checkpoint regulator. In the G_1/G_0, of the late S-phase or early G_2 phase, depending on the cell type, the cilium reassembles, and the BB is duplicated. The BB is utilized as a microtubule-organization centre (MTOC) and turns into the centrosomes of the spindle poles during mitosis [58]. Consequently, primary cilia are absent during mitosis and the occurrence of the primary cilium is conventionally denoted as a ciliary checkpoint within the cell cycle (Bettencourt-Dias et al., 2011). Given that, there are phases in the cell cycle, in which cells are ciliated or unciliated, this creates specific time points for signalling targeting. One process is through budding of extracellular vesicles from the ciliary membrane to transmit signals into the extracellular matrix, which can then be absorbed by other cilia [59]. This indicates that other signalling mechanisms, besides IFT, are indispensable for vital embryonic development and tissue homeostasis. Disruption of the primary cilium machinery can be either characterized by the total absence or by a shortening or prolongation of the primary cilium. These diverse patterns of affected and dysfunctional primary cilia lead to a various spectrum of pathological conditions including e.g. retinal degeneration, obesity and cystic kidney diseases [60–62].

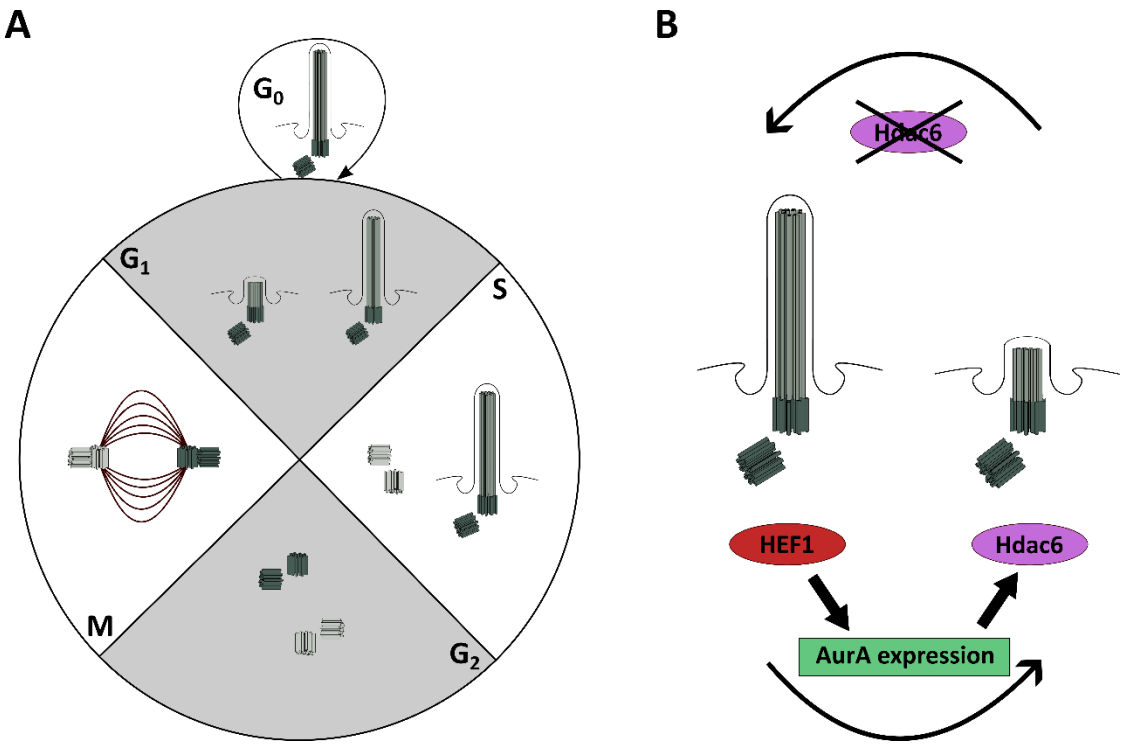

Figure 2 ***Ciliary dynamics. A.*** *Cell cycle-related ciliogenesis (Adapted schematic [49]) .* ***B.*** *Under the control of HEF1, AurA is activated, leading to an increase of HDAC6 expression and subsequently to a regression of the primary cilium. Inactivation of HDAC6 leads to an elongation of the primary cilium. Therefore, modulated expression of these proteins could influence the length of the primary cilium.*

1.1.2 Ciliary signalling pathways

In addition to the role in cell cycle regulation and the dynamics of assembly and disassembly, cilia serve as central signalling hubs for the maintenance of homeostasis [63]. This is important as not every ciliopathy displays a phenotypically affected cilium. Disturbance of ciliary signalling can result in the same contribution to ciliopathy development [64]. To fulfil its specific signalling functions, the entry and exit of proteins is strictly regulated. Therefore, the ciliary membrane is composed of various receptors to receive extracellular signals, such as growth factors or hormones. One receptor family found in this membrane are multiple G-protein coupled receptors (GPCRs) [65], for example, somatostatin receptor 3 (SSTR3) [66], melanin-concentrating hormone receptor 1 (MCHR1) [67], serotonin receptor 6 (5HTR6) [68], and kisspeptin 1 receptor (KISS1R) [69]. These receptors are important for ciliary signalling [70], like neuronal ciliary function and are, therefore, essential for normal brain development [34]. Important signalling pathways and their related signalling proteins include members of *hedgehog* (Hh) [71,72], Platelet-derived growth factor (PDGF) receptor (PDGFR) [73] and *wingless* (Wnt) signalling pathways [74].

Hh signalling is important for normal organ development, cell proliferation and stem cell homeostasis [75], and it is initiated by three ligands: Sonic-Hh (Shh), Indian-Hh (Ihh) and Desert-Hh (Dhh)

[76–78]. Each of the ligands has a specific function when binding to Hh receptors. The first identified receptor was Patched (PTCH) [79]. PTCH is a transmembrane protein which constitutively represses Hh signalling. The binding of the Hh ligand to PTCH inhibits the repression of the GPCR superfamily member: Smoothened (SMO). Subsequently, zinc-finger proteins of the glioma-associated oncogene transcription factors (GLI) family are activated, and, as transcription factors, they can influence transcription. Therefore, the transport of GLI into the nucleus is key in Hh signalling [80]. Importantly, several human diseases, which display symptoms characteristic of defective Hh signalling, are caused by photogenic variants of ciliary components [81]. PDGFR signalling is also described as one of the cilia-associated signalling pathways and is important for directional cell migration of fibroblasts in wound healing [73]. During G_0 fibroblasts, mesenchymal-derived cells, and PDGFR-α are located around the primary cilium to activate the MEK1/2-ERK1/2 and Akt pathways [82]. PDGF is a dimeric glycoprotein that can be composed of two A subunits (PDGFaa) which bind as ligand to the PDGFR-α receptor at the ciliary membrane [83]. Through this, MEK1/2 becomes phosphorylated within the cilium, at the basal body. Thereby, PDGFaa induces the translocation of inversin (INVS) to the basal body and, further, to the CP to interact with the active phosphorylated (p)-Akt [84]. As a result, PDGFRs have been linked with the resorption of cilia, and, therefore, as a key step in cell cycle progression. The accompanying regulation of INVS and Akt levels leads to a functional development and signalling of the primary cilium. However, if the cilium fails to generate PDGFRs, the increased PDGFaa levels enhance the localisation of INVS-p-Akt to the basal body, and as a consequence, the loss of Akt reduces cilia growth [84]. The Wnt signalling pathway has a similar significance, being activated during normal injury repair, and kidney development [85,86]. This pathway is separated into the canonical (β-catenin dependent) and non-canonical (β-catenin independent) pathways [87]. In the canonical pathway, β-catenin translocates into the nucleus, where it binds to either T-cell factor (TCF 1, 3, 4) or the lymphoid enhancer factor (LEF) to activate downstream target genes like cyclin-D1, c-Myc, and Axin-2 [88–90]. Interestingly, over the last couple of years, research has shown an interaction between nuclear factor 'kappa-light-chain-enhancer' of activated B-cells (NF-κB) signalling and the canonical Wnt pathway, consequently linking Wnt to inflammation [91,92]. Otherwise, the non-canonical Wnt pathway is initiated by the binding of Wnt to Frizzled (FZD) and, subsequently, to diverse co-receptors, revealing five potential Wnt pathways [93–96]. Interestingly, mutations in the non-canonical Wnt pathway, e.g. in *Wnt5a*, show urogenital defects in the kidney and urinary tract [97]. All of these pathways are initiated by the primary cilium and are involved in fundamental processes. Disruption of the system leads to critical consequences for cell growth, differentiation, and functionality of organs, in particular the kidney.

1.1.3 Ciliopathies

A large group of inherited genetic disorders and syndromes, summarised under the umbrella term 'ciliopathy', are caused by mutations in ciliary- and ciliopathy-associated genes [98–100]. These result in defects in the assembly, maintenance or function of primary cilia. Nevertheless, the pathomechanisms underlying ciliopathies remain unclear although they have been extensively studied, for example, in genetically engineered flies or mice. Taking the widespread occurrence of the primary cilium on the surface of almost all mammalian cell types into account, the large variety of overlapping phenotypes, e.g. retinopathy, polydactyly and obesity, in different described ciliopathies is not surprising (**Tab. 1**) [101–105]. This significant range of overlapping symptoms is caused by the distinct functions of the primary cilium. In special cases the function is additionally related to specific organs or cell types, one example being the photoreceptors of the eye. The photoreceptor cells of the retina exhibit a highly modified primary cilium, namely the connecting cilium and the outer segment. The connecting cilium hereby corresponds to the ciliary transition zone and the entire outer segment is equivalent to the ciliary axoneme [106]. This, however, implies that ciliary defects have a big impact on such specialised cell types and, subsequently, organs. As functional photoreceptors are essential for vision, it is not surprising that retinal degeneration is one of the most common ciliopathy phenotypes. However, photoreceptors are not the only ocular cells displaying a primary cilium and, therefore, having a significant influence on vision. For example, the retinal pigment epithelium (RPE), which is essential for photoreceptor maintenance and survival, needs a functional primary cilium during development to achieve full maturation and functionality [107] . In the *Bbs8* KO mouse, the RPE showed defective polarization and morphology, and thereby displayed a retinal degeneration phenotype [108,109]. However, the primary cilium is also known as a signalling hub and plays a vital role in various developmental signalling pathways. Symptoms like polydactyl, neuronal defects and *situs inversus* manifest during embryonic development, in which the primary cilium has a critical function in guiding cell migration, proliferation and differentiation [110]. Defective Hh signalling through loss-of-function mutations, for example, results in neural tube phenotypes [76], whereas gain-of-function mutations can lead to polydactyly [111]. Mutations in the ciliary polycystin-1-like protein (PKD1L1) are described to cause *situs inversus* [112]. In addition, it is known that PKD1L1 interacts with the PKD causing protein polycystin-2 (PKD2) [113]. In short, any imbalance in primary cilia function has a significant influence on a living organism. However, among all the symptoms of ciliopathies, the kidney is the most affected.

Table 1 ***Ciliopathies and their phenotypes.***

		Phenotype										
Ciliopathy	**Abbreviation**	**Cognitive impairment**	**Posterior fossa defects/ encephalocoele**	**Obesity**	**Bone malformation**	**Polydactyly**	**Retinopathy**	**Deafness**	***Situs inverus***	**Craniofacial abnormality**	**Hepatic disease**	**Renal cysts**
Leber Congenital Amaurosis	LCA	●					●				●	
Polycystic kidney disease	PKD										●	●
Nephronophthisis	NPHP										●	●
Bardet-Biedl syndrome *	BBS	●	●	●		●	●	●	●	●	●	●
Meckel-Gruber syndrome *	MKS		●			●	●		●	●	●	●
Joubert syndrome *	JBTS	●	●			●	●		●	●	●	●
Senior-Løken syndrome *	SLSN						●				●	●
Juene syndrome *	JATD		●		●	●	●			●	●	●
Oro-facial-digital syndrome	OFD	●			●	●		●		●	●	●
Alström syndrome	ALMS			●			●	●			●	●
Ellis van Creveld syndrome	EVC	●	●		●	●				●		

*** NPH-related ciliopathies**

1.2 Renal ciliopathies

The kidney is an essential bilateral organ, responsible for systemic fluid and electrolyte homeostasis [114]. The overall structure of the kidney is described as having an outer cortical region, a medullary region and the hilum [115] (**Fig. 3 A**). Each human kidneys, contains about 1 million functional units, called nephrons [116,117]. These nephrons are comprised of a microvasculature filtration unit, the so-called glomerulus, and the tubular system, which is divided into the proximal tubule, loop of Henle, distal tubule (each with different segments), and the collecting duct (**Fig. 3 B**). Each of these subunits of the nephron has specific functions. In the glomerulus, about 180 litres of primary urine are generated each day via ultrafiltration of the plasma [118]. Primary urine enters the proximal tubule, where the major part of reabsorption occurs, through the brush borders. Thereby, mainly NaCl, glucose, water, amino acids and some proteins are reabsorbed into the blood [114,119,120]. This occurs alongside the elimination of waste products, like the excretion of creatinine, antibiotics, diuretics and uric acid [121]. Crossing the Loop of Henle, situated in the medulla, urine concentration takes place, as well as further reabsorption of electrolytes, such as sodium, calcium, potassium, and magnesium [122]. Further, the Loop of Henle is responsible for excreting NaCl to regulate the high saline environment in the medullary region. In the distal tubule, calcium and sodium are reabsorbed, but additional secretions of potassium and urea from the surrounding blood vessels occur [123,124]. All of this waste fluid is collected and concentrated in the collecting duct and transported to the ureter through the hilum for secretion [125,126].

Shortly summarized, the kidney is responsible for the selective filtration of metabolic by-products and substances from the bloodstream. Additionally, the kidney is also responsible for other significant roles, for example, in electrolyte and fluid balance. Thereby, the renin-angiotensin-aldosterone system in the kidney orchestrates these electrolytic concentrations within the bloodstream [127,128]. Another example is the regulation of the concentration of erythropoietin, which balances hypoxia or anaemia and also is important for the formation of red blood cells. Furthermore, the kidney mediates essential interactions with several organs to sustain vital functions, including regulation of H_2O balance and thirst, ventilation, potassium balance, erythropoiesis, calcium and phosphate metabolism, and acid-base homoeostasis [120,129].

Many of the cell types in the kidney are ciliated, in particular the cells lining in the nephron tubules and collecting ducts [130]. In 1999, the first specific link of PKD to primary cilia was made by analysing the disease-causing proteins polycystin-1 and -2 (PKD1 and PKD2) [7,131]. PKD1 is a homologue of the *C. elegans* 'location of vulva' (LOV1), proceeding from sensory neuronal cilia, indicating that PKD in human kidneys could be connected to defects in the primary cilia. Later it was described that almost all ciliary proteins are involved in the formation of cystic kidneys [7,8], therefore, kidney diseases display a pronounced genetic overlap. Due to this large cohort of different syndromes all exhibiting kidney

phenotypes caused by ciliary dysfunctions, the term renal ciliopathies was coined. Today, two major and overarching diseases of renal ciliopathies have been described: autosomal dominant polycystic kidney disease, and Nephronophthisis (NPH)-related ciliopathies (NPH-RC). This present thesis focuses in particular on two renal ciliopathies: NPH and NPH-RC Bardet-Biedl Syndrome. However, the main mouse model carrying a mutation in an NPH gene resembles the phenotype of ADPKD. Therefore, the following paragraphs will focus primarily on autosomal dominant polycystic kidney disease (ADPKD), NPH, and Bardet-Biedl Syndrome (BBS).

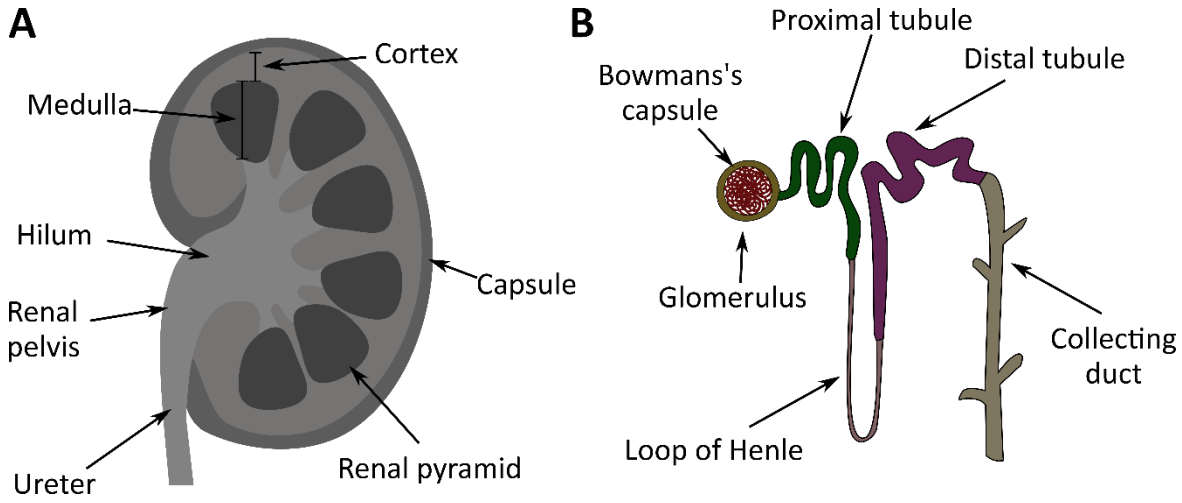

Figure 3 ***The kidney. A.*** *Schematic depiction and anatomy of the kidney* ***B.*** *Anatomy of the nephron.*

1.2.1 Autosomal dominant polycystic kidney disease

Cystic kidney diseases are a group of complex renal disorders characterized by the development and growth of dilated tubules and fluid-filled cysts within the kidney [132,133]. The genetic abnormalities that affect the renal tubular epithelial cells lead to disruptions of the intricate architecture of the renal tubules and varying degrees of impairment in renal function [130]. Most conditions are frequently classified as ADPKD [134,135] and is rooted under the umbrella of PKD associated syndromes. ADPKD occurs with a hereditary prevalence of 1:400-1.000 worldwide [133,136], and is typically diagnosed in early adulthood [137]. Patients with ADPKD present a progressive formation of numerous cysts resulting in massively enlarged kidneys [138], which display a considerable heterogeneity in factors such as cyst number, size, location within the kidneys, symptom severity, and disease progression [139]. In the majority of cases, ADPKD inexorably advances to end-stage renal failure (ESRF), requiring interventions like dialysis and kidney transplantation [133]. ADPKD is caused by mutations in genes for polycystin proteins PKD1 and/or PKD2. PKD1 is located in the primary cilium but can also be found at the plasma

membrane, tight junctions, adherents junctions, desmosomes, and focal adhesions [133]. These proteins are important for many signalling pathways, such as Wnt, Hippo, and mTOR [133,140]. PKD1 is regarded as a cell surface receptor, and with a conformational change of its large N-terminal domain, PKD1 senses the alterations of the extracellular mechanical status. Subsequently, PKD2, which sits not only at primary cilium but also at the endoplasmic reticulum and the plasma membrane, is stimulated and increases the formation of calcium channels to facilitate mechanosensation [141,142]. PKD2 is a nonselective cation channel, among others in the collecting duct, being permeable to Na^+ and K^+ ions. Interestingly, the primary cilium calcium signalling does not react to fluid flow changes [143]. Alterations in the electrolyte balance influence proliferation, cell orientation and differentiation, hence, it is highly likely that RCD is also influenced [144].

To date, mouse models of ADPKD are still a challenge, as heterozygous mutations do not show a phenotype as human dominant heterozygous mutations do. PKD is a hereditary disorder [145,146] and primarily follows a monogenetic pattern, where mutations in single genes play a pivotal role either in a dominant or recessive manner. Autosomal recessive polycystic kidney disease (ARPKD) occurs less frequently (approximately 1:20.000) than ADPKD. ARPKD often progresses to ESRF within the first decade of life in over 50% of cases [147]. Patients typically exhibit cysts predominantly in renal distal tubules and collecting ducts, resulting in kidney enlargement, and hepatic fibrosis, which frequently requires a combined kidney and liver transplantation [147]. The primary genetic causes underlying ARPKD are mutations in the gene *PKD and hepatic disease 1* (*PKHD1*), which encodes for fibrocystin (FC) [148,149]. FC is also known to be localized to the primary cilium and basal body; however, its function remains unclear [150].

1.2.2 Nephronophthisis

In contrast to the enlarged kidneys in ADPKD/ARPKD, kidneys in the pediatric disease Nephronophthisis (NPH) are of a normal or reduced size [151]. NPH is a rare autosomal recessive disease, first described in 1951 [152], with a prevalence between 1:50.000 and 1:900.000 [153–155]. Importantly, patients with NPH are born without a kidney phenotype and the kidneys are not grossly or microscopically conspicuous at this time point. However, NPH is one of the most common genetic causes of ESRF at an average age of 13 years [156]. Thereby, the kidney pathology can be termed a histological triad by cyst formation, inflammation and fibrosis as well as basement membrane disintegration [157]. The ESRF is mainly triggered by the NPH accompanying symptoms, like polydipsia, and polyuria, which are caused by decreased urinary concentrating ability and anaemia [155,157]. NPH is caused by mutations in genes encoding for several NPH proteins (NPHP). So far 20 NPHPs have been identified [158], which in general have been linked to the primary cilium, where the majority are located at the TZ [159,160]. However, more genes, then reported NPHP, are assumed to cause NPH or an NPH-like

phenotype [161,162]. This leads to a phenotypic and genetic overlap of NPH and NPH-RC diseases [158]. The kidney phenotype of NPH, as well as additional the extra-renal manifestations in NPH-RC, are dependent on the affected ciliary gene [151]. However, the cause of NPH and the function of NPHP and NPH-related proteins are still ambiguous; for that reason, there are no specific treatment options available.

The juvenile form of NPH occurs in 21 % of cases, and is mainly described with a pathogenic variant of NPHP1 (average age of ESRF 13 years), whereas the adolescent form, with a mean age of ESRF of 19 years, is commonly caused by NPHP3 [163–165]. The third and rare variant of NPH is called infantile NPH, which displays a severe phenotype already in utero and leads to ESRF within the first year of life [166]. Infantile NPH is displayed by enlarged cystic kidneys and no changes in the tubular basement membrane, in contrast to the other NPH variants.

To study the complex mechanism of ciliopathies and especially NPH, *in vivo* models are crucial. Unfortunately, many NPH mouse models do not recapitulate the human phenotype. Over the last decades many mouse models have been developed, carrying null alleles for *Nphp1-12*, out of which only the *Glis2* (*Nphp7*) displays all hallmarks of human NPH [167,168]. The phenotype of the *Sdccag8* (*Nphp10*) mouse model is at least reminiscent of NPH [169]. The majority of mouse models, however, develop massively enlarged kidneys mimicking the renal phenotype of human ADPKD, contrary to the human pathology of NPH. This was particularly prominent in mice lacking functional alleles of *Nphp3* [170] and *Tmem67* (*Nphp11*) [171]. This ADPKD-phenotype has been also documented in a mouse model carrying a spontaneous juvenile cystic kidney (jck) mutation in the *Nek8* (*Nphp9*) gene, which arose by a double nucleotide substitution 1346G>T and 1348G>T, whereby the second latter leads to valine to glycine non-conservative substitution [172,173]. In contrast to the point mutations, the total knockout of Nphp9 results in perinatal lethality [174]. Overall, it is not surprising that there are differences between mice and human phenotypes as these could be affected by the sterile environment of the mice holding. Furthermore, the function of the conserved proteins in mice and humans can be different, or the protein activity in mice could be compensated by other non-active proteins in human. However, the additional genetic overlap of specific ciliary proteins (BBS16 = NPHP10) makes the investigation of NPH mechanisms much more difficult.

1.2.3 NPH-related ciliopathies

While NPH occurs as an isolated renal phenotype, however it is frequently accompanied by extra-renal manifestations, such as retinopathy, or polydactyly (**Tab. 1**). This group of phenotypically and genetically overlapping diseases is consolidated as autosomal recessive NPH-related ciliopathies [158]. Within this group, we can find associated syndromes like Senior-Løken syndrome (SLSN), Meckel-Gruber syndrome (MKS), Joubert syndrome (JBTS) and Bardet-Biedl syndrome (BBS) [175,176]. BBS depicts

the archetypical ciliopathy, as it shows almost all ciliopathy-related symptoms. This disease was first described by Laurence and Moon in 1866 in a family with *Retinitis Pigmentosa* [177] and was previously referred to as Laurence-Moon-Bardet-Biedl syndrome [178,179]. This rare disorder occurs with a prevalence of 1:100.000 worldwide [180] and is caused by mutations in one of the related BBS genes, encoding for proteins localized to the primary cilium, basal body or centrosome [181], which are important to maintain the structure and the function of the cilium [182]. There is little genotype-to-phenotype correlation, and mutations in any of the BBS genes can cause indistinguishable ciliopathy symptoms [130,183]. However, in some cases BBS1 and BBS10 correlate in the ocular and renal phenotype.

A key aspect in the development of renal ciliopathies, particularly in NPH, is a significant loss of tubular epithelial cells during the course of the disease. Therefore, this work investigates the extent to which pathways of regulated cell death (RCD) might be significant in the pathogenesis of renal ciliopathies. These pathways will be summarized in the following paragraphs.

1.3 Regulated cell death and related signalling pathways

Regulated cell death is a necessary event to maintain homeostasis, and was first discovered in 1842 when Karl Vogt noticed dying cells in toads [184,185]. Following this, more and more reports of dying cells in different organisms, e.g., amphibia and poultry, were published [186]. These early findings of dying cells had already highlighted the importance of the topic and how substantially controlled cell death is for normal development. Dying cells have been observed as part of the normal development of various tissues in many species, including mammals, thus, displaying how fundamental and evolutionary conserved this progress is [187,188]. One pivotal example is the embryonic development of digits (fingers and toes). During embryogenesis, the hand is initially shaped as one related surface, finger digits are formed by the death of cells in between [189]. Similar to this, many other tissues are formed, and in the context of embryonic development the term programmed cell death (PCD) was established. Furthermore, PCD is important to eliminate unrequired or damaged cells, under the control of specific cell death genes [190]. Embryonic PCD does not cause inflammation, therefore, it is mainly referred to as apoptosis. Thus, the role of PCD in physiological and pathological settings is emphasized, and is an attractive target for therapeutic development [191–193]. Non-PCD is defined as occurring by accidental cell death (ACD), initiated by environmental factors like toxins, wounds and infections [194]. However, since many types of so-called ACD have turned out to be strictly regulated, those have been described as RCD, more specifically as stress-driven RCD [195]. Nonetheless, there are still ACD pathways remaining which cannot be impeded by pharmacological or genetic interventions [196]. If a cell is damaged and dying, it sends stress signals, commonly referred as damage-associated molecular patterns (DAMPs) [197,198]. Accordingly, cell death pathways can be classified by the amount of DAMPs released and, thus, the level of inflammation (**Fig.4 A**). Thereby, apoptosis is thought to be the 'clean' death, showing almost no DAMP release and, thus, no inflammation or harm to the surrounding tissue. The level of inflammation starts to increase through pathways such as necroptosis, ferroptosis and pyroptosis, therefore, these are categorized as inflammatory pathways [196,199]. To investigate RCD *in vivo*, examinations of the skin or the kidney are the main focus of research.

The kidney is a particularly well-suited organ to investigate RCD, not only because there are two within the mammalian organisms but also because the kidney can give a clear functional readout. One kidney can be manipulated, for example via pinched off at the single artery, or via ischaemic-reperfused injuries (IRI) to induce acute kidney injury (AKI) without causing a significant systemic effect. This maintains a functional kidney. In comparison, there are other single tissues like the heart, brain or liver, which have a more complex connection to the cardiovascular system, and are, therefore, more difficult to manipulate. To understand how RCD is involved in kidney damage and how the individual pathways contribute to renal diseases, progress has been made in developing mouse models

or treatments. Especially renal cell death in AKI, which has a rising incidence with approximately 13.3 million people each year [200], is providing new insights into this field.

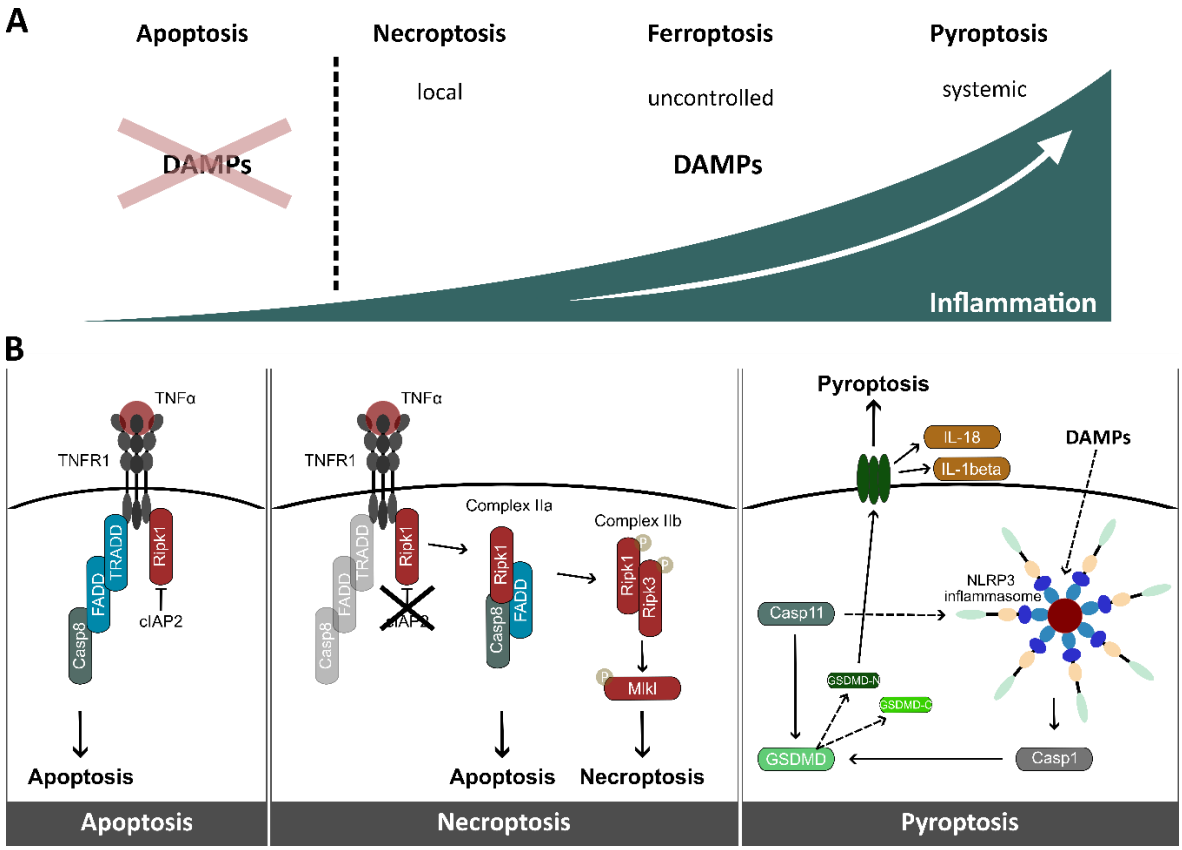

Figure 4 ***Regulated cell death and correspondent level of inflammation. A.*** *Damage-associated molecular patterns (DAMPs) are released upon cell death and vary due to local or systemic inflammation, or even uncontrolled DAMP release. This inflammation increases in inflammatory pathways like necroptosis, ferroptosis and pyroptosis. Adapted schematic* [199]. ***B.*** *RCD pathways, apoptosis and necroptosis are shown with the induction through the TNF receptor. Within the apoptotic pathway, the formation of complex IIa/b is blocked by cIAP2 and, therefore, FADD can activate Casp8, which finally leads to cell death. Upon blocking cIAP2, the formation of either complex IIa or IIb is common. Complex IIa still leads to Casp8 activation and, therefore, to apoptosis. The additional blocking of Casp leads to the complex IIb formation. Here Ripk1 and Ripk3 become autophosphorylated to subsequently phosphorylate Mlkl which, through pore formation, leads to DAMP release and inflammation. Pyroptosis is activated upon e.g. bacterial stimuli, DAMPs or Casp11 activation, which leads to the inflammasome formation. Subsequently, Casp1 is activated and leads to cleavage of GsdmD. The hereby cleaved GsdmD-N is transported to form a pore in the plasma membrane.*

1.3.1 Apoptosis

Apoptosis is referred to as 'cell suicide' and is important for normal tissue development [201]. The term apoptosis was first coined by John Kerr [202] and is derived from the old Grecian word ἀπόπτωσις (apoptosis), meaning "falling off", such as leaves from a tree [203]. Apoptosis can be divided into extrinsic and intrinsic pathways, which are both completely dependent on caspase proteins. Caspases (Casp) have proteolytic activity and cleave proteins. There are three main types of caspases described: initiators (Casp2,8,9,10), effectors or executioners (Casp3,6,7), and inflammatory caspases (Casp1,4,5) [204,205]. Casp11-14 are further described with different functions [206–209]. However, not all Casp proteins play a role in apoptosis, such as Casp1/4/5/11. The intrinsic pathway is initiated by internal stress factors, like DNA damage or biochemical stress, whereas the extrinsic pathway acts in response to extracellular stress, such as ligand binding to 'death' receptors on the cell surface (**Fig. 4 B**). Both pathways lead to cell shrinkage, collapse of the cytoskeleton, release of apoptotic bodies, disassembly of the nuclear envelope, and DNA degradation mediated by caspase proteins [210]. The intrinsic apoptosis pathway affects the inner mitochondrial membrane and subsequently leads to the loss of the mitochondrial transmembrane potential and the release of cytochrome C and Smac/DIABLO [211]. The final 'apoptosome' is formed of cytochrome C which binds and activates Apoptotic protease activating factor-1 (APAF-1) as well as Casp9 [212]. In order to activate apoptosis, Smac/DIABLO inhibits the inhibitors of apoptosis proteins (IAP) [213]. This leads to the release of a second group of proteins from the mitochondria, e.g. apoptosis inhibitor factor (AIF), and caspase-activated deoxyribonuclease (CAD), under the control of the Bcl-2 family of proteins which can be separated in anti-apoptotic proteins (Bcl-2, Bcl-x, Bcl-XL, Bcl-XS, Bcl-w, BAG), and pro-apoptotic proteins (Bcl-10, Bax, Bak, Bid, Bad, Bim, Bik, Blk) [214–216]. AIF translocates to the nucleus and causes DNA fragmentation, referred to as "stage I" condensation [217]. The oligonucleosomal DNA fragmentation and advanced chromatin condensation by CAD, activated through cleavage through Casp3, is referred to as "stage II" condensation [218]. The extrinsic pathway is triggered by death receptors, which define the secondary cascade of apoptosis, e.g. the tumour necrosis factor (TNF) pathway or the fatty acid synthetase (FAS) pathway [219]. The homologous trimeric ligand binds to the death domain of the receptor to initiate a caspase cascade. Here, cytoplasmic adaptor proteins, such as TNF receptor-associated death domain (TRADD) and Fas-associated death domain (FADD), bind to the specific receptor complex to form the death-inducing signalling complex (DISC) [220]. This leads to Casp8 activation, which, in turn, triggers the caspase cascade, culminating in apoptosis. In terms of controlling the process of death receptor-mediated apoptosis, c-FLIP can bind to FADD and Casp8 to inhibit the follow-up cascade [221].

1.3.2 Necroptosis

Necroptosis is a lytic and caspase-independent pathway, which typically causes massive local inflammation and DAMP release. It has been described by studies on its three key proteins (**Fig. 4 B**): Receptor Interacting Serine/Threonine Kinase 1 (RIPK1) [222], RIPK3 [223] and Mixed lineage kinase domain-like protein (MLKL) [224]. These three classical 'necroptosis proteins' work together in a cascade to trigger inflammation. Initiation of necroptosis through the TNF superfamily receptors, the toll-like receptors (TLR3 and TLR4), or through the ligand-bound TNF receptor 1 ($TNFR_1$) is well characterized, of which the latter is the classical and also best described pathway of necroptosis [225]. $TNFR_1$ is responsible for controlling the downstream response of cell survival, apoptosis and necroptosis [226] upon TNFα binding. Binding of TNFα leads to the short-lived membrane signalling complex: complex I [227]. Within Complex I, TRADD recruits RIPK1 to $TNFR_1$, which leads to the reinforcement by binding the cellular inhibitor of apoptosis 1 and 2 ($cIAP_1$/$cIAP_2$), as well as tumour necrosis factor receptor-associated factors ($TRAF_{2/3/5}$) into the complex. Complex I is stabilized by $cIAP_{1/2}$ and $TRAF_{2/5}$ mediated ubiquitination of RIPK1, which leads to the alternative pathway of cell survival: NF-κB and the mitogen-activated protein-kinases (MAPK) mediated pathway [228,229]. NF-κB counteracts the cytotoxic effect of TNFα, and lead to pro-survival, mediated by $cIAP_{1/2}$ and c-FLIP [230]. Thereby, cellular FADD-like IL-1β-converting enzyme-inhibitory protein (c-FLIP) is responsible for inhibiting Casp8, and, therefore, execution of apoptosis, whereas cIAP blocks the formation of complex IIb by inhibition of RIPK1. The formation of complex IIa (TRADD, FADD and Casp8) or complex IIb (RIPK1, RIPK3, FADD and Casp8) can both lead to the activation of apoptosis. As soon as c-FLIP inhibits Casp8, which blocks the activity of RIPK1 and RIPK3, complex I becomes destabilized through deubiquitination of RIPK1 [231]. Thus, RIPK1 interacts with FADD, TRADD and RIPK3, and forms the complex IIb. RIPK1 interacts with RIPK3 through receptor homology domain (RHD) and, therefore, forms the necrosome [232]. Upon recruitment and phosphorylation of Ser227 (mouse: Thr231/Ser232) of RIPK3 by the active autophosphorylation [225,233], MLKL could bind to the necrosome (complex IIc) [234]. Importantly, RIPK1 is not absolutely necessary for necroptosis activation, resulting in a RIPK1-independent necroptosis pathway. Nonetheless, the autophosphorylation of RIPK1 can trigger TNF-induced necroptosis [235]. Autophosphorylated RIPK3 activates MLKL by phosphorylation and further stimulates the inflammatory response and DAMP release. Phosphorylated MLKL leads to conformational change of the protein and activation. The oligomerization of MLKL [236] promotes its membrane translocation and pore formation accompanied by local calcium influx and, thus, to permeabilization of the plasma membrane, release of cellular components and finally to inflammation [237,238].

1.3.3 Ferroptosis

Ferroptosis, which was described for the first time in 2012 [239], differs significantly from apoptosis and necroptosis in terms of activation and morphological consequence. This iron-dependent pathway is characterized by the key events of lipid peroxidation and iron accumulation, which subsequently leads to plasma membrane rupture [240], but also to a decreased mitochondrial volume and an increase in the membrane density. The process of ferroptosis is initiated by the occurrence of oxidative perturbations in the intracellular microenvironment under the control of a variety of metabolomics and molecular signalling pathways [241]. More specifically, lipid peroxidation by reactive oxygen species (ROS) is constitutively regulated by the activity of the glutathione peroxidase 4 (GPX4) in which GPX4 catalyses the reduction of lipid peroxide [242]. Loss of GPX4 leads to an increase in the depletion of glutathione (GSH) and, therefore, to an increase of glyceraldehyde-3-phosphate dehydrogenase (NAPDH) oxidation, as well as pro-inflammatory DAMP release [243].

1.3.4 Pyroptosis

Pyroptosis, one of the RCD pathways with high levels of inflammation, was first described in 2000 [244] as the death of infected macrophages by *Salmonella typhimurium.* Nonetheless, the first indications of pyroptotic cell death were found in 1986, where it was described as cell death in primary mouse macrophages, which had been treated with anthrax lethal toxin [245]. Pyroptosis was finally termed in 2001, with the origin of the name coming from the Greek pyro (fire/fever) and ptosis (to-sis, falling), to describe pro-inflammatory RCD [246]. To date, multiple other bacterial triggers have been described to cause pyroptosis [247–250]. Cells undergoing pyroptosis show cell blebbing, chromatin condensation and DNA damage, all similar morphologies to apoptosis. However, pyroptosis additionally presents with cell swelling, osmotic lysis, pyroptotic bodies, pore formation and inflammation [251]. Pyroptosis also involves different molecular pathways, like the canonical inflammasome pathway (**Fig. 4 B**) which is composed of Casp1, the adaptor protein apoptosis-associated speck-like protein containing a CARD (ASC), and a sensor protein like the nucleotide-binding oligomerization domain (NOD)-like receptors (NLRs) [252–254]. Thereby, each NLR protein has a specific function. For example, NLRP3 is important for DAMP release, whereas other NLRPs, such as NLRP2/6/12, are important for negative regulation of NF-κB [255]. Casp4/5 (in humans) and Casp11 (in mice) are part of the non-canonical inflammasome pathway, which is activated upon direct sensing of cytosolic LPS [256–258]. In the downstream process, Casp1/4/5/11 catalyse the release of pyrogenic interleukin-1β (IL-1β) and IL-18 [259] by cleavage of Gasdermin D (GSDMD). GSDMD is cleaved at a C-terminal-repressor and N-terminal-pore-forming domain, whereby the N-terminal domain can oligomerize to form pores in the cell membrane with an inner diameter of 18–22 nm and, subsequently, lead to membrane rupture [260,261]. Thereby, the cleavage of GSDMD is

assumed to be coupled with Casp1/4/5/11 [260,262]. Further, there is evidence that Casp8 also plays a role in GSDMD cleavage showing how tightly the different RCD pathways are connected [263]. However, the cell also has mechanisms to protect itself, for example, through cleavage of the GSDMD Asp87 site by Casp3/7, which causes the inactivation of the pyroptotic activity [264]. To date, multiple proteins of the conserved superfamily of gasdermins have been described: GSDMA/B/C/D and GSDME/DFNA5, from which GSDMD and GSDME are the most studied [265].

1.3.5 NF-κB

The NF-κB pathway itself is not a pathway of RCD, however, it has a significant impact up- and downstream of RCD [266]. NF-κB can regulate pro-survival signalling and is important for the activation and differentiation of innate immune cells and inflammatory T cells [267]. In the NF-κB signalling cascade, two proteins of the NF-κB transcription factor family form homo- or heterodimers, the best described dimer in the canonical NF-κB pathway being the NF-κB1/p50 and RelA/p65 heterodimer [268]. These dimers are controlled by inhibitory IκB proteins, out of which IκBα regulates p65/p50 [269,270]. The activation of NF-κB signalling typically occurs in response to extracellular stimuli, such as pro-inflammatory cytokines, e.g. TNFα, or various internal and external stress signals [271]. As soon as the cascade is initiated, the inhibitor IκB is phosphorylated and subsequently degraded by the proteasome [272]. Through this, p65/p50 is released, allowing the translocation of RelA/p65 into the nucleus [270], where it orchestrates gene expression, including genes crucial for kidney health. Thereby, the expression outcome depends on the stimuli that leads to the cascade activation and, therefore, could either induce cell survival or inflammation, production of chemokine and cytokine (e.g. IL-1 or IL-6), together with activation of immune cells, such as macrophages [273–275]. In its pro-survival function, NF-κB induces transcription of anti-apoptotic genes, for example, $cIAP_1$, $cIAP_2$, X chromosome-linked inhibitor of apoptosis (XIAP) and c-FLIP [276]. Therefore, NF-κB signalling is essential for immune response modulation and maintaining tissue integrity [277]. For instance, it regulates the expression of pro-inflammatory genes, such as those encoding cytokines and adhesion molecules, facilitating the recruitment of immune cells to sites of infection or injury [278].

1.3.6 Autophagy

Autophagy is not described as RCD and does not lead to inflammation. Nevertheless, it's correlated to other RCD pathways. Autophagy was first described in 1967 [279] and describes 'self-devouring' derived from the Greek word autóphagos. It is a well-preserved cellular process that occurs through the formation of an autophagosome, which fuses with lysosomes and serves to degenerate cellular constituents into their basic components [280]. Those can be reused by the cell to build new compounds or provide energy. To orchestrate autophagy, multiple key players work together: Autophagy-related

proteins (ATG), which are involved in the formation of the autophagosome, including lipidation of Microtubule-associated protein 1A/1B-light chain 3 (LC3) [281]. LC3 helps to identify and mark cells which are degraded by autophagy and it is essential for autophagosome membrane elongation [282]. Sequestosome 1 (SQSTM1/p62) recognizes and binds ubiquitinated proteins or cellular debris marked for degradation and transports them to the autophagosome [283]. For the final fusion of the autophagosome with the lysosome, lysosome-associated membrane protein 2 (LAMP2) is responsible [284]. The activation of autophagy is controlled by the protein kinase mammalian target of rapamycin (mTOR), whereby active mTOR inhibits autophagy. Autophagy is activated through the inhibition of mTOR by nutrients, or by external or energy stress[285]. However, autophagy-dependent RCD has also been described, which depends on the autophagic machinery. It has been reported that the autophagic receptor optineurin (OPTN) actively influences RIPK1 and, therefore, RIPK1-dependent necroptosis, as the loss of OPTN induces axonal degeneration [286]. Further, LC3 was found to be an interactor of RIPK1 and RIPK3, thus LC3 regulates necroptosis [287]. More broadly, the necrosome is associated with the autophagy machinery, in which p62 recruits RIPK1 and, therefore, actively influences the switch between apoptosis and necroptosis [288].

1.4 Regulated cell death in acute kidney injury

Acute kidney injury occurs suddenly, within a few hours to a few days. In this case, the kidney loses the ability to filter properly and consequentially the fluid and electrolyte metabolism is imbalanced. However, acute kidney failure may be reversible. To this fact, AKI is commonly used to investigate RCD and potential treatment.

It has already been described that apoptosis is increased in normal kidneys during development and constitutes a normal part of development [289]. The first link between apoptosis, renal injury, and various kidney diseases was found in 1992 when apoptosis was discovered directly after renal ischemia [290]. Since then, apoptosis has been linked to AKI, by increased levels of cytochrome-C release, the activity of Casp3 or AIF, and TdT-mediated dUTP nick end labelling (TUNEL) staining [291]. Apoptosis is described as contributing to the loss of parenchymal cells in the kidney but not to inflammation [292]. For proof of concept, several therapeutic interventions targeting the apoptotic pathway were used: zVAD, a known pan-caspase inhibitor, was shown to ameliorate the function of the kidney in multiple AKI animals [293,294]. As this caspase inhibition simultaneously decreased renal inflammation observed in cases of IR or sepsis-induced AKI, it remains unclear which of the two pathophysiological processes, apoptosis or inflammation, is more pertinent in the kidney [295].

Notably, the investigation of necroptosis in IRI should give further insights. Necroptosis leads not only to significant damage and loss of renal cells but also results in inflammation affecting other organs [296]. The importance of necroptosis in IRI was initially demonstrated by treatment with necrostatin-1 (Nec-1; inhibitor of Ripk1), which reduced organ damage and renal failure [297]. However, new studies have revealed that the usage of Nec-1 has to be replaced with Nec-1s (stable). Nec-1 in low dosages is sensitized *in vivo* to TNF-induced mortality, whereas Nec-1s could also be used in low doses with fewer side effects [298]. To date, there are multiple rodent models deficient for necroptosis proteins like *Ripk3* or *Mlkl*. Subsequent investigations using *Ripk3* knockout mice revealed Ripk3 as a crucial mediator in IRI-AKI, with prevented tubular necrosis [299,300]. Work on *Ripk3* and *Mlkl* knockout mice supported the role of necroptosis in AKI, where the loss of these necroptosis signature genes diminished the damage of proximal tubules [301]. Additionally, the accommodating upregulation of TNF-α and interferon-γ (IFN-γ), important promotors of necroptosis, could be proven *in vitro* by inducing necroptosis through a treatment combination of TNF-α and IFN-γ, to mimic the *in vivo* environment. This supports the *in vivo* data of cisplatin-induced AKI which also shows an increase in these pro-inflammatory cytokines [302]. Further indications showed that the deletion of either *Ripk1*, *Ripk3,* or *Mlkl* significantly increases the survival upon IRI [303]. Interestingly, the knockout of *Casp8* is lethal[304], however the double knockout of *Ripk3* and *Casp8* showed 100% survival upon IRI [305]. This

shows that Casp8 plays an important role as a regulator of necroptosis, as it inhibits RIPK3-mediated necroptosis and acts as a control module in the molecular switch for apoptosis and necroptosis [263].

Interestingly, especially AKI upon IRI is described with ongoing necroptosis, supplemented through ferroptosis [306]. Ferroptosis is additionally described as a potential pathway for the death of tubule segments, in which NADP(H) concentrations vary along the renal tubule and become insufficient in preventing lipid peroxidation, accompanied with a wave of calcium [307,308]. Therefore, it cannot be ruled out that ferroptosis is a major contributor to AKI and may play a role in other kidney diseases. Ferroptosis has already been described as a critical player in multiple kidney diseases, as well as in many others, such as those affecting the heart [309]. In different rodent models of AKI, e.g. AKI induced by IRI, cisplatin or folic acid (FA), an accumulation of free iron [310,311] and high levels of renal lipid peroxidation [312] have been observed. Through treatments with ferroptosis inhibitors, it could be shown that these factors are diminished and ferroptosis does indeed play a role in FA- and cisplatin-induced AKI models [313].

The role of pyroptosis in sepsis is well studied, as pyroptosis is described in autoimmune and inflammatory diseases. Nonetheless, there is also evidence for pyroptosis in kidney diseases, suggesting pyroptosis as an effector of AKI. Here, pyroptosis is induced through GSDMD cleavage by Casp11 and IL-1β activation in tubule epithelial cells but also through the NLRP3 inflammasome [314,315]. However, these investigations lacked specificity by not focusing specifically on pyroptosis. Therefore, there is the possibility that this lytic cell death is rather caused by ferroptosis [314]. Further studies describe GSDMD-mediated pyroptosis in cisplatin-induced AKI and IRI-AKI, leading to an increase of Casp11 in the whole-kidney and tubular epithelium and, further, excretion of IL-18 via urine [316]. Mice deficient for *Casp11* or *GsdmD* were successfully protected from cisplatin-induced AKI. Already some studies showed GSDME-mediated pyroptosis in a model of cisplatin-induced AKI [317,318]. Strikingly, the deletion of *GsdmE* in mice leads to ameliorated AKI and inflammation [319], showing an convincing approach. Nonetheless, this result needs to be repeated. In contrast, it was shown that *GsdmD* knockout mice are hypersensitive to AKI, leading to an increase of necroptosis [320]. The additional knockout of *Mlkl* reversed this phenotype. Furthermore, the authors showed that GSDMD is not expressed in isolated mouse kidney tubules but in the peritubular interstitial space. This is important as its shows that the expression of GsdmD is cell type specific, but through the systemic inflammation also the tubules are affected. Other researchers have already proposed a role of RIPK3 in the GSDMD-mediated pyroptosis pathway [321]. Currently, it remains unclear to what extent pyroptosis contributes to AKI and other kidney disorders [322–324].

NF-κB signaling is particularly significant in the context of kidney function, where it contributes to both normal physiological processes and the pathogenesis of kidney diseases [325]. In the context of the kidney, NF-κB signalling and RelA translocation play vital roles in both physiological and

pathological processes. In normal renal function, NF-κB signalling is essential for immune response modulation and maintaining tissue integrity [277]. For instance, it regulates the expression of pro-inflammatory genes, such as those encoding cytokines and adhesion molecules, facilitating the recruitment of immune cells to sites of infection or injury [278]. Additionally, NF-κB signalling helps protect renal cells from apoptosis and oxidative stress [326]. Consequently, dysregulated NF-κB signalling is often associated with the pathogenesis of various kidney diseases, including AKI, CKD and glomerulonephritis [327–329]. Excessive activation of NF-κB and aberrant RelA translocation can lead to sustained inflammation, tissue damage and fibrosis, contributing to disease progression [275]. Furthermore, the therapeutic potential of targeting NF-κB signalling in kidney diseases is often addressed by particularly inhibiting RelA translocation, to potentially mitigate renal inflammation and fibrosis, thus preserving kidney function [330].

To protect the kidney, basal autophagy also plays a fundamental role, to maintain kidney homeostasis, structure, and function [331,332]. Autophagy in IRI leads to ROS and damaged mitochondria [333,334], and therefore, to an altered cell cycle, DNA damage and cell death [335]. As ROS triggers ferroptosis, it is considered that autophagy regulates RCD under stress stimuli [336,337]. This also supports the argument that autophagy is crucial for protecting the kidney after AKI [338]. The deletion of autophagy in mice by knocking out *Atg5* or *Atg7* in proximal tubules resulted in an increase of AKI, indicated by renal functional loss, tissue damage, activation of tumour suppressor p53 and apoptosis [339–341], showing the importance of autophagy in healthy kidneys.

Although, AKI is a good model to study RCD, there are multiple problems. Many RCDs are tightly interconnected and cannot not be investigated individually. Furthermore, the cell specific expression of RCD proteins could not be elucidated and needs to be examined further.

1.5 Regulated cell death in chronic kidney disease

As previously described, RCD plays a fundamental role in kidney development and homeostasis, as well as in kidney pathology. However, most studies regarding RCD in kidney injury are described in (IRI-) AKI. Nonetheless, CKD and AKI are admittedly connected but in principle different. The huge difference between both manifestations is that AKI develops suddenly and can be cured completely due to treatment, whereas CKD develops over time and is described as a gradual loss of kidney function which cannot be reversed. Thereby, AKI increases the susceptibility to gain CKD, whereas CKD promotes AKI showing the direct feedback loop of these diseases. Studies addressing the conversion from AKI to CKD, or to single causes of CKD, are limited so far. It is important to note that CKD presents a distinct and specific set of characteristics compared to AKI, such as anaemia, anxiety, cognitive impairment and high blood phosphate level. The common causes of CKD include, for example, glomerulonephritis, PKD, urinary infections, and nephrotoxins [342], and also diabetes and hypertension [343]. These lead to a variety of final manifestations in CKD of non-resolving inflammation, cystic and malfunctioning kidneys, and fibrosis [344]. Hereditary cystic kidney diseases, which are nowadays regarded as ciliopathies, are one of the causes of CKD. The associated massive loss of tubule epithelial cells in the kidney indicates cell death in cystic kidney diseases and, therefore, in CKD [167]. Limited data have already supported the role of necroptosis, ferroptosis and pyroptosis in CDK.

CKD in rats, caused by subtotal nephrectomy leading to loss of function, could be partially reduced through treatment with Nec-1 (Ripk1 inhibitor) [345]. The identical treatment in mice, with unilateral ureteral obstruction (UUO)-induced CKD, decreased inflammation and fibrosis [346]. The same result of reduction of fibrosis and kidney function in UUO and adenine-induced CKD was observed in the knockout of *Ripk3* [347,348]. Interestingly *Mlkl* knockout mice do not show an amelioration in UUO-induced kidney fibrosis [347], leading to the idea that Ripk3 exhibits extra necroptotic functions. The ferroptosis inhibitor Liproxstatin 1 could additionally decrease UUO-dependent renal fibrosis. Further, the role of pyroptosis in UUO or subtotal nephrectomy was investigated by the knockout of *GsdmE* or *GsdmD* [349–351]. Both deletions alleviated renal fibrosis and improved kidney function. Moreover, it has been shown that pyroptosis causes albuminuria, kidney inflammation, and glomerulosclerosis in the podocyte-specific *APOL1 G2* knockout mice, which is accompanied by an increase of NLRP3, Casp1, and GSDMD cleavage [352]. These symptoms could be pharmacologically prevented through treatment with the small-molecule inhibitor of NLRP3: MCC950 [353]. Patient biopsies with high-risk *APOL1* genotypes confirmed the NLRP3 inflammasome-activated pyroptosis in podocytes [352]. The presence of *APOL1* risk alleles further induces albuminuric nephropathy, which could be prevented by treating the mice with disulfiram, a pyroptosis inhibitor [352]. Further genome analysis of CKD revealed the expression of *Dpep1* and *Chmp1a*, which are key regulators of ferroptosis [354]. More specifically, ferroptosis was

found in diabetic nephropathy, in which the ferroptosis-related inhibitor molecule GPX4 is decreased [355]. This was also observed in the context of fibrosis [356]. Dysregulation of iron exporters and a decrease of GPX4 were found in ADPKD through *Pkd1* deficiency [357]. Interestingly, Nec-1 treatment of ADPKD with a deletion of *Pkd1* aggravated the disease [358]. There was evidence that autophagy is also relevant for CKD, because an increased synthesis of LC3 and formation of the autophagosome was found in patient material [359].

The role of RCD in CKD seems to be more complex than in AKI, as the cell death dynamics are modulated and occur over a longer time period. However, one problem in the rodent models is that they do not mimic the full complexity of human CKD. However, RCD in CKD is overall just loosely described and needs to be investigated further to be considered as a potential therapeutic target.

1.6 Thesis Aims

Cystic kidney disease is caused by pathogenic variants of ciliary proteins and characterized by loss of function of the primary cilium. Both the primary cilium and RCD play essential roles in embryonic development but also in tissue homeostasis in adults. For cystic kidney disease, the role of cilia in pathogenesis is well established. The massive loss of epithelial cells suggests that RCD might play a major role as well. This current thesis aims to comprehensively explore and understand the influence of the primary cilium on RCD and the *in vivo* role of RCD in models of ciliopathies. Beyond unravelling a potential connection between cilia and RCD, it aims to provide novel insights into the disease mechanism, which might help to develop future treatment strategies for patients with renal ciliopathies. In particular, this thesis follows three aims:

(1) Unravelling the impact of the primary cilium on regulated cell death

As the connection between the primary cilium and RCD has not yet been described, this thesis aimed to unravel a potentially intricate relationship between the primary cilium and RCD. For this, ciliated and non-ciliated subclones of the mIMCD3 were treated with cell death inducers or inhibitors. These experiments and their in-depth analysis shed light on the impact of the primary cilium and its role in the fundamental biological processes of RCD.

(2) Examining the effect of cell death pathways in murine models of renal ciliopathies

Many studies have shown that RCD plays a role in AKI, however, the role in CKD has not yet been extensively investigated. To that end, this thesis examined the role of RCD in renal ciliopathies in relation to the functionality of the primary cilium. The *Nek8*^{jck} mouse, which displays a PKD-like phenotype in a genetic NPH background, develops a severe renal phenotype early in life. Through the additional knockout of crucial RCD genes, we were able to examine the potential influence of RCD in developing the severe phenotype in the context of a defected primary cilium.

(3) Investigation of the archetypical renal ciliopathy Bardet-Biedl Syndrome (BBS) *in vivo*

The third aim expanded the focus of this thesis to another renal ciliopathy, BBS. The loss of the ciliary protein *Bbs8 in vivo* affects the functionality of the primary cilium and, in consequence, should potentially lead to a renal phenotype. The goal was to characterize the *Bbs8*$^{-/-}$ phenotype and the potential involvement of RCD. This is important to create a better understanding of the mechanisms, and, therefore, improved insight into potential treatments, for either overarching renal ciliopathies or adapted for specific renal ciliopathies.

2. Material and methods

2.1 Material

2.1.1 Chemicals and reagents

Table 2 ***Chemicals and reagents used.*** *All reagents are listed with their respective company and product numbers. Trivial names and/or molecular formulas in brackets.*

Reagent	Product no.	Company
0.05% Trypsin-EDTA Solution (1X), cell culture	25300-054	Gibco
0.9% Isotonic NaCl solution	19PCA510	Fresenius KABI
Acetic acid	7332.1	Carl Roth
Acetonitrile	701881	AppliChem
Agarose	A9539	Sigma-Aldrich
Ammonium bicarbonate (TEAB)	A6141	Sigma-Aldrich
Ammonium persulfate (APS)	A0834	AppliChem
Ampicillin Sodium Salt	K029.2	Carl Roth
Aprotinin	A162.1	Carl Roth
Benzonase® Nuclease	70746-3	Millipore
Birinapant	SEL-S7015	Biozol
Bovine Serum Albumin (BSA)	1066	Gerbu
Bromphenol Blue	A512	Carl Roth
Calcium chloride ($CaCl_2$)	HN04.2	Carl Roth
Casy Clean	5651786001	OMNI Life Science
Casy Ton	5651808001	OMNI Life Science
Chloroacetamide (CAA)	8.02412.0100	Merck
Citric acid monohydrate	27490	Fluka
cOmplete™ EDTA-free Protease Inhibitor Cocktail	4693132001	Roche
Coumaric acid	C9008	Sigma-Aldrich
Cycloheximide	C4859	Sigma-Aldrich
Dextran T 250	9233.1	Carl Roth
Dimethyl sulfoxide (DMSO) for cell culture	A3672,0100	AppliChem
Dithiothreitol (DTT)	6908.1	Carl Roth
Dithiothreitol (DTT) (Mass spec)	A1101,0025	AppliChem
DiYO-1	ABD-17580	Biomol
DMEM-F12	D6421	Sigma-Aldrich

DNase/RNase-Free Distilled Water	15657708	Thermo Fisher Scientific
dNTP Mix (10 mM each)	R0191	Thermo Fisher Scientific
Dulbecco's Modified Eagle Medium (DMEM)	D6429	Sigma-Aldrich
Emricasan	SEL-S7775	Biozol
Ethanol (99.8%) (EtOH)	9065.3	Carl Roth
Ethidium bromide solution	2218.1	Carl Roth
Ethylenediaminetetraacetic acid (EDTA)	E5134	Sigma-Aldrich
Fetal Bovine Serum (FBS)	S 0115	Biochrom AG
Formaldehyde 4%	200-01-8	Walter CMP GmBH & Co
Formic Acid	94318	Fluka
GeneRuler 1 kb DNA Ladder	SM0311	Thermo Fisher Scientific
GeneRuler 50 bp DNA Ladder	SM0372	Thermo Fisher Scientific
Glucose	G7021	Sigma-Aldrich
GlutaMAX	35050061	Thermo Fisher Scientific
Glycerol	3783	Carl Roth
Glycine	3908.2	Carl Roth
Go Taq G2 Flexi Polymerase	M7808	Promega
GSK-872	HY-101872	Sigma-Aldrich
Halt Protease & Phosphatase Inhibitor Cocktail (100x) (PPI)	78444	Thermo Fisher Scientific
Heparin Natrium solution	15782698	Braun
HEPES	H0887	Sigma-Aldrich
Histomount	HS-103	National Diagnostics
Hoechst 33342 Solution (20 mM)	62249	Thermo Fisher Scientific
Hydrogen chloride (HCl)	T134	Carl Roth
Hydrogen Peroxide (H_2O_2) 30%	107209	Merck
IgePAL CA-630	I8896	Sigma-Aldrich
Incidin PLUS	225194	Igefa
Interferon-γ (IFN-γ)	315-05	PeproTech
Isopropanol	5752.3	Carl Roth
KH_2PO_4	P5655	Sigma-Aldrich
Ketaminhydrochlorid (Ketamin)	40031018	Zoetis
LB-Medium	X964.2	Carl Roth
LB-Agar	X965.1	Carl Roth
Leupeptin	108975	Sigma Aldrich

Luminol	09253	Fluka
Magnesium sulphate heptahydrate ($MgSO_4$)	P027.2	Carl Roth
Magnesium chloride ($MgCl_2$)	1.05833.0250	Merck
Methanol (MtOH)	4627.5	Carl Roth
Meyer's hematoxylin solution	A0884	AppliChem
N,N,N´, N´-tetramethylethylenediamine (TEMED)	2367.3	Carl Roth
NEBuffer™ 3.1	B7203	New England Biolabs
Necrostatin-1s	221984	Abcam
Neutral-red	C.I.50040	Sigma-Aldrich
Normal Donkey Serum (NDS)	017-000-121	Dianova
Oxidized L-Gluthathion	G4376	Sigma Aldrich
PageRuler Plus Protein Ladder	26620	Fermentas
Penicillin-Streptomycin 10,000 U/mL (Pst)	15140-122	Thermo Fisher Scientific
Periodic acid (99%)	3257.1	Carl Roth
Phenylmethylsulfonyl fluoride (PMSF)	A0999	AppliChem
Phosphate buffered saline	15374875	Thermo Fisher Scientific
PhosSTOP™	4906845001	Roche
Polyacrylamide (PAA)	T802.1	Carl Roth
Potassium chloride (KCL)	6781	Carl Roth
ProLong™ Diamond w/o DAPI	P36965	Thermo Fisher Scientific
ProLong™ Diamond with DAPI	P36962	Thermo Fisher Scientific
REDTaq® Ready Mix	R2523	Sigma-Aldrich
RNase Inhibitor, murine	M0314L	New England Biolabs
RNase-free water Ultra Pure	10977-035	Thermo Fisher Scientific
RNaseOUT™ Recombinant RNase Inhibitor	10777-019	Thermo Fisher Scientific
Ropun® 2% Xylazine	80721102	Bayer Healthcare GmbH
ROTI® Block	A151.1	Carl Roth
Schiff's reagent	1.090.330.500	Merck
Sodium citrate ($Na_3C_6H_5O_7$)	HN12.4	Carl Roth
Sodium chloride (NaCl)	3957.1	Carl Roth
Sodium deoxycholate	D6750	Sigma-Aldrich
Sodium dodecyl sulfate (SDS) pellets	CN30.3	Carl Roth
Sodium dodecyl sulfate (SDS) powder	A2263	AppliChem
Sodium fluoride (NaF)	S1504	Sigma-Aldrich
Sodium hydrogen phosphate (Na_2HPO_4)	S9390	Sigma-Aldrich

Sodium hydroxide (NaOH)	A3910.1000	AppliChem
Sodium orthovanadate (Na_3VO_4)	S6508	Sigma-Aldrich
T4 ligase buffer (10x)	B69	Thermo Fisher Scientific
Tetrasodium pyrophosphate ($Na_4P_2O_7$)	106591	Merck
TNFα	aa80-235	R&D
TRI Reagent®	T3934-200ML	Sigma-Aldrich
Tris Hydrochloride (Tris-HCL)	9090.3	Carl Roth
Trizma® base	T1503	Sigma-Aldrich
TritonX-100	3051.2	Carl Roth
Trypon	1010817	MP Biomedicals
Tween-20	3472	Caesar & Loretz
Urea	U1250	Sigma-Aldrich
Xylene	371.5	Th. Geyer
Yeast Extract	2363.1	Carl Roth
β-Mercaptoethanol	M7522	Sigma-Aldrich

2.1.2 Assays and Kits

Table 3 ***List of all kits used****. All kits are listed with their respective company and product number.*

Assay/Kit	Product no.	Company
AimPlex™ premixed multiplex kit mouse custom 10-Plex	T2C1020628	Biosciences Inc.
Dako Liquid DAB+ Substrate Chromogen System	K3468	Dako
DeadEnd™ Fluorometric TUNEL System	G3250	Promega
Direct-zol™ RNA Miniprep	2050	Zymo Research
GeneJET Gel Extraction kit	K0691	Thermo Fisher Scientific
High Capacity cDNA Reverse Transcription kit	4368814	Applied Biosystems
High Select TiO2 Kit	A32993	Thermo Fisher Scientific
ImmPACT® DBA Substrate kit, peroxidase	SK-4105	Vector Laboratories
Masson-Goldner's trichrome staining kit	3459	Carl Roth
Nuclei Isolation kit: Nuclei EZ Prep	NUC101-1KT	Sigma
NucleoBond® Xtra Midi Prep kit	740410	Macherey-Nagel
NucleoSpin® Gel and PCR clean-up	740609.250	Macherey-Nagel
NucleoSpin® Plasmid Easy Pure	740727.250	Macherey-Nagel
PCR Mycoplasma Test Kit I/C	PK-CA91-1096	PromoKine
Pierce™ BCA Protein Assay	23225	Thermofisher
Precellys Lysing kit	P000933-LYSK0-A	Precellys
Q5® High-Fidelity DNA Polymerase	M0491L	New England Biolabs
SuperScript™III Reverse Transcriptase	18080093	Invitrogen™
SuperSignal West Femto Chemiluminescent Substrate	34095	Thermo Fisher Scientific
SYBR Green PCR Master Mix	4309155	Thermo Fisher Scientific

2.1.3 Enzymes

Table 4 ***Enzymes for bacteria culture****. Listed with their respective provider and product number.*

Enzyme	Product no.	Provider
MluI	R0198L	New England Biolabs
Not1	RO189L	New England Biolabs
T4 Ligase	M0202M	New England Biolabs
T4 polynucleotide kinase	M0201S	New England Biolabs
Trypsin	37286.03	Serva
Lysyl Endopeptidase (Lys-C)	125-05061	Wako

2.1.4 Buffers and solutions

Table 5 ***Compositions of buffers or other solutions.*** *The compositions were declared with the final concentration or with fixed volumes.*

Buffer	**Composition**
Base Buffer (50x)	12.5 ml NaOH (5 N) 1 ml EDTA (0.5 M) 36.5 ml ddH2O
Blocking Solution	10% (v/v) NDS 0.1% (v/v) PBSTx-100
Cell Culture Medium (HEK293T)	10% (v/v) FBS In DMEM with GlutaMAX
Cell Culture Medium (mIMCD3 - starvation)	1 x Pst 2 mM GlutaMAX In DMEM-F12
Cell Culture Medium (mIMCD3)	10% (v/v) FBS 1 x Pst 2 mM GlutaMAX In DMEM-F12
Citric acid Buffer pH 6.0 (10x)	87.4 mM $Na_3C_6H_5O_7$ 12.6 mM citric acid monohydrate
Destaining Buffer	50 % EtOH 49% ddH_2O 1% acetic acid
Enhanced Chemiluminescence Solution (ECL)	100 mM Tris (pH 8.5) 1.25 mM Luminol 0.2 mM Coumaric acid 0.75% (v/v) H_2O_2
EZ-Lysis Buffer	EZ Lysis Buffer (Sigma NUC-101) 1x Protease Inhibitor (PIM) w/o EDTA 0.1% RNase Inhibitor 40 U/µl
Freezing Medium	70 % (v/v) FBS 20 % (v/v) Cell Culture Medium 10 % (v/v) DMSO

HEBS (2x)	42 mM HEPES, Free Acid 274 mM NaCl 10 mM KCl 1.4 mM Na_2HPO_4 Heptahydrate 15 mM Dextrose pH 7.09
IP Lysis Buffer	20 mM Tris 1% (v/v) TritonX-100 50 mM NaCl 15 mM $Na_4P_2O_7$ 50 mM NaF 44 µg/µl PMSF 2 mM Na_3VO_4 pH 7.5
Laemmli (1x)	50 mM Tris 2% (w/v) SDS 10% (v/v) Glycerol Bromphenol Blue 50 mM DTT pH 6.8
Laemmli (2x)	100 mM Tris 4% (w/v) SDS 20% (v/v) Glycerol Bromphenol Blue 50 mM DTT pH 6.8
Laemmli (5x)	250 mM Tris 10% (w/v) SDS 50% (w/v) Glycerol Bromphenol Blue 50 mM DTT pH 6.8
LICOR wash Buffer (10x)	0.1% (v/v) Tween-20 in 1x PBS

Modified RIPA Buffer (cell lysate)	1% IgePAL 150 mM NaCl 0.25% Na- Deoxycholate 50 mM Tris (pH 7.5) 44 µg/µl PMSF 2 mM Na_3VO_4
Modified RIPA Buffer (tissue lysate)	50 mM Tris-HCl (pH 7.5) 150 mM NaCl 0.1 % NP-40 0.5 % Na-Deoxycholate 1.0 % (v/v) SDS 1:2000 Benzonase® Nuclease 1:25 cOmplete™ 1:20 PhosSTOP™
Narcosis	6.8 ml 0.9% NaCl (sterile) 1 ml Ketamin 400 µl Xylazin
Neutralization Buffer (50x)	15.75 g Tris-HCl in 50 ml of H_2O
Nuclei Suspension Buffer	1x PBS (sterile) 2% BSA 0.1% RNase Inhibitor 40 U/µl
PBST	0.05% Tween-20 in 1x PBS
PBSTx-100	0.1% TritonX-100 in PBS (1x)
Phosphate Buffered Saline (PBS) (10x)	137 mM NaCl 2.7 mM KCl 10 mM Na_2HPO_4 2 mM KH_2PO_4
Protein Wash Buffer (10x)	30 mM Tris 300 mM NaCl 0.3% Tween-20 pH 7.5

Resolving Gel	750 mM Tris 10% (v/v) PAA 0.2% (w/v) SDS pH 8.8
Running Buffer	25 mM Trizma® base 192 mM Glycine 0.1% (w/v) SDS
SOC medium	2% (w/v) Tryptone 0.5% (w/v) Yeast Extract 8.6 mM NaCl 2.5 mM KCl 20 mM $MgSO_4$ 20 mM Glucose
Stacking Gel	250 mM Tris 5% (v/v) PAA 0.2% (w/v) SDS pH 6.8
Stage-tip Buffer A	0.1% formic acid
Stage-tip Buffer B	0.1% formic acid 80% acetonitrile
Staining PBS	1 mM CaCl 0.5 mM $MgCl_2$ in 1 x PBS
TAE Buffer (25x)	121 g Trizma® base 28.5 ml Acetic Acid 18.6 g Na_2EDTA $2xH_2O$ pH 8.5
TAE-EtBr Buffer	TAE Buffer 1x 1% EtBr in ddH_2O

Table continued on the next page

Tissue lysis buffer (Cytokine Assay)	200 mM NaCl 10 mM Tris-HCl (pH 7.4) 5 mM EDTA 1% NP-40 10% Glycerol 1 mM oxidized L-Glutathione 100 µM PMSF 2.1 µM Leupeptin 0.15 µM Aprotinin
Transfer Buffer	25 mM Tris 188 mM Glycine 0.1% (w/v) SDS
Tris Buffered Saline (TBS) (20x)	300 mM Tris-HCl (pH 7.6) 92.5 mM Tris Base 3 M NaCl
Tris-EDTA	10 mM Tris Base 1 mM EDTA 0.05% Tween-20 pH 9.0
Urea Buffer	8 M Urea 50 mM TEAB 1x Halts phosphatase-protease-Inhibitor

2.1.4 Oligonucleotides

Table 6 ***Cloning primer set with MluI/ Not1 modification****. Melting temperature (Tm) in °C was calculated using the NEBTmCalculator®.*

Gene	Forward 5'-3' Clamp MluI	Reverse 5'-3' Clamp Not1	Tm [°C]	size [bp]	source
Bbs8	CCCGCG ACGCGT ATGAGCTCGGAGATG GAGCCG	CCCGCG GCGGCCGC TCAGAGCATAGCAAA ATGCTG	64	1547	NM_144596.4

Table 7 ***Sanger sequencing primer.***

Allele	Forward 5'-3'	Reverse 5'-3'
Bbs8	ATACTCATGTGGAAGCCATCG	ATAGAAGCAACACAGCCCC

Table 8 ***Polymerase chain reaction (qPCR) oligonucleotides.*** *Forward and reverse primer in the direction of 5'-3', with the annealing temperature of 60 °C and their efficiency. No oligonucleotide set amplifies gDNA.*

Target	Forward 5'-3'	Reverse 5'-3'	Efficiency [%]
Casp11	ACAATGCTGAACGCAGTGA	CTGGTTCCTCCATTTCCAGA	105
Casp3	CAAAGGACGGGTCGTGGTT	GCGCGTACAGCTTCAGCAT	95
Casp8	CTAGACTGCAACCGA GAGG	GCAGGCTCAAGTCATCTTCC	97
Ccl2	CTTCTGGGCCTGCTGTTCA	CCAGCCTACTCATTGGGATCA	86
Col1a1	TCAGCTTTGTGGACCTCCG	GGACCCTTAGGCCATTGTGT	-
Ctgf	GGGCCTCTTCTGCGATTTC	ATCCAGGCAAGTGCATTGGTA	-
Fadd	TGCGCCGACACGATCTACTGC	CACACAATGTCAAATGCCACCTG	92
Fibronectin	GCCACCATTACTGGTCTGGA	GAGAGCTTCCTGTCCTGTCT	-
GsdmD	GCGATCTCATTCCGGTGGACAG	TTCCCATCGACGACATCAGAGAC	107
Hprt1	GCTGACCTGCTGGATTACAT	TTGGGGCTGTACTGCTTAAC	105
LC3	GACGGCTTCCTGTACATGGTTT	TGGAGTCTTACACAGCCATTGC	100
Mlkl	CTGTGGACGGTAGGAGTCTT	CGTGGATTCTTCAACCGCAG	95
NF-kB/p50	GAAATTCCTGATCCAGACAAAAAC	ATCACTTCAATGGCCTCTGTGTAG	96

Nlrp3	AGAGCCTACAGTTGGGTGAAATG	CCACGCCTACCAGGAAATCTC	103
RelA/p65	CTTCCTCAGCCATGGTACCTCT	CAAGTCTTCATCAGCATCAAACTG	86
Ripk1	GAAGACAGACCTAGACAGCG	CCAGTAGCTTCACCACTCGA	99
Ripk3	GTGCTACCTACACAGCTTGAAC	CCCTCCCTGAAACGTGGAC	88
Sqstm1/p62	TGTGGAACATGGAGGGAAGAG	TGTGCCTGTGCTGGAACTTTC	90
Tgf-β1	CTCCCGTGGCTTCTAGTGC	GCCTTAGTTTGGACAGGATCTG	-
TNFα	CTA CCT TGT TGC CTC CTC TTT	GAG CAG AGG TTC AGT GAT GTA G	110

Table 9 ***Oligonucleotides used for mouse genotyping.*** *Sequences in the direction of 5' to 3'. Expected signals on base pair (bp) size.*

Allele	Oligonucleotides (5'-3')	Size [bp]
Fadd	TCACCGTTGCTCTTTGTCTAC GTAATCTCTGTAGGGAGCCCT AAGGCATCAGCAAGAGCAGT	wt: 200 bp fl : 280 bp ko: 380 bp
GsdmD	GAGGAAAGACAAGGCAGTGG GAGGAAAGACAAGGCAGTGG	wt: 420 bp ko: 315 bp
Jck	AAGTACTGGAAGCTTCCTTCCCCAGTGG TCTAGCCCACCATTGTAGAAGCCTTGTTG GGGCCACGGAGAGGTAGACAGGTATAGG AGGCCACCTGCACCATCTCATAGTCA	wt: 220 bp ko: 255 bp
Kif3a	AGGGCAGACGGAAGGGTGG TCTGTGAGTTTGTGACCAGCC GGTGGGAGCTGCAAGAGGG	wt: 360 bp fl: 490 bp
Ksp:Cre	GCAGATCTGGCTCTCCAAAG GCAAACGGACAGAAGCATTT CCTGACAGTGACGGTCCAAAG CATGACTCTTCAACTCAAACT	wt: 351 bp tg: 531 bp
Ripk3	CGCTTTAGAAGCCTTCAGGTTGAC GCCTGCCCATCAGCAACTC CCAGAGGCCACTTGTGTAGCG	wt: 320 bp nko: 485 bp

2.1.5 Antibodies

Table 10 ***List of primary antibodies.*** *Antibodies are listed with their respective provider and product number. Further, the host and the dilution, either for western blot (WB) or immunofluorescence (IF), are declared. rb: rabbit; m: mouse; gp: guineapig.*

Antibody	Host	Dilution WB	Dilution IF	Product no.	Provider
acetylated Tubulin	m	1:1000	1:800/ 1:1000	T6793	Sigma Aldrich
ARL13B	rb	-	1:400/ 1:800	17711-1-AP	Proteintech
Calnexin	rb	1:1000	-	10427-2 AP	Proteintech
CD3	rat	-	1:100	MCA-1477	Biorad
Cleaved-Casp3 (Asp175)	rb	1:1000	-	9661	Cell Signaling
Flag	rb	1:1000	-	F7425	Sigma-Aldrich
GAPDH	rb	1:2000	-	5174	Cell Signaling
GSDMD	rb	1:1000	-	ab219800	Abcam
HDAC2	rb	1:1000	-	ab32117	Abcam
HSP27	rb	1:1000	-	2442S	Cell Signaling
IκB-α (C-21)	m	1:1000	-	sc-1643	Santa Cruz
LC3B	rb	1:1000	-	2775S	Cell Signaling
NF-κB (RelA) p65	rb	-	1:1000	8242	Cell Signaling
NLRP3	rb	1:1000	-	15101	Cell Signaling
Pan-Actin	rb	1:1000	-	8456S	Cell Signaling
pIκBα (Ser32/36)	m	1:1000	-	9246S	Cell Signaling
pMLKL (Ser345)	rb	1:1000	-	37333S	Cell Signaling
pNF-κB p65 (Ser536)	rb	1:1000	-	3033	Cell Signaling
RIPK1	m	1:1000	-	610459	BD Bioscience
RIPK3	rb	1:1000	-	ADI-905-242	Enzo
Slc12a3	rb	-	1:500	HPA028748	Sigma Aldrich
SQSTM1/ p62	gp	1:1000	-	GP62-C	Progen
γH2AX	m	-	1:1000	ab22551	Abcam
β-Tubulin	m	1:500/ 1:1000	1:500	E7	DSHB

Table 11 ***List of secondary antibodies.*** *Antibodies are listed with their used dilution as well as respective provider and product number.*

Epitope	Dilution	Product no.	Provider
Cy3-α Smooth muscle actin	1:0000	C6198	Sigma Aldrich
Dapi	1:400	6843.1	Roth
Donkey anti-mouse 555	1:400	A31570	Invitrogen
Donkey anti-mouse A488	1:500	715-545-150	Jackson ImmunoResearch
Donkey anti-mouse Cy3	1:500	715-165-150	Jackson ImmunoResearch
Donkey anti-mouse Cy5	1:500	715-175-150	Jackson ImmunoResearch
Donkey anti-rabbit A488	1:400	A11034	Invitrogen
Donkey anti-rabbit A647	1:500	711-605-152	Jackson ImmunoResearch
Donkey anti-rabbit Cy3	1:500	711-165-152	Jackson ImmunoResearch
Fluorescein Lotus Lectin (LTL)	1:250	VEC-FL-1321	Biozol
Goat Anti-Rabbit IgG (H+L)	1:30.000	111-035-003	Jackson ImmunoResearch
IRDye® 680RD anti-mouse IgG	1:10.000	926-68070	LI-COR Biosciences
IRDye® 680RD anti-rabbit IgG	1:10.000	926-68071	LI-COR Biosciences
IRDye® 800CW anti-mouse IgG	1:10.000	926-32210	LI-COR Biosciences
IRDye® 800CW anti-rabbit IgG	1:10.000	926-32211	LI-COR Biosciences
Rodamin-DBA	1:500	RL-1032-2	Vector Laboratories

2.1.6 Cell lines

Table 12 ***Cell lines used for experiments.*** *Human and mouse cell lines are listed in the table below. If a cell line was sorted or genetically modified, the genotype and the parental cell line were listed as well.*

Name	Species	Parental cell line	Genotype
HEK293T	human	-	WT
mIMCD3 WT	mouse	-	WT
mIMCD3 WT #2	mouse	mIMCD3 WT	WT
mIMCD3 WT #8	mouse	mIMCD3 WT	WT
mIMCD3 Myo5a$^{-/-}$	mouse	mIMCD3 WT	Myo5a$^{-/-}$

2.1.7 Plasmids

Table 13 ***Plasmids used for overexpression in HEK293T cells.*** *All plasmids are listed with the DNA insert and the related tag. The table also includes the vector name. Further, the molecular weight of the construct of DNA insert and tag are declared in kDa.*

Plasmid	Size [kDa]	Provider
F.hBBS8 pcDNA6	65	Generated within this work
F.EPS$^{1-225}$ pcDNA6	32	Nephrolab, Cologne

2.1.8 Consumables

Table 14 ***List of consumables used.*** *All consumables are listed with their respective provider and product number.*

Consumable	Product #	Provider
10 cm dish for Agar Plates	82.1473	Sarstedt
384 PCR-Plate full skirt	72.1984.202	Sarstedt
5 ml Polystyrene Round-Bottom tube	352052	FALCON®
8-Lid chain, flat	65.989.002	Sarstedt
96-well plate, sterile, f-bottom, with lid	655180	Greiner BioOne
Adhesive qPCR seal	95.1999	Sarstedt
Advanced PAP Pen	Z672548	Merck
BeadBeater® Glass-pellets ø 1.0 mm	11079110z	Carl Roth
Blotting paper (Type BF4, 580 x 600)	FT-2-521-580600G	Sartorius Stedim Biotech
Casy Cups	5651794001	OMNI Life Science
Cell lifter, 18 cm, S	3008	Corning
Cell strainers 40 µm	83.3945.040	Sarstedt
Cellstar® tubes, 15 ml, PP, sterile	188 271-N	Greiner BioOne
Cellstar® tubes, 50 ml, PP, sterile	227 261	Greiner BioOne
Combs (10 well, 1 mm) for acrylamide gels	NC3010	Invitrogen
Combs (12 well, 1 mm) for acrylamide gels	NC3012	Thermo Fisher
Cover Glass 22 x 22 mm	631-0215	VWR
Cover Glass ø 12 mm	2	Menzel-Gläser
Cover slips 24 x 50 mm	1.5	Menzel-Gläser
Cryo.S™, PP with screw cap, sterile	123278	Greiner BioOne
Disposable cup 100 ml	75.563	Sarstedt
Disposable Scalpel No.22 pfm	02.001.30.022	Feather®
Filter Tip 1000 µl, sterile	70.3050.255	Sarstedt
Filter Tip 20 µl, sterile	70.3030.265	Sarstedt
Filter Tip 200 µl, sterile	70.3031.255	Sarstedt
Gel cassette (1 mm)	NC2010	Invitrogen
Histosette® I	M499-11	Simport
Immobilon®-FL Transfer Membrane	IPFL00010	Millipore
Immobilon®-P Transfer Membrane	IPVH00010	Millipore
M2 beads (Anti-FLAG) Affinity Gel	A2220	Sigma-Aldrich

Micro tube 1.5 ml	72.690.001	Sarstedt
Micro tube 1.5 ml, PP	72.692.005	Sarstedt
Microcentrifuge tubes wit lid locking 2.0 ml	780546	Brand
Multiply®-µStrip 0.2 ml chain	72.985.002	Sarstedt
Needle 21G x 1½"	304432	BD Microlance™ 3
Needle 23G x 1"	300800	BD Microlance™ 3
Needle 27G x 3/4"	4657705	Braun
Needle 30G x 1½"	8300054707	Covetrus™
Nitrile Examination glove, Ultra long, M	D1402-26	Dermagrip®
Parafilm® M	HS234526B	Th. Geyer
PCR Soft-tubes 0.2 mL 8 Tubes/Flat Caps, clear	710970	Biozym
Peha-soft® nitrile S	942206	Hartmann
Petri dish, PS, 35/10 mm with vents, sterile	627161	Greiner BioOne
SafeSeal tube 1.5 ml, brown	72.706.001	Sarstedt
Screw cap for 100 ml cup	76.564	Sarstedt
Stripettes (10 ml)	86.1254.001	Sarstedt
Stripettes (25 ml)	86.1685.001	Sarstedt
Stripettes (5 ml)	86.1253.001	Sarstedt
SuperFrost®/Plus microscope slides	7695002	Th.Geyer Group
Syringe 1 ml	303172	BD Plastic™
TC Dish 100, Standard, F	83.3902	Sarstedt
TC Plate 12 Well, Standard, F	83.3921	Sarstedt
TC Plate 24 Well, Standard, F	83.3922	Sarstedt
TC Plate 6 Well, Standard, F	83.3920	Sarstedt
TipOne (0.1-10 µl XL), sterile	S1110-3810	Starlab
TipOne (101-1000 µl graduated), sterile	S1111-6811	Starlab
TipOne (1-200 µl beveled), sterile	S1111-1816	Starlab
TipOne Pipette Tip 10 µl, refill	S1111-3700	Starlab
TipOne Pipette Tip 1000 µl, refill	S1111-6700	Starlab
TipOne Pipette Tip 200 µl, refill	S1111-1700	Starlab
Weighing tray 140 x 140 mm	2159.1	Carl Roth
Weighing tray 89 x 89 mm	2150.1	Carl Roth

2.1.9 Equipment

Table 15 ***List of appliances used.*** *All appliances are listed with their respective product number and manufacturers.*

Appliances	Model	Manufacturer
Autoclave	V-150	Systec
Avanti centrifuge	J-26S XPI	Beckman Coulter
AxioCam	MRm	Zeiss
Axiovert microscope	200M	Zeiss
Casy® counter	05651697001	Roche
Cell Freezing Containers	Biocision	Biocision
Centrifuge	5424	Eppendorf
Centrifuge (refrigerated)	5810 R	Eppendorf
Centrifuge (refrigerated)	5415 R	Eppendorf
Centrifuge (refrigerated)	5430 R	Eppendorf
Centrifuge (refrigerated)	5417 R	Eppendorf
Centrifuge Mini G	S000	IKA
Cold Plate	HistoCore Arcadia C	Leica
Cold Plate	EG1150C	Leica
Digital Heatblock	460-3207	VWR
Dumont #5 forceps	91150-20	WPI
Electrophoresis Power Supply	E831	Consort
Electrophoresis Power Supply	EPS 200	Pharmacia Biotech
Electrophoresis Power Supply	EPS 601	Pharmacia Biotech
EnSpire Multimode Plate Reader	2300-0000	Perkin Elmer
Fine Scissors-TroughCut, gerade, 11.5 cm	14058-11	FSI Fine Science
Fine Scissors-TroughCut, gerade, 9 cm	14058-09	FSI Fine Science
FiveEasy pH meter F20	30266658	Mettler Toledo
Fusion Solo chemiluminometer	60-FU-SOLO	PeqLab
Hamilton syringe (50 µl Type 705)	549-1155	VWR
Heraeus B12 Function Line incubator	50042307	Kendro Laboratory Products
HistoCore Multicut	00919	Leica
HistoCore Water Bath	W00212	Leica
Homogenisator	Precellys® 24	Bertin instruments
Horizontal electrophoresis system size	L 40-1214	PeqLab

Horizontal electrophoresis system size	S 40-0708	PeqLab
IKA®-Schüttler	MTS 4	IKA
IKAMAG® RET Stirring Hotplate	RET	IKA
Incubator	940053	Biometra APT Line
Incubator (Agarose)	T 6030	Heraeus
Incubator (cell culture)	9140-0038	Binder
IncuCyte® S3	S3	Sartorius
Infinite® M Plex plate reader	200Pro	TECAN
Intelli-Mixer	RM-2S	LTF
Leica Embedding Station	EG1150H	Leica
MACSmix	001459	Miltenyi Biotec
Microscope Revolve-M270	RVL-100M	ECHO
Microtome	RM2235	Leica
Mini Gel Tank	A25977	Thermo Fisher Scientific
Minishaker	MS1	IKA
MixMate	535303154	Eppendorf
Multifuge	4 KR	Heraeus
Multitron Pro	S-000120234-003	INFORS HT
Odyssey® M Imaging System	ODM-0325	LI-COR
Pipetboy acu	155 015	Integra Biosciences AG
Pipetman Pipette set (P2, P10, P100)	F167500	Gilson
Pipetman Pipette set (P20, P200, P1000)	F167300	Gilson
Plate washer	LIPN2580PA/4	Millipore
PowerPac™ HC High-Current Power Supply	1645052	Bio-Rad
QuantStudio™ 5 Real-Time PCR System	A34322	Applied Biosystems™
Research® plus, 8-channel, 10-100 µl	3122000035	Eppendorf
Roller mixer	SRT6	Stuart
S3e Cell Sorter	12007058	Bio-Rad
Scale	PCB1000-2	KERN®
Scale	EMB 100-3	KERN®
Schieferdecker Staining Jar, 10 Slides	042.	Lab Commercial
Semi-Dry Blotter Owl™ HEP-1	EF7310	PeqLab
Shaker	KS 260	IKA
Slidescanner	SCN400	Leica
Slidescanner	S360	Hamamatsu

Sonicator	Bioruptor® Pico	Diagenode Diagnostics
Staining Jars	036.001	Lab Commercial
Standard Pattern forceps, gerade	91100-12	WPI
Sterile hood	Mars Safety Class 2	SCANLAF
Suction pump	181-0067DE	VWR
Suction pump (cell culture)	HLC	DITABIS
Thermal cycler	S1000™	Bio-Rad
Thermal cycler	C1000 Touch™	Bio-Rad
Thermomixer Comfort shaker & heating plate	5355 04712	Eppendorf
Tissue grinder PSTL LC	885301-0015	Kimble
Tissue grinder Tube - 15 ml	885303-0015	Kimble
Trans-Blot® SD Cell	44115	Bio-Rad
UV Transilluminator system	MW312	Intas
Vortex Mixer	444-1372	VWR
Vortex Mixer VF2	434550	IKA
Vortex-Genie 2™	G-560E	Scientific Industry
Water bath	1003	GFL
Water bath (cell culture)	1004	GFL
Water bath (digital heating bath)	HBR4	IKA
Water bath (for paraffin sections)	HI1210	Leica
Wheaton Dounce tissue grinder	357538	Kimble

2.1.10 Software and online tools

Table 16 ***List of all used software.*** *The different software are listed with the used version in this study and its provider.*

Software	Version	Provider
Aperio ImageScope	12.4.6.5003	Leica
Bioimage Analysis software	0.4.0	QuPath
FlowJo	10.7.1	FlowJo, LLC
GraphPad Prism 10	10.0.0	GraphPad Software Inc.
HID Real-Time PCR Analysis Software	1.3	Applied Biosystems
i-Control™ software	2.0.10.0	TECAN
ImageJ/Fiji	1.53c	Wayne Rasband
ImageStudio	5.2.5	LI-COR
IncuCyte® Cell-by-cell	9600-0031	Sartorius
Inkscape	1.2	Inkscape.org
INTAS GelDoc	2019	Intas
Mausoleum	7.3.8 b4	Dr. H.-E. Stöffler
MaxQuant	1.5.2.8.	Computational Systems Biochemistry
Mendeley	1.19.8	Elsevier
Microsoft Office Suite	Professional Plus 2016	Microsoft
Nanodrop 1000	3.8.1	Thermo Scientific
Perseus	1.6.15.0	Computational Systems Biochemistry
ZEN Blue	3.0	Zeiss

Table 17 ***List of all used online tools.*** *Online tools are listed with their current website.*

Online Tool	Website
NEBioCalculator® v1.15.4	https://nebiocalculator.neb.com/
NEBTmCalculator® v1.16.5	https://tmcalculator.neb.com/
Benchling	https://www.benchling.com/
Ensembl	https://www.ensembl.org
The Human Protein Atlas	https://www.proteinatlas.org/
NCBI	https://www.ncbi.nlm.nih.gov/
NCBI PrimerBlast	https://www.ncbi.nlm.nih.gov/tools/primer-blast/
PRIDE	https://www.ebi.ac.uk/pride/
NCBI PubMed	https://pubmed.ncbi.nlm.nih.gov/
UCSC In-Silico PCR	https://genome.ucsc.edu/cgi-bin/hgPcr

2.2 Methods

2.2.1 Bacterial culture

2.2.1.1 Cloning PCR

To construct a new plasmid, firstly, human embryonic kidney cells (HEK293T) RNA was transcribed into cDNA using the SuperScript™ III Reverse Transcriptase kit to generate a human DNA library, from where the target gene was then amplified. To set up the PCR, the RNA was mixed with specific components (step 1; **Tab. 18**) and incubated for 5 min at 65°C, followed by a cool down on ice for at least 1 min. Hereafter, to the first mixture, additional reagents were added (step 2; **Tab. 18**) and incubated for 60 min at 50°C. The reaction was inactivated at 70°C for 15 min, followed by an incubation of 20 min at 37°C with 2 U of *Escherichia coli* (*E. coli*) RnaseH. Subsequent PCR amplification was conducted with the Q5® High-Fidelity DNA Polymerase according to the manufacturer's instructions and incorporated the use of target-specific cloning primers designed with a modification of an additional clamp MluI (forward) or clamp Not1 (reverse) site (**Tab. 6**). The prepared reaction (**Tab. 19**) was incubated in a preheated thermocycler for denaturation at 98°C for 3 min. This was followed by 34 annealing cycles: 98°C 30 s; 64°C 30 s (BBS8 specific); 72°C 90 s. The final extension was at 72°C for 10 min. To purify Q5® PCR products, the GeneJET Gel Extraction kit was used following the manufacturer's instructions. The used plasmids of NPHP1 or EPS1-225 have been previously documented [360–362].

Table 18 ***Cloning reaction mix.*** *Volume of designated reagents. Stock concentrations in brackets.*

Step 1	1 µl	Oligo$(dT)_{20}$ (50 µM)
	1 µg	Total RNA
	1 µl	dNTP mix (10 mM)
		Fill up to 13 µl with ddH_2O
Step 2	4 µl	5X First-Strand Buffer
	1 µl	DTT (0.1 M)
	1 µl	RNaseOUT™ Recombinant RNase Inhibitor (40 U/µl)
	1 µl	Super Script™ III RT (200 U/µl)

Table 19 ***Components for amplification of insert.***

Volume	Components
5 µl	5X Q5 Reaction Buffer
0.2 µl	25 mM dNTPs
1.25 µl	10 µM Forward primer
1.25 µl	10 µM Reverse primer
50 ng	Human library (template cDNA)
0.25 µl	Q5 High-Fidelity DNA polymerase
5 µl	5X Q5 High GC Enhancer
	Fill up to 25 µl with ddH_2O

2.2.1.2 Agarose gel electrophoresis

To verify the DNA amplicon size, the standard procedure of agarose gel electrophoresis was used [363]. Depending on the experiment, either a 1% or 2% agarose gel was used and run in 1x TAE buffer containing ethidium bromide. For 1% agarose gels, a 1 kbp DNA ladder served as the reference marker, while for 2% agarose gels a 50 bp DNA ladder was used. If no loading dye was added in the experimental set-up, 5 µl of PCR product was supplemented with 1 µl Flexi Buffer before loading onto the gel. To visualize DNA fragments, the Intas UV Transilluminator system together with the Intas GDS Windows software was used.

2.2.1.3 Restriction enzyme digestion

To insert or exchange an insert into a specific vector backbone, the restriction enzymes MluI and Not1 were used. First, both purified Q5® insert and vector (2 µg) were digested for 2-6 h at 37°C (**Tab. 20**). To extract the pure backbone of the vector, the digest was loaded in an agarose gel electrophoresis (**2.2.1.2**), from which it was excised. This gel piece was purified using the NucleoSpin® Gel and PCR clean-up kit, following the manufacturer's instructions. A ligation reaction was prepared to incorporate the purified insert into the purified backbone. To ensure a proper ligation with an N-terminal MluI and a C-terminal Not1 restriction site, the used vector was previously modified with removed internal MluI sides. For ligation (**Tab. 21**), the reaction was incubated for 2 h at room temperature (RT) and finally stored at 4°C.

Table 20 ***Digestion mix.***

Volume	Components
26 µl	purified Q5® product
3 µl	Buffer 3.1
0.3 µl	MluI
0.3 µl	NotI
	Fill up to 30 µl with ddH_2O

Table 21 ***Ligation mix.***

Volume	Components
2 µl	Digested pcDNA6 vector
1.5 µl	10x T4 buffer
0.3 µl	T4 Ligase (5 U/µl)
7.2 µl	ddH_2O
4 µl	Digested insert

2.2.1.4 Transformation and isolation of plasmid

For the production of a plasmid, the generated ligation was transformed into a chemo-competent DH10B T1 Phage-Resistant strain of *E. coli* DH10. Therefore, 50 µl of DH10 mixed with 5 µl ligation was incubated on ice for 30 min. Subsequently, a precise 45 s heat shock at 42°C was performed. The mixture was returned to ice for 2 min and complemented with 500 µl of pre-warmed SOC medium, followed by a 1 h incubation at 37°C at 800 rpm. This bacterial suspension was streaked onto LB-Miller Medium [364] agarose dishes, supplemented with 100 µg/ml of ampicillin antibiotic. The bacterial cultures were cultivated overnight at 37°C. To isolate the plasmid from the bacteria, single colonies were selectively picked and separately cultured in LB medium (20 g/l) with 100 µg/ml of ampicillin. These mini cultures were incubated for 16 h at 37°C and 120 rpm. On the following day, 2 ml of the bacterial suspension was pelleted by centrifugation for 5 min at 10.000 rpm. The isolation of the plasmid DNA was executed using the NucleoSpin® Plasmid Easy Pure kit, following the manufacturer's instructions. The correct insert size was confirmed with a control digest (**2.2.1.3**). To generate a larger quantity of plasmid, 2 ml of the remaining mini culture was transferred into a larger amount of LB medium/ampicillin. This midi culture was incubated as before. The plasmid was extracted using the

NucleoBond Xtra Midi kit, following the manufacturer's instructions. The final plasmid concentration was determined using the Nanodrop 1000.

2.2.1.5 Sanger sequencing

The accuracy of the plasmid insert sequence was validated by Sanger sequencing. Sample preparation involved the use of 480 ng of plasmid, 3 µl of sequencing primer (diluted in a 1:10 ratio; **Tab. 7**), and subsequent filling up with ddH_2O, to a total volume of 15 µl. Sequencing samples were handed in to the Microsynth Seqlab which offers an automated DNA sequencing service. The obtained sequencing data were aligned and analysed using Benchling. Detailed map of the plasmid, generated for this thesis can be found in the supplements (Supp. Fig. 2).

2.2.2 Mammalian cell culture

2.2.2.1 Culture of immortalized cell lines

Murine inner medullary collecting duct 3 (mIMCD3) cells were sourced from ATCC®. The used ciliated (Ckc) and non-ciliated (Nckc) cells were generated through monoclonal cultures from the original mIMCD3 clone, obtained from Lena Ebert. The original mIMCD3 cells were additionally used to generate the already published *Myo5*$^{-/-}$ cell line [365]. mIMCD3 cells were cultured in Dulbecco's Modified Eagle Medium/Nutrient Mixture F-12 Ham (DMEM-F12), supplemented with 10% Fetal Bovine Serum (FBS), 2 mM GlutaMax, and 1% penicillin-streptomycin (Pst). HEK293T, also obtained from ATCC®, were cultivated in Dulbecco's Modified Eagle Medium (1x) + GlutaMAX™ (DMEM) supplemented with 10% FBS. Cells were kept at 37°C in a humidified atmosphere with 5% CO_2. Cells were regularly tested for mycoplasma using the mycoplasma kit, following the manufacturer's instructions.

2.2.2.2 Passaging, counting, freezing and thawing of immortalized cells

To passage cells, they were washed once with 1x PBS, followed by an incubation in 1 ml 0.05% trypsin at 37°C until almost all cells detached. This reaction was inactivated by adding pre-warmed medium. Cells for experimental set-ups were counted and the desired number (mentioned in the single experiments) of cells were seeded into a required culturing container: 10 cm dish, 6-, 12-, 24- or 96-well plate. For counting, the Casy® counter was used according to the manufacturer's instructions. Cells for maintenance were seeded in 10 cm dishes.

For long-time storage, 100% confluent cells were trypsinized, resuspended in medium and, subsequently, centrifuged for 5 min at 1.500 rpm (RT). The resulting pellet was resuspended in 1 ml freezing medium and transferred into a cryogenic tube. Subsequently, the cells were initially frozen at -80°C in a slow cell-freezing container before transferring them to N_2 tanks.

To thaw cells, the slightly thawed cell suspension was transferred into 4 ml pre-warmed medium and centrifuged for 5 min at 1.500 rpm (RT). The supernatant was discarded, and the cells were resuspended in fresh cell culture medium prior to plating them in a 10 cm dish. After 24 h, the medium was exchanged, and cells could be used for maintenance or experimental set-ups.

2.2.2.3 Treatment of mIMCD3 cells

To investigate cell death, cells were treated with different reagents over a specific time. Before treatment, cells were seeded and cultured for 24 h. Upon reaching a confluency of 60-70%, cells were treated with 0.04 ng/µl TNFα and 2 µg/100 µl cycloheximide (CHX) to induce general cell death. The combination of 0.04 ng/µl TNFα and 5 µM SMAC mimetic birinapant (Biri) specifically activated RIPK1-dependent cell death. Rescue of cell death was initiated by additional 10 µM Casp-8 inhibitor of

emricasan (Em), 40 µM RIPK1 inhibitor necrostatin-1s (Nec1s) or 5 µM RIPK3 inhibitor GSK872 in different combinations. After applying the treatment, cells were incubated at 37°C for 16 or 24 h, depending on the experiment. To induce TNFα independent cell death, 1.000 U/ml Interferon-γ (IFNγ) was used and pre-incubated for 8 h before combining the treatment with other reagents. Since all reagents were dissolved in DMSO, the control treatment was comprised of an equivalent quantity of DMSO.

2.2.2.4 Live-cell imaging

For live-cell imaging, 15.000 cells per well were seeded in triplicates in a 96-well plate 24h prior to treatment (**2.2.2.3**). The treatment master mixes were additionally supplemented with DiYO-1 to visualize dead cells, and, immediately after adding the treatment, the plate was transferred into the IncuCyte® S3 (37°C, 5% CO_2), where the first picture was captured (T0). Over a period of 24 h, three pictures from each well were taken every two hours with a 20x magnification, thereby capturing the green channel with an exposure time of 300 ms and the phase contrast channel. The analysis was performed with the included IncuCyte® Cell-by-Cell Analysis Software.

2.2.2.5 Neutral red assay

Cell viability was determined under cell death stimuli (**2.2.2.3**). For this assay, 30.000 cells/well were seeded in a 96-well plate 24 h prior to treatment. Triplicates for each reagent were incubated for 16 h. After 14 h of treatment neutral-red (4 mg/ml in ddH_2O) in a dilution of 1:100 was added, including the medium-only control (blank value), and incubated for the remaining 2 h. After the incubation time, the medium was removed, and the wells were washed thrice with 1x PBS. Finally, 100 µl of destaining buffer was incubated for 15 min at RT under gentle shaking [263]. The absorbance at 540 nm was determined using the Infinite® M Plex plate reader.

2.2.2.6 Immunofluorescence staining

Fluorescence staining was performed on mIMCD3 cells cultured on coverslips. Cells were carefully washed with 1x PBS and fixed via 4% formaldehyde, 5 min at RT, and ice-cold 100% MtOH for 4 min at -20°C. Samples were washed thrice with 1x PBS, blocked with 1x PBSTx-100, supplemented with 10 % normal donkey serum (NDS) for 1h at RT and incubated for 80 min at RT with the primary antibody in blocking solution (**Tab. 10**). Respective secondary antibodies (**Tab. 11**), diluted in 1xPBS, were incubated for 1 h at RT. Coverslips were washed with 1x PBS prior to mounting the samples onto glass slides with ProLong™ Diamond with DAPI. Images were acquired using the AxioObserver microscope with an axioCam ICc 1, Axiocam 702 mono Apotome system with a 20x magnification objective. Images were analysed for cell count and further processed with the open-source software ImageJ/Fiji.

2.2.2.7 Transfection of HEK293T cells

Overexpression of proteins was performed by transfection of HEK293T cells. The desired amount of plasmids (method section Chapter 3) was precisely dispensed into 1.5 ml tubes, containing 500 µl of 0.25 M $CaCl_2$ solution. Into the solution, 500 µl of 2x HEBS were gradually added, while thoroughly mixing, drop by drop. The combined mixture was slowly added to the cells with a confluence of approximately 60%. The medium was replaced after 6-8 h. After a total of 24 h, the cells were either harvested or subjected to an additional 24 h period of serum starvation by omitting FBS.

2.2.2.8 Co-Immunoprecipitation

To investigate interactions between different proteins, a co-immunoprecipitation (co-IP) was performed. Transfected HEK293T cells (**2.2.2.7**) were scraped in ice-cold 1x PBS, centrifuged at 1.000 rpm for 5 min at 4°C, resuspended in 1 ml IP-Buffer and incubated on an overhead shaker for 30 min at 4°C. Samples were centrifuged at full speed at 4°C for 30 min. 50 µl of lysate (input) was supplemented with 2x Laemmli. The remaining lysate (co-IP sample) was supplemented with 30 µl anti-FLAG M2 Beads and incubated for 2 h at 4°C on an overhead shaker. Samples were washed thrice with IP-Buffer for 10 min at 4°C on an overhead shaker, followed by 3 min centrifugation at 4°C and 4.000 rpm. The supernatant was carefully removed, and the remaining beads were lysed in 30 µl 2x Laemmli. Both samples were boiled at 95°C for 5 min prior to storage at -20°C or immune blotting (**2.2.6.2 and 2.2.6.3**).

2.2.3 Mouse work

2.2.3.1 Mouse holding and mouse lines

Mice were housed in the CECAD *in vivo* Research Facility, where they were maintained under standardized specific pathogen-free conditions, with a 12-hour light/dark cycle and continuous access to food and water. All the mouse experiments conducted in this thesis were approved by both the Animal Care Committee of the University of Cologne and the LANUV NRW (Landesamt für Natur, Umwelt und Verbraucherschutz Nordrhein-Westfalen, State Agency for Nature, Environment, and Consumer Protection North Rhine-Westphalia). All animals used were crossed on a C57BL6/N background.

To generate the transgenic *Kif3a*^{tko} animals, lacking primary cilia specifically in the distal tubules and collecting ducts, *Kif3a*^{fl} mice [45] were crossed with Ksp:cre mice [366]. These mice do not loose cilia right from birth; therefore, two ages were investigated: 4 and 28-days-old.

Our ciliopathy mouse model carries a *jck* point mutation in the *Nek8* (*Nphp9*) gene, develops an ADPKD-like renal phenotype [172] and was acquired from Jackson Laboratory (Bar Harbor, ME). These animals were crossed with either *Ripk3* or *GsdmD* deficient mice to investigate the role of RCD in renal ciliopathies. Animals were investigated at the age of 12 weeks. *Ripk3* and *GsdmD* knockout animals were shared from the SFB1403 repository.

The *Bbs8*$^{-/-}$ mouse has been previously described [367].

2.2.3.2 DNA extraction from mouse tissue via HotSHOT

To determine the genotype of specific mice, ear or tail biopsies were used for HotSHOT DNA extraction as previously described [368]. Briefly, the biopsies, depending on their size (ear tissue or tail) were boiled for 30 min at 95°C in 65-150 µl 1x base buffer, cooled down and the reaction was stopped by adding an equal amount of 1x neutralization buffer. This genomic DNA (gDNA) was stored at -20°C or used immediately for polymerase chain reaction (PCR).

2.2.3.3 Genotyping PCR

The extracted gDNA was mixed with gene-specific primers (**Tab. 9**) and REDTaq® ReadyMix™ PCR reaction mix, according to the manufacturer's instructions. The PCR was performed with unique cycler conditions for each gene. After completing the PCR, the product was loaded and run in a 2% agarose gel (**2.2.1.2**).

2.2.3.4 Sample collection

Animals, at specific ages, were weighed and narcotized with ketamine (100 mg/kg body weight) and xylazine (20 mg/kg body weight). The abdominal cavity was carefully opened, and a bilateral thoracotomy was performed. Blood samples were collected from the right ventricle and, hereafter, cardiac perfused with 1x PBS. After total perfusion, the kidneys were collected. For histological analysis, half of a kidney was fixed in 4% PFA overnight at 4°C, dehydrated and embedded in paraffin. For other experiments, the kidney tissue was immediately frozen in liquid-N_2 to preserve its molecular characteristics.

Blood samples were centrifuged at 3.000 rpm at RT and the clear serum was collected. These samples were either measured by the Institute of Clinical Chemistry, University Hospital of Cologne, Germany, to determine the level of serum creatinine, or kept frozen at -20°C.

Kidney and blood samples of 46-week-old *Bbs8*$^{-/-}$ mice were provided by the working group of Professor Dr. May-Simera at the Johannes-Gutenberg University in Mainz.

2.2.3.5 Staining of renal tissue

To characterize the phenotype of the tissue histologically, several stainings were performed on paraffin-embedded tissue sections. Briefly, the tissue was cut into 4 µm thick sections for primary cilia staining or into 2 µm thick sections for the rest of the stainings. Sections were dried at 60°C for at least 1 h before deparaffinization through a decreasing ethanol row (Xylene, 2x 5 min; EtOH 100%, 3x 3 min; EtOH 95%, 2x 2 min; EtOH 70%, 1x 1min, water) prior to staining.

2.2.3.5.1 Periodic-Acid Schiff staining

To perform Periodic-Acid Schiff (PAS) staining, sections were oxidized with 0.9 % periodic acid for 10 min, washed in H_2O, transferred into Schiff's reagent for 10 min and washed again. Nuclei were visualised with Mayer's Haematoxylin for 20 s, thereafter the slides were washed under running tap water for 10 min. Rehydration was performed by incubating the slides in an ascending ethanol row (EtOH 70%, 1x 1 min; EtOH 95%, 2x 2 min; EtOH 100%, 3x 3 min; Xylene, 2x 5 min). Samples were mounted with Histomount and scanned with the magnification of 20x in the Slidescanner. Further analysis was then performed with the software ImageScope or QuPath.

2.2.3.5.2 Masson Trichrome Staining

The Masson-Goldner trichrome staining was performed according to the manufacturer's instructions with the following incubation times: Goldner's stain I for 5 min, Goldner's stain II and Goldner's stain III for 3 min, followed by a 3 min washing step with 1% acetic acid solution. Finally, the samples were

incubated in the ascending ethanol row (**2.2.3.5.1**), however, not more than 1 min per step, and embedded with Histomount. Samples were imaged as previously mentioned (**2.2.3.5.1**).

2.2.3.5.3 TUNEL staining

The DeadEnd™ Fluorometric TUNEL System was performed on deparaffinised samples. Sections were washed with 0.85% NaCl for 5 min before the apoptosis detection was performed according to the manufacturer's instructions, with an incubation time of 10 min for Proteinase K. Afterwards, the kidney samples were incubated with Hoechst (1:1.000 in 1x PBS) for 10 min, washed in 1x PBS and mounted in Prolong™ Diamond w/o DAPI. Images were acquired using the AxioObserver microscope with an axioCam ICc 1, Axiocam 702 mono Apotome system, with a magnification of 20x.

2.2.3.5.4 Immunostaining

For fluorescence labelling, deparaffinised slides were washed twice in special staining PBS. For antigen retrieval, either Tris-EDTA or citrate buffer were used to boil the samples for 10 min at 110°C. After cooling for 20 min, the samples were washed twice in TBS. This was followed by endogenous peroxidase blocking in 3% H_2O_2 for 15 min. After washing three times in staining PBS, each sample was surrounded with an advanced PAP Pen, prior to blocking with 1% BSA and 5% NDS in PBST for 1 h at RT. Thrice washing with staining PBS was then performed prior to incubating the primary antibody, diluted in 5% BSA PBST, overnight at 4°C. The samples were washed three times in PBST, followed by incubation with respective secondary antibodies, diluted in PBST with 5% BSA, for 1 h at RT in the dark. The secondary antibodies were selected according to the staining method, for either immunohistochemistry or immunofluorescence. The samples were finally washed in PBST. To finalize the immunohistochemistry staining, the DBA kit was used, and the sections were counterstained with Mayer's Haematoxylin for 20 s and embedded with Histomount. Images were acquired with the Slidescanner (20x objective) and analysed in the software ImageScope. For immunofluorescence, the samples were incubated for a short time in Hoechst, diluted 1:5.000 in PBST to counter-stain the nuclei and then rapidly washed for 10 min with PBST. The samples were mounted with Prolog™ Diamond w/o DAPI. Images were acquired as mentioned previously (**2.2.3.5.3**) and processed with ImageJ/Fiji.

2.2.3.6 Cyst index analysis

The cyst index was determined for the entire kidney slice with PAS staining, using an open-source bioimage analysis software QuPath v0.40 [369]. Cysts were initially identified by employing an Artificial Neural Network-based pixel classifier. Subsequently, the identified cysts were filtered based on two criteria: having a minimum area of 400 µm², and a minimum circularity value dependent on the mouse

line: 0.35 for *Bbs8*; 0.09 for *Nek8*^{jck} *Ripk3* and 0.1 for *Nek8*^{jck} *GdsmD*. Data plots were generated using the Plots of Data web application, developed by Postma and Goedhart in 2019.

2.2.3.7 Cytokine assay

One-quarter of the kidney tissue was homogenized with a douncer 25-30 times in lysis buffer with different protease inhibitors with a Wheaton Dounce tissue grinder [370], and incubated overnight at -20°C. The samples were centrifuged for 1 h at 12.400 rpm at 4°C, of which the supernatant was centrifuged a second time for 30 min and the protein concentration was determined (**2.2.6.1**). The AimPlex™ assay was performed according to the manufacturer's instructions, with the addition that in the final step 150 µl reading buffer was added. The assay was measured using the S3e^{TM} Cell Sorter using the detector channels FL3 and FL4 and analysed with FlowJo™ Software v10.7.1.

2.2.3.8 Single-nuclei sequencing

The used protocol was adjusted from a previously described one[371]. To generate the samples, one-quarter of a kidney was chopped on dry ice and afterwards transferred into a tissue grinder containing 7 ml EZ lysis buffer (incl. inhibitors). The tissue was slowly dounced 25 times and incubated for 5 min on ice. The tissue suspension was filtered through a 40 µm Cell strainer and centrifuged at 500 x g for 5 min at 4°C. The supernatant was discarded. The remaining pellet was carefully resuspended in 4 ml EZ lysis buffer (incl. inhibitors) and incubated on ice for 5 min. After another centrifugation step (500 x g, 5 min, 4°C), the supernatant was discarded, and the pellet was resuspended in 5 ml nuclei suspension buffer. Finally, the samples were strained again (40 µm cell strainer) and handed in, to the facility. Libraries were generated using Chromium Next GEM Single Cell 3' HT Reagent kits v3.1 (10x Genomics) aiming for a target of 10.000 cells/sample. Pooled libraries were sequenced on an Illumina NovaSeq 6000 sequencing instrument with 29+89 bp read length (CCG). A detailed description of data processing and analysis is provided in the supplementary materials of the manuscript in Chapter 2.

2.2.4 RNA isolation and cDNA transcription

Ribonucleic acid (RNA) isolation was performed with the Direct-zol RNA Miniprep kit, following the manufacturer's instructions, including the DNase1 treatment step. For kidney tissue, an eighth of a kidney was shredded with BeadBeater® Glass-pellets in 1 ml TRI reagent® using the Precellys, followed by adding an equal amount of EtOH and continuing with the protocol. For *in vitro* samples (6-well plate) 600 µl TRI reagent® were added and incubated for 5 min. Samples were transferred to a fresh tube, an equal amount of EtOH was added and the protocol resumed. Total RNA was used as template for a reverse transcription into coding DNA (cDNA) using the High-Capacity cDNA Reverse Transcription kit, according to the manufacturer's instructions.

2.2.5 Quantitative real-time Polymerase Chain Reaction (qPCR)

To measure the transcription level of mRNA, a quantitative real-time polymerase chain reaction (qPCR) was performed. Primers were previously validated using different dilutions of cDNA (50 ng; 5 ng; 0.5 ng; 0.05 ng) including genomic DNA control. Efficiency was determined using the NEBioCalculator® v1.15.4. For the experimental set-up, an equal amount of cDNA was mixed with SYBR Green, RNase/DNase-free H_2O and target-specific primers (**Tab. 8**) prior to loading onto a plate. After shortly spinning down the plate, the experiment was performed with the QuantStudio™5 Real-Time PCR system, and afterwards analysed with HID Real-Time PCR Analysis Software v1.3 and Prism.

2.2.6 Sample and tissue lysis for immune blotting

To measure protein expression, samples were lysed prior to immune blotting. *In vitro* samples were carefully washed and scraped in 5 ml 1xPBS and pelleted at 1.000 rpm for 5 min and 4°C. The pellet was resuspended in 100 µl modified RIPA buffer for cell lysates (**Tab. 5**) and incubated for 30 min on ice. Whole cell lysates were harvested by washing, scraping in 1xPBS and centrifugation as before. However, cell pellets were immediately lysed in 1x Laemmli, without protein concentration measurement and boiled at 95°C for 10 min. For kidney tissue, one-quarter of a kidney was chopped on ice and afterwards transferred into a tissue grinder containing 700 µl modified RIPA buffer for tissue. After grinding, the samples were sonicated using the Bioruptor® Pico for 5 cycles of 30 s on/off, followed by centrifugation for 10 min at full speed and 4°C. For samples, the protein concentrations were determined via Bicinchoninic Acid (BCA) Protein assay (**2.2.6.1**).

2.2.6.1 BCA assay

The protein concentration of cell lysates was determined with the Pierce™ BCA Protein Assay, according to the manufacturer's instructions. Cell culture samples were measured undiluted, whereas tissue samples were diluted 1:5 in ddH_2O. The prepared assay was incubated at 37°C for 15 min, before measuring the absorbance at 562 nm in the EnSpire Multimode Plate Reader. Thereafter, the sample

volume was adjusted with ddH_2O accordingly to ensure an equal amount of protein was loaded. For western blot, samples were additionally supplemented with Laemmli and boiled at 95°C for 10 min.

2.2.6.2 SDS polyacrylamide gel electrophoresis

To separate proteins by size, a SDS polyacrylamide gel electrophoresis (SDS-PAGE) was performed. To prepare a 10% resolving gel, resolving gel buffer was mixed with ddH_2O and supplemented with APS and TEMED, poured into a gel cassette and covered with isopropanol for 20 min. After polymerization, the isopropanol was washed, and the stacking gel was added. Likewise, the stacking solution was diluted with ddH_2O and supplemented with APS and TEMED. Immediately after the gel was poured, a comb was inserted. Equal amount of protein lysates was loaded as well as 3 µl of the PageRulerPlus, as reference. The SDS-PAGE was performed in 1x running buffer with the setting of 15 min at 110 V, followed by 220 V for 40 min. Depending on the analysis and the proteins of interest, either a chemiluminescent or a fluorescent western blot was performed.

2.2.6.3 Chemiluminescent western blot

After running the SDS-PAGE (**2.2.6.2**), proteins were transferred onto a Millipore Immobilon-P membrane. The membrane was previously activated in MtOH for 1 min. Filter paper and activated membrane were wetted in 1x transfer buffer and assembled in the Owl™ HEP-1 semi-dry electroblotting system according to the following order: filter paper, membrane, polyacrylamide gel, filter paper. Transfer was performed for 54 min at 12 V. Membrane was dried and reactivated in MtOH, washed in ddH_2O and blocked in 5% BSA in 1x protein wash buffer for 1 h at RT. The membrane was washed thrice with 1x protein wash prior to primary antibody incubation (**Tab. 10**) overnight at 4°C. Hereafter, the membrane was washed thrice with 1x protein wash buffer and incubated with the appropriate secondary HRP-conjugated antibody (**Tab. 11**) for 1 h at RT. After the final three washing steps, the signal was developed by incubating the membrane with ECL detection solution or SuperSignal West Femto Chemiluminescent Substrate. The signal was visualized using the Fusion Solo chemiluminometer.

2.2.6.4 Fluorescent western blot

Proteins were transferred onto a Millipore Immobilon-FL membrane. The activation and transfer were performed exactly as previously described (**2.2.6.3**), with the addition that all trays were rinsed with MtOH. After blotting, the membrane was dried, reactivated in MtOH and blocked in 1x ROTI®Block solution for 1h at RT. The membrane was washed three times in 1x LICOR wash buffer before overnight incubation at 4°C with the primary antibody (**Tab. 10**). Next, the membrane was washed thrice with 1x LICOR wash buffer prior to the incubation with the respective secondary LICOR antibody (**Tab. 11**) for 1 h at RT in the dark. Afterwards, the membrane was washed again with 1x PBS. Protein expression

was detected with the Odyssey® M Imaging System, and finally, the densitometry was determined with the Image Studio™ software (version 5.2.5).

2.2.7 Proteomics and phosphoproteomics

The samples used to examine protein expression, interaction or even changes in phosphorylation, were sent to the CECAD proteomics core facility. For *in vitro* experiments, treated cells (**2.2.2.3**) were harvested in ice-cold 1x PBS and pelleted by centrifugation at 3.000 rpm for 5 min at 4°C. Cell pellets were immediately snap-frozen in liquid N_2. Samples were suspended in 200 µl 8 M Urea-Puffer in 50 mM TEAB supplemented with 1:100 Halt phosphatase-protease-inhibitor (PPI). This suspension was thoroughly mixed until dissolved, and sonicated using the Bioruptor® Pico for 5 cycles of 30 s on/off, followed by 1 h centrifugation at full speed and 4°C. Kidney tissue samples (30-45 ng) were shredded in Precellys Lysing kit tubs containing 200 µl 8 M Urea-Puffer in 50 mM TEAB supplemented with 1:100 PPI, three times for 20 s. The supernatant was transferred, sonicated, and centrifuged as before. For all samples, the protein concentration was determined (**2.2.6.1**). Equal protein amounts were filled up to the total volume of 160 µl with UREA buffer supplemented with PPI.

Prior to submission, samples were reduced with 10 mM dithiothreitol (DTT), followed by alkylation with 50 mM chloroacetamide (CAA), both for 1 h at RT. Tissue samples were additionally digested with LysC (1:75) for 2 h at RT. All samples were diluted 1:4 with 50 mM TEAB to reduce the concentration of UREA to 2 M, and finally, trypsinized (1:75) for 17 h at RT in the dark. Tissue samples for phospho-proteomics were handed in immediately after 17 h to the facility for further processing using the High Select TiO2 Kit. For all other proteome samples, the reaction was stopped by acidification with formic acid (1:200).

2.2.7.1 Stage-tip

The double-layered stage-tip clean-up (C18) was performed, after acidification [372]. At first, the stage tip, consisting of two layers of SDB-RPS discs, was equilibrated by adding MtOH, Stage-tip Buffer B and twice Stage-tip Buffer A, with centrifugation at 2.600 rpm for 1 min in between. Samples were loaded and centrifuged at 2.600 rpm until the whole sample had passed through. Thereafter, the stage-tip was washed with Stage-tip Buffer A, and twice with Stage-tip Buffer B. The stage-tips were dried completely and handed into the facility.

2.2.7.2 Proteome analysis

Samples were subjected to analysis at the CECAD proteomics facility using an Orbitrap Exploris 480 mass spectrometer, which was equipped with a FAIMSpro differential ion mobility device and coupled to an UltiMate 3000 system (both Thermo Scientific). The Label-Free Quantification values (LFQ) were computed using the DIA-NN R-package [373]. To generate a spectral library, a SwissProt mouse canonical

database (UP589, downloaded on 18.06.2020) was employed and the library settings were adjusted to match the acquisition parameters, with the "match-between-runs" function enabled. Subsequently, the same samples were used to refine the library for a second search of the sample data. During this process, DIA-NN was executed with additional command-line prompts, including "-report-lib-info" and "-relaxed-prot-inf". The resulting data was subjected to further filtering, with a stringent criterion of a false discovery rate (FDR), 0.01 N-terminal methionine excision, the maximum number of missed cleavages was set to 1 and the minimum peptide length constraints were set between 7 and 30 amino acids. Additionally, the precursor ion m/z values were limited to a range of 400 to 1.000, and cysteine carbamidomethylation was considered a fixed modification. Thereafter, the DIA-NN output underwent additional filtration based on library q-values and global q-values (both ≤ 0.01), with a requirement of at least two identified peptides per protein, which was performed using R v4.1.3. After the removal of decoy and potential contaminant data [374], data was filtered for 4 out of 4 values in at least one condition using LFQ values with Perseus (version 1.6.15.0). The remaining missing values were imputed with random values drawn from a normal distribution by sigma downshift (0.3 σ width, 1.8 σ downshift), using Perseus default settings. Further statistical analysis was performed, including Student's t-tests (S0=0, FDR ≤ 0.05) and Fisher exact tests.

2.2.7.3 Phosphoproteome analysis

At the CECAD proteomics facility, measurements were performed using the Q Exactive Plus Orbitrap mass spectrometer coupled with an EASY nLC system (Thermo Scientific). Peptides were stage-tipped as previously described (**2.2.7.1**) in the facility. The mass spectrometer operated in a data-dependent acquisition mode, with an MS1 survey scan covering the range of 300-1750 m/z and a resolution of 70.000. The top 10 most abundant peptides were isolated within a 1.8 Th window and subjected to HCD fragmentation with a normalized collision energy of 27%. The AGC target was set at 5e5 charges, allowing a maximum injection time of 55 ms. Product ions were detected in the Orbitrap at a resolution of 17.500, and precursors were dynamically excluded for 25 s. Raw data underwent processing using MaxQuant (version 2.2.0.0) [375] with default parameters against the UniProt canonical murine database (UP10090, downloaded on 20.01.2023). The "match-between-runs" option was enabled to facilitate the comparison between replicates. The samples were categorized into two parameter groups: one with enriched samples, featuring phosphorylation (STY) as a variable modification, and the other with non-enriched samples, quantified using LFQ. Further analysis was performed using Perseus 1.6.15 [374]. The protein groups of the whole proteome (WP) were filtered for potential contaminants and insecure identifications and, in the case of non-enriched fractions, those only identified by modified peptides were removed. The enriched fractions of the phosphoproteome (PP) were cleaned up for reverse identified. Data were filtered for completeness for at least one condition using LFQ values (WP) or

intensities (PP). Imputation was performed with standard parameters by sigma downshift (0.3 σ width, 1.8 σ downshift). Finally, Student's t-test between sample groups was performed (S0=0, FDR ≤ 0.05) as well as a 1D enrichment.

2.2.8 Raw data deposition

The proteomics data have been deposited in the ProteomeXchange Consortium (http://proteomecentral.proteomexchange.org) via the PRIDE partner repository [376]. Login information is available upon request.

Table 22 ***Raw data deposition.*** *Raw data can be found with the respective identifier.*

Experiment	**Identifier**
Ciliated vs. Non-ciliated mIMCD3 cells	PXD035290

2.2.9 Statistics

Data are reported as mean values along with their respective ± standard deviation (SD). Statistical analysis was performed using GraphPad Prism version 9.5.1. The differences between means were assessed using one-way ANOVA, Šídák's multiple comparisons test, Tukey test, uncorrected Fisher's LSD test or unpaired Student's t-test as deemed suitable and indicated in figure legends. P-value: <0.001***; 0.002**; 0.033*; ns = 0.12 was used for all figures. All experiments were performed in at least 3 independent biological replicates. All results were normalized to the control group as outlined in the figure legends.

3. Results

The results section is divided into three chapters, presented in the form of three manuscripts. Each chapter will commence with a brief overview of the primary objective of that specific manuscript within the broader context of the entire thesis. This introduction will also provide information about the authors and their contributions to the manuscript, along with an update on the manuscript's status.

3.1 Chapter 1 - Primary cilia suppress Ripk3-mediated necroptosis

Title: Primary cilia suppress Ripk3-mediated necroptosis

Authors: **Emilia Kieckhöfer**, Gisela G Slaats, Lena K Ebert, Marie-Christine Albert, Claudia Dafinger, Hamid Kashkar, Thomas Benzing, Bernhard Schermer

Status: Published in 'Cell Death Discovery'; 02. December 2022

Emilia Kieckhöfer, Gisela G Slaats, Lena K Ebert, Marie-Christine Albert, Claudia Dafinger, Hamid Kashkar, Thomas Benzing, Bernhard Schermer. *Primary cilia suppress Ripk3-mediated necroptosis.* (2022) *Cell Death Discov* 2;8(1):477.

doi: 10.1038/s41420-022-01272-2

PMID: 3646063

As elaborated above, the early pathogenesis of Nephronophthisis (NPH) involves a pronounced loss of epithelial cells in the kidney. However, NPH is considered a disease primarily caused by ciliary dysfunction. Therefore, we aimed to investigate to what extent cilia can modulate regulated cell death response. For this purpose, we used kidney cells incapable of forming cilia and compared them to corresponding ciliated control cells. Our study revealed that cells lacking cilia are significantly more susceptible to necroptosis upon induction of cell death. This implies that cells with impaired ciliary function or upon disassembly of primary cilia are prone to undergo necroptosis, which could explain both the loss of epithelial cells and the development of interstitial inflammation in NPH. Beyond this manuscript, which only contains data on *Nphp1* deficient cells, we also started to examine RCD in cells lacking other NPH proteins (NPHP9 or NPHP10). However, these results were less conclusive, which could be correlated to unaffected ciliogenesis. Thus, these findings will be part of subsequent manuscripts, where we will investigate the role of individual NPH genes in the modulation of RCD in more detail *in vivo*. The phenotypic differences within NPH and NPH-related ciliopathies (NPH-RC) suggest that different ciliary proteins modulate cell death to varying extents. Considering the slow progression of NPH, it seems plausible that during the pathogenesis, the repair of epithelial damage might not be executed properly. Typically, damage in the renal epithelium is repaired by

the proliferation of the remaining surviving cells. In this process, cells have to lose their cilia, which makes them at the same time more susceptible to necroptosis. The ensuing inflammation could make subsequent damage more likely, leading to a progressive disease. However, we cannot rule out the involvement of additional cell death pathways, as will be suggested in the following chapter.

Author contributions:

Emilia Kieckhöfer	performed all experiments except Figure 6 created final figures and wrote the draft of the manuscript
Gisela G Slaats	revised the manuscript
Lena K Ebert	helped with the analysis of the data performed experiments (Figure 6)
Marie-Christine Albert	performed experiments (Figure 6)
Claudia Dafinger	provided *in vivo* materials
Hamid Kashkar	supports the interpretation of the results
Thomas Benzing	designed the study and revised the manuscript
Bernhard Schermer	designed the study, supervised the writing of the manuscript, and revised it for the final version

CDDpress

www.nature.com/cddiscovery

ARTICLE OPEN

Check for updates

Primary cilia suppress Ripk3-mediated necroptosis

Emilia Kieckhöfer[1,2], Gisela G. Slaats[1,2,3], Lena K. Ebert[1,2], Marie-Christine Albert[2,4], Claudia Dafinger[1,2], Hamid Kashkar[2,4], Thomas Benzing[1,2] and Bernhard Schermer[1,2]✉

Cilia are sensory organelles that project from the surface of almost all cells. Nephronophthisis (NPH) and NPH-related ciliopathies are degenerative genetic diseases caused by mutation of cilia-associated genes. These kidney disorders are characterized by progressive loss of functional tubular epithelial cells which is associated with inflammation, progressive fibrosis, and cyst formation, ultimately leading to end-stage renal disease. However, disease mechanisms remain poorly understood. Here, we show that targeted deletion of cilia in renal epithelial cells enhanced susceptibility to necroptotic cell death under inflammatory conditions. Treatment of non-ciliated cells with tumor necrosis factor (TNF) α and the SMAC mimetic birinapant resulted in Ripk1-dependent cell death, while viability of ciliated cells was almost not affected. Cell death could be enhanced and shifted toward necroptosis by the caspase inhibitor emricasan, which could be blocked by inhibitors of Ripk1 and Ripk3. Moreover, combined treatment of ciliated and non-ciliated cells with TNFα and cycloheximide induced a cell death response that could be partially rescued with emricasan in ciliated cells. In contrast, non-ciliated cells responded with pronounced cell death that was blocked by necroptosis inhibitors. Consistently, combined treatment with interferon-γ and emricasan induced cell death only in non-ciliated cells. Mechanistically, enhanced necroptosis induced by loss of cilia could be explained by induction of Ripk3 and increased abundance of autophagy components, including p62 and LC3 associated with the Ripk1/Ripk3 necrosome. Genetic ablation of cilia in renal tubular epithelial cells in mice resulted in TUNEL positivity and increased expression of Ripk3 in kidney tissue. Moreover, loss of *Nphp1*, the most frequent cause of NPH, further increased susceptibility to necroptosis in non-ciliated epithelial cells, suggesting that necroptosis might contribute to the pathogenesis of the disease. Together, these data provide a link between cilia-related signaling and cell death responses and shed new light on the disease pathogenesis of NPH-related ciliopathies.

Cell Death Discovery (2022)8:477 ; https://doi.org/10.1038/s41420-022-01272-2

INTRODUCTION

Primary cilia are antenna-like sensory organelles that receive signals from the environment, transmit them to the interior of the cell, and thus modulate the response of cells to environmental influences [1–3]. For this purpose, cilia are covered by a highly specialized plasma membrane whose protein composition is precisely regulated [4]. At the base, a cilium is anchored by its basal body, which resembles a modified centriole. The import and export of ciliary proteins are primarily regulated at the transition zone, located between the basal body and the ciliary shaft [5]. Cilia modulate multiple signaling pathways, including Hedgehog, Wnt, Notch, PDGF, and additional GPCR signaling [1]. Dysfunction or loss of the primary cilium inevitably leads to perturbations of these signaling pathways and results in diseases known as ciliopathies [6]. The spectrum of ciliopathies ranges from severe neuronal developmental disorders and retinal or skeletal ciliopathies to endocrinological conditions and hepatic and renal diseases [7]. While most ciliopathies occur as syndromes that affect different organ systems, a significant feature of many ciliopathies is the involvement of the kidneys. Therefore, this large subgroup is also referred to as renal ciliopathies [8].

Among renal ciliopathies, autosomal-dominant polycystic kidney disease (ADPKD) is the most frequent form, with an incidence of 1:1000, typically affecting adults and leading to end-stage kidney failure at the age of 50 to 60 years [9]. In children, nephronophthisis (NPH), an autosomal-recessive renal ciliopathy, is the most frequent genetic cause of renal failure and is responsible for approximately 10% of children requiring dialysis [10]. The renal phenotype of ADPKD and NPHP differs: Kidneys in ADPKD enlarge significantly during the disease and are progressively interspersed with numerous cysts. In contrast, significantly fewer cysts develop in NPH. Here, kidneys are relatively small and characterized by tissue degeneration and interstitial inflammatory fibrosis [11, 12]. Notably, patients with ADPKD or NPH are born without any overt renal phenotype but massively lose renal tubular epithelial cells with disease onset and progression. In ADPKD, apoptosis has been described very early by TUNEL assays [13] and was later found in several animal models of ADPKD (reviewed in ref. [14]). More recently, the role of apoptosis in cyst lumen formation in ADPKD has been suggested [15]. Remarkably, primary cilia appear to be normal or elongated in kidneys of ADPKD mouse models [16–18], while loss of NPHP genes often

[1]Department II of Internal Medicine and Center for Molecular Medicine Cologne, University of Cologne, Faculty of Medicine and University Hospital Cologne, Cologne, Germany. [2]CECAD, University of Cologne, Faculty of Medicine and University Hospital Cologne, Cologne, Germany. [3]Department of Nephrology and Hypertension, University Medical Center Utrecht, Utrecht, The Netherlands. [4]Institute for Molecular Immunology, University of Cologne, Faculty of Medicine and University Hospital Cologne, Cologne, Germany. ✉email: bernhard.schermer@uk-koeln.de

Received: 12 September 2022 Revised: 21 November 2022 Accepted: 23 November 2022
Published online: 02 December 2022

results in ciliary abnormalities and lower numbers of primary cilia [19–22].

In addition to apoptosis, various pathways of regulated cell death, specifically regulated necrosis (termed necroptosis), have been described [23] that could contribute to tissue defects associated with the loss of primary cilia. In contrast to immunogenically relatively silent apoptotic cell death, necroptosis involves cellular membrane damage, the release of damage-associated molecular patterns (DAMPs), and provokes inflammatory tissue conditions which further enhance inflammatory tissue destruction [24]. The role of necroptosis in the kidney, in particular in acute kidney injury (AKI) induced by ischemia-reperfusion damage or by pharmacological means, is well-established [25]. Necroptosis is typically activated downstream of receptor activation, including death or toll-like receptors, in conditions when caspase-8 is inhibited [26]. Here, the mechanisms of TNFα (tumor necrosis factor α) signaling are best understood [27, 28]: Binding of TNFα to the TNFR1 receptor recruits TRAAD (TNF-receptor-associated death domain), Ripk1 (receptor-interacting serine/threonine kinase 1), Traf2 and Traf5 (TNF-receptor-associated factor 2/5) as well as cIAP1 and cIAP2 (cellular inhibitor of apoptosis1/2). This active complex I initially results in NF-κB (nuclear factor κB) and MAPK (mitogen-activated protein kinases) activation and transcription of pro-survival genes. Dissociation of the receptor from Ripk1 can result in three different types of complex II, each promoting cell death. The apoptotic complex IIa includes TRADD, FADD, and Caspase-8. Complex IIb requires the absence of cIAP1/2 and results in Ripk1- and Casp-8-dependent apoptosis. Upon inhibition of Caspase-8 Ripk1 and Ripk3 (receptor-interacting serine/threonine-protein kinase 1/3) form a complex often called the necrosome (complex IIc) [29]. Subsequently, active Ripk3 phosphorylates its substrate mixed lineage kinase domain-like (Mlkl), which executes cell death. This most likely involves translocation of Mlkl to the plasma membrane and the formation of pores that disrupt membrane integrity [29, 30]. Remarkably, either expression of a kinase-dead mutant Ripk1, loss of Ripk3, or loss of Mlkl protects mice from kidney failure in different scenarios of AKI [31–33]. In addition, synchronized cell death through the ferroptotic pathway has also been demonstrated to contribute to acute damage and to the loss of entire tubular segments [34]. Upon ferroptotic cell death, however, the immunological response might be much milder as compared to necroptosis. Therefore, the kidneys might be able to cope with ferroptotic cell loss more efficiently than with necroptosis [25]. While the different pathways of necroptosis have been extensively studied in AKI, their role in renal ciliopathies and, in particular, their connection with primary cilia remained elusive. Here, we study how primary cilia modulate cell death induced by TNFα in combination with the SMAC mimetic birinapant or cycloheximide (CHX) or by interferon-gamma (IFNγ) under the inhibition of caspase-8, which typically would promote necroptotic death. Remarkably, these conditions do not induce necroptosis in wild-type renal epithelial cells carrying primary cilia, while cells without cilia display an increased susceptibility towards necroptosis and Ripk1-dependent apotosis. Mechanistically, this can be explained by increased expression of Ripk3 and components of the autophagy-lysosomal pathway in cells without cilia. Moreover, the deletion of the major gene involved in NPH in non-ciliated cells further enhanced the susceptibility to necroptosis, supporting the role of necroptotic death in renal ciliopathies.

RESULTS

Loss of cilia increases the susceptibility to necroptosis

To study the role of primary cilia in apoptotic and necroptotic cell death of renal epithelial cells, we used mouse inner medullary collecting duct (mIMCD3) cells, a well-established model in renal and cilia research. Notably, several classical ciliary proteins, including critical components of the intraflagellar transport (IFT) machinery, can affect inflammatory signaling independent of primary cilia [35]. Therefore, instead of targeting proteins involved in IFT to interfere with cilia and ciliogenesis, we generated subclones from the parental wild-type mIMCD3 cell line by FACS and screened those subclones for the presence and absence of primary cilia. We randomly selected two subclones: Ckc (ciliated kidney cells), with about 80% of cells carrying a primary cilium, and Nckc (non-ciliated kidney cells) displaying almost no cilia at all (1%), as demonstrated by cilia staining (Fig. 1A). Induction of Ripk1-dependent cell death with TNFa and the SMAC mimetic birinapant (complex IIb) for 16 hours resulted in Ripk1-dependent cells death and reduced the number of viable cells to 38% in the non-ciliated cells (Fig. 1B). The Ripk1-inhibitor Nec1s partially protected from cell death, while inhibition of Ripk3 with GSK872 further enhanced cells death by inhibiting necroptosis but promoting apoptosis. Combined treatment of non-ciliated-cells with TNFa, birinapant and the caspase-8 inhibitor emricasan [36] resulted in almost no surviving cells. Caspase-8 inhibition is known to unleash necroptotic cell death by involving kinase activity of Ripk1 and Ripk3 [26]. Consistently, this could be almost rescued either by inhibition of Ripk1 or by inhibition of Ripk3, indicating that cell death was caused by nectroptosis. Ciliated cells showed almost no cell death response upon TNFa and birinapant treatment. Here, treatment with Ripk1/3 inhibitors slightly enhanced cell death by promoting apoptosis. Caspase-8 inhibition, which killed almost all non-ciliated cells, had no significant effect on cells with cilia (Fig. 1B). To investigate the role of complex IIa activation, we performed similar assays with induction of cell death by TNFα and CHX (TC) for 16 hours (Fig. 1C). Here, only 24% of cells with primary cilia survived, whereas 44% of non-ciliated cells did not respond to TNFα and CHX, indicating some protection from apoptosis. Remarkably, simultaneous inhibition of caspase activity using emricasan (TCE treatment) positively affected cell survival of ciliated cells (47% viability), while almost all non-ciliated cells underwent cell death (0.3% viability). Consistent with the induction of necroptotic death, the Ripk1-inhibitor Nec1s and the Ripk3 inhibitor GSK872 efficiently reduced TNF-induced cell death only when caspase activity was blocked by emricasan (TCEN treatment) in the non-ciliated cells (Fig. 1C). Immunoblots for cleaved caspase-3 indicated apoptosis occurring primarily in TC-treated ciliated cells, while phospho-Mlkl (pMlkl) as a marker for necroptosis was detected only upon TCE treatment in non-ciliated cells (Fig. 1D). To analyze the temporal dynamics of cell death and the cellular morphology, we performed a live-cell analysis of cells upon treatment with DMSO, TC, or TCE over the period of 24 h. These data confirmed our findings and revealed rapid cell death upon caspase-8 inhibition in the non-ciliated cells already at very early time points (Fig. 1E). Ciliated cells exposed to TC treatment showed membrane blebbing, condensation, and fragmentation of nuclei indicative of apoptosis, while upon TCE treatment, they did neither display nuclear condensation nor formation of apoptotic bodies (Suppl. Fig. 1A). Similarly, dead cells upon TCE treatment of non-ciliated cells did not resemble morphological changes of apoptotic cells. Notably, TNFα-independent induction of cell death via interferon γ (IFNγ) combined with caspase-8 inhibition induced necroptotic death only in cells lacking primary cilia but not in ciliated cells, as shown by additional live-cell assays (Suppl. Fig. 1B).

For additional confirmation that this switch in the death response resulted from the lack of cilia and to exclude any clonal effects, we used Myosin5a-deficient mIMCD3 cells. Myosin5a (Myo5a) is an actin-based motor and transport protein. Cells deficient in Myo5a are unable to assemble primary cilia [37]. Here, loss of cilia is caused by defective transport of the pre-ciliary vesicle to the mother centriole, the later basal body [38]. Loss of cilia in Myo5a$^{-/-}$ compared to Myo5a$^{+/+}$ control cells was confirmed by immunofluorescence staining using antibodies

against Arl13B and acetylated tubulin as ciliary markers (Suppl. Fig. 2A). Cell viability assays with TC, TCE, and TCEN treatments confirmed the findings from the Ckc and Nckc subclones in all aspects: Myo5a$^{-/-}$ cell without cilia were partially protected from apoptosis in response to TC treatment. Induction of necroptosis by TCE treatment led to massive cell death only in Myo5a$^{-/-}$ cells, which again was sensitive to necrostatin-1s (Fig. 2A). Immunoblots confirmed cleavage of caspase-3 primarily in ciliated Myo5a$^{+/+}$ cells which was reduced in Myo5a$^{-/-}$ cells lacking cilia, indicating a lower rate of apoptosis, while the phosphorylation of Mlkl was detectable in both, however slightly increased in non-ciliated cells after caspase inhibition with emricasan (Fig. 2B). Live-cell imaging

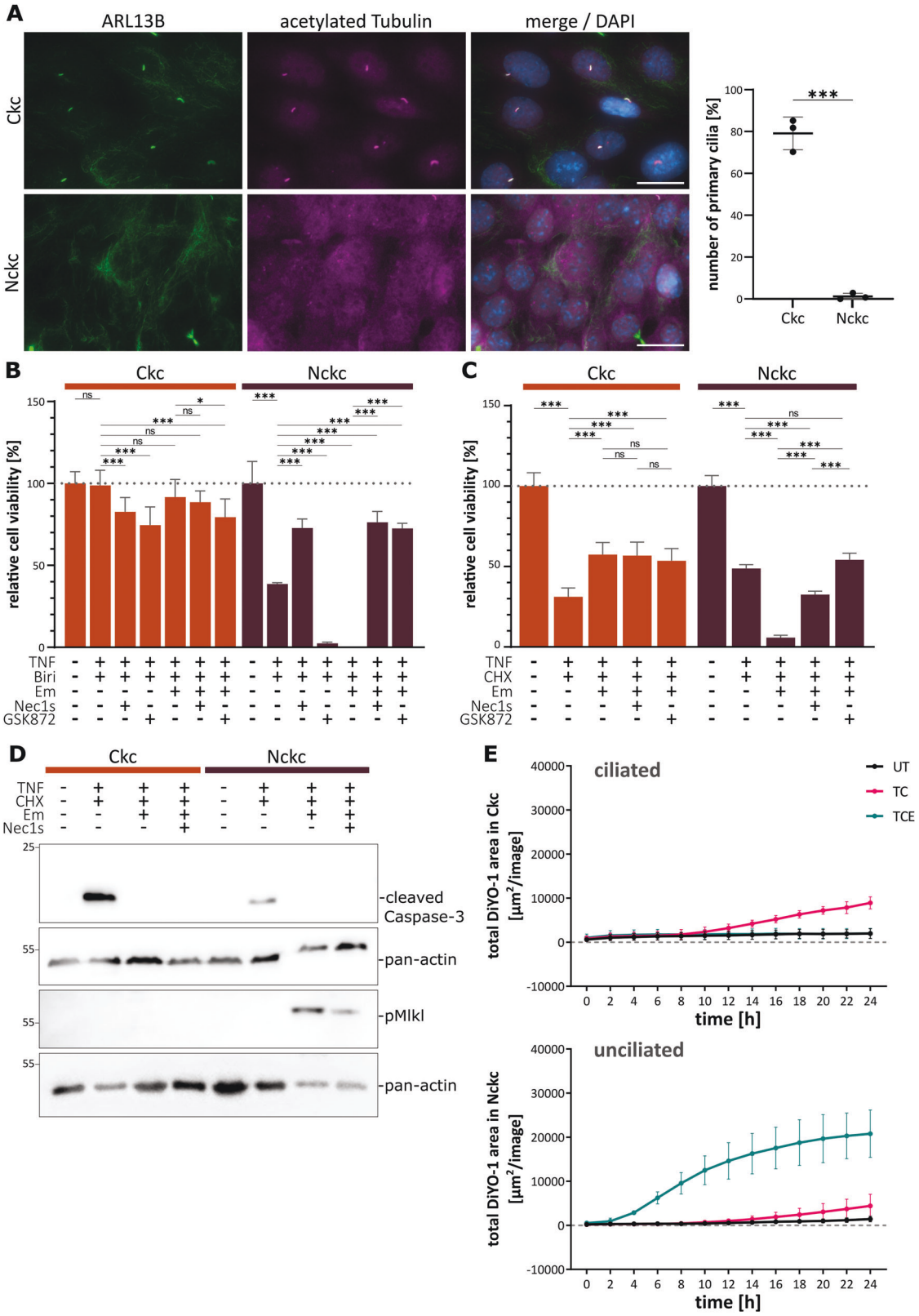

Fig. 1 Primary cilia inhibit necroptotic cell death in renal epithelial cells. A Immunofluorescence staining of primary cilia in the mIMCD3 subclones Ckc (ciliated kidney cells) and Nckc (non-ciliated kidney cells; ARL13B (magenta), acetylated tubulin (green) and DAPI (blue); scale bar 20 µm). Quantification of cells carrying primary cilia ($n = 3$; total count of 404 cells for Ckc and 613 cells for Nckc). **B** Neutral-red assay in Ckc and Nckc cells after RCD induction with TNFα (TNF, 4 ng/100 µl) and birinapant (biri, 5 µM) for 16 h. Additionally, caspase-8 inhibitor emricasan (Em, 10 µM), Ripk1 inhibitor necrostatin-1s (Nec1s, 40 µM), and Ripk3 inhibitor GSK872 (GSK872, 5 µM) were used for 16 h ($n = 4$). **C** Neutral-red assay in Ckc and Nckc cells after RCD induction with TNFα (TNF, 4 ng/100 µl) and cycloheximide (CHX, 2 µg/100 µl) for 16 h. Additionally, caspase-8 inhibitor emricasan (Em, 10 µM) and necroptosis inhibitor necrostatin-1s (Nec1s, 40 µM) were used for 16 h ($n = 4$). **D** Immunoblot analysis of ciliated and non-ciliated cells using the apoptosis marker cleaved-Caspase-3 (~17 kDa) and the necroptosis marker phospho-Mlkl (~56 kDa). Either pan-actin (~44 kDa) or beta-tubulin (~55 kDa) were used as control ($n = 3$). **E** Live-cell imaging over the period of 24 h after treatment with TNF and CHX (TC), and TNF, CHX, and Em (TCE) or DMSO as control. Cells were stained with the dead cell marker DiYO-1. Images were captured every 2 h ($n = 3$).

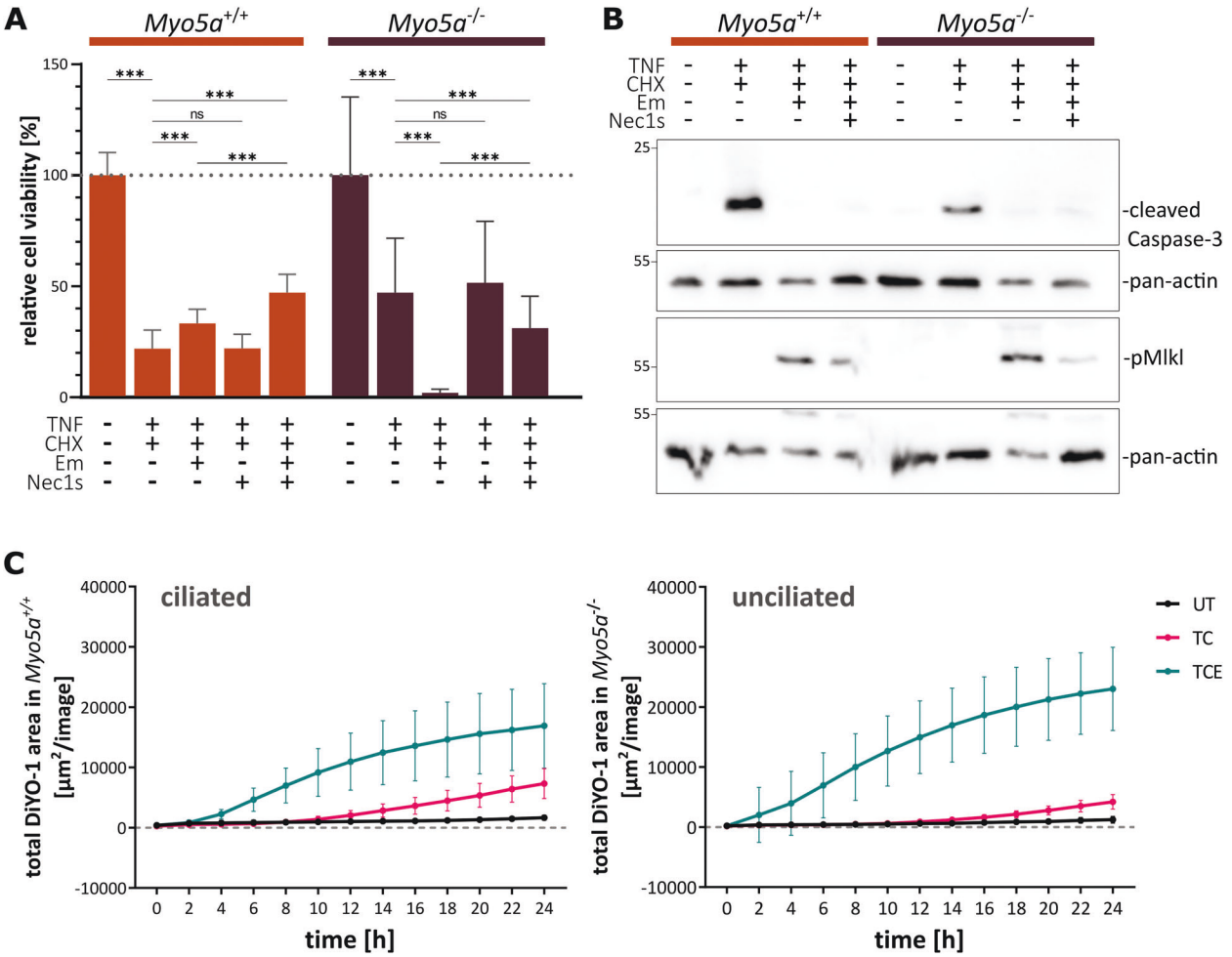

Fig. 2 Loss of cilia in Myo5a-deficient cells increases susceptibility to necroptotic death. A Neutral-red assay in control and *Myo5a*$^{-/-}$ cells after RCD induction through TNFα (TNF, 4 ng/100 µl) and cycloheximide (CHX, 2 µg/100 µl) for 16 h. Additionally, caspase-8 inhibitor emricasan (Em, 10 µM) and necroptosis inhibitor necrostatin-1s (Nec1s, 40 µM) were used for 16 h ($n = 4$). **B** Immunoblot analysis of ciliated and non-ciliated cells using the apoptosis marker cleaved caspase 3 (~17 kDa) and the necroptosis marker phospho-Mlkl (~56 kDa). As housekeeping control either pan-actin (~30 kDa) or beta-tubulin (~55 kDa) were used ($n = 3$). **C** Live-cell imaging over the period of 24 h after treatment with TNF and CHX (TC), and TNF, CHX, and Em (TCE) or DMSO as control. Cells were stained with the dead cell marker DiYO-1. Images were captured every 2 h ($N = 8$).

again revealed the increased occurrence of cell death at a very early time point after TCE treatment (Fig. 2C and Suppl. Fig. 2B). Interestingly, in contrast to the viability assay in Fig. 2A ciliated cells also underwent cell death upon TCE, although to a lower rate as non-ciliated cells. This can be explained by the low cell density required for live-cell imaging, which results in a higher number of proliferating and, therefore, transiently non-ciliated cells as compared to the viability assays. In contrast to the subclones Ckc and Nckc, differences between Myo5a$^{+/+}$ and Myo5a$^{-/-}$ cells, in general, were slightly less pronounced, which might be due to the fact that the number of ciliated cells in the parental Myo5a$^{+/+}$ cells (25%) was much lower (Suppl. Fig. 2A) as compared to the ciliated subclone Ckc used in Fig. 1 (79%; Fig. 1A). Taken together, these data show that loss of cilia results in a shift from apoptotic to necroptotic cell death.

Altered Ripk3 and Ripk1 in cells lacking primary cilia

To understand how the loss of primary cilia increases susceptibility to necroptotic cell death, we analyzed mRNA expression of cell death-related genes both in untreated and TC-treated cells, again

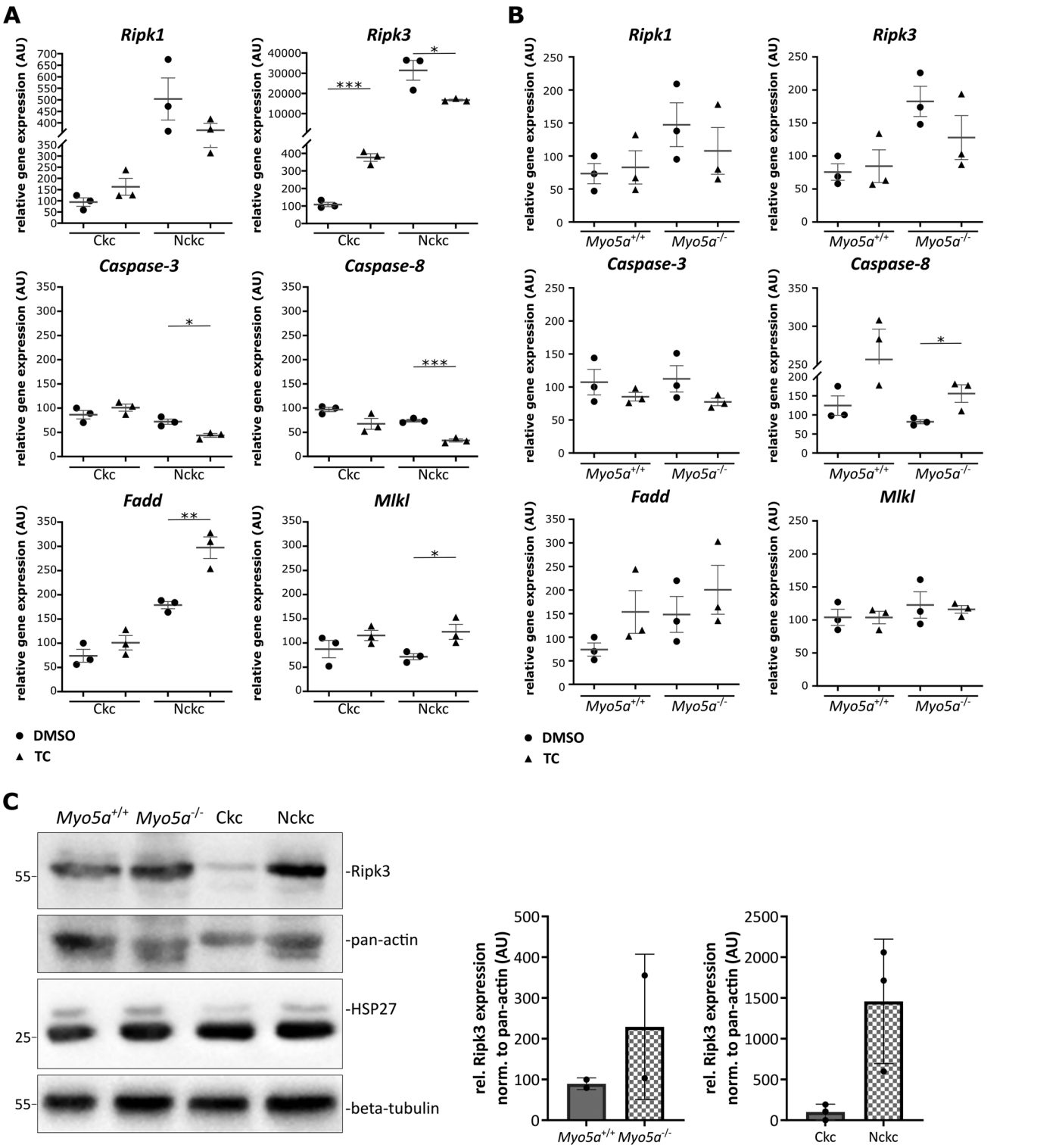

Fig. 3 Increased expression of Ripk3 in cells lacking primary cilia. A, **B** Quantitative real-time PCR of several cell death-related genes in mIMCD3 cells revealed upregulation of necroptosis players in non-ciliated cells: **A** Ckc versus Nckc ($n = 3$); **B** control versus *Myo5a*$^{-/-}$ ($n = 3$). Cells were treated with TNFα (TNF, 4 ng/100 µl) and cycloheximide (CHX, 2 µg/100 µl) for 16 h or with DMSO. Statistical analysis was performed by using a one-way ANOVA followed by a two-sided Student's *t* test (*p* value: >0.001***; 0.002**; 0.033*; ns = 0.12). **C** Immunoblot analysis of lysates from untreated ciliated (*Myo5*$^{+/+}$/Ckc) and non-ciliated (*Myo5a*$^{-/-}$/Nckc) cells using Ripk3 (~57 kDa) and HSP27 (~27 kDa) antibodies. Pan-actin (~30 kDa) or beta-tubulin (~55 kDa) were used as controls.

comparing Ckc with Nckc (Fig. 3A) as well as Myo5a$^{+/+}$ with Myo5a$^{-/-}$ cells (Fig. 3B). While caspase-3 and caspase-8 expression levels were independent of the presence of primary cilia, these data revealed significantly higher expression levels of Ripk3 mRNA in non-ciliated cells and a trend toward increased expression for Ripk1 and Fadd. Immunoblotting confirmed increased levels of Ripk3 on the protein level in both cell lines without cilia (Fig. 3C). Susceptibility to TNFα could result from

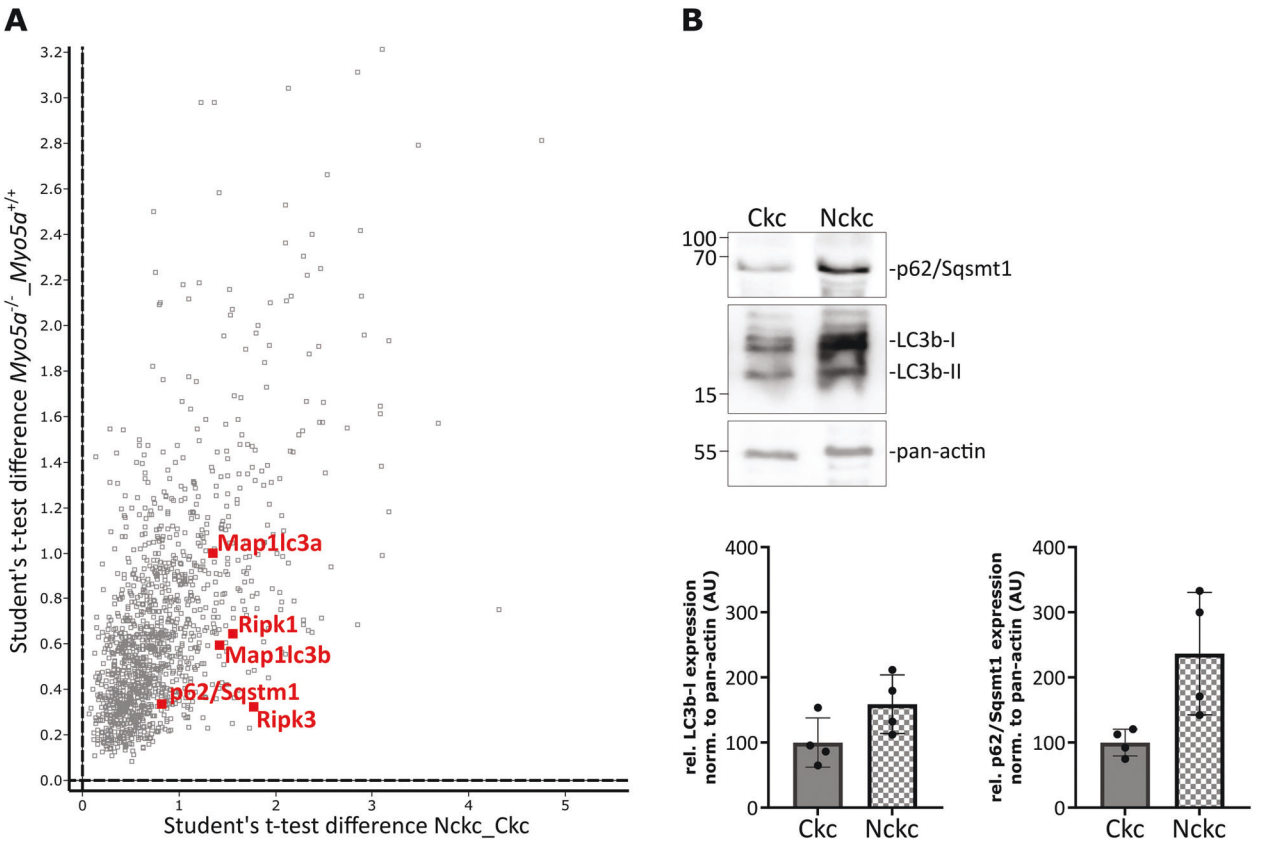

Fig. 4 Loss of cilia induces upregulation of the p62/Ripk1 module. A Details from the scatter blot (total plot in Suppl. Fig. 4E) highlighting proteins connecting the autophagosome and the necrosome. **B** Immunoblot analyses of DMSO treated Nckc versus Ckc for LC3 (~17 kDa) and p62/Sqstm1 (~62 kDa) expression ($n = 4$) and densitometric analysis, normalized to pan-actin ($n = 4$).

reduced NF-κB signaling in non-ciliated cells. However, immunoblots revealed increased levels of the NF-κB inhibitor IκBα in cells lacking cilia (Suppl. Fig. 3A, B), indicating increased NF-κB activity. Short-term stimulation with TNFα led to increased phosphorylation and consistently degradation of IκBα while inducing phosphorylation of NF-κB p65 at Ser536. Consistently, qPCR data on NF-κB expression (Suppl. Fig. 3C, D) confirmed that NF-κB activity is not reduced in non-ciliated cells. Therefore, the upregulation of Ripk3 and Ripk1 in non-ciliated cells can explain their marked susceptibility to necroptosis, and the underlying molecular mechanisms leading to Ripk3/Ripk1 upregulation remain elusive.

Proteomic profiling identifies deregulation of autophagy-related and lysosomal proteins

To gain additional mechanistic insights into the increase in necroptotic death and in Ripk3 expression in non-ciliated cells, we performed an unbiased proteomic analysis to identify differentially expressed proteins and pathways related to the loss of cilia in the respective cell lines. Principal component analyses clearly separated CkC from Nckc (Suppl. Fig. 4A), as well as Myo5a$^{-/-}$ from Myo5a$^{+/+}$ control cells (Suppl. Fig. 4B). Compared to the respective controls and based on a Student's *t*-test with standard parameter (S0 = 0 and threshold *p* value > 0.05), we found 3094 differentially expressed proteins in Nckc and 2980 differentially expressed proteins in Myo5a$^{-/-}$ (Supplementary Table S2). The identified differentially expressed proteins were used as input for clustered heat maps of both datasets (Suppl. Fig. 4C, D). To identify the common proteins and pathways altered upon loss of cilia, we compared significantly regulated proteins from both datasets to visualize the similarities of both unciliated cell lines. Student's t-test difference of non-ciliated cells versus ciliated cells correlates, which reveals 2282 equally upregulated and 832 down-regulated proteins demonstrating the similarity between the two loss-of-cilia models (Suppl. Fig. 4E). Gene ontology and KEGG pathway analyses of the clustered non-ciliated data set of significantly up or down-regulated proteins revealed terms related to spliceosome and lysosome to be enriched (Suppl. Fig. 5A). Indeed, many autophagy proteins were significantly altered in both unciliated cell lines, as shown in representative volcano blots (Suppl. Fig. 5B, C). Strikingly, we observed an enrichment of proteins previously shown to connect the autophagosome with the necrosome, particularly an increased expression of Map1lc3a/b (LC3) and p62/Sqsmt1, as well as Ripk1 and Ripk3 (Fig. 4A). This increased expression of LC3 and p62/Sqsmt1 in non-ciliated cells could be further confirmed by immunoblotting (Fig. 4B).

Necroptosis in the kidney upon loss of cilia

To understand the significance of our findings in vivo, we studied cell death in mice lacking functional primary cilia in the distal part of the nephron. Specifically, we knocked out the kinesin Kif3a in the distal tubules and collecting ducts of the kidney using the Ksp:Cre line. Kif3a is a subunit of the kinesin-2 motor required for intraflagellar transport, the transport of cargo along ciliary microtubules [39]. These mice develop cystic kidney disease starting with tubular dilatations in the first week of their life [40]. We used kidneys of Kif3a$^{fl/fl}$:ksp:cre$^{+/-}$ (Kif3a^{tko}) and Kif3a$^{fl/wt}$:ksp:cre$^{+/-}$ (control) mice at postnatal days P4 and P28 and found TUNEL positivity increasing with age (Fig. 5A). Notably, qPCR analysis revealed a significant upregulation of Ripk3 in Kif3a^{tko} kidneys together with an increase in TNFα mRNA levels at P28, while caspase-3, caspase-8, Fadd, Mlkl, and Ripk1 were not significantly altered (Fig. 5B). Moreover, we detected high levels of

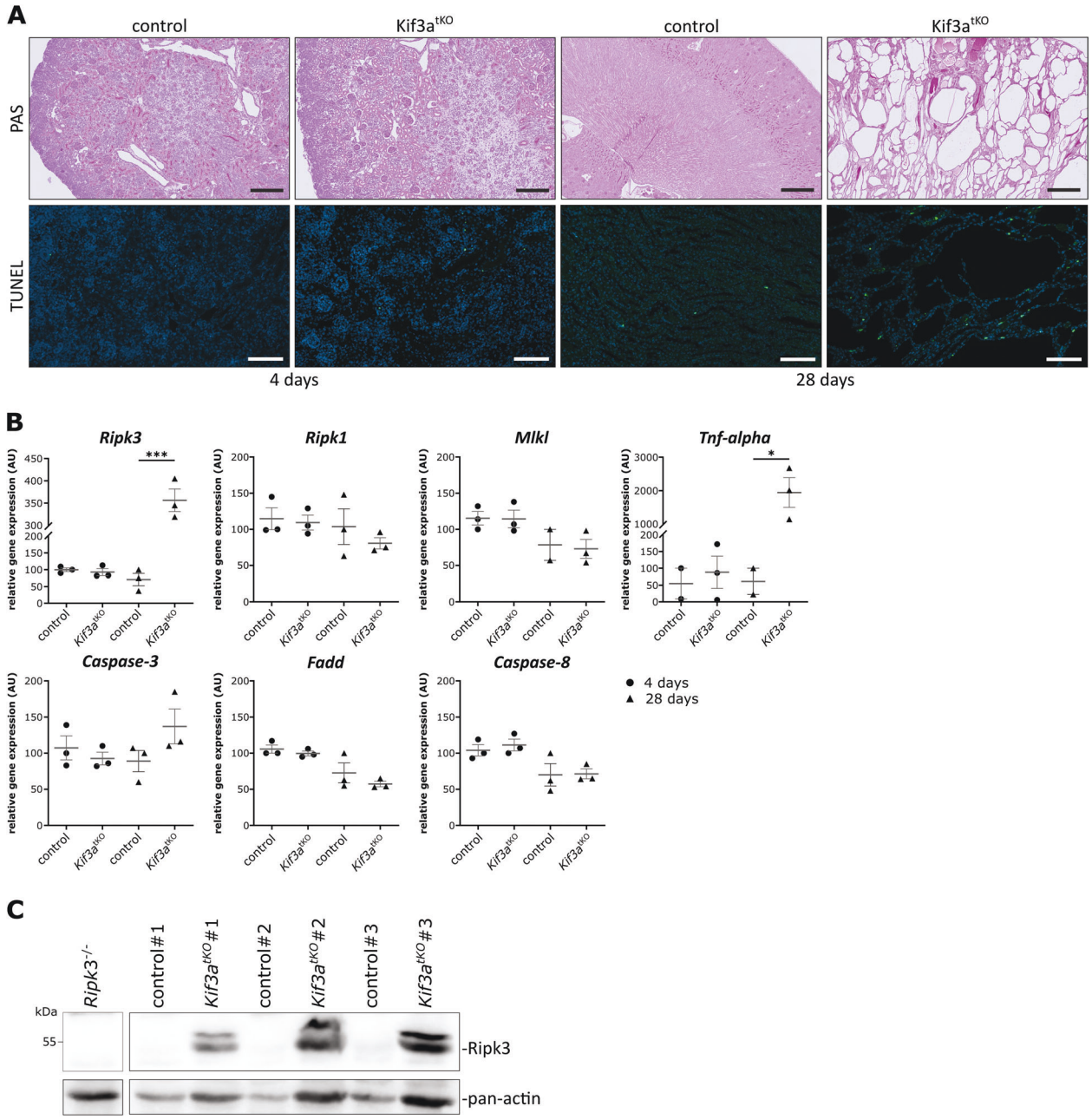

Fig. 5 Genetic targeting of ciliogenesis leads to cell death and increased Ripk3 expression in vivo. A PAS staining of kidneys from *Kif3a*$^{fl/fl}$:Ksp:cre$^{+/-}$ and *Kif3*$^{fl/wt}$:Ksp:cre$^{+/-}$ mice at a postnatal age of 4 days (scale bar 200 µm) and 28 days (scale bar 500 µm) showing the loss of kidney architecture and cyst formation over time. TUNEL staining (scale bar 100 µm) indicates cell death. **B** Quantitative real-time PCR of several cell death genes showing upregulation of necroptosis-specific genes in mouse tissue lacking primary cilia ($n = 3$). Statistical analysis was performed by using a one-way ANOVA followed by a two-sided Student's *t* test (*p* value: >0.001***; 0.002**; 0.033*; ns = 0.12). Control, heterozygous transgenic mice. **C** Immunoblot analysis of 28-day-old mice for Ripk3 expression (~57 kDa; $n = 3$ individual animals shown).

Ripk3 in protein lysates from those kidneys, indicating an increased propensity to necroptosis during renal cyst formation and tissue degeneration (Fig. 5C). It is important to note that we did not detect any significant alterations in the expression of cell death genes at P4 at the time when kidney tissue showed almost no signs of cyst formation. However, cilia were described to be normal at birth (P0) in this mouse model [40], and cells of the distal nephron still carry some primary cilia at P4 (Suppl. Fig. 6, DBA-positive tubules). This is in line with the fact that loss of cilia itself is not sufficient to trigger cell death but can increase susceptibility to necroptosis under inflammatory conditions involving TNF or IFNγ. So far, we can only speculate about the factors that trigger necroptotic cell death during the early phase prior to cyst formation in Kif3a^{tko} mice.

The loss of the ciliary signaling protein Nphp1 enhances necroptotic cell death

Deletions of *NPHP1* are the most frequent cause of NPH, a pediatric ciliopathy and kidney disease that is characterized by tubular atrophy, cyst formation, interstitial fibrosis, and inflammation [11, 12, 41]. Nphp1 does not encode for a structural ciliary protein but for the key protein of the NPHP-protein complex involved in ciliary signaling [21]. Nphp1 is localized at the transition zone of primary cilia [42]. Therefore, Nphp1 deficiency

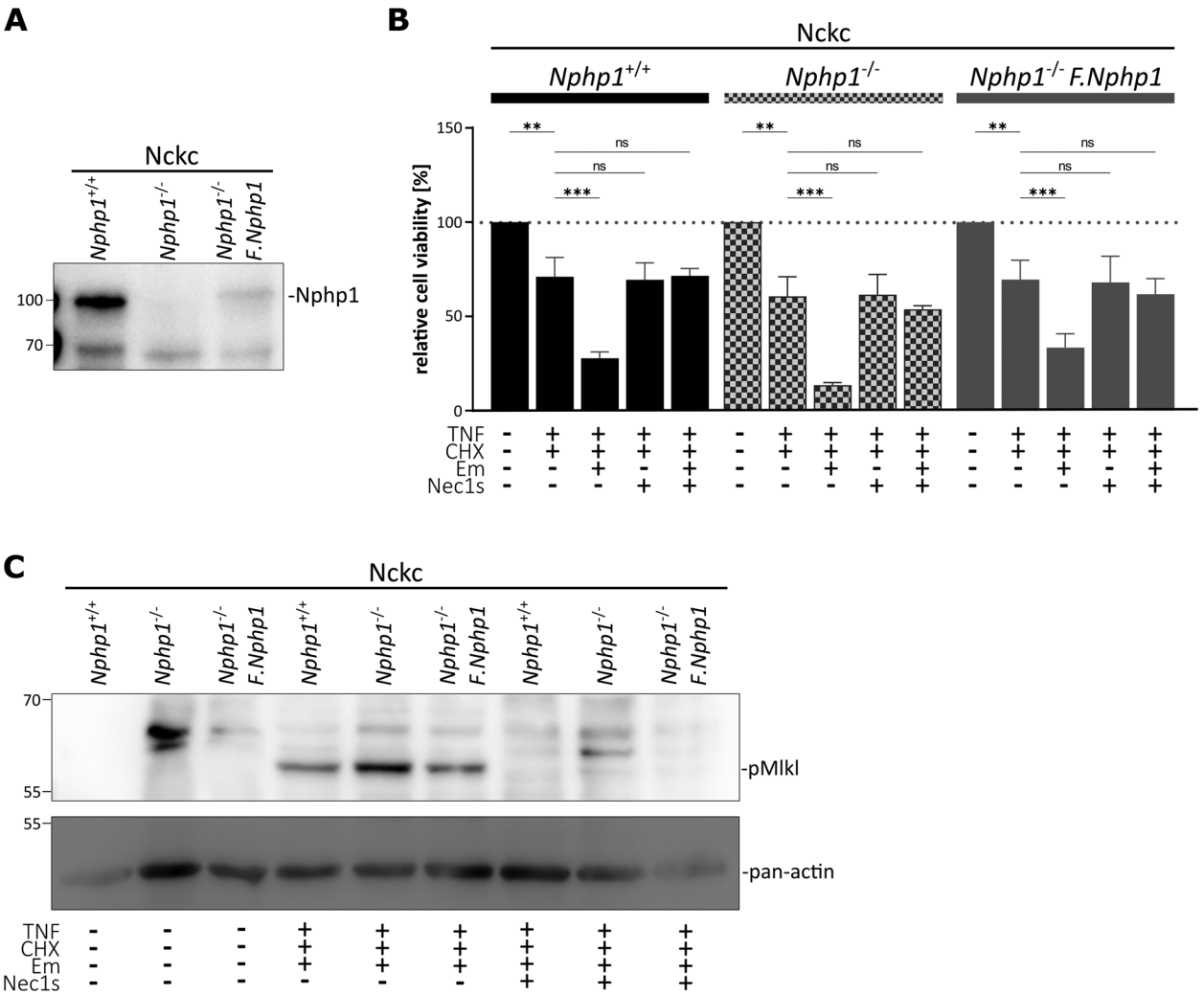

Fig. 6 Loss of the functional but not structural ciliary protein Nphp1 enhances the necroptotic response. A Immunoblot analysis demonstrating Nphp1 deficiency in Nphp1$^{-/-}$ cells and confirming re-expression of FLAG.Nphp1 by using Nphp1 (~83 kDa). **B** Neutral-red assay in Nckc proficient and deficient in Nphp1. RCD induction with TNFα (TNF, 4 ng/100 µl) and cycloheximide (CHX, 2 µg/100 µl) for 16 h. Additionally, caspase-8 inhibitor emricasan (Em, 10 µM) and necroptosis inhibitor necrostatin-1s (Nec1s, 40 µM) were used for 16 h ($n = 3$). Knockout of Nphp1 resulting in increased necroptotic death. **C** Immunoblot of phospho-Mlkl (~56 kDa) in Nphp1 proficient and deficient cells upon TC and TCE treatment for 8 h. Pan-actin was used as a loading control ($n = 3$).

does not result in the loss of primary cilia but rather causes cilia signaling defects. Kidneys have the capacity for intrinsic repair. Repair is based on dedifferentiation and proliferation of renal tubular cells without the need for prespecified stem cell populations and involves regulated disassembly and reassembly of primary cilia [43, 44], allowing the cells to reenter the cell cycle and undergo cell division [45]. Since the ciliary basal body, a modified centriole, is required to form the later spindle poles, cells have to disassemble the cilium prior to cell cycle re-entry. In this scenario, increased susceptibility to necroptosis might be of particular importance. To study whether loss of *Nphp1* might promote necroptotic damage under such conditions, we generated *Nphp1*$^{-/-}$ cells in the non-ciliated Nckc subclone. As an additional control, we used single-copy integration into the *Rosa26* locus to re-express low levels of FLAG-tagged Nphp1. Expression of Nphp1/F.Nphp1 was controlled by immunoblotting of cell lysates using a specific Nphp1 monoclonal antibody [46] (Fig. 6A). When performing cell viability assays, we shortened the treatment time to 8 h to gain a larger number of surviving cells upon TCE treatment. The knockout of *Nphp1* indeed enhanced necroptotic response, which could be rescued by necrostatin-1s and partially by the re-expression of FLAG.Nphp1 (Fig. 6B). Immunoblotting again revealed the activation of Mlkl as indicated by phosphorylation (Fig. 6C). These data might indicate that in the absence of cilia Nphp1-related signaling is responsible for suppressing necroptosis.

DISCUSSION

Given the massive loss of tubular epithelial cells during the progression of renal ciliopathies, we investigated whether cilia could shape the response of renal epithelial cells upon induction of cell death. Interestingly, while the majority of ciliated renal epithelial cells underwent apoptosis after exposure to TNF and CHX, they did not appear to involve necroptosis as the inhibition of caspase activity did not induce necroptosis in these cells. Remarkably, this changed with the loss of primary cilia. In cells lacking cilia, apoptosis was reduced when exposed to TNF and CHX. Such protection from apoptosis might be important under physiological conditions when cells transiently disassemble their cilium prior to cell cycle re-entry and repair of tubular injuries. However, further inhibition of caspase activity in non-ciliated cells, mimicking inflammatory conditions, led to massive RIPK1-mediated necroptotic cell death, as indicated by the phosphorylation of MLKL. We can thus show for the first time that the absence of cilia

switches the response of cells from apoptosis to necroptosis. Notably, the mere loss of cilia is not sufficient to drive cells into necroptosis. This is consistent with the phenotype of mice bearing genetic alterations that affect cilia or related human diseases since kidneys typically are unaffected at birth. Defective cilia, however, increase susceptibility to necroptosis under inflammatory conditions, and there must be additional factors in the progression of kidney disease that eventually initiate necroptotic cell death.

Mechanistically, we found Ripk3 to be upregulated both in mIMCD3 cell lines without cilia as well as in kidneys from mice lacking cilia in the distal tubules. We could detect both increased levels of mRNA expression as well as of Ripk3 protein. A number of factors have been recently described to modulate Ripk3 expression, which includes methylation of the Ripk3 promotor [47] and components of the NF-κB signaling pathway. It has recently been demonstrated that NF-κB1 and NF-kappa-B essential modulator (Nemo) bind to the *Ripk3* promotor and suppress TNFα-induced Ripk3 expression and necroptosis in endothelial cells [48]. Consistently, genetic inhibition of NF-kB signaling in the murine skin triggered TNFR1-mediated necroptosis and inflammation [49]. With respect to cilia, previous studies have found repression of NF-κB upon loss of cilia due to loss of Kif3a in hippocampal neurons [50] or due to hypomorphic *Ift88* mutation in chondrocytes [51]. The latter study suggested a crucial role of Hsp27 as a ciliary protein and known regulator of IKK [52–54]. Notably, we found no evidence for increased NF-κB signaling in mIMCD3 cells lacking cilia, as indicated by IκBα expression and its phosphorylation and degradation upon TNFα stimulation. Moreover, we found Hsp27 expression to be unaffected by loss of cilia (Fig. 3C). Therefore, the shift in cell death response toward necroptosis and the increase in Ripk3 might not be related to altered NF-κB activity.

Our unbiased approach provided additional mechanistic insights. Comparing protein expression of ciliated and non-ciliated cells followed by KEGG pathway analyses highlighted the enrichment of spliceosomal and lysosomal components in cells without cilia. The latter finding was surprising since the loss of cilia has been shown to negatively regulate autophagy [55–57]. Interestingly, the autophagy machinery is connected to the necrosome through p62/Sqsmt1 and Map1lc3a/b (LC3) interacting with Ripk1, and this interaction can control switching from apoptosis to necroptosis [58]. In particular, p62-mediated recruitment of Ripk1 to the autophagy machinery turns cell death from apoptosis toward necroptosis. Strikingly, our proteome data set demonstrates an increased abundance of p62/Sqsmt1, Map1lc3a/b (LC3), and Ripk1 in cells lacking primary cilia, which could be confirmed independently by immunoblots. In conclusion, the increased propensity to necroptosis upon loss of cilia might result from increased Ripk3 levels combined with a high abundance of the necrosome – autophagosome connecting module.

Loss of *NPHP1* is the most frequent genetic cause of pediatric cystic kidney diseases [41]. Here, we demonstrate that loss of *Nphp1* further promotes necroptosis in cells without cilia. As described above, loss of cilia occurs regularly in the kidney: the repair of tubular cellular damage requires surviving resident cells to disassemble the cilium prior to cell cycle re-entry [43, 44]. At this point, the increased susceptibilities to necroptosis due to the ciliopathy mutation on the one side and due to the missing cilium on the other side might add up in such a way that a critical threshold is exceeded and the necroptotic rate in the tissue increases. Given the increasing number of pharmacological interventions targeting different routes of cell death, including necroptosis [59, 60], it will be critical to analyze the specific role of this cilia cell-death switch in the pathogenesis of individual ciliopathies.

MATERIAL AND METHODS

Cell lines and cell culture

Murine inner medullary collecting duct 3 cells (mIMCD3, ATCC CRL-2123™) [61], were cultured in DMEM-F12 medium (Sigma) supplemented with 10% fetal bovine serum (FBS, Gibco™), 2 mM GlutaMAX (Gibco™) and 1.0% Penicillin and Streptomycin (Gibco™). Cells were maintained at 37 °C in the presence of 5% CO_2. All cell lines were tested negative for mycoplasma (PCR Mycoplasma Test Kit I/C, PromoKine). *Myo5a*$^{-/-}$ mIMCD3 cells generated with CRISPR/Cas9 mediated genome editing has been described earlier [37]. mIMCD3 subclones (ciliated kidney cells (Ckc) and non-ciliated kidney cells (Nckc)) were generated by sorting single cells into a 96-well plate using a FACSAria*III*. After expansion, cell clones were screened for the number of ciliated cells using immunofluorescence stainings (acetylated tubulin/Arl13b). *Nphp1* deficient cells were generated based on Nckc's using vector-based genome editing as described [37]. The sgRNA (5′-AGCGCCTGCAGCGGGTCCCG–CGG-3′) was cloned into PX458. pSpCas9(BB)-2 A-GFP (PX458), a kind gift from Feng Zhang (Addgene plasmid # 48138) [62].

Live-cell Imaging

Myo5a$^{+/+}$ and *Myo5a*$^{-/-}$ mIMCD3 cells, as well as the mIMCD3 subclones Ckc and Nckc, were seeded, with 15,000 cells per well, into 96-well plates in triplicates. 24 h after seeding, cells were treated with DMSO (AppliChem), 4 ng/100 µl TNFα (aa80–235; R&D), 2 µg/100 µl cycloheximide (C4859; Sigma), and 10 µM emricasan (Em; SEL-S7775; Biozol). For the IFNγ stimulation experiments, 10,000 cells per well were seeded. On the following day, cells were preincubated with 1000 U/ml IFNγ (#315–05; PeproTech) for 8 h, before combined treatment with IFNγ and 10 µM Em. For both experiments, cell death was visualized by adding DiYO-1 (ABD-17580, Biomol). Immediately after adding the reagents, the plates were transferred to the IncuCyte® S3 (Sartorius; 37 °C and 5% CO_2), and the first images were captured (T0). Subsequently, every 2 hours, pictures were taken. Per well, three single images were generated for each time point. In total, plates were scanned over the period of 24 h, thereby imaging the green channel with 300 ms exposure time and the phase contrast channel with ×20 objective. The analysis was done by teaching the machine for positive events within the included IncuCyte® Cell-by-Cell Analysis Software Module (#9600–0031, Sartorius). For analysis, a multiple comparison one-way ANOVA was performed, using the Turkey test with $p < 0.05$.

Immunofluorescence staining

mIMCD3 cells were seeded on coverslips to stain for primary cilia [37]. Cells were fixed with 4% PFA for 5 min at RT followed by 4 min incubation with ice-cold methanol at −20 °C. Next, cells were incubated with blocking solution 1xPBS containing 0.1% Triton X-100 and 10% normal donkey serum (Jackson ImmunoResearch) for 1 h at RT, followed by an 80 min incubation at RT with primary antibody (anti-acetylated tubulin, T6793 Sigma, 1:1000; anti-Arl13B, 17711–1-AP ProteinTech, 1:400). The following secondary antibodies were used: donkey-anti-rabbit Cy3, 715-165–150, and donkey-anti-mouse-Alexa 488, 715–545–150; both Jackson ImmunoResearch, 1:500; for 45 min at RT. Samples were mounted in ProLong™ Diamond with DAPI (ThermoFisher Scientific). Kidney tissue staining of 4 µm fixed sections were performed as previously described [63]. Firstly, the sections were deparaffinized by xylene treatment followed by rehydration in graded ethanol (70%, 95%, 100%). Antigen retrieval was achieved using heat-induced epitope retrieval and citrate buffer. For immunohistochemical staining, endogenous peroxidases and unspecific antibody binding sites were blocked by incubating with 1% BSA and 5% donkey serum (Jackson ImmunoResearch) for 1 h at RT. The primary antibody (anti-acetylated Tubulin, T6793 Sigma, 1:1000) was incubated overnight at 4 °C in the blocking solution, followed by incubation with fluorophore-coupled secondary antibody anti-mouse-Cy5, # 715–175–150, Jackson ImmunoResearch, 1:500) or tubule markers (Rodamin-DBA (RL-1032–2); FITC-Lotus Tetragonolobus Lectin (LTL, FL-1321–2; Vector laboratories) both 1:500) for 1 h at RT. The samples were mounted after a short pre-incubation of Hoechst33342 (ThermoFisher Scientific, 1:1000) with ProLong™ Diamond (ThermoFisher Scientific). Images were acquired using the AxioObserver microscope with an axioCam ICc 1, Axiocam 702 mono, Apotome system (Carl Zeiss MicroImaging, Jena, Germany; objectives Plan-Apochromat 20x/0.8 and EC Plan-Neofluar 40x/1.3).

Cell viability assay

Neutral-red release (NR) assays for cell viability were performed as described [64]. In brief, 30,000 cells were seeded as triplicates in 96-well plates 24 h prior to treatments. Cells were treated with DMSO (AppliChem), 4 ng/100 µl TNFα (aa80–235; R&D), 2 µg/100 µl cycloheximide (C4859; Sigma), 5 µM. birinapant (SELS7015, Biozol), 10 µM emricasan (SEL-S7775;

Biozol), 40 µM Necrostatin-1s (ab221984; Abcam), and 5 µM GSK872 (HY-101872, Sigma) as indicated in the figures and incubated for 16 h at 37 °C. Once 14 h of treatment was passed, neutral-red (C.I.50040, Sigma) was added to the medium. After additional 2 h, the cells were washed thrice with PBS followed by a 15 min incubation of destaining buffer (50% EtOH, 49% ddH_2O, and 1% acetic acid) under gentle shaking [65]. The absorbance was measured at 540 nm using the Infinite® M Plex plate reader (TECAN).

Mouse lines

To generate mice lacking primary cilia in the distal tubules and collecting ducts of the kidneys, *Kif3a*^{fl} mice [40] were crossed with Ksp:cre [66] mice on a C57Bl/6 N background. The mice were housed according to standardized specific pathogen-free conditions in the in vivo research facility of CECAD at the University of Cologne. All matings and experiments were conducted in accordance with European, national and institutional guidelines, as approved by the State Office of North Rhine-Westphalia, Department of Nature, Environment and Consumer Protection (8.87-50.10.31.08.049 and 84–02.04.2013.A152). For the preparation of the mice, the mice were sacrificed by cervical dislocation, and kidneys were perfused with PBS through the aorta. Tissue was processed by fixation in 4% formaldehyde and embedding in paraffin as well as snap-frozen for further tissue analysis.

Immunohistology and TUNEL staining

For histological analysis, tissue was cut into 1-µm-thick sections and deparaffinized by xylene treatment and rehydration in graded ethanol. Sections were stained with 0.9% periodic acid (cat# 3257.1, Roth) and Schiffsches Reagent (cat#1.09033, Merck) both for 10 min embedded into washing steps with H_2O. Finally, to visualize nuclei in blue, the samples were stained with Mayer's Haematoxylin for 20 s. After dehydration of the sections, they were embedded with Histomount (HS-103, National Diagnostics). The DeadEnd™ Fluorometric TUNEL System (Promega) was performed following the manufacturer's instructions, with the exception that the samples were mounted, with a pre-incubation of Hoechst (ThermoFisher Scientific, 1:1000) as nuclear staining, with ProLong™ Diamond (ThermoFisher Scientific). The antibody signals were visualized by using the Axio Observer as described above.

Immunoblotting

mIMCD3 cells were seeded in six-wells plates/dishes and treated with DMSO, TNFα, CHX, Nec1s, or emricasan as described above for 16 h. For whole-cell extracts for pMlkl analysis, cells were immediately lysed in 1× Laemmli buffer. For protein lysates, cells were harvested in medium and, after centrifugation, lysed in RIPA buffer (1% IgePAL, 150 mM NaCl, 0.25% Na-Deoxy, 50 mM Tris pH 7.5) supplemented with cOmplete™ Protease Inhibitor Cocktail (Roche). For immunoblotting of kidney samples, 30 mg of tissue were homogenized with a Wheaton Dounce tissue grinder in RIPA buffer on ice. After 30 min on ice, lysates were centrifuged at 14,000 rpm for 30 min at 4 °C. Protein concentration was measured from the supernatants using Pierce BCA Protein Assay Kit (ThermoFisher Scientific) according to the manufacturer's instructions. Finally, samples were diluted with 5x sample buffer. Proteins were separated by SDS–PAGE and transferred to a PVDF-FL membrane (Millipore) and, after blocking with Intercept blocking solution (Licor) and washing (1× PBS, 0.1% Tween-20), stained with antibodies against phospho-Mlkl Ser345 (#37333, CST, 1:1000), Ripk1 (#610459, bd biosciences, 1:1000), Ripk3 (ADI-905–242, Enzo, 1:1000), cleaved-caspase-3 Asp175 (#9661, CST, 1:1000), LC3 (#2775 S, CST, 1:1000), p62/Sqstm1 (GP62-C, Progen, 1:1000), total IκBa (sc-371, Santa Cruz, 1:1000), pIκBa (#9246, CST, 1:1000), pNFκB (#3033, CST, 1:1000), Nphp1 (Homemade polyclonal rabbit, 1:1000), β-Tubulin (E7, DSHB, 1:500) or pan-actin (#8456, CST, 1:1000) at 4 °C overnight. Fluorescence-coupled secondary antibodies (anti-mouse IgG (H + L) IRDye 680RD, cat# 926–68070; anti-rabbit IgG (H + L) IRDye 680RD, cat# 926–68071; anti-mouse IgG (H + L) IRDye 800CW, cat# 926–32210; anti-rabbit IgG (H + L) IRDye 800CW, cat# 926–32211; Licor) were incubated for 45 min at RT. Finally, the membranes were scanned using Odyssey CLx (Licor). Densitometry was performed by using ImageJ, normalized to the housekeeping protein, and statistically analyzed with a two-tailed Student's *t* test; $p < 0.05$.

Mass spectrometry

For each of the four biological replicates per point, one 10 cm dish of mIMCD3 cells of the indicated genotype was harvested and snap-frozen. Pellets were resuspended in urea buffer (8 M Urea, 50 mM ammonium bicarbonate) containing Halt protease-phosphatase-inhibitor cocktail (Thermo Scientific). After clearing of the sample (16,000 × *g*, 1 h at 4 °C), the lysates were reduced (10 mM dithiothreitol, 1 h, at RT) and alkylated (50 mM chloroacetamide, 1 h, at RT). Samples were diluted to 2 M urea and subjected to tryptic digestion (enzyme:substrate ratio of 1:50). After overnight incubation, a double-layered stage-tip clean-up (C18) was performed. Samples were handed in for analysis into two separated experiments: Nckc versus Ckc and Myo5a$^{-/-}$ versus Myo5a$^{+/+}$ control cells. Samples were analyzed at the CECAD proteomics facility on an Orbitrap Exploris 480 (Thermo Scientific) mass spectrometer equipped with a FAIMSpro differential ion mobility device coupled to an UltiMate 3000 (Thermo Scientific). LFQ values were calculated using the DIA-NN R-package [67]. A Swissprot mouse canonical database (UP589, downloaded 18/06/20) was used for library building with settings matching acquisition parameters and the match-between-runs function enabled. Here, samples are directly used to refine the library for a second search of the sample data. DIA-NN was run with the additional command-line prompts "—report-lib-info" and "—relaxed-prot-inf". Further output settings were: filtered at 0.01 FDR, N-terminal methionine excision enabled, maximum number of missed cleavages set to 1, min peptide length set to 7, max peptide length set to 30, min precursor m/z set to 400, max precursor m/z set to 1000, cysteine carbamidomethylation enabled as a fixed modification. Afterward, DIA-NN output was further filtered on library q-value and global *q* value $<= 0.01$ and at least two identified peptides per protein using R (4.1.3). Student's t-tests and Fisher exact tests were calculated in Perseus (version 1.6.15.0) after the removal of decoys and potential contaminants [68]. Data were filtered for at least four out of four values in at least one condition. The remaining missing values were imputed with random values from a normal distribution using Perseus defaults. The mass spectrometry proteomics data have been deposited to the ProteomeXchange Consortium via the PRIDE [69] partner repository with the data set identifier PXD035290.

Quantitative real-time PCR

mIMCD3 cells were seeded in 12 well plates, treated with DMSO (AppliChem), 4 ng/100 µl TNFα (aa80–235; R&D), 2 µg/100 µl cycloheximide (C4859; Sigma) for 16 h and washed with PBS right before lysis in Tri-Reagent (Sigma). For RNA isolation from kidney tissue, one-quarter of a kidney was ground with BeadBeater (Roth) using a Precelly24 with 5000 rpm two times for 30 s in Tri-Reagent. RNA extraction was performed with the Direct-zol RNA Miniprep kit (Zymo Research) following the manufacturer's instructions, including a DNase1 treatment step. Prior to the reverse transcription by using the High-Capacity cDNA Reverse Transcription kit (Applied Biosystems), RNA concentration and sample quality were assessed on a Nanodrop spectrophotometer (Peqlab). mRNA was assessed by SYBR Green (ThermoFisher Scientific) qPCR using mHprt1 as endogenous control. Primers are listed in Supplementary Table S1. The qPCR experiments were performed on a QuantStudio 12 K Flex Real-time PCR System (ThermoFisher Scientific). For data analysis, all results were normalized to the housekeeping gene *Hphrt1* using the delta-delta CT followed by a two-tailed Student's *t* test ($p < 0.05$).

Quantification and statistical analysis

Data are expressed as mean ± standard deviation (SD). All experiments were performed in at least three independent biological replicates. The data were statistically analyzed with GraphPad Prism version 8.0.2.

DATA AVAILABILITY

The mass spectrometry proteomics data have been deposited to the ProteomeXchange Consortium via the PRIDE [69] partner repository with the data set identifier PXD035290. All additional data generated or analyzed during this study are included in the article.

REFERENCES

1. Wheway G, Nazlamova L, Hancock JT. Signaling through the primary cilium. Front Cell Dev Biol. 2018,6:8.
2. Gerdes JM, Davis EE, Katsanis N. The vertebrate primary cilium in development, homeostasis, and disease. Cell. 2009;137:32–45.
3. Malicki JJ, Johnson CA. The cilium: cellular antenna and central processing unit. Trends Cell Biol. 2017;27:126–40.

4. Rohatgi R, Snell WJ. The ciliary membrane. Curr Opin Cell Biol. 2010;22:541–6.
5. Garcia-Gonzalo FR, Reiter JF. Open sesame: how transition fibers and the transition zone control ciliary composition. Cold Spring Harb Perspect Biol. 2017;9:a028134.
6. Hildebrandt F, Benzing T, Katsanis N. Ciliopathies. N. Engl J Med. 2011;364: 1533–43.
7. Reiter JF, Leroux MR. Genes and molecular pathways underpinning ciliopathies. Nat Rev Mol Cell Biol. 2017;18:533–47.
8. McConnachie DJ, Stow JL, Mallett AJ. Ciliopathies and the kidney: a review. Am J Kidney Dis. 2021;77:410–9.
9. Bergmann C, Guay-Woodford LM, Harris PC, Horie S, Peters DJM, Torres VE. Polycystic kidney disease. Nat Rev Dis Prim. 2018;4:50.
10. Stokman MF, Saunier S, Benmerah A. Renal ciliopathies: sorting out therapeutic approaches for nephronophthisis. Front Cell Dev Biol. 2021;13:653138.
11. Bollée G, Fakhouri F, Karras A, Noël L-H, Salomon R, Servais A, et al. Nephronophthisis related to homozygous NPHP1 gene deletion as a cause of chronic renal failure in adults. Nephrol Dialysis Transplant. 2006;21:2660–3.
12. Srivastava S, Molinari E, Raman S, Sayer JA. Many genes-one disease? genetics of nephronophthisis (NPHP) and NPHP-associated disorders. Front pediatrics. 2017;5:287.
13. Woo D. Apoptosis and loss of renal tissue in polycystic kidney diseases. N. Engl J Med. 1995;333:18–25.
14. Peintner L, Borner C. Role of apoptosis in the development of autosomal dominant polycystic kidney disease (ADPKD). Cell Tissue Res. 2017;369:27–39.
15. Forschbach V, Goppelt-Struebe M, Kunzelmann K, Schreiber R, Piedagnel R, Kraus A, et al. Anoctamin 6 is localized in the primary cilium of renal tubular cells and is involved in apoptosis-dependent cyst lumen formation. Cell Death Dis. 2015;6:e1899.
16. Hopp K, Ward CJ, Hommerding CJ, Nasr SH, Tuan HF, Gainullin VG, et al. Functional polycystin-1 dosage governs autosomal dominant polycystic kidney disease severity. J Clin Invest. 2012;122:4257–73.
17. Ma M, Tian X, Igarashi P, Pazour GJ, Somlo S. Loss of cilia suppresses cyst growth in genetic models of autosomal dominant polycystic kidney disease. Nat Genet. 2013;45:1004–12.
18. Shibazaki S, Yu Z, Nishio S, Tian X, Thomson RB, Mitobe M, et al. Cyst formation and activation of the extracellular regulated kinase pathway after kidney specific inactivation of Pkd1. Hum Mol Genet. 2008;17:1505–16.
19. Ghosh AK, Hurd T, Hildebrandt F. 3D spheroid defects in NPHP knockdown cells are rescued by the somatostatin receptor agonist octreotide. Am J Physiol Ren Physiol. 2012;303:F1225–1229.
20. Delous M, Hellman NE, Gaudé H-M, Silbermann F, Le Bivic A, Salomon R, et al. Nephrocystin-1 and nephrocystin-4 are required for epithelial morphogenesis and associate with PALS1/PATJ and Par6. Hum Mol Genet. 2009;18:4711–23.
21. Sang L, Miller JJ, Corbit KC, Giles RH, Brauer MJ, Otto EA, et al. Mapping the NPHP-JBTS-MKS protein network reveals ciliopathy disease genes and pathways. Cell. 2011;145:513–28.
22. Giles RH, Ajzenberg H, Jackson PK. 3D spheroid model of mIMCD3 cells for studying ciliopathies and renal epithelial disorders. Nat Protoc. 2014;9:2725–31.
23. Vanden Berghe T, Linkermann A, Jouan-Lanhouet S, Walczak H, Vandenabeele P. Regulated necrosis: the expanding network of non-apoptotic cell death pathways. Nat Rev Mol Cell Biol. 2014;15:135–47.
24. Bertheloot D, Latz E, Franklin BS. Necroptosis, pyroptosis and apoptosis: an intricate game of cell death. Cell Mol Immunol. 2021;18:1106–21.
25. Maremonti F, Meyer C, Linkermann A. Mechanisms and models of kidney tubular necrosis and nephron loss. J Am Soc Nephrol. 2022;33:472–86.
26. Holler N, Zaru R, Micheau O, Thome M, Attinger A, Valitutti S, et al. Fas triggers an alternative, caspase-8-independent cell death pathway using the kinase RIP as effector molecule. Nat Immunol. 2000;1:489–95.
27. Grootjans S, Vanden Berghe T, Vandenabeele P. Initiation and execution mechanisms of necroptosis: an overview. Cell Death Differ. 2017;24:1184–95.
28. Liu Y, Liu T, Lei T, Zhang D, Du S, Girani L, et al. RIP1/RIP3-regulated necroptosis as a target for multifaceted disease therapy (Review). Int J Mol Med. 2019;44:771–86.
29. Kondylis V, Kumari S, Vlantis K, Pasparakis M. The interplay of IKK, NF-κB and RIPK1 signaling in the regulation of cell death, tissue homeostasis and inflammation. Immunol Rev. 2017;277:113–27.
30. Flores-Romero H, Ros U, Garcia-Saez AJ. Pore formation in regulated cell death. EMBO J. 2020;39:e105753.
31. Linkermann A, Brasen JH, Himmerkus N, Liu S, Huber TB, Kunzendorf U, et al. Rip1 (receptor-interacting protein kinase 1) mediates necroptosis and contributes to renal ischemia/reperfusion injury. Kidney Int. 2012;81:751–61.
32. Linkermann A, Heller JO, Prokai A, Weinberg JM, De Zen F, Himmerkus N, et al. The RIP1-kinase inhibitor necrostatin-1 prevents osmotic nephrosis and contrast-induced AKI in mice. J Am Soc Nephrol. 2013;24:1545–57.
33. Newton K, Dugger DL, Maltzman A, Greve JM, Hedehus M, Martin-McNulty B, et al. RIPK3 deficiency or catalytically inactive RIPK1 provides greater benefit than MLKL deficiency in mouse models of inflammation and tissue injury. Cell Death Differ. 2016;23:1565–76.
34. Linkermann A, Skouta R, Himmerkus N, Mulay SR, Dewitz C, De Zen F, et al. Synchronized renal tubular cell death involves ferroptosis. Proc Natl Acad Sci USA. 2014;111:16836–41.
35. Mc Fie M, Koneva L, Collins I, Coveney CR, Clube AM, Chanalaris A, et al. Ciliary proteins specify the cell inflammatory response by tuning NFκB signalling, independently of primary cilia. J Cell Sci 2020;133:jcs239871.
36. Brumatti G, Ma C, Lalaoui N, Nguyen N-Y, Navarro M, Tanzer MC, et al. The caspase-8 inhibitor emricasan combines with the SMAC mimetic birinapant to induce necroptosis and treat acute myeloid leukemia. Sci Transl Med. 2016;8:339ra369–339ra369.
37. Kohli P, Hohne M, Jungst C, Bertsch S, Ebert LK, Schauss AC, et al. The ciliary membrane-associated proteome reveals actin-binding proteins as key components of cilia. EMBO Rep. 2017;18:1521–35.
38. Wu CT, Chen HY, Tang TK. Myosin-Va is required for preciliary vesicle transportation to the mother centriole during ciliogenesis. Nat Cell Biol. 2018;20:175–85.
39. Marszalek JR, Ruiz-Lozano P, Roberts E, Chien KR, Goldstein LS. Situs inversus and embryonic ciliary morphogenesis defects in mouse mutants lacking the KIF3A subunit of kinesin-II. Proc Natl Acad Sci USA. 1999;96:5043–8.
40. Lin F, Hiesberger T, Cordes K, Sinclair AM, Goldstein LS, Somlo S, et al. Kidney-specific inactivation of the KIF3A subunit of kinesin-II inhibits renal ciliogenesis and produces polycystic kidney disease. Proc Natl Acad Sci USA. 2003;100: 5286–91.
41. Halbritter J, Porath JD, Diaz KA, Braun DA, Kohl S, Chaki M, et al. Identification of 99 novel mutations in a worldwide cohort of 1,056 patients with a nephronophthisis-related ciliopathy. Hum Genet. 2013;132:865–84.
42. Schermer B, Hopker K, Omran H, Ghenoiu C, Fliegauf M, Fekete A, et al. Phosphorylation by casein kinase 2 induces PACS-1 binding of nephrocystin and targeting to cilia. EMBO J. 2005;24:4415–24.
43. Humphreys BD, Czerniak S, DiRocco DP, Hasnain W, Cheema R, Bonventre JV. Repair of injured proximal tubule does not involve specialized progenitors. Proc Natl Acad Sci USA. 2011;108:9226–31.
44. Kusaba T, Lalli M, Kramann R, Kobayashi A, Humphreys BD. Differentiated kidney epithelial cells repair injured proximal tubule. Proc Natl Acad Sci. 2014;111: 1527–32.
45. Kim S, Tsiokas L. Cilia and cell cycle re-entry: more than a coincidence. Cell Cycle. 2011;10:2683–90.
46. Liebau MC, Hopker K, Muller RU, Schmedding I, Zank S, Schairer B, et al. Nephrocystin-4 regulates Pyk2-induced tyrosine phosphorylation of nephrocystin-1 to control targeting to monocilia. J Biol Chem. 2011;286:14237–45.
47. Koo G-B, Morgan MJ, Lee D-G, Kim W-J, Yoon J-H, Koo JS, et al. Methylation-dependent loss of RIP3 expression in cancer represses programmed necrosis in response to chemotherapeutics. Cell Res. 2015;25:707–25.
48. Gao S, Menendez M, Kurylowicz K, Griffin CT. Genomic locus proteomic screening identifies the NF-κB signaling pathway components NFκB1 and IKBKG as transcriptional regulators of Ripk3 in endothelial cells. PLoS One. 2021;16:e0253519.
49. Kumari S, Van T-M, Preukschat D, Schuenke H, Basic M, Bleich A, et al. NF-κB inhibition in keratinocytes causes RIPK1-mediated necroptosis and skin inflammation. Life Sci Alliance. 2021;4:e202000956.
50. Baek H, Shin HJ, Kim J-J, Shin N, Kim S, Yi M-H, et al. Primary cilia modulate TLR4-mediated inflammatory responses in hippocampal neurons. J Neuroinflammation. 2017;14:189.
51. Wann AK, Chapple JP, Knight MM. The primary cilium influences interleukin-1beta-induced NFkappaB signalling by regulating IKK activity. Cell Signal. 2014;26:1735–42.
52. Dodd SL, Hain B, Senf SM, Judge AR. Hsp27 inhibits IKKbeta-induced NF-kappaB activity and skeletal muscle atrophy. FASEB J. 2009;23:3415–23.
53. Parcellier A, Schmitt E, Gurbuxani S, Seigneurin-Berny D, Pance A, Chantôme A, et al. HSP27 is a ubiquitin-binding protein involved in I-kappaBalpha proteasomal degradation. Mol Cell Biol. 2003;23:5790–802.
54. Park KJ, Gaynor RB, Kwak YT. Heat shock protein 27 association with the I kappa B kinase complex regulates tumor necrosis factor alpha-induced NF-kappa B activation. J Biol Chem. 2003;278:35272–8.
55. Morleo M, Franco B. The autophagy-cilia axis: an intricate relationship. Cells. 2019;8:905.
56. Pampliega O, Orhon I, Patel B, Sridhar S, Díaz-Carretero A, Beau I, et al. Functional interaction between autophagy and ciliogenesis. Nature. 2013;502:194–200.
57. Wang S, Livingston MJ, Su Y, Dong Z. Reciprocal regulation of cilia and autophagy via the MTOR and proteasome pathways. Autophagy. 2015;11:607–16.
58. Goodall ML, Fitzwalter BE, Zahedi S, Wu M, Rodriguez D, Mulcahy-Levy JM, et al. The autophagy machinery controls cell death switching between apoptosis and necroptosis. Dev Cell. 2016;37:337–49.
59. Kist M, Vucic D. Cell death pathways: intricate connections and disease implications. EMBO J. 2021;40:e106700–e106700.

60. Lou J, Zhou Y, Feng Z, Ma M, Yao Y, Wang Y, et al. Caspase-independent regulated necrosis pathways as potential targets in cancer management. Front Oncol. 2021;10:616952.
61. Rauchman MI, Nigam SK, Delpire E, Gullans SR. An osmotically tolerant inner medullary collecting duct cell line from an SV40 transgenic mouse. Am J Physiol. 1993;265:F416–424.
62. Ran FA, Hsu PD, Wright J, Agarwala V, Scott DA, Zhang F. Genome engineering using the CRISPR-Cas9 system. Nat Protoc. 2013;8:2281–308.
63. Dafinger C, Rinschen MM, Borgal L, Ehrenberg C, Basten SG, Franke M, et al. Targeted deletion of the AAA-ATPase Ruvbl1 in mice disrupts ciliary integrity and causes renal disease and hydrocephalus. Exp Mol Med. 2018;50:1–17.
64. Reader SJ, Blackwell V, O'Hara R, Clothier RH, Griffin G, Balls M. A vital dye release method for assessing the short-term cytotoxic effects of chemicals and formulations. Altern. Lab Anim. 1989;17:28–33.
65. Fritsch M, Günther SD, Schwarzer R, Albert MC, Schorn F, Werthenbach JP, et al. Caspase-8 is the molecular switch for apoptosis, necroptosis and pyroptosis. Nature. 2019;575:683–7.
66. Shao X, Somlo S, Igarashi P. Epithelial-specific Cre/lox recombination in the developing kidney and genitourinary tract. J Am Soc Nephrol. 2002;13:1837–46.
67. Demichev V, Messner CB, Vernardis SI, Lilley KS, Ralser M. DIA-NN: neural networks and interference correction enable deep proteome coverage in high throughput. Nat Methods. 2020;17:41–44.
68. Tyanova S, Temu T, Sinitcyn P, Carlson A, Hein MY, Geiger T, et al. The Perseus computational platform for comprehensive analysis of (prote)omics data. Nat Methods. 2016;13:731–40.
69. Perez-Riverol Y, Bai J, Bandla C, Garcia-Seisdedos D, Hewapathirana S, Kamatchinathan S, et al. The PRIDE database resources in 2022: a hub for mass spectrometry-based proteomics evidences. Nucleic Acids Res. 2022;50:D543–D552.

ACKNOWLEDGEMENTS

We would like to thank Stefanie Keller, Serena Greco-Torres, and Angelika Köser for expert technical assistance. We acknowledge the help of the CECAD imaging facility and the CECAD proteomics facility. We thank the FACS & IMAGING Core Facility at Max Plank Institute for Biology of Ageing, Cologne, for assisting with sorting cells for the generation mIMCD subclones. In addition, we would like to express our gratitude to all members of our laboratory and many members of the SFB1403 for helpful discussions and support. This study was supported by the German Research Foundation (DFG; SFB1403, project number 414786233, A09 to BS and TB). BS was also supported by the German Federal Ministry of Research and Education (BMBF grant 01GM1515; NEOCYST consortium). The CECAD proteomics facility was supported by the large instrument grant INST 1856/71–1 FUGG by the German Research Foundation (DFG Großgeräteantrag). GGS was supported by a Fritz Thyssen Foundation grant (project 10.20.1.012MN). We acknowledge support for the article processing charge from the DFG (German Research Foundation, 491454339).

AUTHOR CONTRIBUTIONS

BS and TB designed the study. EK performed most experiments under supervision of GGS and BS. LKE and MCA performed the work with Nphp1-deficient cells, CD provided in vivo materials. HK and MCA provided materials and support for the interpretation of results. EK assembled the final figures. BS and EK wrote the original draft. All the authors discussed the project and contributed to the final version of the manuscript.

FUNDING

Open Access funding enabled and organized by Projekt DEAL.

COMPETING INTERESTS

The authors declare no competing interests.

ADDITIONAL INFORMATION

Supplementary information The online version contains supplementary material available at https://doi.org/10.1038/s41420-022-01272-2.

Correspondence and requests for materials should be addressed to Bernhard Schermer.

Reprints and permission information is available at http://www.nature.com/reprints

Publisher's note Springer Nature remains neutral with regard to jurisdictional claims in published maps and institutional affiliations.

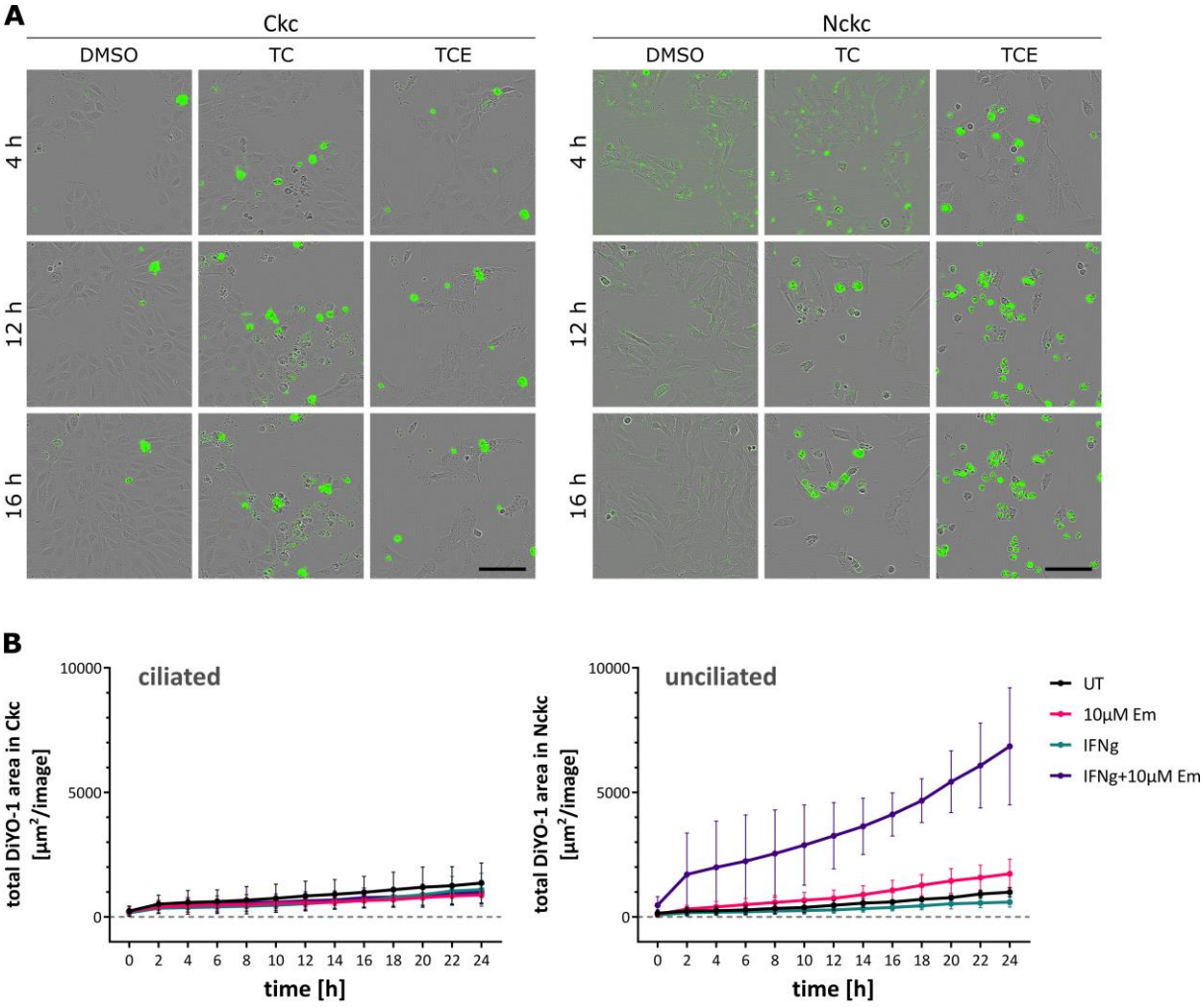

Supplementary figure 1

Suppl. Fig. 1: Necroptosis in non-ciliated kidney cells upon TCE and IFNγ/Emricasan treatment
(A) Representative pictures of cells from (Fig. 1 D). **(B)** Live-cell imaging over the period of 24 h after prestimulation with 1000 U/ml IFNγ for 8 h, and treatment with IFNγ and 10 µM Em or DMSO as control. Dead cells were stained with DiYO-1. Images were captured every 2 h (Ckc n=3; Nckc n=4).

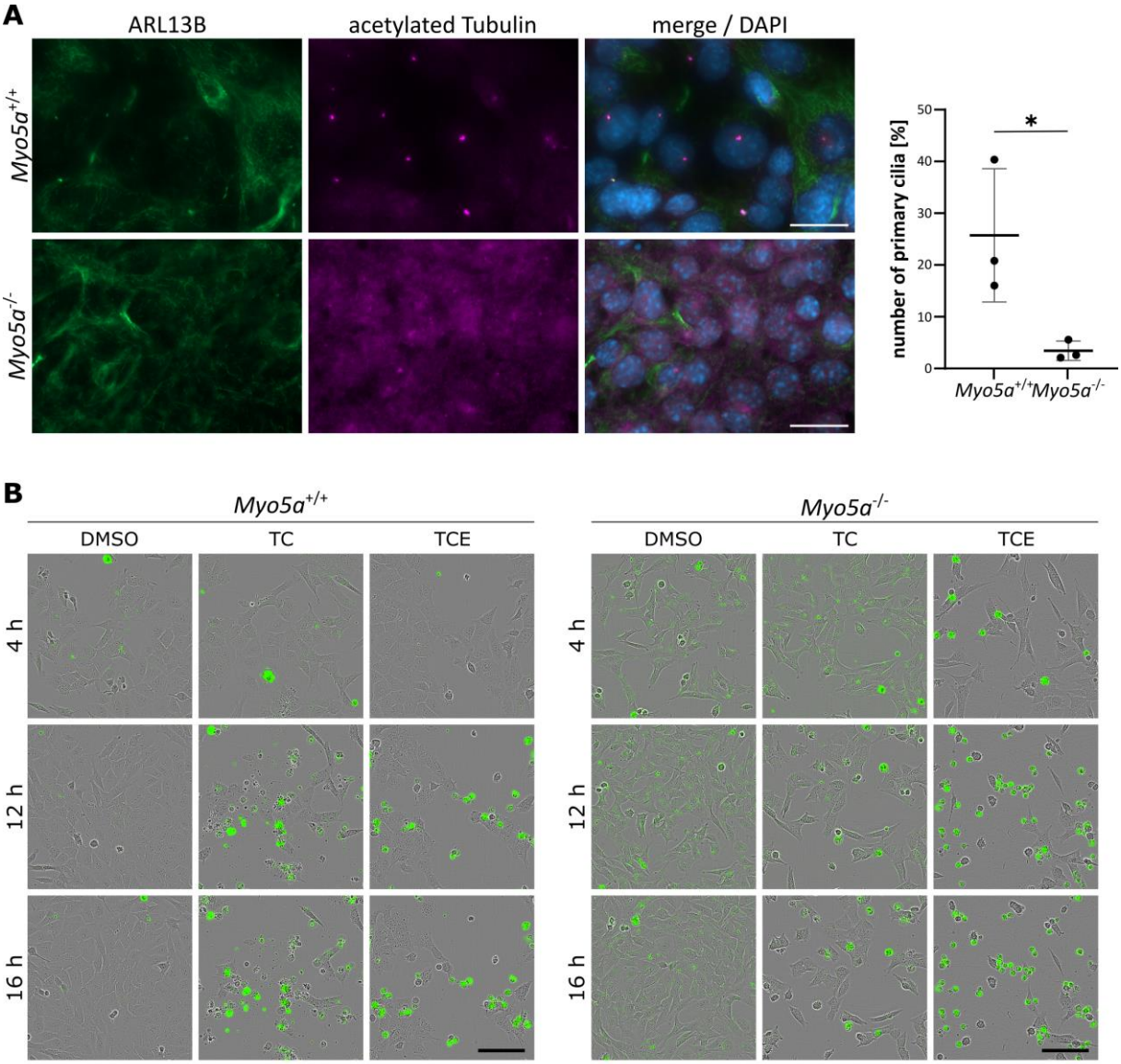

Supplementary figure 2

Suppl. Fig. 2: Loss of ciliogenesis and necroptosis susceptibility in Myo5a$^{-/-}$ cells
(A) Immunofluorescence of primary cilia in *Myo5a*$^{+/+}$ and *Myo5a*$^{-/-}$ cells (ARL13B (magenta), acetylated tubulin (green) and nuclei marker DAPI (blue); scale bar 20 µm). Quantification of primary cilia (n=3; total count of 924 cells for control and 875 cells for *Myo5a*$^{-/-}$). **(B)** Live-cell imaging of control and *Myo5a*$^{-/-}$ cells, over the period of 24 h, beginning with treatment induction of TNF, CHX (TC) and Em (TCE) or either DMSO as control. Cells were stained with the dead cell marker DiYO-1 (green). Images were captured every 2 h with a 20x objective (n=8).

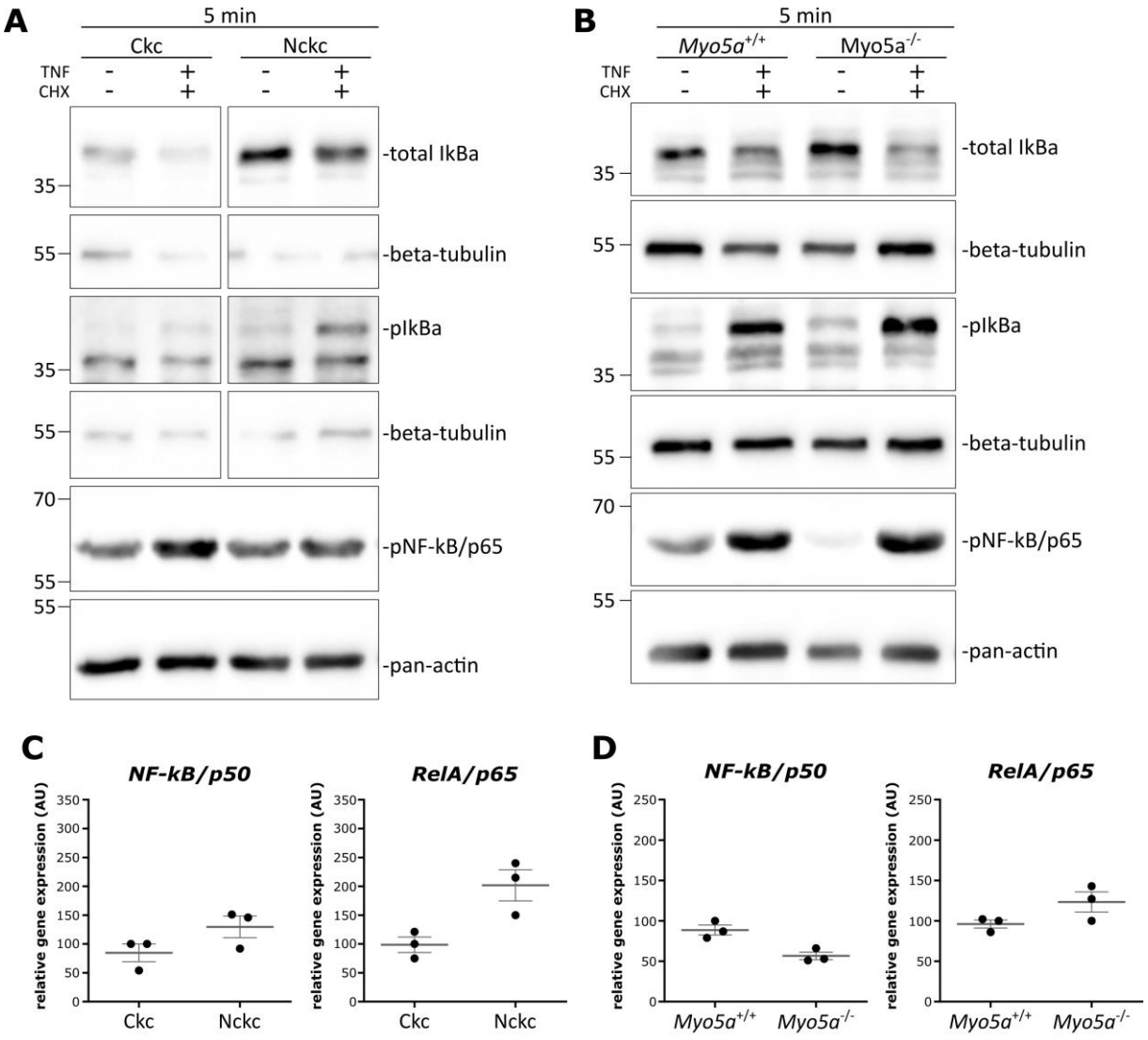

Supplementary figure 3

Suppl. Fig. 3: Loss of cilia does not inhibit NF-kB signaling

(A,B) Immunoblot analysis of **(A)** Ckc vs Nckc (n=3); **(B)** control vs *Myo5a*$^{-/-}$, stimulated with TNFα and CHX for 5 min or either DMSO as control, stained for total IκBα (~40 kDa),pIκBα (~40 kDa) and pNF-κB. As housekeeping control either pan-actin (~44 kDa) or beta-tubulin (~55 kDa) were used (n=3). **(C,D)** Quantitative real-time PCR of NF-kB/p50 and RelA/p65 in mIMCD3 cells: **(C)** Ckc vs Nckc (n=3); **(D)** *Myo5a*$^{+/+}$ vs *Myo5a*$^{-/-}$ (n=3). Cells were treated with DMSO for 16 h. Statistical analysis was performed by using a one-way ANOVA followed by a two-sided Student's t-test (p-Value: >0.001***; 0.002**; 0.033*; ns=0.12).

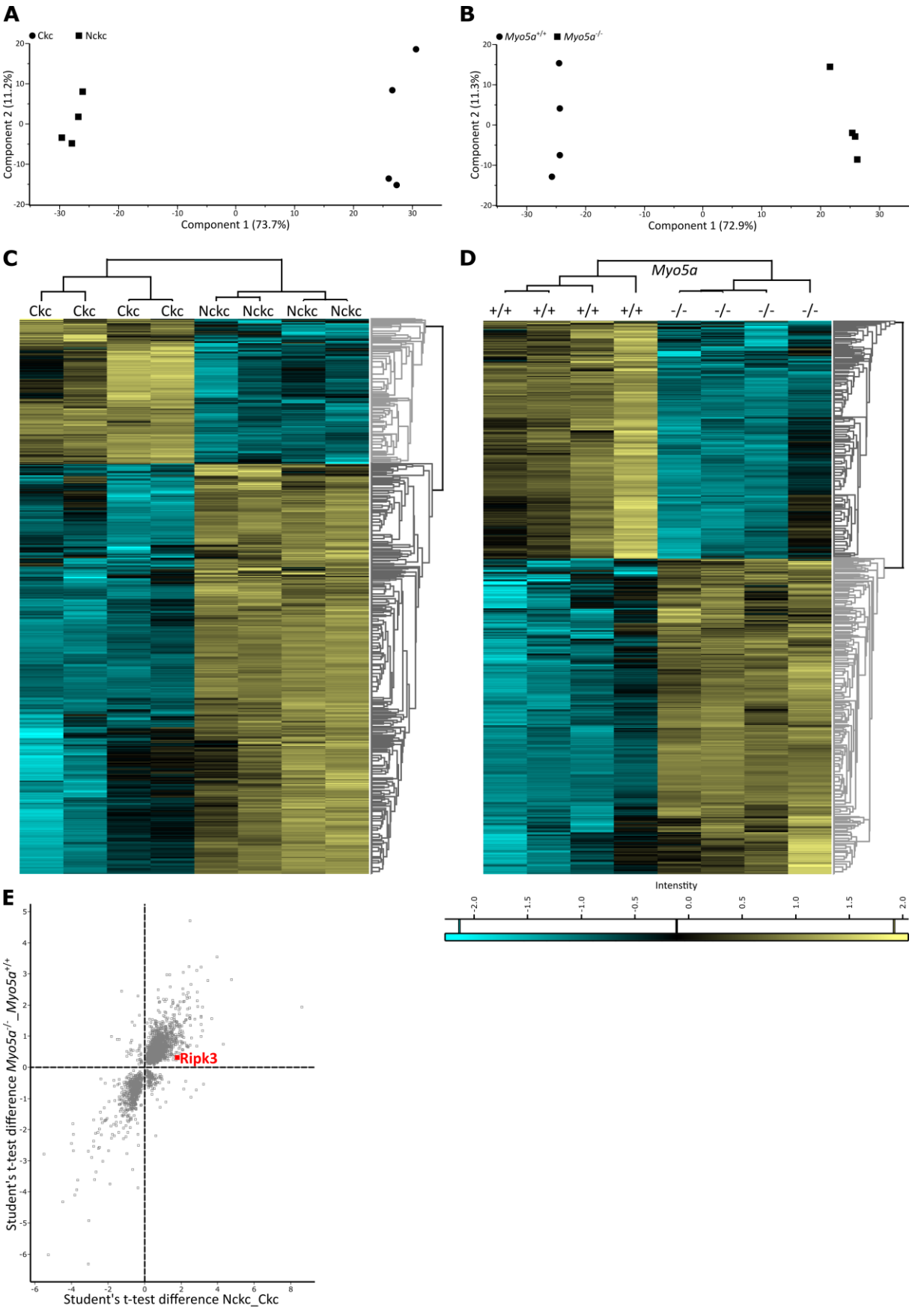

Supplementary figure 4

Suppl. Fig. 4: Proteomic analyses: separation of ciliated from non-ciliated cells

(A, B) Principal component analysis (PCA) plots of the protein expression data of ciliated vs. unciliated mIMCD3 cells. Depicted are the first two principal components. The axes represent the percentages of variation explained by the principal components. **(C,D)** Clustered heatmap based on log(2) LFQ values of identified differentially expressed proteins of Nckc versus Ckc (C) and *Myo5a*$^{-/-}$ versus *Myo5a*$^{+/+}$ cells (D), visualizing the differences among the groups of significantly upregulated (yellow) or downregulated (cyan) proteins. **(E)** Representative scatter plot of the combined data set visualizing only the significant regulated proteins for non-ciliated cells compared to ciliated cells. Depicted are the t-test differences of Nckc versus Ckc in protein expression on the x-axis and the t-test differences of *Myo5a*$^{-/-}$ versus *Myo5a*$^{+/+}$ control in protein expression on the y-axis.

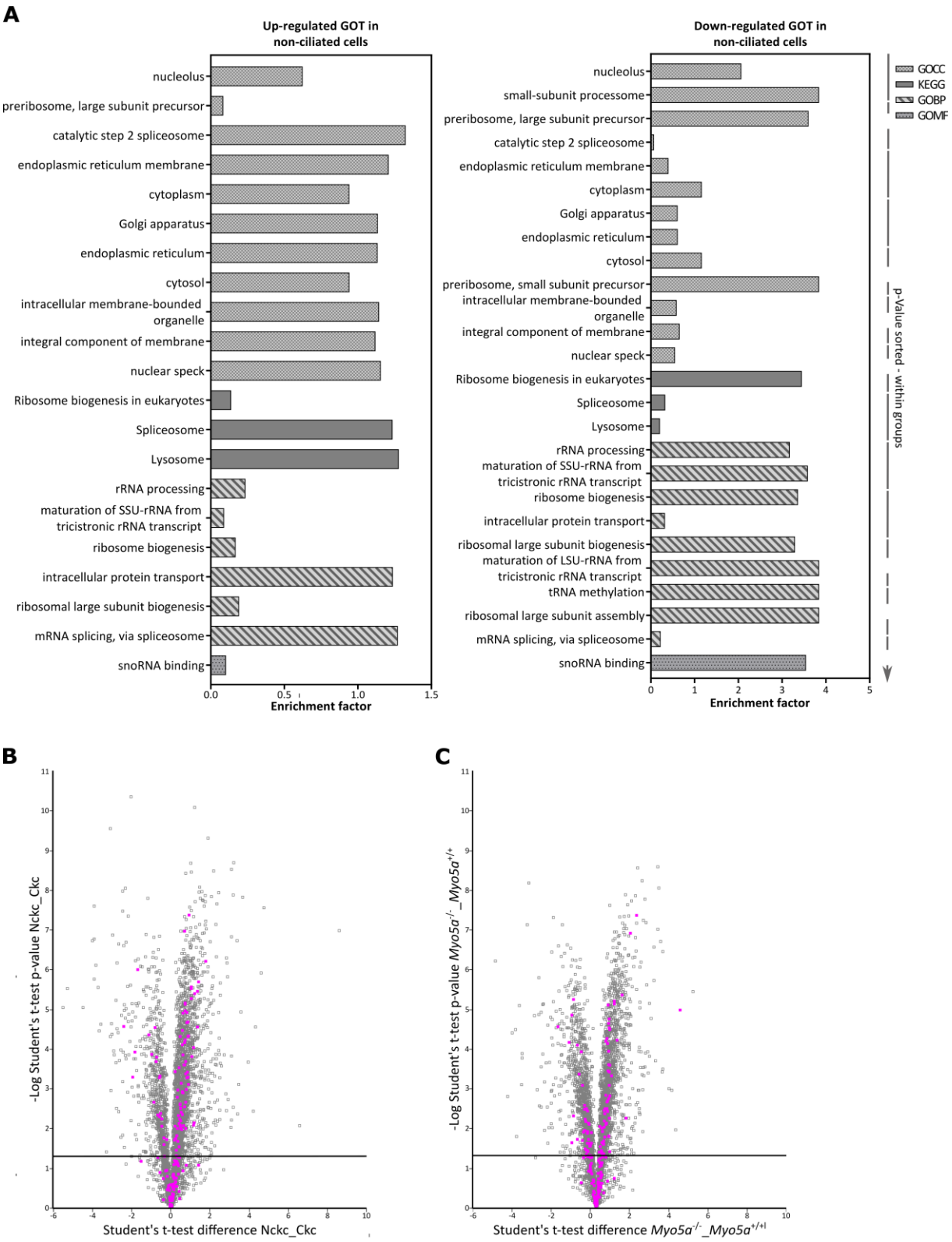

Supplementary figure 5

Suppl. Fig. 5: Shared proteomic alterations of non-ciliated cells

(A) GO and KEGG pathway enrichment based on a Fisher exact test of the proteins found to be regulated in the combined non-ciliated data set, separated for up-and down-regulation. Ordered by p-values within the groups. **(B, C)** Representative volcano plots for Nckc (B) and *Myo5a*$^{-/-}$ (C), with the t-test differences in protein expression of both non-ciliated cell lines and their respective controls, on

the x-axis and the statistical significance (-log10 Student's t-test p-value) on the y-axis. Proteins associated with autophagy are highlighted in magenta.

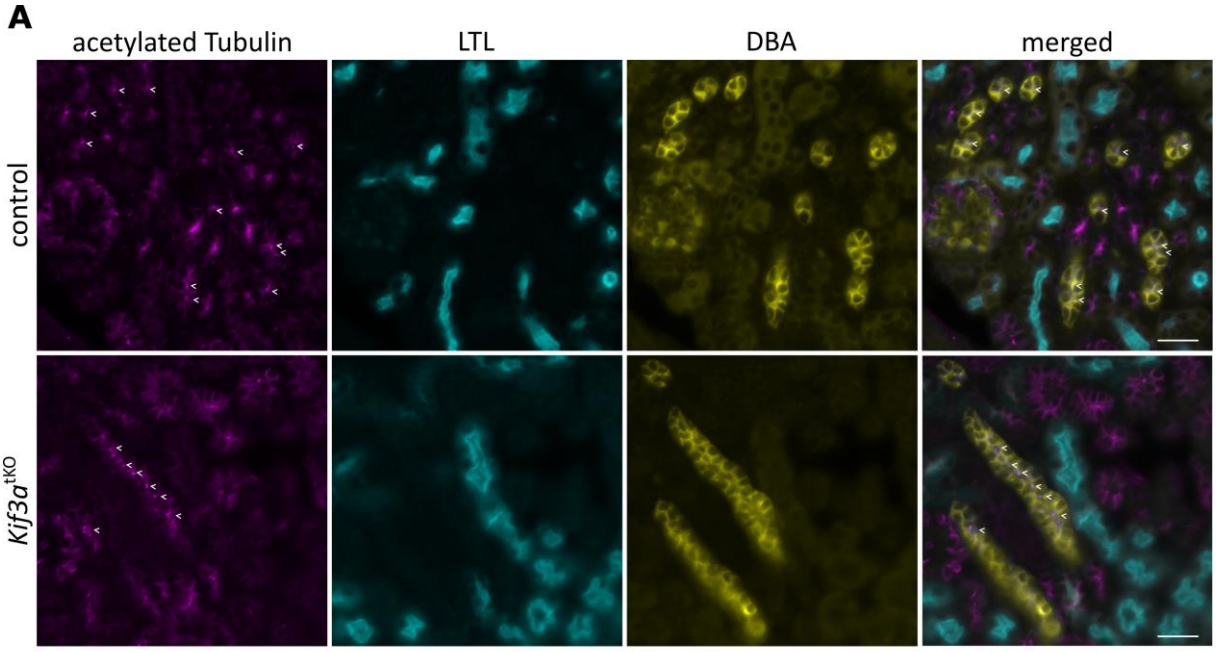

Supplementary figure 6

Suppl. Fig. 6: Primary cilia in distal tubules of Kif3a^{tko} at postnatal day P4
(A) Staining of primary cilia on paraffin-embedded kidney tissue revealed the presence of primary cilia in distal tubule in *Kif3a*$^{fl/fl}$:Ksp:cre$^{+/-}$ at postnatal day P4. Acetylated tubulin (magenta), LTL (proximal tubule marker; cyan), DBA (distal tubule marker; yellow) and nuclei (blue; scale bar 50 µm).

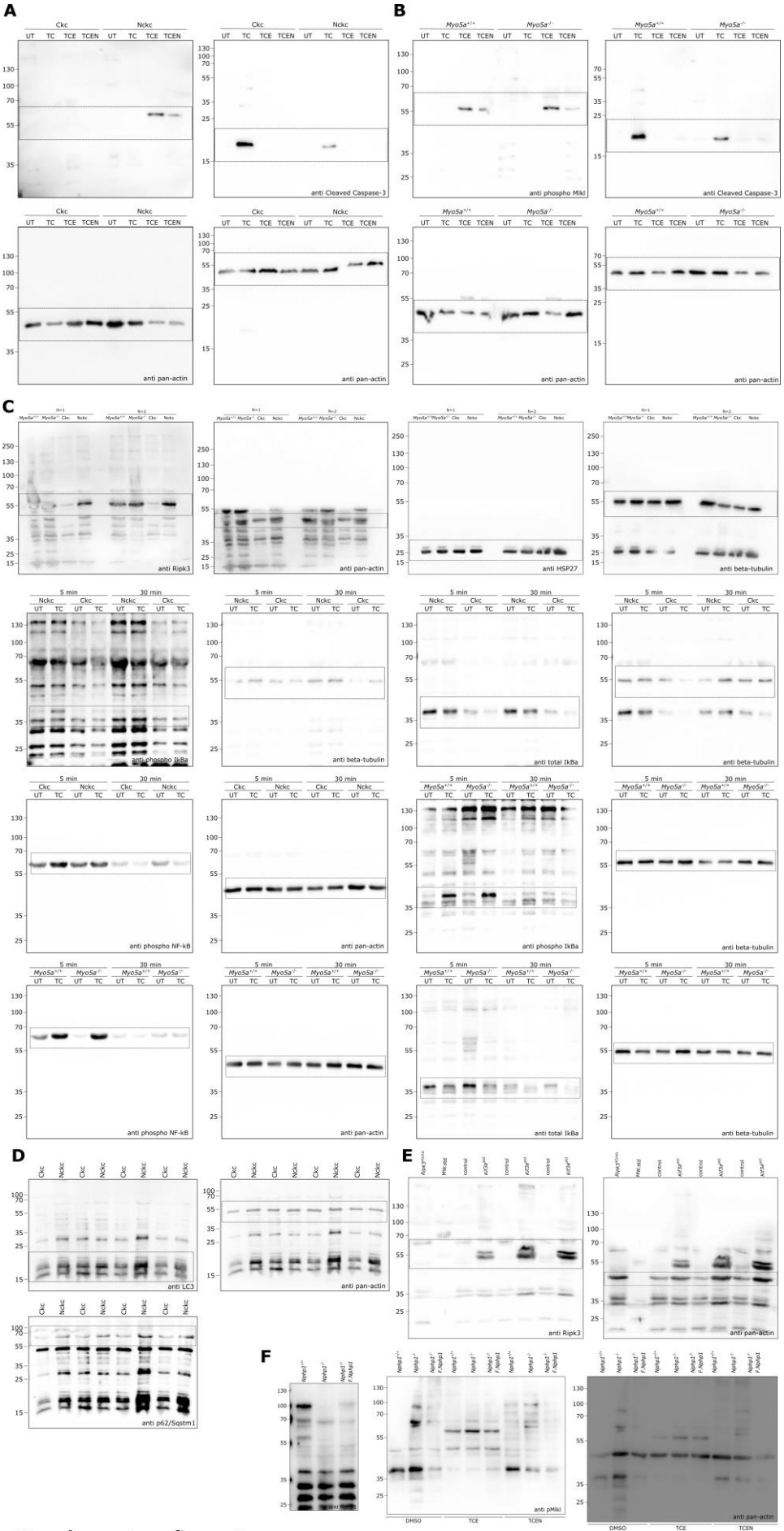

Supplementary figure 7

Suppl. Fig. 7: Original data: full-sized immunoblots

Original western blots, only cropped to gel size **(A)** of Figure 1, **(B)** of Figure 2, **(C)** of Figure 3, and Supplementary Figure 2 (one blot was covered by foil due to exposure issues), **(D)** of Figure 4 **(E)** of Figure 5 and **(F)** of Figure 6.

3.2 Chapter 2 - Deletion of *Ripk3* or *GsdmD* improves cystic kidney disease in *Nek8*^{jck} mice

Title: Deletion of *Ripk3* or *GsdmD* improves cystic kidney disease in *Nek8*^{jck} mice

Authors: Emilia Kieckhöfer, Lena K Ebert, Gisela G Slaats, Thomas Benzing, Bernhard Schermer

Status: draft manuscript, submission planned by mid-2024

Based on our finding that cilia negatively regulate necroptosis in kidney epithelial cells we investigated the role of RCD in the pathogenesis of cystic kidney disease in an *in vivo* ciliopathy model for NPH. The *Nphp9*/*Nek8*^{jck} mouse model, which displays a point mutation in the *Nphp9* (*Nek8*) gene, develops early-onset cystic kidney disease. This phenotype shows loss of epithelial cells, cyst development, inflammation, and fibrosis. Interestingly, the affected kidneys show an increased expression of the necroptosis marker RIPK3, similar to the kidney epithelial cells lacking cilia in Chapter 1. To investigate the role of necroptosis in the pathogenesis of cystic kidney disease in this model, we deleted *Ripk3* in *Nphp9*/*Nek8*^{jck} mice. Remarkably, the loss of *Ripk3* in this model ameliorates the phenotype and function of the kidney. However, the local levels of inflammation and fibrosis in the kidney were only slightly reduced, and markers for other RCD pathways including pyroptosis were still prominently upregulated. To investigate the role of pyroptosis, we bred *Nphp9*/*Nek8*^{jck} with a mouse line deficient of *GsdmD*. These mice also showed an amelioration of kidney architecture and function. Single nucleus (sn)RNA-Seq analysis was performed on kidney samples from *Nphp9*/*Nek8*^{jck}, as well as from mice additionally lacking either *Ripk3* or *GsdmD*. This revealed several cell populations affected in *Nphp9*/*Nek8*^{jck} that were positively affected by the lack of one of the RCD genes, hinting towards the mechanisms underlying RCD in NPH. In summary, this chapter points out the *in vivo* relevance of RCD for NPH and provides new insights into the mechanism of deregulated cell death in ciliopathies. Beyond this preliminary manuscript, ongoing experiments include the treatment of mice with inhibitors of RIPK3 and inhibitors of key players. In addition, we aim to confirm the findings of the snRNA-Seq analyses by independent methods. Therefore, we aim to submit a final manuscript by mid-2024.

Author contributions:

Emilia Kieckhöfer	performed all experiments, data analysis created final figures and wrote the manuscript
Lena K Ebert	data analysis of snRNA-seq data
Gisela G Slaats	Involved in the initial management of the mouse colony and generation of associated knockout cell lines
Thomas Benzing	designed the study and revised the manuscript
Bernhard Schermer	designed the study, supervised the writing of the manuscript, and revised it for the final version

Deletion of Ripk3 or GsdmD improves cystic kidney disease in Nek8^{jck} mice

Emilia Kieckhöfer[1,2], Lena K. Ebert[1,2], Gisela G. Slaats[3], Thomas Benzing[1,2], Bernhard Schermer[1,2]

[1] *Department II of Internal Medicine and Center for Molecular Medicine Cologne, University of Cologne, Faculty of Medicine and University Hospital Cologne, Cologne, Germany*

[2] *Cologne Excellence Cluster on Cellular Stress Responses in Aging-Associated Diseases (CECAD), University of Cologne, Faculty of Medicine and University Hospital Cologne, Cologne, Germany*

[3]*Department of Nephrology and Hypertension, Regenerative Medicine Center Utrecht, University Medical Center Utrecht, Utrecht, The Netherlands*

corresponding author:

bernhard.schermer@uk-koeln.de

Keywords: Jck, CKD, necroptosis, primary cilium, kidney, ciliopathies, RIPK3, GSDMD, pyroptosis

Abstract

Nephronophthisis (NPH) is an autosomal recessive cystic kidney disease caused by mutations in the NPHP genes. While the kidneys usually appear normal at birth, kidney disease develops during childhood and adolescence. NPH is triggered by mutations in the NPHP genes, which encode proteins located in the primary cilium or at the ciliary base. Therefore, NPH is classified as a ciliopathy. During the progression of NPH, there is a massive loss of renal tubular cells through a so far unknown mechanism. To elucidate this, we studied the *juvenile cystic kidney* (*Nphp9*/*Nek8*^{jck}) mouse model in which we observed increased TUNEL activity and an elevated expression of the cell death markers RIPK3 and GSMD. Remarkably, knockout of either RIPK3 or GSDMD led to a significant improvement in the kidney phenotype and kidney function in *Nphp9*/*Nek8*^{jck} mice, as well as less pronounced renal fibrosis. An in-depth analysis of these regulated cell death (RCD) pathways revealed a complex interrelationship. Specifically, knocking out either RIPK3 or GSDMD did not fully mitigate cell death or inflammation. Moreover, the knockout of one gene did not lead to a decrease in the expression levels of the other, indicating that these pathways are interconnected yet function independently to some extent. Moreover, single-nucleus RNA sequencing (snRNA-Seq) analyses revealed a complex picture: while many cell clusters were affected, the number of cells expressing markers of renal damage seemed to be particularly high in the cluster of the distal tubular cells in the *Nphp9*/*Nek8*^{jck} mouse, and our analyses also show numerous other genes whose expression is normalized by the knockout of RIPK3 or GSDMD. In summary, our study highlights the importance of necroptosis and pyroptosis *in vivo* and provides numerous mechanistic insights into kidney damage in NPH and its dependence on cell death pathways.

Introduction

Nephronophthisis is a rare autosomal-recessive disorder that manifests in children and young adults and is the most common genetic cause of kidney failure in this age group (Srivastava *et al.*, 2018). To date, over 20 genes responsible for NPHP have been identified, accounting for about 50% of cases (Wolf *et al.*, 2023). Thus, the genetic cause remains unclear in a large number of patients. Clinically, mild symptoms initially present, including polydipsia, polyuria, anaemia, and secondary enuresis (Hildebrandt and Zhou, 2007). Kidney insufficiency develops, progressing to kidney failure over a few years. Histologically, the kidneys are characterized by the triad of tubular basement membrane disruption, tubulointerstitial fibrosis, and the development of corticomedullary cysts (Hildebrandt and Zhou, 2007). To date, there are no causal therapies, but research over the last few years has begun to outline promising approaches for potential therapeutic interventions (Benmerah *et al.*, 2023).

NPHP genes encode proteins that localize to primary cilia. Hence, NPH is classified as ciliopathy. Cilia are sensory organelles found in nearly all tissues. Tubular cells of the kidney bear them on their apical surface, from where the cilia extend into the tubular lumen and receive mechanical and chemical signals which they transmit into the epithelial cell. Recently, we demonstrated that primary cilia regulate the susceptibility of tubular epithelial cells to undergo necroptosis (Kieckhöfer *et al.*, 2022). Notably, during the development of NPH, there is a massive loss of tubular epithelial cells in the kidneys, and early studies on NPH suggest regulated cell death in some models. However, the mechanistic and molecular details have remained unclear. Numerous fundamental studies on acute kidney injury (AKI) revealed the significant role of regulated cell death (RCD) in tubular epithelial cells and that the machinery for RCD pathways is present and activatable (Maremonti, Meyer and Linkermann, 2022). However, knowledge about the role of RCD in chronic kidney diseases and data from genetic preclinical CKD models are limited (Sanz *et al.*, 2023).

The signaling pathways of RCD demonstrate varying levels of inflammation due to the gradual release of DAMPs. While apoptosis is generally largely ignored by the immune system, the release of pro-inflammatory DAMPs associated with necroptosis and pyroptosis leads to accompanying inflammation and more extensive tissue damage. Necroptosis acts in a specific cascade to disrupt the plasma membrane, including three key proteins: receptor interacting serine/threonine kinase 1 (RIPK1) (Holler *et al.*, 2000), RIPK3 (Zhang *et al.*, 2009) and mixed lineage kinase domain-like protein (MLKL) (Sun *et al.*, 2012). The autophosphorylation of RIPK3 is essential to phosphorylate MLKL (Zhao *et al.*, 2012; Chen *et al.*, 2013) and this triggers the final execution of cell death. Interestingly it has been shown that, in animal models of induced acute kidney injury (AKI), either the knockout of *Ripk3* (Linkermann *et al.*, 2013; Newton *et al.*, 2016) or the treatment with Nec-1, a RIPK1 inhibitor, led to an increase of

survival rate (Martin-Sanchez *et al.*, 2018). Pyroptosis plays a significant role in macrophages to defend the host against bacteria (Vande Walle and Lamkanfi, 2016), while its role in tubular epithelial cells and tubular necrosis is still debated (Linkermann *et al.*, 2014; Belavgeni *et al.*, 2020). Pyroptosis is described as lytic cell death by pore-forming gasdermins e.g. GSDMD(Broz and Dixit, 2016). The cleavage of GSDMD can either be mediated through the canonically inflammasome pathway, composed of caspase 1 (Casp1), the adaptor protein apoptosis-associated speck-like protein containing a CARD (ASC) and a sensor protein like the nucleotide-binding oligomerization domain (NOD) -like receptors (NLRs)(Broz *et al.*, 2012), or the cleavage of GSDMD is mediated by Casp11 and leads to the cleavage and release of the proinflammatory cytokines Interleukin-1 beta (IL-1β) and 18 (IL-18) (Sansonetti *et al.*, 2000; Kayagaki *et al.*, 2011). One study on cisplatin-induced AKI already demonstrated protection of Casp11 and GSDMD knockout mice from AKI together with an upregulation of Casp11 in tubular epithelium and excretion of IL-18 (Miao *et al.*, 2019). Furthermore, IL-1β activation was shown in tubular epithelial cells upon either NLR family pyrin domain containing 3 (NLRP3)-inflammasome activity or GSDMD cleavage through Casp11 (Lau *et al.*, 2018; Zhang *et al.*, 2018). In contrast, another study describes hypersensitivity of GSDMD-deficient mice to ischemia-reperfusion or Cisplatin induced injury (Tonnus *et al.*, 2022). Taken together, while GSDMD and pyroptosis in involved in AKI, the exact role of tubular GSDMD remains unclear.

When investigating the loss of epithelia cells in kidneys of jck mice, that displayed cystic kidney disease and impaired kidney function, we observed increased expression levels of both, RIPK3 and GSDMD. TO understand the contribution of RIPK3 and GSDMD to the pathogenesis of chronic kidney disease in this model, we bred *Nphp9*/*Nek8*^{jck} mice with knockout of *Ripk3* and *GsdmD*, respectively. Both resulted in an amelioration of the cysto-fibrotic kidney phenotype and of kidney function. To understand the mechanisms on the level of different cell populations, we performed snRNA-seq analyses and gained mechanistic insights into the role of RIPK3 and GSDMD in this model of chronic and cystic kidney disease.

Methods

Mouse holding and breeding

To generate a CKD phenotype we used *Nphp9*/*Nek8*^{jck} mice, carrying a point mutation in the *Nek8* gene (Atala *et al.*, 1993). To show the influence of cell death, these mice were crossed with either *Ripk3*$^{-/-}$ or *GsdmD*$^{-/-}$ mice, kindly provided by the SFB1403 of Cologne. The animals were housed according to standardized specific pathogen-free conditions in the *in vivo* research facility of CECAD at the University of Cologne. All matings and experiments were conducted following European, national and institutional guidelines, as approved by the State Office of North Rhine-Westphalia, Department of Nature, Environment and Consumer Protection (8.87-50.10.31.08.049 and 84-02.04.2013.A152). For the preparation, after anesthesia with ketamine (Zoetis) and xylazine (Bayer) the mice were sacrificed by cardiac perfusion with PBS. Kidney tissue was processed by fixation in 4% formaldehyde and embedded in paraffin as well as snap-frozen for further tissue analysis. The blood serum creatinine levels were measured by the Institute of Clinical Chemistry, University Hospital of Cologne, Germany.

Immunochemistry and immunofluorescence staining

In preparation for histological examination, tissue samples were sliced into 2-µm-thick sections, and deparaffinised. Periodic Acid-Schiff (PAS) staining, CD3, Slc12a3/LTL and TUNEL (Promega) staining were executed as before (Kieckhöfer *et al.,* 2024). α-SMA/LTL was performed the same way, with only the secondary antibodies FITC-Lotus Tetragonolobus Lectin (LTL, FL-1321-2; Vector laboratories, 1:250) as well as Cy3-α- smooth muscle actin (α-SMA, C6198, Sigma Aldrich, 1:1000) were used.

Cyst index

The cyst index was computed as before described (Bankhead *et al.*, 2017), with the changed settings of a minimum circularity value of 0.09 for RIPK3 and 0.1 for GSDMD experimental and its control mice. For statistical analysis, all results were standardized relative to the control group, followed by a two-tailed Student's t-test with a significance level set at $p<0.05$.

Quantitative RT-PCR

For quantitative RT-PCR a quarter of the kidney was processed as described before (Kieckhöfer *et al.*, 2022). Samples were prepared with SYBR Green (ThermoFisher Scientific) and primers **(Supp. Tab.1)** and run with the annealing temperature of 60°C. Results were standardized to the reference gene *Hprt1* using the delta-delta CT method, followed by a two-tailed Student's t-test with a significance level of $p<0.05$.

Single nuclear RNA-sequencing

The main protocol is based on a previously described method (Wu *et al.*, 2019). One-quarter of a kidney was shopped on dry ice and grinded in EZ lysis buffer containing 1x Protease inhibitor/ without EDTA (Cat#: 11697498001, Roche) and 0.1% RNase Inhibitor (40U/µl; Cat#: M0314L, NEB). The tissue was stroked prior to incubation on ice. The suspension was filtered through a 40 µm cell strainer and centrifuged by 500 x g for 5 min and 4°C. The pellet was carefully resuspended in inhibitor supplemented EZ lysis buffer, lysed for 5 min on ice and centrifuged by 500 x g, 5 min at 4°C. Final pellets were resuspended in nuclei suspension buffer. Finally, the samples were strained again (40 µm cell strainer) and handed in, to the facility. Libraries were generated using Chromium Next GEM Single Cell 3' HT Reagent kits v3.1 (10x Genomics) aiming for a target of 10,000 cells/sample. Pooled libraries were sequenced on an Illumina NovaSeq 6000 sequencing instrument with 29+89 bp read length (CCG). A detailed description of data processing and analysis is provided in the supplementary materials.

Immunoblotting

A quarter of kidney tissue were mechanically homogenized using a Wheaton Dounce tissue grinder in inhibitor-supplemented RIPA buffer (50 mM Tris/HCL pH 7.5, 150 mM NaCl, 0.1 % NP-40, 0.5 % Na-Deoxycholat, 0.1 % SDS) supplemented with Benzonase® (70746-3 Millipore), cOmplete™ (4693159001, Roche) and PhosSTOP™ (4906845001, Roche), on ice. Samples were sonicated for 5 min 30 sec on/off, followed by centrifugation at 14.000 rpm for 10 min at 4°C. Lysates were boiled for 10 min and boiled with 5x Laemmli after determination of the protein concentration measurement. Proteins were transferred to a PVDF-FL membrane (Millipore), blocked with Roti®-Block (Roth) and probed with antibodies against RIPK3 (ADI-905-242, Enzo, 1:1000) and GSDMD (ab219800, Abcam, 1:1000) overnight at 4°C. The housekeeping antibody GAPDH (5174, Cell Signaling, 1:2000) was incubated for 2 h at RT. Secondary antibodies were applied for 1 h at RT, with the following specifications: Li-COR Biosciences IRDye680 and IRDye800 at 1:10,000 dilution (rb680, 926-68071; mm800, 926-32210; rb800, 926-32211). Densitometric analysis was carried out using Image Studio (v5.2.5) and was normalized to the housekeeping protein.

Cytokine Assay

A quarter of kidney tissue was subjected to homogenization using a Wheaton Dounce tissue grinder and then incubated overnight at 4°C in a lysis buffer containing protease inhibitors (Breyne *et al.*, 2014). After incubation, the protein concentration was determined after collecting the supernatant (12.400 rpm, 1 h at 4°C) and further precipitation (12.400 rpm, 30 min at 4°C). The cytokine AimPlex™ premixed multiplex kit for mice (cat# T2C1020628; Biosciences Inc.) was performed accordance with

144 the manufacturer's instructions. The assay was quantified using the S3eTM Cell Sorter (405/488/561
145 nm, BioRad) with detection channels FL3 and FL4. The data were analysed utilizing FlowJo™ Software
146 version 10.9 (BD Life Sciences).

147 *Quantification and statistical analysis*

148 Data are expressed as mean ± standard deviation (SD). All experiments were performed in at least 3
149 independent biological replicates. Statistical analysis was performed as indicated in the figure legends.
150 The data were statistically analyzed with GraphPad Prism version 9.5.1.

Results

Increased expression of Ripk3 and GsdmD in Nek8^{jck} mice

Nek8^{jck} mice that carry a point mutation in the *Nek8* (*Nphp9*) gene develop cystic kidney disease already at the age of 2 weeks. Kidney histology shows dilated tubules and positive TUNEL signals, indicating ongoing cell death and potential inflammation (**Fig. 1 A**). This phenotype is progressing and presents with a higher number and larger-sized cysts at 12 weeks (**Fig. 1 B**). The further characterisation of the *Nek8*$^{jck/jck}$ mouse revealed, that the formation of cysts mainly occurs in the distal tubules of the kidney (**Fig. 1 C**). We previously described that a defect in primary cilium influences RCD and more specifically necroptosis, which might explain the development of the present phenotype (Kieckhöfer *et al.*, 2022). A FACS-based chemo- and cytokine assay of kidney tissue further revealed an increase of the interferon-gamma-induced protein 10 kD (IP-10/ Cxcl10), as well as of the interleukins 6 (IL-6) and 33 (IL-33) in *Nek8*$^{jck/jck}$ (**Fig. 1 D**). This indicated local inflammation and could be caused by the release of DAMPs, chemo- and cytokines which in turn could be the consequence of RCD. Notably, both RIPK3 and GSDMD levels were increased at 12 weeks in the knockout as compared to control animals which could be confirmed on the protein level by immunoblotting (**Fig. 1 E**). Taken together, kidneys of *Nek8*$^{jck/jck}$ mice do not just show cyst development by proliferation of distal tubular epithelial cells, but additional inflammation and fibrosis, which might be linked to RCD, in particular necroptosis or pyroptosis.

Deletion of *Ripk3* or *GsdmD* ameliorates kidney histology and function in *Nek8*^{jck} mice

To investigate the pathophysiological relevance of necroptosis and pyroptosis in the progression of NPH, we generated *Nek8*^{jck} mice lacking either *Ripk3* or *GsdmD*. Interestingly, both additional knockouts in *Nek8*^{jck} led to an amelioration of the kidney phenotype, indicated in a decreased cystic index used to quantify cyst formation, further indicated by smaller cysts and smaller kidneys at 12 weeks of age (**Fig. 2 A, B; Supp. Fig. 1 A**). Importantly, the knockout of either Ripk3 or GsdmD positively affected kidney function of the *Nek8*^{jck} kidney as measured by the level of urea in the blood serum as a retention marker (**Fig. 2 C**). Thereby, the loss of *Ripk3* seems to show a slightly higher pronounced amelioration of kidney function and histology than the knockout of *GsdmD*. Heterozygous deletion of *Ripk3* or *GsdmD* hadn't any obvious effect on either *Nek8*$^{jck/wt}$ *or Nek8*$^{jck/jck}$. Overall, the improvement of the phenotype through the additional knockout of Ripk3 and GsdmD indicate a role of RCD in the pathogenesis of the phenotype.

Loss of *Ripk3* or *GsdmD* affect renal fibrosis

NPH and related renal ciliopathies are often accompanied by interstitial fibrosis as a common process of tissue repair response (Luo and Tao, 2018), triggered by e.g. necroptosis and pyroptosis (Hao *et al.*,

2023; Liu *et al.*, 2023). α-Smooth muscle actin (α-SMA), is used as a common marker for a subset of activated fibrogenic cells, involved in inflammation, wound healing and fibrosis. Numerous α-SMA-positive cells are found all over *Nek8*$^{jck/jck}$ kidneys (**Fig. 2 D; Supp. Fig. 1 B**) and is not limited to one specific cell type but widely expressed. In contrast, in kidneys lacking *Ripk3* or *GsdmD* we found fewer SMA-positive cells. Additional transcriptional analysis of well-known fibrosis markers, such as CC-chemokine ligand 2 (*Ccl2*), collagen type I alpha 1 chain (*Col1α1*), cellular communication network factor 2 (*Ccn2/Ctgf*), fibronectin (*FN*) and transforming growth factor beta 1 (*TGF-β1*), showed increased expression in the *Nek8*^{jck} mice, but except from *Ccl2* no significant reduction in the *Ripk3* or *GsdmD* knockouts (**Supp. Fig. 1 C**). Thus, the *Nek8*$^{jck/jck}$ renal phenotype is accompanied by RCD influenced fibrosis.

Loss of either Ripk3 or GsdmD does not result in the elimination of cell death

Given the only partial amelioration of the cystic phenotype and kidney dysfunction in the *Ripk3* and *GsdmD* knockout *Nek8*^{jck} mice, we investigated the persistence of cell death in these models by TUNEL assays. RCD pathways are tightly interconnected, through which the removal of one important component of one pathway could also lead to a shift into another cell death pathway. We found in *Nek8*^{jck} kidneys lacking *Ripk3* or *GsdmD* still TUNEL positive cells, indicating active cell death in the tissue (**Fig. 3 A, Supp. Fig. 1 B**). We also observed an increased level of T-cells (CD3^{+}) in the kidney almost indistinguishable between jck and the two knockout lines. The cross-activation of different cell death pathways could be further assessed by mRNA transcription analysis of multiple cell death markers (**Supp. Fig.2 A**) of which for example *Casp8* transcription was significantly increased in *Nek8*$^{jck/jck}$ *GsdmD*$^{-/-}$ mice. This could indicate a Casp8-activated inflammasome in absence of GSDMD-dependent pyroptosis (Schneider *et al.*, 2017). In the knockout of *Ripk3*$^{-/-}$in *Nek8*$^{jck/jck}$, the expression of *GsdmD* is not altered as compared to *Nek8*^{jck} mice (**Fig. 3 B**). Similarly, in *Nek8*$^{jck/jck}$ *GsdmD*$^{-/-}$ mice, *Ripk3* remains upregulated (**Fig. 3 C**). This upregulation of the respective other RCD key gene in the *Nek8*^{jck} mice is also visible at the protein expression level (**Fig. 3 D, E**). Showing the strong interconnection of RCD pathways involved in the progression of the renal phenotype.

snRNA-seq analyses of *Nek8*^{jck}mice with and without deletion of *Ripk3* or *GsdmD*

To gain insights into the development of renal disease in *Nek8*^{jck}mice as well as in the mechanisms of the amelioration by deletion of *Ripk3* or *GsdmD*, we conducted single-nucleus RNA-sequencing (snRNA-seq) from kidney tissue of pooled control (*Nek8*$^{jck/wt}$ *Ripk3*$^{+/-}$ with *Nek8*$^{jck/wt}$ *GsdmD*$^{+/-}$) versus pooled *Nek8*$^{jck/jck}$ (*Nek8*$^{jck/jck}$ *Ripk3*$^{+/-}$ with *Nek8*$^{jck/jck}$ *GsdmD*$^{+/-}$) versus *Nek8*$^{jck/jck}$ *Ripk3*$^{-/-}$and *Nek8*$^{jck/jck}$ *GsdmD*$^{-/-}$ at the age of 12 weeks. To visualize and resolve different nuclear cell populations we used Uniform Manifold Approximation and Projection (UMAP) (**Fig. 4 A, Supp. Fig. 3 A**). We identified 21 unsupervised clusters representing the major kidney cell types based on their transcriptional profiles

(**Supp. Fig. 3 B**). The relative percentage of the nuclei populations of different cell types across genotypes revealed a reduction of proximal tubule cells in *Nek8*$^{jck/jck}$ compared to the control (**Fig. 4 B**). The reduced relative abundance of proximal tubule cells is almost unaffected by the additional loss of *Ripk3* or *GsdmD*. Interestingly, we observe in increase in immune cells consistent with our observations in histology (**Fig. 3 A**). Next, we performed a gene set enrichment analysis (GESA) on up- and downregulated genes in the proximal tubules between *Nek8*$^{jck/jck}$ and the control (**Fig. 4 C**). We identified an upregulation of genes related to cell proliferation in *Nek8*$^{jck/jck}$ appropriate to repair mechanism in the tubules. Among the differentially regulated genes was lipocalin 2 (*Lcn2*), which encodes for the established renal damage marker NGAL (**Fig. 4 D**) (Martin-Sanchez *et al.*, 2018). Moreover, we also saw the already described damaged marker clusterin (Clu) and secreted phosphoprotein 1 (SPP1) strongly regulated (Ming *et al.*, 2018; Gao *et al.*, 2022). Remarkably, these candidates were downregulated both upon the additional knockout of *Ripk3* as well as *GsdmD*. This effect was stronger for *Ripk3* and therefore indicating a stronger impact of necroptosis on cystogenesis. We then identified a gene set which follows a similar expression pattern (same direction of regulation in control, *Nek8*$^{jck/jck}$ *Ripk3*$^{-/-}$, and *Nek8*$^{jck/jck}$ *GsdmD*$^{-/-}$ and divergent regulation in *Nek8*$^{jck/jck}$) and preformed GESA (**Fig. 4 E**). This showed an increase of activating transcription factor 6 (ATF6) mediated protein response in both of the RCD knockouts. ATF6 is already described to influence both necroptosis and pyroptosis (Simard *et al.*, 2015; Huang *et al.*, 2021). To investigate the differences between the knockout of *Ripk3* or *GsdmD*, we selected genes showing regulation in the same direction in control and *Nek8*$^{jck/jck}$ *Ripk3*$^{-/-}$ and divergent regulation in *Nek8*$^{jck/jck}$ and *Nek8*$^{jck/jck}$ *GsdmD*$^{-/-}$ and genes showing regulation in the same direction in control and *Nek8*$^{jck/jck}$ *GsdmD*$^{-/-}$ and divergent regulation in *Nek8*$^{jck/jck}$ and *Nek8*$^{jck/jck}$ *Ripk3*$^{-/-}$ (**Fig. 4 F**). GESA of this gene set revealed differently affected biosynthetic processes.

Discussion

Nephronophthisis (NPH) is a rare renal disease without effective therapy, due to the lack of research in this field, and it progresses most times in ESRF. In patients, kidney function can be tested by measuring blood creatinine and the phenotype via ultrasound (Arts and Knoers, 2013). Up to the present, there are no mouse models available which completely mimic the human phenotype. The *Nek8*^{jck} mouse, presented with a point mutation in the *Nphp9* gene, develops a cystic fibrotic kidney phenotype at a rather early age and only in homozygous mice. Therefore, it closely resembles NPH in essential aspects, whereas the kidneys also bear resemblance to ADPKD, in particular with the proliferation and massive cyst formation. Interestingly, mutation in *Nphp9* do not just lead to NPH (Otto *et al.*, 2008), but heterozygous mutations have recently been shown to result in ADPKD in patients (Claus *et al.*, 2023). *Nphp9* encodes the never-in-mitosis A-related kinase (NEK8) which influences Hippo signalling, by stimulating nuclear translocation of YAP/TAZ, and thereby regulating

the downstream activation of target genes (Habbig *et al.*, 2012). Thereby, NEK8 is linked to the primary cilium, as mutations affect ciliary localization and therefore influences ciliary signalling (Otto *et al.*, 2008). Through this left-right symmetry defects could occur (Manning *et al.*, 2013) as well as the expression of polycystin-1 and 2 (Sohara *et al.*, 2008) and thus in a cystic renal phenotypes (Claus *et al.*, 2023). This cyst formation is highly likely influenced by RCD. We recently showed that primary cilia modulate the RCD response in kidney epithelial cells, therefore RCD might be affected in *Nek8*$^{jck/jck}$ (Kieckhöfer *et al.*, 2022; Kieckhöfer *et al.*, 2024). Our *in vivo* data suggests that RCD and the inflammasome contribute to disease progression. Interestingly, cell death occurs already early on in the kidney of *Nek8*$^{jck/jck}$ and goes along with upregulation of RIPK3 and GSDMD. Notably, with the additional conventional knockout of either *Ripk3* or *GsdmD* in *Nek8*^{jck}, the histological phenotype was ameliorated as was the function of the kidney. This is similar to data from induced AKI mice, in which the knockout or the inhibition of the necroptotic or pyroptotic pathways resulted in an increased survival rate (Chen *et al.*, 2020; Tonnus *et al.*, 2022). Nonetheless, we could not generate a total rescue of the phenotype, showing the intrigue and tight interconnection between cell death pathways in a chronic kidney disease. Interestingly, we could show that in the majority cysts arise from the distal tubules, which is distinct from other ciliopathies (Braun and Hildebrandt, 2021). In addition, snRNA-seq data, revealed the loss of proximal tubule epithelial cells and an increase of immune cells in *Nek8*$^{jck/jck}$, referring to the increased levels of inflammation. However, although cysts derive form proliferating distal tubules, a higher abundance of distal tubule cells was not visible in the snRNA- Seq data. Interestingly, the increased expression of damage markers in the *Nek8*$^{jck/jck}$ was decreased in the additional knockout of *Ripk3* and *GsdmD*, however to a greater extent in *Ripk3*, consistent with the functional data. Furthermore, we found gene enriched clusters equally expressed in *Nek8*$^{jck/jck}$ *Ripk3*$^{-/-}$ and *Nek8*$^{jck/jck}$ *GsdmD*$^{-/-}$compared to the control, one of which was ATF6 mediated protein response. ATF6 is already described in the relation to RIPK3, in which the downregulation of RIPK3 improves positive effects in acute liver injury (Huang *et al.*, 2021). Interestingly, a decrease of ATF6 support the activation of the NLRP3 inflammasome (Simard *et al.*, 2015) . Indicating a potential role of both cell death pathways in the progression of the phenotype. Differentially expressed between *Nek8*$^{jck/jck}$ *Ripk3*$^{-/-}$ and *Nek8*$^{jck/jck}$ *GsdmD*$^{-/-}$ are macromolecular biosynthetic processes, which are important in the RCD pathway of pyroptosis (Tsuchiya, 2021). This difference may contribute to the milder amelioration compared to *Nek8*$^{jck/jck}$ *Ripk3*$^{-/-}$. Overall, we were able to show that the triad of NPH (loss of epithelial cells, cyst formation and fibrosis) is to a certain extent caused by necroptosis and pyroptosis. Additional experiments need to address, whether RCD, and in particular necroptosis, might represent a potential target of future therapeutic strategies.

JCK Manuscript Figure legends

Figure 1. **Cell death and RIPK3/GSDMD levels in cystic kidney disease of *Nek8*$^{jck/jck}$ mice**

(A) TUNEL staining of 2-week-old control (*Nek8*$^{jck/wt}$) and *Nek8*$^{jck/jck}$, as well as an overview PAS image of the whole kidney of these animals; Scale bar TUNEL: 250 µm, scale bar PAS: 500 µm.

(B) PAS staining of 12-week-old control and *Nek8*$^{jck/jck}$ animal kidneys; Scale bar: 250 µm.

(C) Histology of renal tubules of 12-weel-old control and *Nek8*$^{jck/jck}$ kidneys, stained for distal tubules (Slc12a3, magenta) and proximal tubules (LTL, green); Scale bar: 500 µm.

(D) Chemo/cytokine profiling (AimPlex) of kidney tissue lysates of control and *Nek8*$^{jck/jck}$. Statistically analysed with the uncorrected Fisher's LSD test (*p*-value: <0.001***; 0.002**; 0.033*; ns = 0.12) ± SD.

(E) Immunoblot analysis of kidney samples against RIPK3 (~55 kDa) and GSDMD (~57 kDa). All samples were normalized to GAPDH (~39 kDa). Densitometry were measured and statistically analysed using a two-sided student's *T-test* (*p*-value: <0.001***; 0.002**; 0.033*; ns = 0.12) ± SD (n=3).

Figure 2. **Loss of *Ripk3* or *GsdmD* ameliorates kidney histology and function in *Nek8*$^{jck/jck}$ mice**

Characterization of kidney tissue of 12-week-old mice, analysed in sets with corresponding control. Set 1: control (*Nek8*$^{jck/wt}$ *Ripk3*$^{+/-}$; n=3), *Nek8*$^{jck/jck}$ (*Nek8*$^{jck/jck}$ *Ripk3*$^{+/-}$; n=7) and *Nek8*$^{jck/jck}$ *Ripk3*$^{-/-}$ (n=7). Set 2: control (*Nek8*$^{jck/wt}$ *GsdmD*$^{+/-}$; n=8), *Nek8*$^{jck/jck}$ (*Nek8*$^{jck/jck}$ *GsdmD*$^{+/-}$; n=9), and *Nek8*$^{jck/jck}$ *GsdmD*$^{-/-}$ (n=6). Statistical analysis: uncorrected Fisher's LSD test (*p*-value: <0.001***; 0.002**; 0.033*; ns = 0.12) ± SD.

(A) Pas staining of the whole kidney; Scale bar: 2 mm.

(B) Cyst index described in a cyst-to-tissue area ratio normalised to the related control animals.

(C) Functional recue of the kidney revealed by the blood serum urea level.

(D) Representative images of the fibrosis marker α-Smooth muscle actin (α-SMA, magenta) expression, co-stained for proximal tubules (LTL, green) in 12-week-old mice: control; Scale bar: 100 µm. Equivalent controls for *Nek8*$^{jck/jck}$ *GsdmD*$^{-/-}$ are shown in supplementary figure 1.

Figure 3. **RIPK3 and GSDMD are elevated in the respective knockout of the other, and cell death persists**

(A) 12-week-old kidney tissue stained for TUNEL (scale bar: 100 µm) and CD3, positive events indicated with arrowhead (scale bar: 400 µm). Equivalent controls for *Nek8*$^{jck/jck}$ *GsdmD*$^{-/-}$ are shown in supplementary figure 1.

(B) qPCR executed for the cell death markers RIPK3 and GSDMD in kidney samples of : control (*Nek8*$^{jck/wt}$ *Ripk3*$^{+/-}$; n=3), *Nek8*$^{jck/jck}$ (*Nek8*$^{jck/jck}$ *Ripk3*$^{+/-}$; n=4) and *Nek8*$^{jck/jck}$ *Ripk3*$^{-/-}$ (n=4) mice. Statistical analysis was performed using the Šídák's multiple comparisons test (*p*-value: <0.001***; 0.002**; 0.033*; ns = 0.12) ± SD.

(C) qPCR executed for the cell death markers RIPK3 and GSDMD in kidney samples of control (*Nek8*$^{jck/wt}$ *GsdmD*$^{+/-}$; n=3), *Nek8*$^{jck/jck}$ (*Nek8*$^{jck/jck}$ *GsdmD*$^{+/-}$; n=6), and *Nek8*$^{jck/jck}$ *GsdmD*$^{-/-}$ (n=6). Statistical analysis was performed using the Šídák's multiple comparisons test (*p*-value: <0.001***; 0.002**; 0.033*; ns = 0.12) ± SD.

(D/E) Kidney samples of double knockout and corresponding controls were immunoblotted against RIPK3 (~55 kDa) and GSDMD (~57 kDa). All samples were normalized to GAPDH (-39 kDa). Densitometry were measured and statistically analysed using the Tukey test (*p*-value: <0.001***; 0.002**; 0.033*; ns = 0.12). **(D)** control (*Nek8*$^{jck/wt}$ *Ripk3*$^{+/-}$), *Nek8*$^{jck/jck}$ (*Nek8*$^{jck/jck}$ *Ripk3*$^{+/-}$), *Nek8*$^{jck/jck}$ *Ripk3*$^{-/-}$. **(E)** Control (*Nek8*$^{jck/wt}$ *GsdmD*$^{+/-}$), *Nek8*$^{jck/jck}$ (*Nek8*$^{jck/jck}$ *GsdmD*$^{+/-}$), *Nek8*$^{jck/jck}$ *GsdmD*$^{-/-}$.

Figure 4. **snRNA-seq analysis revealed loss of proximal tubule cells and pathways underlying RCD in *Nek8*$^{jck/jck}$**.

(A) Identification of major renal cell types in a Uniform Manifold Approximation and Projection (UMAP) visualization for the combined snRNA-seq data set (renal tissue of pooled control (*Nek8*$^{jck/wt}$ *Ripk3*$^{+/-}$, *Nek8*$^{jck/wt}$ *GsdmD*$^{+/-}$), pooled *Nek8*$^{jck/jck}$ (*Nek8*$^{jck/jck}$ *Ripk3*$^{+/-}$, *Nek8*$^{jck/wt}$ *GsdmD*$^{+/-}$), *Nek8*$^{jck/jck}$ *Ripk3*$^{-/-}$ and *Nek8*$^{jck/jck}$ *GsdmD*$^{-/-}$ samples). PT: proximal tubule, DCT: distal tubule, PO: podocyte, IM: immune cells, MX: mixed cells, Endo: endothelial cell, TAL: thick ascending limp of the loop of Henle, CNT: connecting tubule, ICA+ICB: intercalated cells type A and B, CC: cycling cells, FI: fibroblasts, PC: principal cells, DTL+ATL: descending and ascending thin limp of the loop of Henle.

(B) Percentage of nuclei in each cell type determined by genotype.

(C) Gene set enrichment analysis (GSEA) of upregulated and downregulated genes in *Nek8*$^{jck/jck}$ vs control nuclei populations of the PT.

(D) Violin plots showing normalized expression levels of selected damage markers in the PT across genotypes.

(E) GESA of genes exhibiting coordinate regulation in control, *Nek8*$^{jck/jck}$ *Ripk3*$^{-/-}$, and *Nek8*$^{jck/jck}$ *GsdmD*$^{-/-}$ and divergent regulation in *Nek8*$^{jck/jck}$.

(F) GESA of genes exhibiting coordinate regulation in control and *Nek8*$^{jck/jck}$ *Ripk3*$^{-/-}$ and divergent regulation in *Nek8*$^{jck/jck}$ and *Nek8*$^{jck/jck}$ *GsdmD*$^{-/-}$ or genes exhibiting coordinate regulation in control and *Nek8*$^{jck/jck}$ *GsdmD*$^{-/-}$ and divergent regulation in *Nek8*$^{jck/jck}$ and *Nek8*$^{jck/jck}$ *Ripk3*$^{-/-}$.

Supplementary Figure 1. **Characterisation of *Nek8*$^{jck/jck}$ mice and role of RCD**

(A) Kidney to body weight ratio in 12-week-old animals Set1: control (*Nek8*$^{jck/wt}$ *Ripk3*$^{+/-}$), *Nek8*$^{jck/jck}$ (*Nek8*$^{jck/jck}$ *Ripk3*$^{+/-}$), *Nek8*$^{jck/jck}$ *Ripk3*$^{-/-}$; set 2: control (*Nek8*$^{jck/wt}$ *GsdmD*$^{+/-}$), *Nek8*$^{jck/jck}$ (*Nek8*$^{jck/jck}$ *GsdmD*$^{+/-}$), *Nek8*$^{jck/jck}$ *GsdmD*$^{-/-}$. Statistical analysis with the uncorrected Fisher's LSD test (*p*-value: <0.001***; 0.002**; 0.033*; ns = 0.12) ± SD.

(B) Prober control images of *Nek8*$^{jck/jck}$ *GsdmD*$^{+/-}$ and respective control (*Nek8*$^{jck/wt}$ *GsdmD*$^{+/-}$). α-SMA/LTL and TUNEL, scale bar: 100 µm; CD3, scale bar: 400 µm.

(C) qPCR detection of fibrosis marker transcription in the kidney of Set 1 and Set 2 mice (minimum of n=3 mice for each group). Statistical analysis: Šídák's multiple comparisons test (*p*-value: <0.001***; 0.002**; 0.033*; ns = 0.12) ± SD.

Supplementary Figure 2. **Transcription of key genes in RCD pathways in *Nek8*$^{jck/jck}$**

(A) qPCR detection of cell death marker transcription in the kidney of Set 1 and Set 2 mice (minimum of n=3 mice for each group). Statistical analysis: Šídák's multiple comparisons test (*p*-value: <0.001***; 0.002**; 0.033*; ns = 0.12) ± SD.

Supplementary Figure 3. **Additional data on snRNA-seq analysis regarding annotation**

(A) UMAP visualization of the snRNA-seq data set colored by the different genotypes: pooled control (*Nek8*$^{jck/wt}$ *Ripk3*$^{+/-}$, *Nek8*$^{jck/wt}$ *GsdmD*$^{+/-}$), pooled *Nek8*$^{jck/jck}$ (*Nek8*$^{jck/jck}$ *Ripk3*$^{+/-}$, *Nek8*$^{jck/wt}$ *GsdmD*$^{+/-}$), *Nek8*$^{jck/jck}$ *Ripk3*$^{-/-}$ and *Nek8*$^{jck/jck}$ *GsdmD*$^{-/-}$.

(B) Dot plot of the snRNA-seq dataset showing gene expression patterns of cluster markers. The diameter of the dot corresponds to the fraction of cells in each group and the density of the dot corresponds to mean expression in the group.

Supplementary Figure 5. **Full-sized immunoblots**

Original western blots only cropped to gel size **(A)** of Figure 1 and **(B)** of Figure 4.

Supplementary Method

Single nuclear RNA-sequencing

The datasets were processed through the 10x Genomics pipeline CellRanger count (v7.0.0). The GRCm38m10 reference genome was used for aligment. Samples were pre-processed independently. Nuclei with greater than 4,000 and less than 200 features were removed from the samples. Only nuclei with less than 1% expression of mitochondrial genes were kept. After pre-processing, Scrublet (v.0.2.3) was used to identify and remove putative doublets in each dataset (Wolock, Lopez and Klein, 2019). The threshold was set to 0.2. Dimension reduction and unsupervised clustering were performed using the standard pipeline in Scanpy (v.1.9.6) (Wolf, Angerer and Theis, 2018).

Highly variable genes for downstream analysis by using the "scanpy.pp.highly_variable_genes" function using the individual libraries as batch key and the flavor "Seurat". After scaling the data, principal component analysis was performed. Clusters were computed using "scanpy.pp.neighbors" with 29 components and "scanpy.pp.neighbors" with a resolution of 0.4. A dimensional reduction UMAP was performed with the "scanpy.tl.umap" function for visualization.

Marker genes for the individual clusters were identified using "scanpy.tl.rank_genes_groups". Published literature was used to annotate cluster identities based on the expression of known marker genes and the computed marker genes. For the analysis of cell type distribution, differentially expressed genes, and gene set enrichment analysis (GSEA) the clusters were grouped based on their major cell types. Differentially expressed genes were calculated using the "scanpy.tl.rank_genes_groups" function. GSEApy (v.1.1.2) with the "GO_Biological_Process_2023" library were used for GSEA (Fang, Liu and Peltz, 2023).

Acknowledgments

We wish to express our sincere thanks to Angelika Köser and Serena Greco-Torres for their invaluable technical support. Additionally, we'd like to recognize and appreciate the great assistance provided by the CECAD imaging facility and the CECAD proteomics facility. Moreover, we extend our gratitude to all the members of our laboratory and the numerous individuals from the SFB1403 for their meaningful discussions and unwavering support.

Funding: This study was supported by the German Research Foundation (DFG; SFB1403, project number 414786233, A09 to B.S. and T.B.). B.S. was also supported by the German Federal Ministry of Research and Education (BMBF grant 01GM1515; NEOCYST consortium.) and by the European Union (TheraCil). The CECAD proteomics facility was supported by the large instrument grant INST 1856/71-1 FUGG by the German Research Foundation (DFG Großgeräteantrag).

References

Arts, H. H. and Knoers, N. V. A. M. (2013) 'Current insights into renal ciliopathies: what can genetics teach us?', *Pediatric nephrology (Berlin, Germany)*, 28(6), pp. 863–74. doi: 10.1007/s00467-012-2259-9.

Atala, A. *et al.* (1993) 'Juvenile cystic kidneys (jck): a new mouse mutation which causes polycystic kidneys', *Kidney international*, 43(5), pp. 1081–1085. doi: 10.1038/KI.1993.151.

Bankhead, P. *et al.* (2017) 'QuPath: Open source software for digital pathology image analysis', *Scientific Reports 2017 7:1*, 7(1), pp. 1–7. doi: 10.1038/s41598-017-17204-5.

Belavgeni, A. *et al.* (2020) 'Ferroptosis and Necroptosis in the Kidney', *Cell chemical biology*, 27(4), pp. 448–462. doi: 10.1016/J.CHEMBIOL.2020.03.016.

Benmerah, A. *et al.* (2023) 'Repurposing small molecules for nephronophthisis and related renal ciliopathies', *Kidney international*, 104(2), pp. 245–253. doi: 10.1016/J.KINT.2023.04.027.

Braun, D. A. and Hildebrandt, F. (2021) 'Nephronophthisis and Related Ciliopathies', *Pediatric Nephrology*, pp. 1–28. doi: 10.1007/978-3-642-27843-3_119-1.

Breyne, K. *et al.* (2014) 'Non-Classical ProIL-1beta Activation during Mammary Gland Infection Is Pathogen-Dependent but Caspase-1 Independent', *PLoS ONE*, 9(8), p. 105680. doi: 10.1371/journal.pone.0105680.

Broz, P. *et al.* (2012) 'Caspase-11 increases susceptibility to Salmonella infection in the absence of caspase-1', *Nature*, 490(7419), pp. 288–291. doi: 10.1038/NATURE11419.

Broz, P. and Dixit, V. M. (2016) 'Inflammasomes: mechanism of assembly, regulation and signalling', *Nature reviews. Immunology*, 16(7), pp. 407–420. doi: 10.1038/NRI.2016.58.

Chen, H. *et al.* (2020) 'RIPK3 collaborates with GSDMD to drive tissue injury in lethal polymicrobial sepsis', *Cell death and differentiation*, 27(9), pp. 2568–2585. doi: 10.1038/S41418-020-0524-1.

Chen, W. *et al.* (2013) 'Diverse Sequence Determinants Control Human and Mouse Receptor Interacting Protein 3 (RIP3) and Mixed Lineage Kinase domain-Like (MLKL) Interaction in Necroptotic Signaling', *Journal of Biological Chemistry*, 288(23), pp. 16247–16261. doi: 10.1074/JBC.M112.435545.

Claus, L. R. *et al.* (2023) 'Certain heterozygous variants in the kinase domain of the serine/threonine kinase NEK8 can cause an autosomal dominant form of polycystic kidney disease', *Kidney international*, 104(5), pp. 995–1007. doi: 10.1016/J.KINT.2023.07.021.

Fang, Z., Liu, X. and Peltz, G. (2023) 'GSEApy: a comprehensive package for performing gene set enrichment analysis in Python', *Bioinformatics*, 39(1). doi: 10.1093/BIOINFORMATICS/BTAC757.

Gao, W. *et al.* (2022) 'SPP1 is a prognostic related biomarker and correlated with tumor-infiltrating immune cells in ovarian cancer', *BMC Cancer*, 22(1), p. 1367. doi: 10.1186/S12885-022-10485-8.

Habbig, S. *et al.* (2012) 'The ciliopathy disease protein NPHP9 promotes nuclear delivery and activation of the oncogenic transcriptional regulator TAZ', *Human Molecular Genetics*, 21(26), pp. 5528–5538. doi: 10.1093/HMG/DDS408.

Hao, M. *et al.* (2023) 'The pathogenesis of organ fibrosis: Focus on necroptosis', *British Journal of Pharmacology*, 180(22), pp. 2862–2879. doi: 10.1111/BPH.15952.

Hildebrandt, F. and Zhou, W. (2007) 'Nephronophthisis-associated ciliopathies.', *Journal of the American Society of Nephrology : JASN*, 18(6), pp. 1855–71. doi: 10.1681/ASN.2006121344.

Holler, N. *et al.* (2000) 'Fas triggers an alternative, caspase-8-independent cell death pathway using

the kinase RIP as effector molecule', *Nature immunology*, 1(6), pp. 489–495. doi: 10.1038/82732.

Huang, M. Y. *et al.* (2021) 'Downregulation of RIP3 Improves the Protective Effect of ATF6 in an Acute Liver Injury Model', *BioMed Research International*, 2021. doi: 10.1155/2021/8717565.

Kayagaki, N. *et al.* (2011) 'Non-canonical inflammasome activation targets caspase-11', *Nature*, 479(7371), pp. 117–121. doi: 10.1038/NATURE10558.

Kieckhöfer, E. *et al.* (2022) 'Primary cilia suppress Ripk3-mediated necroptosis', *Cell Death Discovery 2022 8:1*, 8(1), pp. 1–12. doi: 10.1038/s41420-022-01272-2.

Kieckhöfer, E *et al.* (2024) 'Loss of Bbs8 leads to cystic kidney disease in mice and affects tubulin acetylation through HDAC2. BIORXIV/583949

Lau, A. *et al.* (2018) 'Renal immune surveillance and dipeptidase-1 contribute to contrast-induced acute kidney injury', *The Journal of clinical investigation*, 128(7), pp. 2894–2913. doi: 10.1172/JCI96640.

Linkermann, A. *et al.* (2013) 'Two independent pathways of regulated necrosis mediate ischemia-reperfusion injury', *Proceedings of the National Academy of Sciences of the United States of America*, 110(29), pp. 12024–12029. doi: 10.1073/PNAS.1305538110/SUPPL_FILE/PNAS.201305538SI.PDF.

Linkermann, A. *et al.* (2014) 'Synchronized renal tubular cell death involves ferroptosis', *Proceedings of the National Academy of Sciences of the United States of America*, 111(47), pp. 16836–16841. doi: 10.1073/PNAS.1415518111.

Liu, Y. *et al.* (2023) 'Pyroptosis in renal inflammation and fibrosis: current knowledge and clinical significance', *Cell Death & Disease 2023 14:7*, 14(7), pp. 1–14. doi: 10.1038/s41419-023-06005-6.

Luo, F. and Tao, Y. H. (2018) 'Nephronophthisis: A review of genotype–phenotype correlation', *Nephrology*. Blackwell Publishing, pp. 904–911. doi: 10.1111/nep.13393.

Manning, D. K. *et al.* (2013) 'Loss of the ciliary kinase Nek8 causes left-right asymmetry defects', *Journal of the American Society of Nephrology : JASN*, 24(1), pp. 100–112. doi: 10.1681/ASN.2012050490.

Maremonti, F., Meyer, C. and Linkermann, A. (2022) 'Mechanisms and Models of Kidney Tubular Necrosis and Nephron Loss', *Journal of the American Society of Nephrology : JASN*, 33(3), p. 472. doi: 10.1681/ASN.2021101293.

Martin-Sanchez, D. *et al.* (2018) 'TWEAK and RIPK1 mediate a second wave of cell death during AKI', *Proceedings of the National Academy of Sciences of the United States of America*, 115(16), pp. 4182–4187. doi: 10.1073/PNAS.1716578115/-/DCSUPPLEMENTAL.

Miao, N. *et al.* (2019) 'The cleavage of gasdermin D by caspase-11 promotes tubular epithelial cell pyroptosis and urinary IL-18 excretion in acute kidney injury', *Kidney international*, 96(5), pp. 1105–1120. doi: 10.1016/J.KINT.2019.04.035.

Ming, X. *et al.* (2018) 'Clusterin, a Novel DEC1 Target, Modulates DNA Damage-Mediated Cell Death', *Molecular cancer research : MCR*, 16(11), pp. 1641–1651. doi: 10.1158/1541-7786.MCR-18-0070.

Newton, K. *et al.* (2016) 'RIPK3 deficiency or catalytically inactive RIPK1 provides greater benefit than MLKL deficiency in mouse models of inflammation and tissue injury', *Cell death and differentiation*, 23(9), pp. 1565–1576. doi: 10.1038/CDD.2016.46.

Otto, E. A. *et al.* (2008) 'NEK8 mutations affect ciliary and centrosomal localization and may cause nephronophthisis', *Journal of the American Society of Nephrology : JASN*, 19(3), pp. 587–592. doi: 10.1681/ASN.2007040490.

Sansonetti, P. J. *et al.* (2000) 'Caspase-1 activation of IL-1beta and IL-18 are essential for Shigella

flexneri-induced inflammation', *Immunity*, 12(5), pp. 581–590. doi: 10.1016/S1074-7613(00)80209-5.

Sanz, A. B. *et al.* (2023) 'Regulated cell death pathways in kidney disease', *Nature reviews. Nephrology*, 19(5), pp. 281–299. doi: 10.1038/S41581-023-00694-0.

Schneider, K. S. *et al.* (2017) 'The Inflammasome Drives GSDMD-Independent Secondary Pyroptosis and IL-1 Release in the Absence of Caspase-1 Protease Activity', *Cell Reports*, 21(13), p. 3846. doi: 10.1016/J.CELREP.2017.12.018.

Simard, J. C. *et al.* (2015) 'Silver Nanoparticles Induce Degradation of the Endoplasmic Reticulum Stress Sensor Activating Transcription Factor-6 Leading to Activation of the NLRP-3 Inflammasome', *The Journal of Biological Chemistry*, 290(9), p. 5926. doi: 10.1074/JBC.M114.610899.

Sohara, E. *et al.* (2008) 'Nek8 Regulates the Expression and Localization of Polycystin-1 and Polycystin-2', *Journal of the American Society of Nephrology : JASN*, 19(3), p. 469. doi: 10.1681/ASN.2006090985.

Srivastava, S. *et al.* (2018) 'Many Genes-One Disease? Genetics of Nephronophthisis (NPHP) and NPHP-Associated Disorders', *Frontiers in pediatrics*, 5. doi: 10.3389/FPED.2017.00287.

Sun, L. *et al.* (2012) 'Mixed lineage kinase domain-like protein mediates necrosis signaling downstream of RIP3 kinase', *Cell*, 148(1–2), pp. 213–227. doi: 10.1016/J.CELL.2011.11.031.

Tonnus, W. *et al.* (2022) 'Gasdermin D-deficient mice are hypersensitive to acute kidney injury', *Cell death & disease*, 13(9). doi: 10.1038/S41419-022-05230-9.

Tsuchiya, K. (2021) 'Switching from Apoptosis to Pyroptosis: Gasdermin-Elicited Inflammation and Antitumor Immunity', *International Journal of Molecular Sciences*, 22(1), pp. 1–23. doi: 10.3390/IJMS22010426.

Vande Walle, L. and Lamkanfi, M. (2016) 'Pyroptosis', *Current biology : CB*, 26(13), pp. R568–R572. doi: 10.1016/J.CUB.2016.02.019.

Wolf, F. A., Angerer, P. and Theis, F. J. (2018) 'SCANPY: Large-scale single-cell gene expression data analysis', *Genome Biology*, 19(1), pp. 1–5. doi: 10.1186/S13059-017-1382-0/FIGURES/1.

Wolf, M. T. F. *et al.* (2023) 'Nephronophthisis: a pathological and genetic perspective', *Pediatric Nephrology 2023*, pp. 1–24. doi: 10.1007/S00467-023-06174-8.

Wolock, S. L., Lopez, R. and Klein, A. M. (2019) 'Scrublet: Computational Identification of Cell Doublets in Single-Cell Transcriptomic Data', *Cell Systems*, 8(4), pp. 281-291.e9. doi: 10.1016/J.CELS.2018.11.005.

Wu, H. *et al.* (2019) 'Advantages of single-nucleus over single-cell RNA sequencing of adult kidney: Rare cell types and novel cell states revealed in fibrosis', *Journal of the American Society of Nephrology*, 30(1), pp. 23–32. doi: 10.1681/ASN.2018090912/-/DCSUPPLEMENTAL.

Zhang, D. W. *et al.* (2009) 'RIP3, an energy metabolism regulator that switches TNF-induced cell death from apoptosis to necrosis', *Science (New York, N.Y.)*, 325(5938), pp. 332–336. doi: 10.1126/SCIENCE.1172308.

Zhang, Z. *et al.* (2018) 'Caspase-11-mediated tubular epithelial pyroptosis underlies contrast-induced acute kidney injury', *Cell death & disease*, 9(10). doi: 10.1038/S41419-018-1023-X.

Zhao, J. *et al.* (2012) 'Mixed lineage kinase domain-like is a key receptor interacting protein 3 downstream component of TNF-induced necrosis', *Proceedings of the National Academy of Sciences of the United States of America*, 109(14), pp. 5322–5327. doi: 10.1073/PNAS.1200012109/SUPPL_FILE/PNAS.201200012SI.PDF.

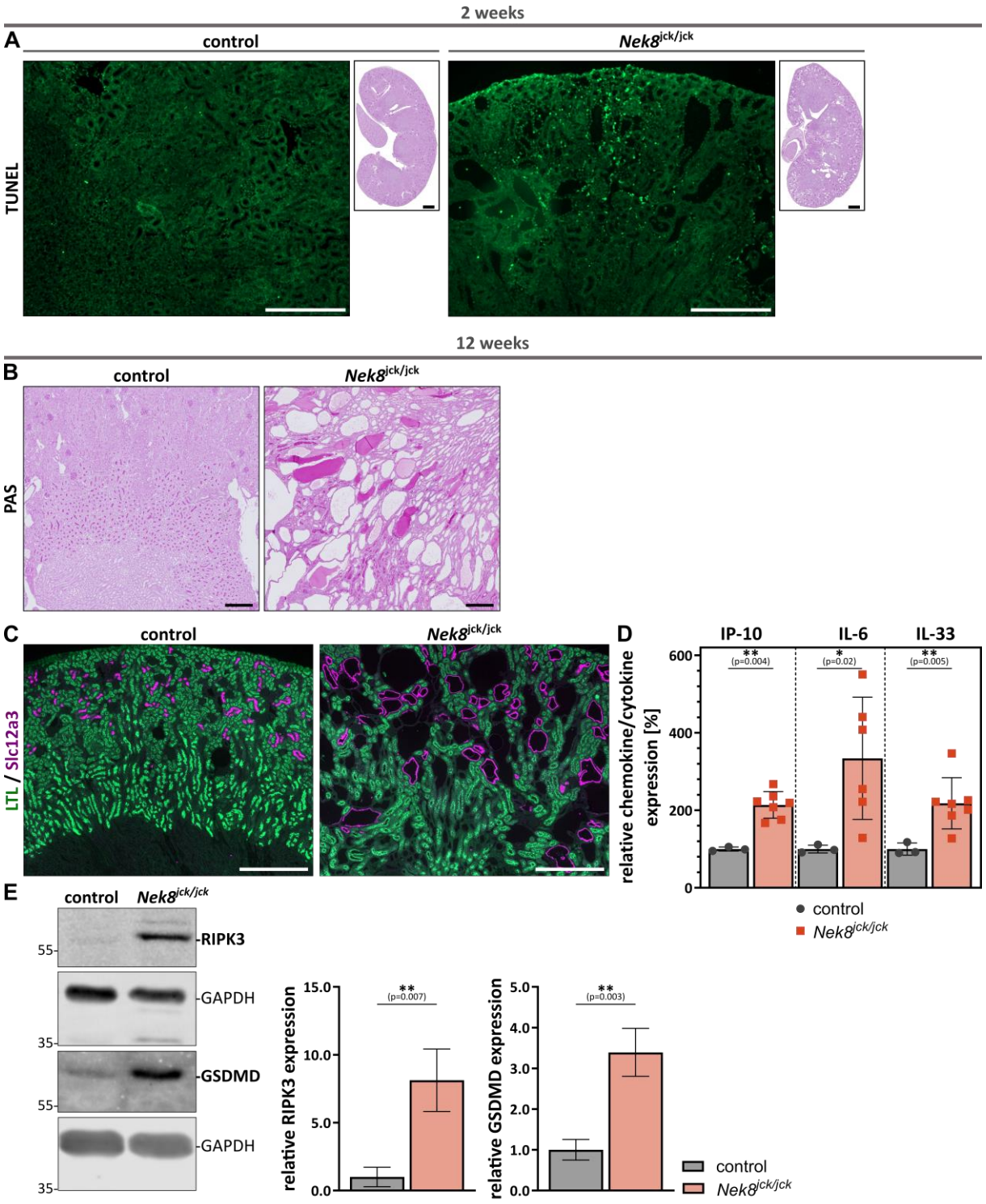
2 weeks
A
control
Nek8jck/jck
TUNEL
12 weeks
B
control
Nek8jck/jck
PAS
C
control
Nek8jck/jck
LTL / Slc12a3
D
IP-10
IL-6
IL-33
**
(p=0.004)
*
(p=0.02)
**
(p=0.005)
relative chemokine/cytokine expression [%]
600
400
200
0
control
Nek8jck/jck
E
control
Nek8jck/jck
55
RIPK3
GAPDH
35
55
GSDMD
GAPDH
35
relative RIPK3 expression
15.0
10.0
5.0
0.0
**
(p=0.007)
relative GSDMD expression
5.0
4.0
3.0
2.0
1.0
0.0
**
(p=0.003)
control
Nek8jck/jck

Figure 1

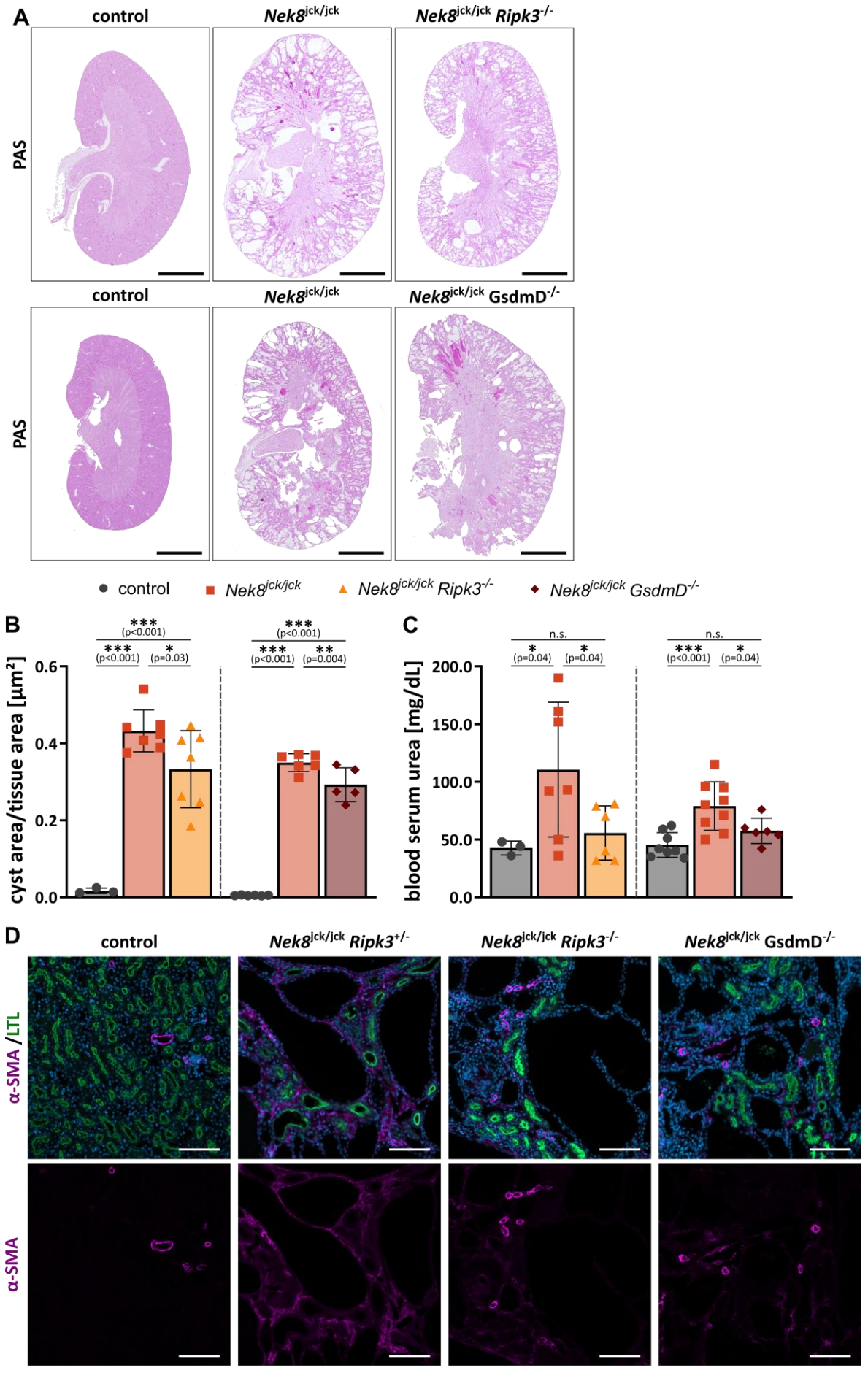
A
control
Nek8jck/jck
Nek8jck/jck Ripk3-/-
PAS
control
Nek8jck/jck
Nek8jck/jck GsdmD-/-
PAS
control
Nek8jck/jck
Nek8jck/jck Ripk3-/-
Nek8jck/jck GsdmD-/-
B
cyst area/tissue area [µm²]
0.6
0.4
0.2
0.0
***
(p<0.001)
***
(p<0.001)
*
(p=0.03)
***
(p<0.001)
***
(p<0.001)
**
(p=0.004)
C
blood serum urea [mg/dL]
200.0
150.0
100.0
50.0
0.0
n.s.
*
(p=0.04)
*
(p=0.04)
n.s.
***
(p<0.001)
*
(p=0.04)
D
control
Nek8jck/jck Ripk3+/-
Nek8jck/jck Ripk3-/-
Nek8jck/jck GsdmD-/-
α-SMA /LTL
α-SMA

Figure 2

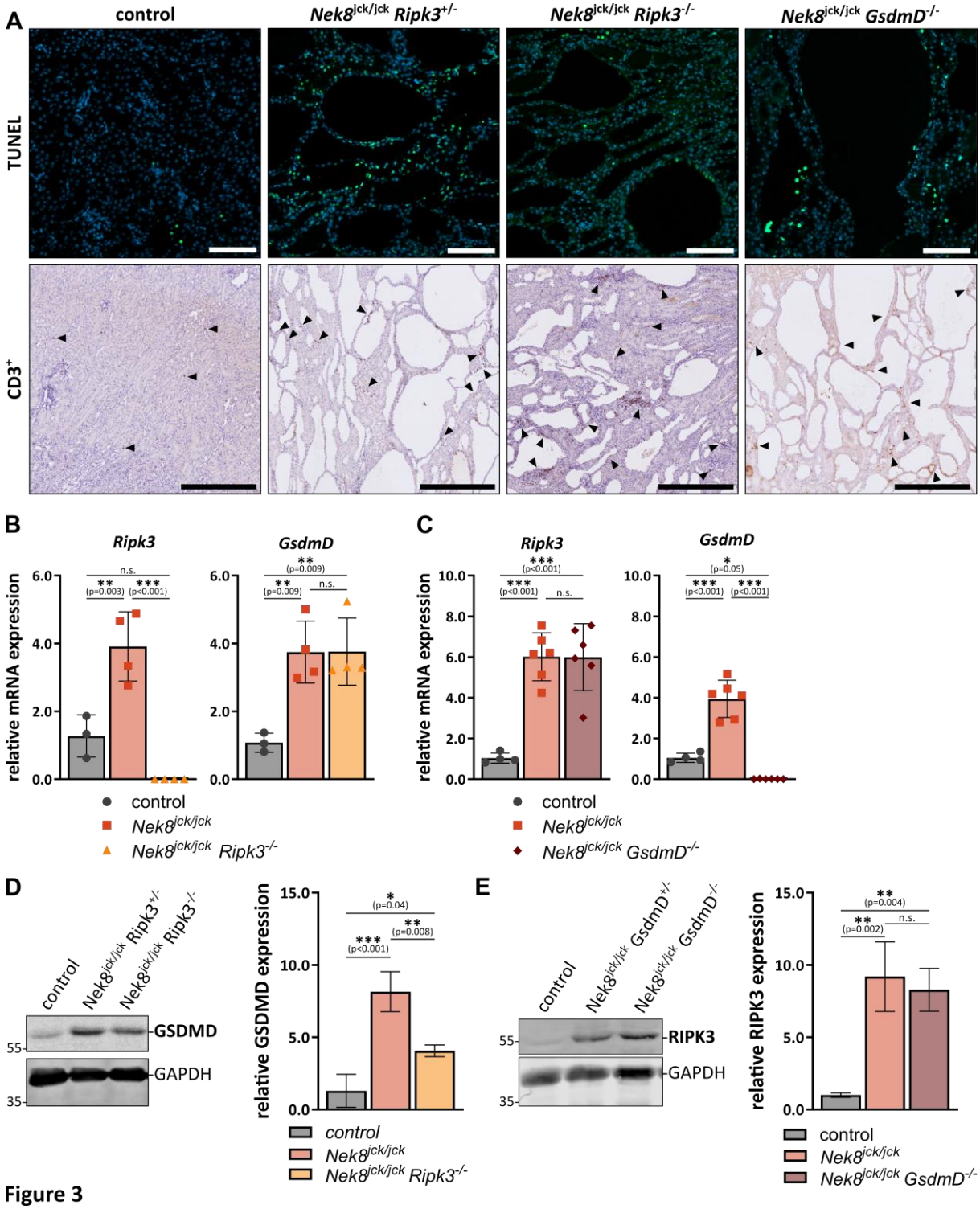
A
control
Nek8jck/jck Ripk3+/-
Nek8jck/jck Ripk3-/-
Nek8jck/jck GsdmD-/-
TUNEL
CD3+
B
Ripk3
GsdmD
relative mRNA expression
control
Nek8jck/jck
Nek8jck/jck Ripk3-/-
C
Ripk3
GsdmD
relative mRNA expression
control
Nek8jck/jck
Nek8jck/jck GsdmD-/-
D
control
Nek8jck/jck Ripk3+/-
Nek8jck/jck Ripk3-/-
GSDMD
GAPDH
relative GSDMD expression
control
Nek8jck/jck
Nek8jck/jck Ripk3-/-
E
control
Nek8jck/jck GsdmD+/-
Nek8jck/jck GsdmD-/-
RIPK3
GAPDH
relative RIPK3 expression
control
Nek8jck/jck
Nek8jck/jck GsdmD-/-

Figure 3

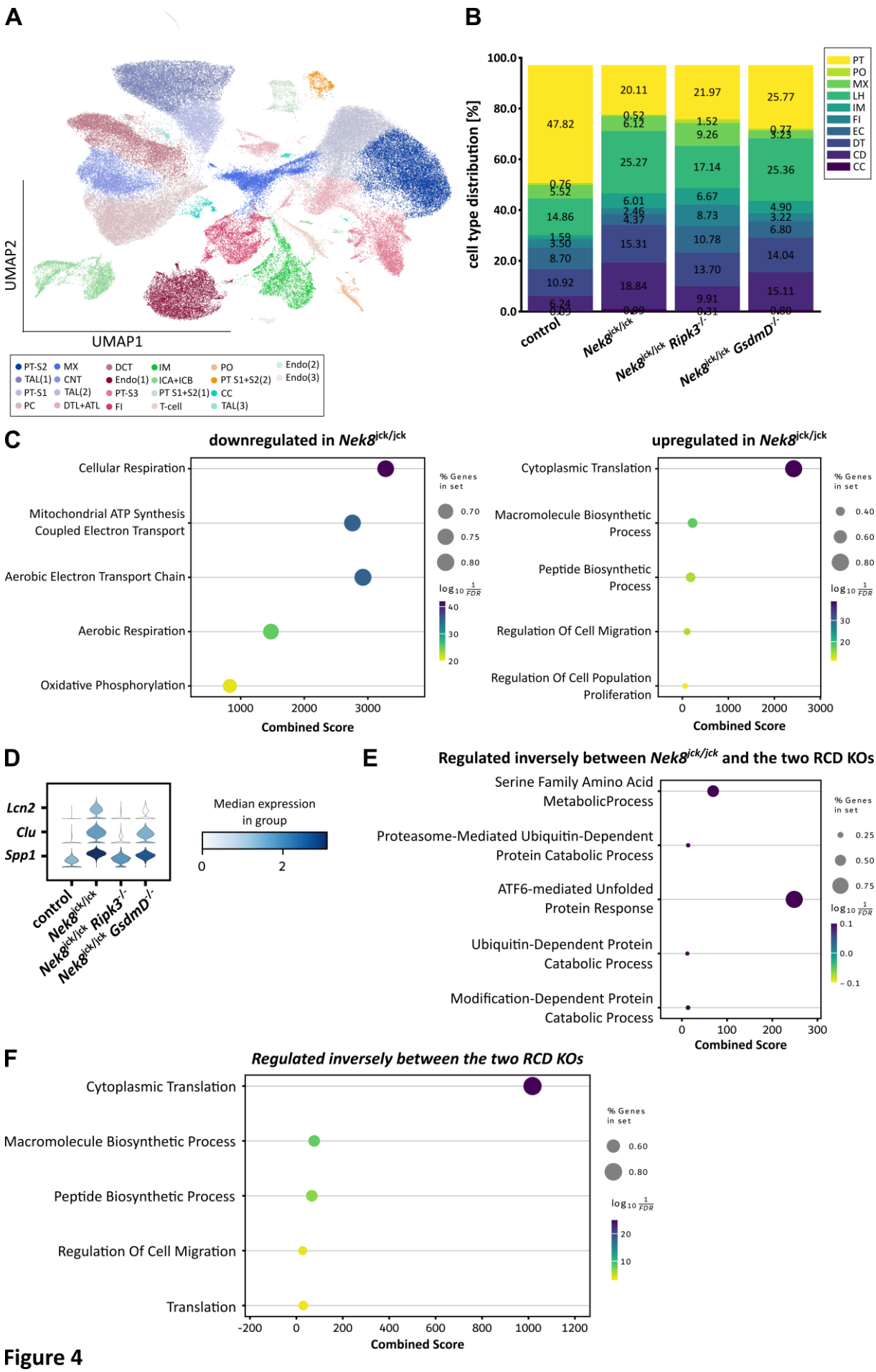
A
UMAP2
UMAP1
PT-S2
MX
DCT
IM
PO
Endo(2)
TAL(1)
CNT
Endo(1)
ICA+ICB
PT S1+S2(2)
Endo(3)
PT-S1
TAL(2)
PT-S3
PT S1+S2(1)
CC
PC
DTL+ATL
FI
T-cell
TAL(3)
B
cell type distribution [%]
control
Nek8jck/jck
Nek8jck/jck Ripk3-/-
Nek8jck/jck GsdmD-/-
PT
PO
MX
LH
IM
FI
EC
DT
CD
CC
C
downregulated in Nek8jck/jck
Cellular Respiration
Mitochondrial ATP Synthesis Coupled Electron Transport
Aerobic Electron Transport Chain
Aerobic Respiration
Oxidative Phosphorylation
Combined Score
% Genes in set
upregulated in Nek8jck/jck
Cytoplasmic Translation
Macromolecule Biosynthetic Process
Peptide Biosynthetic Process
Regulation Of Cell Migration
Regulation Of Cell Population Proliferation
D
Lcn2
Clu
Spp1
Median expression in group
E
Regulated inversely between Nek8jck/jck and the two RCD KOs
Serine Family Amino Acid MetabolicProcess
Proteasome-Mediated Ubiquitin-Dependent Protein Catabolic Process
ATF6-mediated Unfolded Protein Response
Ubiquitin-Dependent Protein Catabolic Process
Modification-Dependent Protein Catabolic Process
F
Regulated inversely between the two RCD KOs
Translation

Figure 4

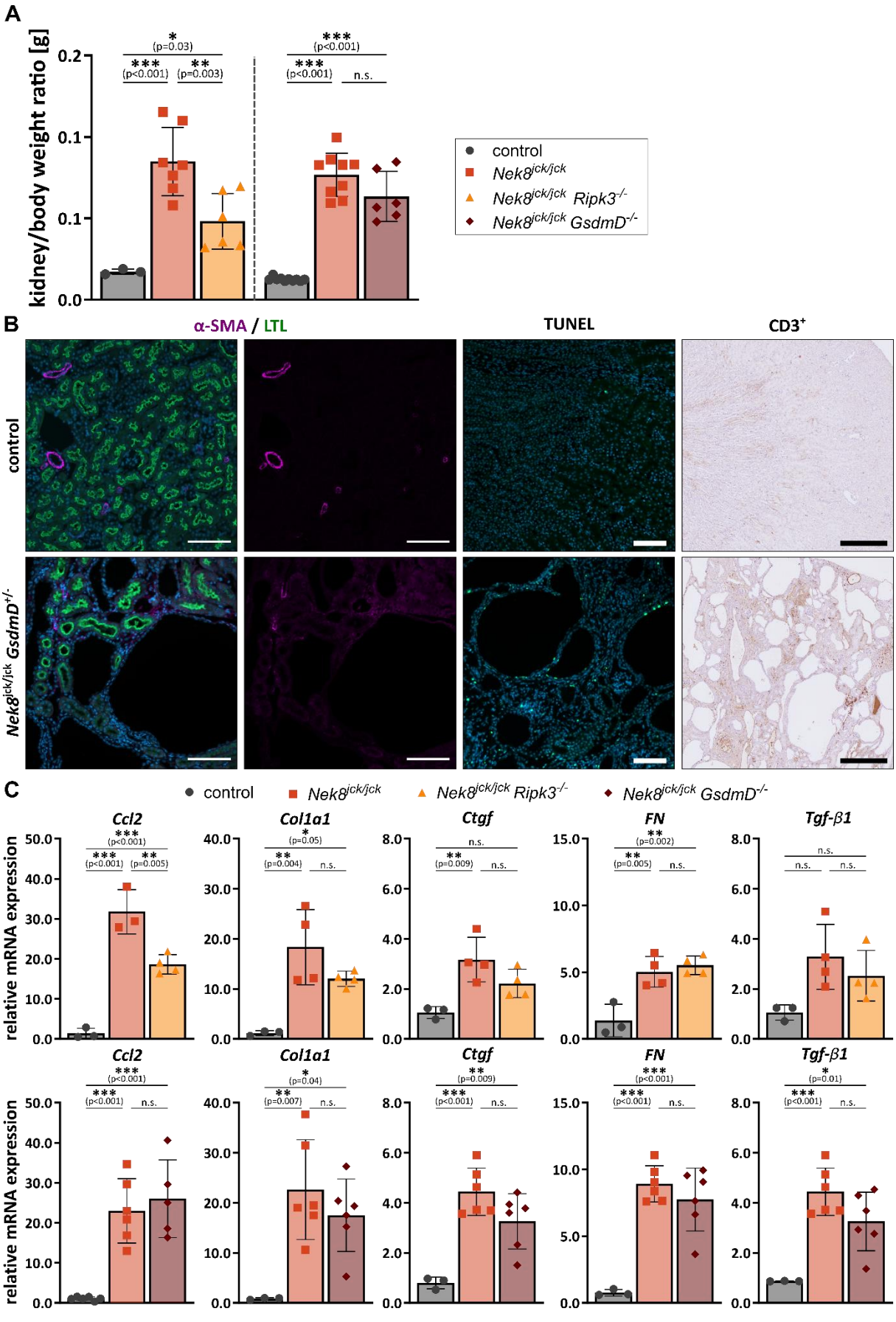

Supplementary figure 1

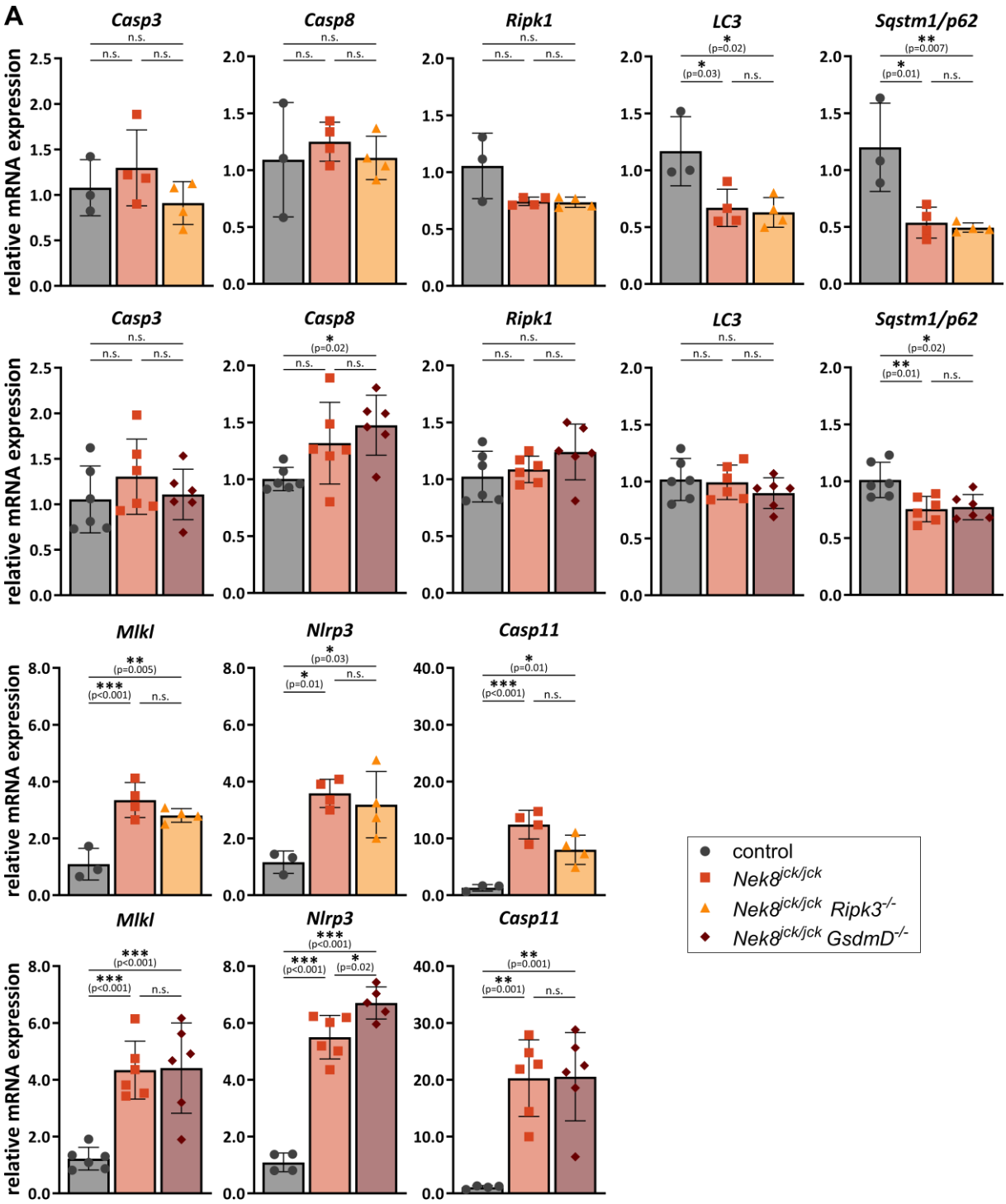

Supplementary figure 2

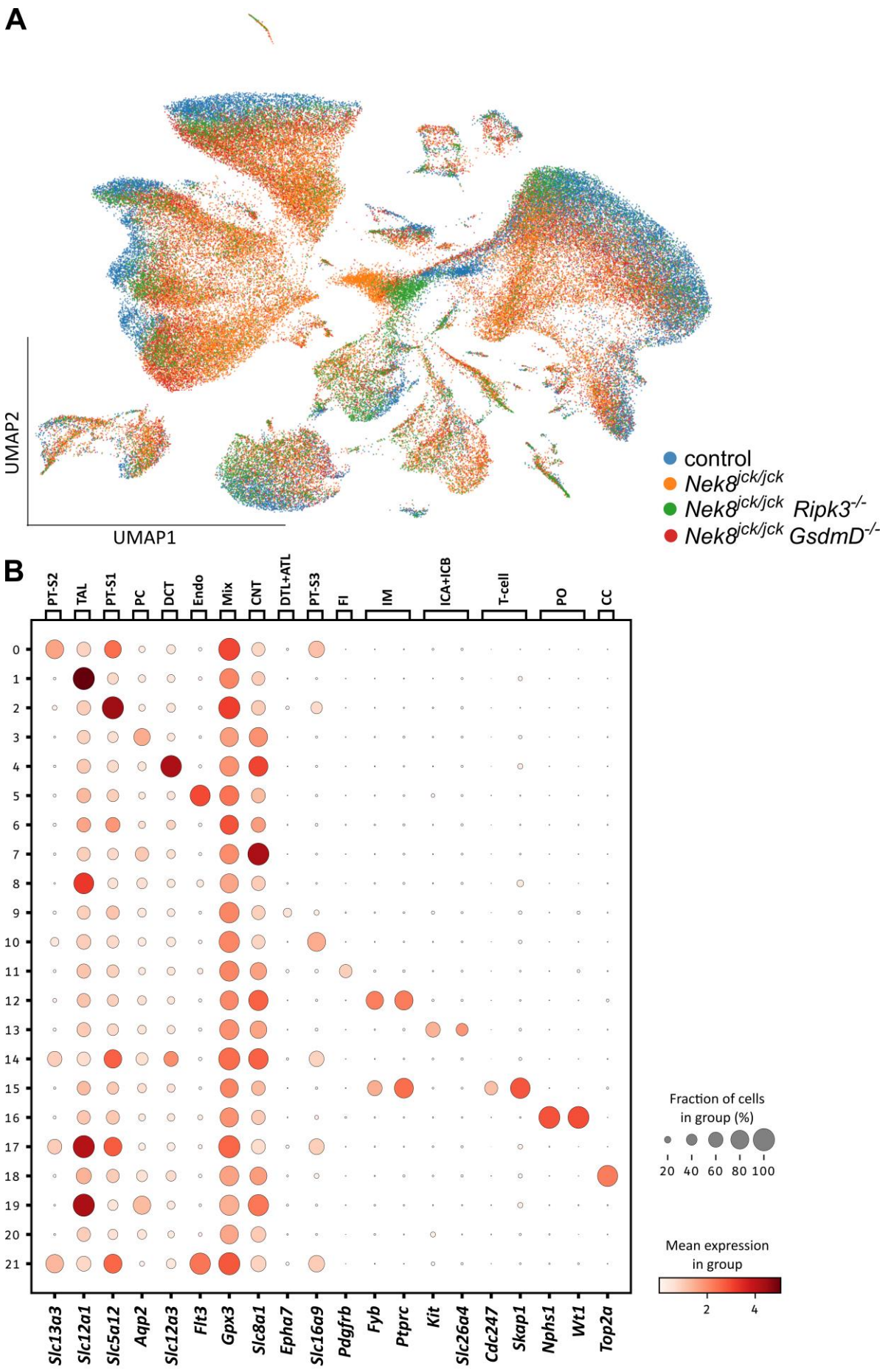

Supplementary figure 3

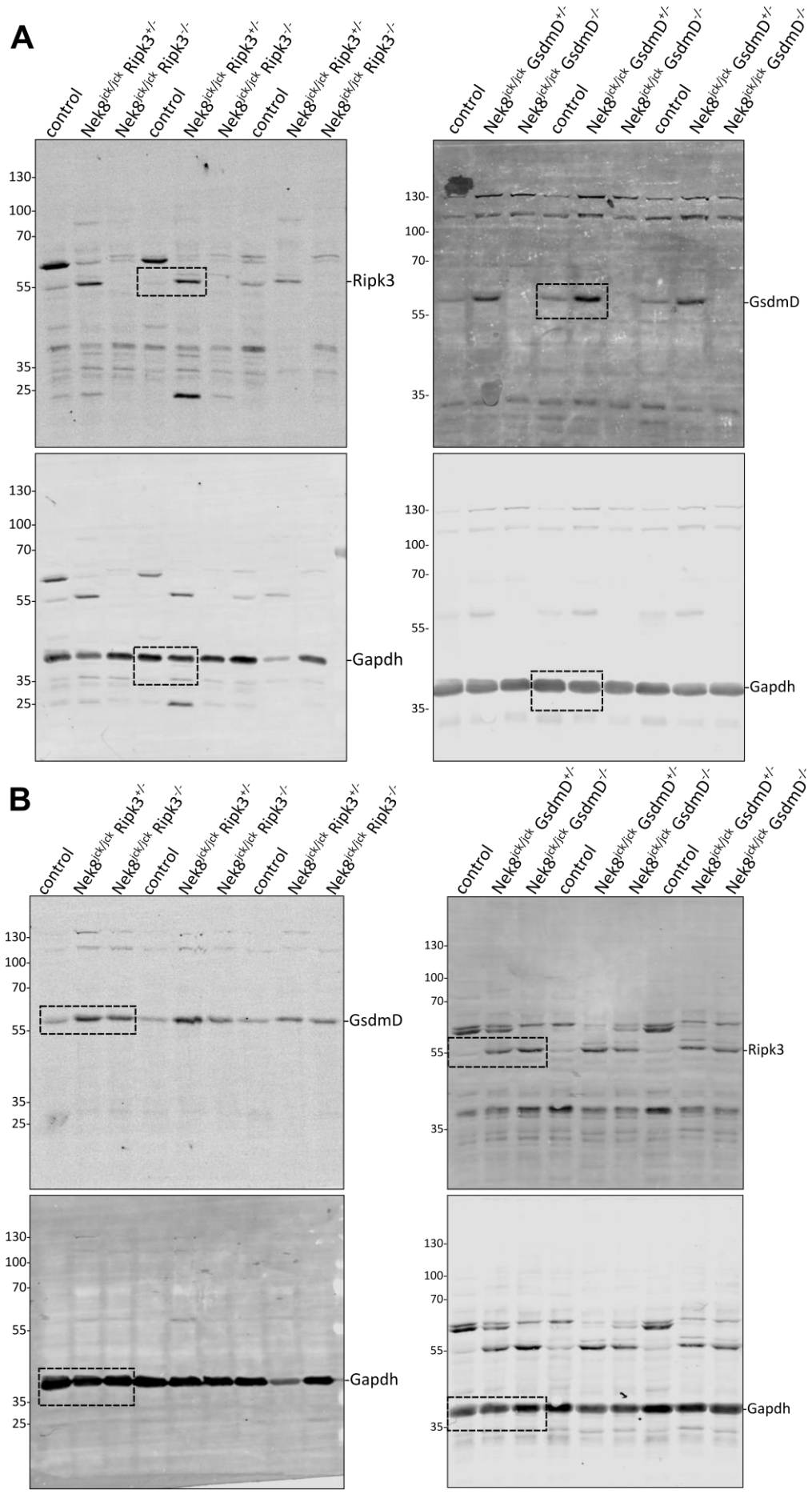

Supplementary figure 4

3.3 Chapter 3 - Loss of Bbs8 leads to cystic kidney disease in mice and affects tubulin acetylation through HDAC2

Title: Loss of Bbs8 leads to cystic kidney disease in mice and affects tubulin acetylation through HDAC2

Authors: Emilia Kieckhöfer, Peter A Matthiessen, Lena K Ebert, Christina Klausen, Dagmar Wachten, Thomas Benzing, Helen May-Simera*, Bernhard Schermer*

Status: published as a preprint in BioRxiv

Emilia Kieckhöfer, Peter A Matthiessen, Lena K Ebert, Christina Klausen, Dagmar Wachten, Thomas Benzing, Helen May-Simera*, Bernhard Schermer*. *Loss of Bbs8 leads to cystic kidney disease in mice and affects tubulin acetylation through HDAC2*. (2024) BIORXIV/583949

Our discovery of RCD as a significant factor in NPH raises the question of the role of RCD in additional NPH-related ciliopathies (NPH-RC). One important NPH-RC that often affects the kidney is the Bardet-Biedl Syndrome (BBS). BBS is described as an archetypical ciliopathy, with patients displaying almost all symptoms typically present in ciliopathies, such as retinopathy, polydactyl, cystic kidney disease or obesity. However, up to now, BBS mouse models are just rarely described to manifest in a kidney phenotype. Remarkably, we characterised a mouse deficient for *Bbs8* and could show the development of late-onset cystic kidney disease, displaying slow progressing cyst formation at 46 weeks of age. Due to the late-onset and the rather mild phenotype, we did not consider breeding with RCD knockout alleles as in Chapter 2. However, we observed inflammation and fibrosis similar to the *Nphp9*/*Nek8*^{jck} model at earlier time points. In contrast, the inflammation in *Bbs8*$^{-/-}$ mice potentially occurs systemically and supports the symptoms caused by the ciliary defect, as the kidney phenotype is accompanied by significant obesity and non-alcoholic fatty liver disease (NAFLD). Thus, we cannot exclude that systemic proinflammatory signalling influences RCD in the kidneys of these mice. Expression analysis in these kidneys revealed key genes of pyroptosis more strongly deregulated than those of necroptosis. Unbiased proteomic analyses of those kidneys revealed increased expression of histone deacetylase 2 (HDAC2) and a subsequent reduction of tubulin acetylation in the axoneme of the primary cilium, which could be confirmed *in vitro* in

MEFs derived from those mice. The lack of alpha-tubulin acetylation typically destabilizes primary cilia, which could explain the late cystic phenotype and might provide a link to understand deregulated RCD in this model.

Author contributions:

Emilia Kieckhöfer	performed experiments (Figure 1-3, Supplementary) analysis of *in vitro* data (MEFs) created the final figures and wrote the manuscript
Peter A Matthiessen	performed experiments with MEF cells
Lena K Ebert	performed the interactome and related proteomic analyses
Christina Klausen	generation of MEF cell line
Dagmar Wachten	revised the manuscript
Thomas Benzing	supported the study design; revised the manuscript
Helen May-Simera	provided the mouse model and revised the manuscript
Bernhard Schermer	designed the study, supervised the writing of the manuscript, and revised it for the final version

Loss of Bbs8 leads to cystic kidney disease in mice and affects tubulin acetylation through HDAC2

Emilia Kieckhöfer[1,2], Peter A. Matthiessen[3], Lena K. Ebert[1,2], Christina Klausen[4], Dagmar Wachten[4], Thomas Benzing[1,2], Helen May-Simera[3,*], Bernhard Schermer[1,2,*,§]

[1] *Department II of Internal Medicine and Center for Molecular Medicine Cologne, University of Cologne, Faculty of Medicine and University Hospital Cologne, Cologne, Germany*

[2] *Cologne Excellence Cluster on Cellular Stress Responses in Aging-Associated Diseases (CECAD), University of Cologne, Faculty of Medicine and University Hospital Cologne, Cologne, Germany*

[3] *Faculty of Biology, Ciliary Cell Biology Institute of Molecular Physiology, Johannes Gutenberg-University, Mainz, Germany*

[4] *Institute of Innate Immunity, Biophysical Imaging, Medical Faculty, University of Bonn, Bonn, Germany.*

**** These authors contributed equally***

[§]***corresponding author:*** bernhard.schermer@uk-koeln.de

Keywords: BBS, primary cilium, kidney, ciliopathies, cysts, HDAC2

Abstract

Bardet-Biedl Syndrome (BBS) is a genetic disorder marked by considerable genetic and phenotypic diversity. BBS often presents as a combination of retinitis pigmentosa, obesity, polydactyly, and cystic kidney disease and is considered a model ciliopathy. The syndrome is caused by pathogenic variants in BBS genes, some of which encode components of a ciliary multi-protein complex, known as the BBSome, as well as a chaperonin-like complex, which is required for BBSome assembly. In this study, we describe the occurrence of kidney cysts in a BBS mouse model. Specifically, loss of BBS8 led to the development of cystic kidney disease by the end of the first year of life. In addition to transcriptional changes of key genes involved in regulated cell death and inflammation, proteomic approaches revealed increased expression and altered phosphorylation of histone deacetylase HDAC2 in knockout kidneys. Consistently, loss of *Bbs8* resulted in a reduction of acetylated alpha-tubulin in primary cilia. This leads to diminished stability and altered dynamics of primary cilia, potentially contributing to the formation of cystic kidneys and other BBS manifestations previously described in *Bbs8* deficient mice.

Introduction

The primary cilium is a specialized microtubule-based sensory organelle that extends from the surface of most mammalian cells (Pazour and Bloodgood, 2008). It consists of the axoneme, ensheathed by the ciliary membrane, the transition zone and the basal body, which anchors the cilium to the cell body. The transition zone, located between the basal body and the main ciliary shaft, is critical for protein trafficking to and from the ciliary compartment (Reiter, Blacque and Leroux, 2012; Garcia-Gonzalo and Reiter, 2017). Stringent regulation of the protein composition is required for cilia to function as a hub for chemo- and mechano-transduction, as well as signaling (Reiter, Blacque and Leroux, 2012) and as such, primary cilia play a pivotal role in modulating various signaling pathways, e.g. Hedgehog, Wnt, and TGF-β signaling (Fan and Tessier-Lavigne, 1994; Munsterberg *et al.*, 1995; Pourquié *et al.*, 1996). Unlike any other organelle, cilia periodically disappear during the mitotic cell cycle: When cells re-enter mitosis, cilia are typically disassembled to subsequently release the basal body, a modified mother centriole, to serve as microtubule organizing centers at the spindle poles. Disassembly of cilia mechanistically involves the deacetylation and thus destabilization of microtubules among others (Pugacheva *et al.*, 2007; Gopalakrishnan *et al.*, 2023). It is well established that pathogenetic variants in proteins, which alter the structure or function of cilia, lead to a heterogeneous group of genetic diseases and syndromes referred to as ciliopathies (Hildebrandt, Benzing and Katsanis, 2011). Ciliopathies comprise a diverse group of genetic disorders with overlapping manifestations in different organs and tissues, such as the brain, eye, skeleton, liver, vasculature and kidney (Forsythe and Beales, 2013; Reiter and Leroux, 2017). Thereby, cystic and fibrotic kidney disease is a common occurrence among many ciliopathies, leading to the frequent classification of a significant

subgroup, namely the renal ciliopathies (Hildebrandt and Zhou, 2007; McConnachie, Stow and Mallett, 2021).

The Bardet-Biedl-Syndrome (Bardet, 1995; Biedl, 1995; Laurence and Moon, 1995) is an archetypical autosomal-recessive ciliopathy characterized by obesity, retinopathy, polydactyly and kidney disease (Forsythe and Beales, 2013). This syndrome is caused by mutations in BBS genes leading to pathogenetic variants of BBS proteins. BBS proteins can be classified according to the particular protein complex they are part of. The so called BBSome complex (Nachury *et al.*, 2007; Loktev *et al.*, 2008) (BBS1, BBS2, BBS4, BBS5, BBS7, BBS8, BBS9, BBS18) is required for trafficking of ciliary membrane proteins. The 2nd group of BBS proteins build the chaperonin-like complex (BBS6, BBS10 and BBS12), which catalyzes the assembly of the BBSome (Seo *et al.*, 2010). The remaining BBS proteins have varying specific functions but are ultimately thought to influence ciliary trafficking.

Studies on various *Bbs* mutant mice, including *Bbs1*^{M390R} transgenic, *Bbs2*$^{-/-}$, *Bbs4*$^{-/-}$, *Bbs5*$^{-/-}$, *Bbs6*$^{-/-}$, *Bbs8*$^{-/-}$ and *Bbs10*$^{-/-}$, revealed significant parallels to human disease. These mice exhibit a broad spectrum of vision impairment, obesity, male fertility impairment, and neurological deficits (Kulaga *et al.*, 2004; Mykytyn *et al.*, 2004; Nishimura *et al.*, 2004; Fath *et al.*, 2005; Davis *et al.*, 2007; Rahmouni *et al.*, 2008; Seo *et al.*, 2009; Cognard *et al.*, 2015; Bentley-Ford *et al.*, 2021). For BBS10, total body knockout resulted in renal abnormalities primarily affecting glomeruli and podocytes without any cyst formation, while a tubular epithelial cell-specific knockout did not show any overt phenotype (Cognard *et al.*, 2015). Cyst formation has been observed in *Bbs2*$^{-/-}$ and *Bbs4*$^{-/-}$ mice, but again primarily affecting glomeruli (Nishimura *et al.*, 2004; Guo *et al.*, 2011). Loss of *Bbs8* has so far shown to cause the most severe retinal phenotype in mice (Tadenev *et al.*, 2011; Dilan *et al.*, 2018; Schneider *et al.*, 2021), which is not only caused by ciliary defects of photoreceptor cells themselves but also due to ciliary defects in the adjacent retinal pigmental epithelial cells (RPE) (Kretschmer *et al.*, 2019, 2023; Schneider *et al.*, 2021). The severity of *Bbs8* loss is likely due to the fact that BBS8 is one of the key components of the BBSome. BBS8 (TTC8) is a tetratricopeptide repeat (TPR) protein with a critical role in planar cell polarity and laterality (May-Simera *et al.*, 2010, 2015). Loss of *Bbs8* leads to changes in the composition of the octameric BBSome complex, where BBS8 is a direct interactor of the scaffold protein BBS9 (Zhang *et al.*, 2012).

Until now, research into BBS8's function has predominantly focused on embryonic development and ocular health, leaving its specific role in cilia maintenance within the kidney and in preserving kidney architecture and function largely unexplored. In this study, we report on tubular cystic and fibrotic kidney disease in adult mice deficient in *Bbs8*. We further provide evidence for cell death and inflammation in these kidneys. An unbiased proteomic analysis of kidney tissue revealed alterations in protein expression and phosphorylation, including increased levels of HDAC2, which we also found to

co-precipitate with BBS8. Increased HDAC2 levels upon loss of *Bbs8* also resulted in deacetylation of ciliary microtubules and impaired ciliary stability, which we suggest might be contributing to BBS pathomechanisms.

Methods

Mouse lines

Bbs8$^{-/-}$ mice have been previously described (Tadenev *et al.*, 2011). All animals were housed and handled, and animal studies conducted, in accordance with approved institutional animal care and use committee procedures. All experiments had ethical approval from the Landesuntersuchungsamt Rheinland-Pfalz and were performed in accordance with institutional guidelines for animal welfare, German animal protection law and the guidelines given by the ARVO Statement for the Use of Animals in Ophthalmic and Vision Research. Animal maintenance and handling were performed in line with the Federation for Laboratory Animal Science Associations (FELASA) recommendations. Animals were housed in a 12 h light/dark cycle with food and water available ad libitum. For the preparation, mice were weighted, followed by cervical dislocation; blood was collected prior to the perfusion of the kidney with PBS through the aorta. Further, other organs and fat tissue were taken and, as the kidney, processed by fixation in 4 % formaldehyde and embedded in paraffin as well as snap-frozen for further tissue analysis. The blood was incubated for 2 h at RT, followed by centrifugation. Serum creatinine levels were measured by the Institute of Clinical Chemistry, University Hospital of Cologne, Germany.

Immunohistology

For histological analysis, tissue was cut into 2-µm-thick sections and deparaffinized by xylene treatment and rehydration in graded ethanol. For PAS staining the sections were stained with 0,9 % periodic acid (cat# 3257.1, Roth) and Schiffsches Reagent (cat#1.09033, Merck) both for 10 min embedded into washing steps with H_2O. Finally, to visualize nuclei in blue, the samples were stained with Mayer's Haematoxylin for 20 s. For the Masson staining the Masson-Goldner's trichrome staining kit (cat#3459, Roth) was used and performed according to the manufacturer instructions. After dehydration of the sections, they were embedded with Histomount (HS-103, National Diagnostics).

Isolation and Immortalization of mouse embryonic fibroblasts

For the isolation of mouse embryonic fibroblasts (MEFs), timed matings were set-up with one male and two females of the desired genotype. At day 13, the pregnant mouse was anesthetized using isoflurane (Piramal Healthcare) followed by a cervical dislocation. The lower abdomen was opened by an abdominal incision to extract the two uterine horns. Embryos were isolated, transferred into a 24-well plate filled with PBS, and the head and the red organs (heart and liver) were removed. The rest of the embryo was placed into a 12-well plate filled with 2 ml ice-cold 0.25 % Trypsin/PBS (diluted from

2.5 % Trypsin, Gibco). The embryos were chopped into small pieces and incubated overnight at 4 °C. Then, the trypsin solution was discarded and the remaining Trypsin/tissue mixture was incubated for 30 min in a 37 °C water bath. Afterwards of medium (composition: DMEM/Glutamax, 10 % FCS, 1 % sodium pyruvate (100x), 1 % Pen Strep), was added, and the cell suspension was pipetted vigorously up and down to break up the digested tissue into a single cell suspension. After 1 min to allow sedimentation of the remaining tissue, the cell suspension was transferred into a new tube. This step was repeated and afterwards, the cell suspension was filtered through a 100 µm cell-strainer (Corning). Cells were plated and after 24 h, the medium was changed. Immortalization of MEFs was performed as described previously (Todaro and Green, 1963). Briefly, cells are split every three days and seeded with the same cell density. From passage three onwards, cells were seeded on at least two 10 cm culture dishes. After around 15 passages, cells started to regrow. When MEFs were immortalized, frozen back-ups were made.

Cell culture

Human embryonic kidney 293T cells (HEK293T, ATCC®) as well as wildtype and *Bbs8*$^{-/-}$ mouse embryonic fibroblasts were cultivated at 37°C and 5% CO_2. Thereby HEK293T cells were maintained in DMEM + GlutaMAX™ medium (Gibco™) supplemented with 10% fetal bovine serum (FBS, Gibco™) and MEFs in DMEM/F-12 + GlutaMAX™ medium (Gibco™) complemented with 10% FBS and 1% penicillin-streptomycin. All cell lines were tested negative for mycoplasma (PCR Mycoplasma Test Kit I/C, PromoKine). To induce ciliogenesis, cells were grown in serum-free media for 24 h. HEK293T cell transfection was performed with 2x HEBS and 0.25 M $CaCl_2$, thereby 5 µg (IP) or 6 µg (Interactome) of the F.hBBS8 pcDNA6 was used and as control, 5 µg (IP) or 6 µg (Interactome) F.EPS$^{1-225}$ pcDNA6 as negative control protein.

Co-Immunoprecipitation

Co-immunoprecipitation (Co-IP) was performed as previously described (Habbig *et al.*, 2011) using the IP Buffer (20 mM Tris, 1% (v/v) TritonX-100, 50 mM NaCl, 15 mM $Na_4P_2O_7$, 50 mM NaF, pH 7.5) supplemented with inhibitors (44 µg/µl PMSF, 2 mM Na_3VO_4). Input samples were collected, and the remaining samples were incubated with anti-FLAG M2 Beads (A2220, Sigma-Aldrich) for 2 h. Samples were lysed in 2x Laemmli (beads) and 1x Laemmli (input). For proteomic analysis, the IP Buffer was supplemented with cOmplete™ Protease Inhibitor Cocktail (Roche). Samples were ultracentrifugated (45.000 rpm, 45 min, and 4°C) before being lysed with 80% SDS in PBS. Subsequently, samples were reduced with 10 mM dithiothreitol and alkylated 40 mM chloroacetamide.

Immunofluorescence, Immunochemistry and TUNEL staining

The kidney tissue staining of 4 µm (cilia staining) and 2 µm (other stainings) fixed sections were performed as previously described (Dafinger *et al.*, 2021). The primary antibodies (NF-kB, #8242 Cell Signaling, 1:1000; CD3, MCA-1477 Biorad, 1:100; acetylated Tubulin, T6793 Sigma, 1:1000; Slc12a3, HPA028748, Sigma Aldrich, 1:500; ARL13B, 17711-1-AP ProteinTech, 1:500) were incubated overnight at 4°C, followed by incubation with secondary antibodies. For immunochemistry, the DBA kit (K3468 DAKO, 30 min for NF-kB; SK-4105 Vector, 5 min for CD3) was used and samples counterstained with Hematoxylin. For immunofluorescence, fluorophore-coupled antibodies (Jackson ImmunoResearch, 1:500: anti-mouse-Cy5, # 715-175-150; anti-rabbit A647, 711-605-152; anti-mouse-Cy3, 715-165-150; and FITC-Lotus Tetragonolobus Lectin (LTL), FL-1321-2; Vector laboratories, 1:500) were used for 1 h at RT, samples were mounted after a short incubation of Hoechst 33342 (ThermoFisher Scientific, 1:5000) with ProLong™ Diamond (ThermoFisher Scientific). The DeadEnd™ Fluorometric TUNEL System (Promega) was performed following the manufacturer's instructions, with the exception that the samples were mounted, with a pre-incubation of Hoechst with ProLong™ Diamond. MEFs were cultured on glass coverslips until confluent. Cells were fixed with 4% PFA for 10 min and washed with 1x PBS. Samples were quenched with 50 mM NH_4Cl for 10 min, before permeabilisation with 0,3% PBS-TritonX-100 for 20 min. Antibodies were diluted in Fish-Block (0.1 % (w/v) ovalbumin, 0.5 % (w/v) fish gelatine, in PBS), supplemented with 0,3% TritonX-100. The primary antibody (ARL13B 1:800; acetylated Tubulin, 1:800) were incubated overnight at 4°C followed by the secondary antibodies (anti-rabbit 488, A11034 Invitrogen, 1:400; anti-mouse 555, A31570, Invitrogen, 1:400; DAPI, Roth, 1:400). Finally, coverslips were mounted with Fluoromount-G (ThermoFisher, 00-4958-02) and imaged with the Leica microscope CTR6000, with DM6000B Laser and DFC360FX camera. MEF cell images were deconvoluted with the Leica imaging software LASX. Cilia number and length were determined with the open-source Fiji software.

Cyst index analysis

The cyst index was calculated for whole slide images using open-source software for bioimage analysis QuPath (v0.4.0) (Bankhead *et al.*, 2017). Cysts were detected using an Artificial Neural Network-based pixel classifier. Initially detected cysts were filtered for the minimal area of 400 µm² and a minimum circularity value of 0.35. Plots were generated using the Plots of Data web app (Postma and Goedhartid, 2019). For statistical analysis, all results were normalized to the control followed by a two-tailed Student's t-test ($p<0.05$).

Immunoblotting

Confluent grown MEF cells were starved 24 h prior to harvest with 200 µl RIPA buffer (50 mM Tris HCl, 150 mM NaCl, 1% (v/v) NP-4O, 0.5% (w/v) Sodium deoxycholate, 0.1% (w/v) SDS), supplemented with 1% Halt Protease and Phosphatase Inhibitor Cocktail (Thermo Scientific™) (Brücker *et al.*, 2023). Cells were lysed on ice and sonicated for 2 s. Protein concentration of lysates was determined and 70 µg protein was loaded onto a 10% SDS-PAGE and subsequently transferred to a PVDF-FL membrane (Millipore). Membranes were incubated overnight at 4°C in primary antibodies (Flag, F7425, Sigma-Aldrich, 1:1000; HDAC2, ab32117 Abcam, 1:1000; acetylated Tubulin, T6793 Sigma, 1:1000; Calnexin, 10427-2 AP ProteinTech, 1:1000). Secondary antibodies were incubated for 1 h at RT (Li-COR Biosciences IRDye680 and IRDye800 1:10.000: rb680, 925-68073; mm680, 925-68072; rb800, 925-32213). Signals were visualized using the Odyssey Infrared Imaging System 2800 (Li-COR).

Phospho- and proteome analysis

For each biological replicate a quarter of kidney tissue was used and dounced with a Wheaton Dounce tissue grinder in urea buffer (8 M Urea, 50 mM ammonium bicarbonate) supplemented with Halt protease-phosphatase-inhibitor cocktail (Thermo Scientific™). After clearing of the sample (16.000 xg, 1 h at 4°C), the lysates were reduced (10 mM dithiothreitol), alkylated (50 mM chloroacetamide) and digested (LysC; 1:75). Samples (800 µg) were diluted to 2 M urea and subjected to tryptic digestion (1:50). After overnight incubation, phosphoenrichment was performed in the CECAD proteomics facility using the Thermo Scientific™ Kit High Select TiO2 Kit (#A32993). All samples were analyzed as well by the CECAD proteomics facility on a Q Exactive Plus Orbitrap mass spectrometer that was coupled to an EASY nLC (both Thermo Scientific™). Peptides were loaded with solvent A (0.1% formic acid in water) onto an in-house packed analytical column (50 cm, 75 µm inner diameter, filled with 2.7 µm Poroshell EC120 C18, Agilent). Peptides were chromatographically separated at a constant flow rate of 250 nL/min using the following gradient: 3-5% solvent B (0.1% formic acid in 80 % acetonitrile) within 1.0 min, 5-30% solvent B within 121.0 min, 30-40% solvent B within 19.0 min, 40-95% solvent B within 1.0 min, followed by washing and column equilibration. The mass spectrometer was operated in data-dependent acquisition mode. The MS1 survey scan was acquired from 300-1750 m/z at a resolution of 70,000. The top 10 most abundant peptides were isolated within a 1.8 Th window and subjected to HCD fragmentation at a normalized collision energy of 27%. The AGC target was set to 5e5 charges, allowing a maximum injection time of 55 ms. Product ions were detected in the Orbitrap at a resolution of 17,500. Precursors were dynamically excluded for 25.0 s. All mass spectrometric raw data were processed with MaxQuant (Tyanova, Temu and Cox, 2016) (version 2.2.0.0) using default parameters against the UniProt canonical murine database (UP10090, downloaded 20.01.2023) with the match-between-runs option enabled between replicates. Samples were sorted into two parameter

groups, either containing the enriched or non-enriched samples. Enriched samples had the phosphorylation (STY) variable modification added, whereas non-enriched samples were quantified by LFQ. A follow-up analysis was done in Perseus 1.6.15 (Tyanova *et al.*, 2016). Results were cleaned up by removing hits from the decoy database, the contaminant list and, in case of non-enriched fractions, those only identified by modified peptides were removed. Afterwards, results were filtered for data completeness in at least one condition and LFQ values (WP) or intensities (PP), imputed using sigma downshift with standard settings. Finally, FDR-controlled two-sided t-tests between sample groups were performed (S0=0, FDR≤0.05) as well as a 1D enrichment using Perseus (version 1.6.15.0).

Interactome

Samples were analyzed by the CECAD Proteomics Facility on an Orbitrap Exploris 480 (Thermo Scientific, granted by the German Research Foundation under INST 1856/71-1 FUGG) mass spectrometer equipped with a FAIMSpro differential ion mobility device that was coupled to an Vanquish neo in trap-and-elute setup (Thermo Scientific). Samples were loaded onto a precolumn (Acclaim 5µm PepMap 300 µ Cartridge) with a flow of 60 µl/min before reverse-flushed onto an in-house packed analytical column (30 cm length, 75 µm inner diameter, filled with 2.7 µm Poroshell EC120 C18, Agilent). Peptides were chromatographically separated with an initial flow rate of 400 nL/min and the following gradient: initial 2% B (0.1% formic acid in 80 % acetonitrile), up to 6 % in 3 min. Then, flow was reduced to 300 nl/min and B increased to 20% B in 26 min, up to 35% B within 15 min and up to 98% solvent B within 1.0 min while again increasing the flow to 400 nl/min, followed by column wash with 98% solvent B and re-equilibration to initial condition. The FAIMS pro was operated at -50V compensation voltage and electrode temperatures of 99.5 °C for the inner and 85 °C for the outer electrode. The mass spectrometer was operated in data-dependent acquisition top 24 mode with MS1 scans acquired from 350 m/z to 1400 m/z at 60k resolution and an AGC target of 300%. MS2 scans were acquired at 15 k resolution with a maximum injection time of 22 ms and an AGC target of 300% in a 1.4 Th window and a fixed first mass of 110 m/z. All MS1 scans were stored as profile, all MS2 scans as centroid. All mass spectrometric raw data were processed with Maxquant (version 2.4) (Tyanova, Temu and Cox, 2016) using default parameters against the Uniprot HUMAN canonical database (UP5640) with the match-between-runs option enabled between replicates. Follow-up analysis was done in Perseus 1.6.15 (Tyanova *et al.*, 2016). Protein groups were filtered for potential contaminants and insecure identifications. Remaining IDs were filtered for data completeness in at least one group and missing values imputed by sigma downshift (0.3 σ width, 1.8 σ downshift). Afterwards, FDR-controlled two-sided t-tests were performed (S0=0, FDR≤0.05).

Quantitative real-time PCR

RNA isolation from kidney tissue, one-quarter of a kidney was ground with BeadBeater (Roth) using a Precelly24 with 5.000 rpm two times for 30 s in Tri-Reagent. RNA extraction was performed with the Direct-zol RNA Miniprep kit (Zymo Research) following the manufacturer's instructions, including a DNase1 treatment step. Before the reverse transcription using the High-Capacity cDNA Reverse Transcription kit (Applied Biosystems, 4368814), RNA concentration and sample quality were assessed on a Nanodrop spectrophotometer (Peqlab). mRNA was assessed by SYBR Green (Thermo Scientific™, 4309155) qPCR using mHprt1 as endogenous control. Primers are listed in the supplementary table S1. The qPCR experiments were performed on a QuantStudio 12K Flex Real-time PCR System (ThermoFisher Scientific). For data analysis, all results were normalized to the housekeeping gene *Hprt1* using the delta-delta CT followed by a two-tailed Student's t-test ($p<0.05$).

IL-6 Elisa

Mouse IL-6 Uncoated ELISA kit (cat# 88-7064; Invitrogen) was used to measure Interleukin-6 concentrations of mouse tissue lysates. If not stated otherwise, the ELISA plate was prepared, and the assay was conducted after manufacturer’s instructions. For all washing steps 1x PBS supplemented with 0.05% Tween™20 was used. To lyse tissue, approx. 10 mg of snap-frozen tissue was cut into small pieces on dry ice before adding 200 µl of lysis buffer (200 mM NaCl, 10 mM Tris-HCl pH=7.4, 5 mM EDTA, 1% NP-40, 1% Halt Protease-Phosphatase inhibitor (Thermo Scientific™). Tissue was homogenized using a Disruptor Genie Digital (Scientific Industries; SI-DD38). Therefore, the tubes were filled halfway with pre-chilled glass beads and the samples were homogenized with eight 1 min runs at 2.640 rpm, placing the samples on ice in between runs. Kidney tissue was additionally homogenized using a pellet pestle, before all lysates were incubated for further 30 min on ice. Samples were spun down at 21.130 x g and 4°C for 10 min, the supernatant was transferred into a fresh reaction tube and protein concentration was determined via BCA assay. Following amounts of protein were loaded in triplicates and incubated overnight at 4°C: Kidney 300 µg; Liver 300 µg; Fat 125 µg. Sulphuric acid (2 N) was used to stop the colorimetric reaction of Avidin-HRP, before measuring the absorbance at 450 nm and 570 nm, for wavelength subtraction, using the TECAN Spark microplate reader (TECAN).

Quantification and statistical analysis

Data are expressed as mean ± standard deviation (SD). All experiments were performed in at least 3 independent biological replicates. The data were statistically analysed with GraphPad Prism version 9.5.1 unless otherwise mentioned.

Results

Cystic kidney disease in Bbs8 knockout mice

To investigate the function of BBS8 in the kidney, we analyzed kidneys of a conventional *Bbs8* knockout mouse line (Tadenev *et al.*, 2011). Kidney tissue did not show any obvious phenotypic alterations by 24 weeks, so we continued monitoring the mice until 46 weeks of age. At this age *Bbs8*$^{-/-}$ animals displayed significant obesity, with a body weight approximately 30% higher than in control **(Fig.1 A, B)**, a common BBS phenotype. Remarkably, loss of *Bbs8* significantly affected the kidneys at this age, as indicated by the small increase in kidney weight **(Fig.1 C),** as well as slightly elevated although not significantly altered blood urea levels **(Fig.1 D)**. PAS staining of kidney tissue revealed cyst formation and dilated tubules **(Fig.1 E/F)** and, remarkably, the cystic index used to quantify cyst formation was 6-fold higher in *Bbs8*$^{-/-}$ as compared to control mice **(Fig.1 G)**. Further analysis revealed that the size of individual cysts detected in *Bbs8*$^{-/-}$ was similar to dilated tubules and cysts from age-related dilated tubules of control animals **(Supp. Fig.1),** however the number of these cysts was significantly increased. Staining for proximal and distal tubules in the kidney revealed that the majority of cysts originated from distal tubules, as they were positive for Slc12a3 **(Fig.1 H)**. Interestingly, in keeping with the theory that BBS proteins are typically not essential for ciliogenesis per se, but rather for the sustained maintenance of cilia, epithelial cells of kidney tubules in *Bbs8*$^{-/-}$ mice exhibited primary cilia on their apical surface, even within dilated or cystic areas **(Supp. Fig.3)**. Taken together, *Bbs8* knockout mice, in addition to obesity, fatty liver disease, retinal degeneration, and occasional polydactyly, exhibit cystic kidney disease by 46 weeks of age, where cyst formation predominantly originates from the distal tubular segments.

Cell death and fibrosis in cystic kidneys of Bbs8 knockout mice

Bbs8$^{-/-}$ kidneys showed a significant increase in fibrosis, as visualized by Masson's trichrome staining, which indicated an accumulation of connective tissue and collagen **(Fig.2 A**; blue color**)**. Further, this staining also showed clusters of inflammatory cells, as seen by aggregation of nuclei **(Fig.2 A**; dark red**)**. Increased TUNEL positive cells indicated increased cell death in *Bbs8*$^{-/-}$ kidneys, while elevated γH2AX levels pointed to DNA damage and genomic instability. Additionally, we observed an accumulation of T-cells ($CD3^{+}$), as well as an increased nuclear translocation of the NF-κB protein RelA/p65, in particular in inflammation-rich areas, in *Bbs8*$^{-/-}$ kidney tissue **(Fig.2 B)**. mRNA expression analysis revealed an increase of NF-κB *p50* and *p65* transcription **(Fig.2 C)**. Although mRNA expression level of the necroptosis key kinase *Ripk3* was not significantly altered, we detected a significant increase of the pyroptosis markers *Nlrp3* and *GsdmD*. To gain more information on modulators of the ongoing fibrotic change, we also examined interleukin-6 (IL-6) expression with an ELISA assay and found it significantly upregulated specifically in kidney lysates, with only a non-significant increase in fat or liver tissue **(Fig.2**

D). Thus, the loss of *Bbs8*, in addition to cyst formation and dilated tubules, leads to an increased rate of cell death in the kidney, elevated expression of genes related to pyroptosis and the inflammasome, as well as to renal fibrosis and inflammation.

Proteomic analyses of Bbs8-deficient kidneys

To gain insights into the mechanisms behind the kidney pathology, we performed unbiased proteomic expression analysis of the whole proteome (WP); **(Fig.3 A)** and a phospho-proteome (PP) **(Fig.3 B)** of lysates from both *Bbs8*$^{-/-}$ and control kidneys. The principal component analysis clearly separated the two genotypes in both datasets **(Supp. Fig.3 A)**. After quality control (QC), we found 2926 proteins in the WP (**Fig.3 A)**. Based on the student's T-test (S0=0; FDR≤0.05), only 10 proteins were significantly up- and 16 significantly downregulated in *Bbs8*$^{-/-}$**.** Analysis of the phospho-proteome identified 6223 phosphosites after QC, within a total of 2188 individual proteins **(Fig.3 B)**. From these phosphosites, 151 were significantly up- and 1041 significantly down-regulated. GO-term analysis of the significantly regulated PP proteins revealed an enrichment of biological processes related to protein kinase signaling. In general this analysis represents the kidney phenotype of inflammation, ECM remodelling, and cell death **(Fig.3 C)**. Furthermore, consistent with the presence of inflammation **(Fig.2 D/E)**, KEGG pathway analysis of the same protein set indicated enrichment of pathways related to a type II inflammatory phenotype (Th1,2,17 cell differentiation), as well as toll-like receptor signaling **(Fig.3 D)**. Among the differentially expressed proteins within the WP, some were specifically related to cystogenesis and disease progression: here, dynein cytoplasmic 2 heavy chain 1 (DYNC2H1) and dystrobrevin binding protein 1 (DTNBP1) were found to be downregulated in the knockout. Genetic variants in DYNC2H1 are causative for skeletal and retinal ciliopathies, whereas mutations in DTNBP1 causes late-onset cystic kidney disease in mice (Monis, Faundez and Pazour, 2017). Over expressed proteins include retinol binding protein 4 (RBP4), uromodulin (UMOD), nucleoporin 98 (NUP98), and histone deacetylase 2 (HDAC2), each of which has a direct association to kidney diseases or ciliary biology **(Supp. Fig.4 B)** (Zaucke *et al.*, 2010; Kobayashi *et al.*, 2017; Endicott and Brueckner, 2018; Xun *et al.*, 2018). To explore the impact of phosphorylation alterations in *Bbs8*$^{-/-}$, we identified candidates that were significantly regulated in both the WP and PP, exhibiting a minimum fold change of 1.5 and showing counter-regulation. These candidates are presented in a hierarchical clustered heat map **(Fig.3 E)**. Remarkably, this included differences in HDAC2 serine (Ser) residues: Ser424 and Ser422/424. Phosphorylation of pSer394 and pSer422, as well as the double phosphorylation of pSer422/424 occurred predominantly in the wild type kidney, however in *Bbs8* knockout kidneys we only detected the peptide phosphorylated at pSer424 **(Supp. Fig.3 C)**. Since this protein has been described to suppress ciliogenesis in cancer cells via AuroraA (Kobayashi *et al.*, 2017), HDAC2 is an interesting candidate, which could contribute to the pathogenesis of BBS. It has been suggested previously that BBS proteins protect against HDAC6-mediated ciliary disassembly and loss of *Bbs8* results in increased

HDAC6 (Patnaik *et al.*, 2019). In *Bbs8*$^{-/-}$ kidneys, the histone deacetylases HDAC6 and HDAC1 were detected in the WP but, in contrast to HDAC2, not significantly altered. Therefore, we concluded that HDAC2 could indicate a direct mechanistic link between BBS8 and ciliary tubulin deacetylation, as well as ciliary destabilization.

BBS8 co-precipitates with HDAC2

In light of the significant changes in HDAC2 expression and phosphorylation, we sought to identity a direct link between HDAC2 and BBS8. Therefore, we employed two different approaches to investigate whether HDAC2 and BBS8 are part of a common protein complex. First, we expressed exogenous human FLAG-tagged BBS8 in HEK293T cells and we were able to co-precipitate endogenous HDAC2 as detected via immunoblotting **(Fig.4 A)**. Subsequently, we conducted a similar experiment but analysed the co-precipitated proteins using MS/MS. The principal component analysis clearly separated the F.hBBS8 pulldown from the control **(Supp. Fig.4 A, Supp. Tab. 2)**. We identified 1146 proteins of which 981 were potential significant BBS8 interactors **(Fig.4 B)**. Among those were not only many known members of the BBSome (BBS1, BBS2, BBS4, BBS5, BBS7, BBS9) and the chaperonin complex (CCT6A, CCT5, CCT3, CCT2, TCP1, CTT8, CCT4 and CCT7), but also HDAC2. Additional protein groups shown to interact with BBS8 are heat shock binding proteins and proteins related to the Wnt signaling pathway **(Supp. Fig.4 B)**. To investigate this further we compared the list of putative interactors with the published CiliaCarta proteins (Van Dam *et al.*, 2019) **(Fig.4 C)** and found a total of 67 ciliary proteins co-precipitating with BBS8. Comparing the potential BBS8 interactors with significantly differential expressed targets of the WP results in only four candidates, HDAC2 and 3 additional proteins (AGO2, NUP98 and MTHFD1; **Supp. Fig.4 C**).

Increased levels of HDAC2 in Bbs8 deficient cells affects ciliary tubulin acetylation

We could confirm an increased expression of HDAC2 in lysates from mouse embryonic fibroblasts (MEFs) generated from *Bbs8*$^{-/-}$ and matched control mice by immunoblotting **(Fig.4 D)**. This suggests that enhanced HDAC2 expression in *Bbs8*$^{-/-}$ mice might not be restricted to the kidney, but represents a mechanism relevant in other tissues as well. In parallel to immunoblotting, we performed qPCRs, which revealed an upregulation of *Hdac2* mRNA in these cells, indicating that enhanced transcription contributes to the increased levels of HDAC2 expression **(Fig.4 E)**. Since MEFs typically exhibit high levels of ciliation and HDAC2 might be similar to HDAC6 in terms of affecting ciliary disassembly, we analyzed the number and length of cilia in *Bbs8*$^{-/-}$ and control MEFs. Quantification of cilia number and length via ARL13B staining revealed no significant difference in serum starved MEFs **(Fig.4 F),** similar to our findings in the kidney of *Bbs8*$^{-/-}$ mice. Since HDAC2, similar to HDAC6, might negatively regulate acetylation of alpha tubulin within the ciliary axoneme, we co-stained the ciliary membrane marker ARL13B with acetylated tubulin. Quantification revealed that a significant number of cilia in the *Bbs8*$^{-/-}$

cells visualized by ARL13B staining did not exhibit labelling for acetylated tubulin **(Fig.4 G)**. Strikingly, we could confirm this reduced acetylation of ciliary tubulin in the kidney tissue of *Bbs8*$^{-/-}$ mice **(Fig.4 H)**. In summary, the finding of high HDAC2 levels and reduced acetylation in cilia of both, *Bbs8*$^{-/-}$ kidney epithelial cells *in vivo* and in *Bbs8*$^{-/-}$ MEFs, aligns perfectly with the previously described positive effect of HDAC inhibition in ADPKD zebrafish and mouse models (Cao *et al.*, 2009), suggesting a potentially relevant therapeutic option.

Discussion

In this work, we describe the occurrence of a tubular cystic kidney disease in a mouse model with a knockout of a *Bbs* gene. Notably, these animals have long been known to exhibit symptoms such as obesity, polydactyly and blindness. The ocular phenotype of *Bbs8*$^{-/-}$ mice has been studied in great detail, however the renal phenotype has not been previously examined. Here, we describe a relatively late-occurring cystic fibrotic kidney disease in homozygous mouse knockouts, accurately reflecting the patient renal manifestation. The kidney phenotype in BBS patients is variable with kidneys showing parenchymal cysts, medullary and most often corticomedullary cysts, but also renal fibrosis, unilateral agenesis or dysplastic kidneys (Beales *et al.*, 1999; Putoux *et al.*, 2012; Elawad *et al.*, 2022). However, these phenotypes are highly variable among families and could be caused by the type of mutations (Putoux *et al.*, 2012). In general, kidney disease in BBS patients is diagnosed in approximately 25% of cases, through the fact that many patients do not undergo any specific kidney examination and thereby kidney disease might not be recognized (Beales *et al.*, 1999).

It was the identification of BBS8 mutations that first suggested that the BBS phenotype might be attributed to defective primary cilia (Ansley *et al.*, 2003). The loss of *Bbs8* causes a much more severe phenotype than other patient mutations, which could be the reason why BBS8 variants are rare among patients (Stoetzel *et al.*, 2006). Consistently, the phenotype of *Bbs8* deficient mice is likely the most severe among BBS mouse models. Kidney phenotypes have been observed in *Bbs2*, *Bbs4* or *Bbs10* knockout mice where the knockout primarily affected glomeruli and podocytes with indirect systemic effects on tubular cells (Nishimura *et al.*, 2004; Guo *et al.*, 2011; Cognard *et al.*, 2015). The at hand study now describes a tubular cystic kidney phenotype in a BBS mouse model which will allow to conduct preclinical studies on tubular cystic kidney disease in a BBS genetic context.

Regarding the precise mechanisms underlying kidney disease in *Bbs8*$^{-/-}$, our proteomic analyses revealed a number of interesting candidates, which potentially contribute to kidney pathomechanisms. The downregulation of DTNBP1, a subunit of the biogenesis of lysosome-related organelles complex-1 (BLOC-1), could contribute to the kidney phenotype as it is known to cause cystic kidney disease upon mutation in mice by reducing ciliary expression of polycystin-2 (Monis, Faundez and Pazour, 2017). In addition, we observed decreased levels of DYNC2H1 in *Bbs8*$^{-/-}$ mice. DYNC2H1 is

a known subunit of the IFT-dynein motor, which drives retrograde IFT-rafts and plays a role in the formation of the transition zone. Mutations lead to the skeletal ciliopathies Jeune asphyxiating thoracic dystrophy and short-rib polydactyly and also to non-syndromic retina degeneration (Jensen *et al.*, 2018; Vig *et al.*, 2020). Reduced levels of DYNC2H1 in *Bbs8*$^{-/-}$ could contribute both to the renal and retinal phenotype (Vig *et al.*, 2020). Another interesting finding is the increased abundance of UMOD, a protein expressed in renal primary cilia. Variants of the UMOD gene lead to autosomal-dominant tubulointerstitial kidney diseases (Zaucke *et al.*, 2010). Additionally, UMOD is found to be involved in renal cyst formation in human kidney biopsies, which is in line with the upregulation in *Bbs8*$^{-/-}$ (Gresh *et al.*, 2004). The proteomic analysis also revealed increased expression of RBP4 in kidney tissue. Increased RBP4 has been suggested as a biomarker for renal damage and proteinuria (Ratajczyk *et al.*, 2022), which has also been suggested for UMOD (Thielemans *et al.*, 2023). Therefore, further studies need to address whether serum or urinary RBP4 or UMOD levels could be used as a potential biomarker for kidney disease onset and progression in BBS patients (Xun *et al.*, 2018; Swa *et al.*, 2022), similar to what has been suggested for UMOD in ADPKD (Cansever *et al.*, 2021). In addition to the individual expression and phosphorylation analysis, comparing the unbiased proteome- and phosphoproteome with the BBS8 interactome unearthed further interesting candidates. Here, in particular four genes showed up in all three analyses. Among those candidates, NUP98 is particularly notable, which is a nucleoporin that plays a crucial role in size-selective diffusion at the base of cilia (Endicott and Brueckner, 2018). AGO-2 has also been described at the base of cilia in astrocytes and could play a role in BBS (Moser, Fritzler and Rattner, 2011), while *Mthfd1*, which codes for a protein in folate metabolism, has not yet been associated with cilia or cystic kidneys.

Based on the role of tubulin acetylation in cilia and fundamental previous studies on HDAC6 in regard to ciliary disassembly (Pugacheva *et al.*, 2007), we focused on HDAC2. HDAC2 showed increased expression in our proteome analyses and we also found a strong interaction between HDAC2 and BBS8 upon IP. In addition to its nuclear functions, HDAC2 could regulate the stability and, thus, dynamics of cilia through the deacetylation of tubulin, similar to HDAC6. HDAC6 is enriched at the centrosome and basal body, where it catalyzes the deacetylation of alpha-tubulin and, therefore, plays a role in the disassembly of primary cilia (Ran *et al.*, 2015). This process can be prevented by BBS proteins through the recruitment of Inversin to the ciliary base (Patnaik *et al.*, 2019). In general, HDAC6 is activated by phosphorylation after HEF1-dependent activation of the oncogenic Aurora A (AurA) kinase (Pugacheva *et al.*, 2007). We found increased levels of HDAC2 in *Bbs8*$^{-/-}$ kidneys, as well as *Bbs8*$^{-/-}$ MEFs and observed diminished acetylation of tubulin inside cilia on *Bbs8* knockout cells. This might result in a subtle defect in ciliary dynamics.

Even though we found differences in HDAC2, we did not expect cilia to be severely affected. This would not be in line with data from other BBS genes, nor would it explain the late-onset phenotype we

observed. Similarly, our findings related to cell death, fibrosis, and inflammation are relatively moderate. Given the late onset and slow progression of kidney disease in this model, we would not expect the loss of *Bbs8* to result in massive overactivity of any specific cell death pathway. Our results suggest that cell death and inflammation are rather secondary processes that, while present, do not constitute the primary cause of the kidney disease. Since the activity of HDAC2 is regulated by phosphorylation through casein kinase II and the regulation of expression levels by proteasomal degradation (Eom and Kook, 2015), it might open potential options for pharmacologically interventions targeting HDAC2-dependent deacetylation. To what extent the nuclear functions of HDAC2 are also altered and contribute to the pathogenesis of kidney disease requires further investigation.

Figure legends:

Figure 1. *Bbs8*$^{-/-}$ mice develop late-onset cystic kidney disease.

(A/B) Image of 46-week-old control (*Bbs8*$^{+/+}$) and *Bbs8*$^{-/-}$ mice, and the body weight indicated significant obesity in knockout animals (n=4). **(C)** Kidney weight of the mice did not significantly alter between both mouse models. **(D)** Serum urea of control and *Bbs8*$^{-/-}$ mice show an increasing trend (n=4). **(E/F)** PAS staining of the whole kidney in control and *Bbs8*$^{-/-}$ animals; Scale bar: 1 mm. The area in the zoom-in comprises the cortex and medullary area of the kidney; Scale bar: 200 µm. **(G)** Cyst index described in a cyst-to-tissue area ratio, normalised to control animals. **(H)** Kidney image for distal tubules (Slc12a3, magenta) and proximal tubules (LTL, green) show cyst formation in clustered distal tubules; Scale bar: 500 µm.

Figure 2. Cell death, fibrosis and inflammation in *Bbs8*$^{-/-}$ kidneys.

Representative microscopic images of control and Bbs8$^{-/-}$ mice for **(A)** Masson's trichrome stain; Scale bar: 300 µm **(B)** TUNEL staining and yH2AX, Scale bar: 100 µm; CD3^{+} and NF-kB expression, Scale bar: 300 µm. Arrowheads, indicates positive events. **(C)** Quantitative real-time PCR of *NF-kB/p50*, *RelA/p65* and inflammasome genes in control and *Bbs8*$^{-/-}$ kidney samples (n=4). Statistical analysis was performed using a two-sided student's *T-test* (*p*-value: <0.001***; 0.002**; 0.033*; ns = 0.12). **(D)** IL-6 Elisa performed for kidney, liver and fat tissue.

Figure 3. Proteomic analysis hints toward HDAC2 as putative key player in *Bbs8*$^{-/-}$ kidneys.

Scatter blot of **(A)** whole proteome (WP) or **(B)** phosphoproteome (PP) marked with significantly (FDR≤0.05) up- (yellow) or downregulated (cyan) proteins. Labelled HDAC proteins and their activator kinase CK2 as well as further interesting candidates. **(C/D)** GOBP and KEGG pathway based on 1D-enrichment of the proteins found in the PP, separated for up- (yellow) and downregulation (cyan). Top

10 candidates are ordered by p-values within the groups. **(E)** Clustered hierarchal heat map based on log_2 LFQ intensities and fold change=1.5 of WP and PP proteins wither their phosphorylation position in the protein which are significantly, and counter regulated.

Figure 4. HDAC2 interacts with BBS8 and increased levels affect ciliary tubulin acetylation

(A) Co-IP from HEK293T cells, overexpressing F.hBBS8 or F.hEPS as control, show an interaction of BBS8 with HDAC2. Protein extracts (Lysate) were immunoprecipitated with α-Flag (IP) and detected and detected with α-Flag (F.hBBS8 ~65 kDa, F.hEPS ~30 kDa) and α-HDAC2 (55 kDa) (n=3). **(B)** Scatter blot of BBS8 interactors, performed in HEK293T cells overexpressing F.hBBS8 or F.hEPS as control. Potential Interactors (FDR≤0.05), marked in magenta, revealed HDAC2 as an interactor of BBS8. **(C)** Venn-Diagram showing the overlap between the BBS8 interactors and the published CiliaCarta**. (D)** Control or *Bbs8*$^{-/-}$ mouse embryonic fibroblasts (MEFs) were immunoblotted against HDAC2 (~55 kDa), acetylated Tubulin (~55 kDa). All samples were normalized to Calnexin (~96 kDa). **(E)** qPCR of *Hdac2* in control and *Bbs8*$^{-/-}$ MEFs samples (n=3). Statistical analysis was performed using a two-sided student's *T-test* (*p*-value: <0.001***; 0.002**; 0.033*; ns = 0.12). **(F)** Representative images of cultured MEF *Bbs8* knockout and control cells, stained with the cilia marker ARL13B and counterstained with DAPI; Scale bar: 20 µm. Primary cilia are quantified for the number and length of cilia (n=4). **(G)** Primary cilia count in MEFs, which are ARL13B and acetylated Tubulin (ac-Tub) positive. Representative images of primary cilia in MEFs with the overlay of marker ARL13B and ac-Tub, counterstained with DAPI; Scale bar: 10 µm. **(H)** ARL13B (green) and acetylated tubulin (magenta) staining of cilia in kidney tissue of control and Bbs8$^{-/-}$ mice and the ratio of ARL13B and acetylated tubulin positive cilia (n=3). All data in this figure were statistically analysed using an unpaired Student's *t-test* (*p*-value: <0.001***; 0.002**; 0.033*; ns = 0.12).

Supplementary Figure 1. **Small-cyst formation in *Bbs8*$^{-/-}$ kidney.**

(A) Measured cyst area depicted as jittered dots with the mean as a horizontal line. The values are plotted on a log_{10} scale. The overall number of cysts was scientifically increased in knockout animals. The data were statistically analysed using a two-sided student's *t-test* (*p*-value: <0.001***; 0.002**; 0.033*; ns = 0.12).

Supplementary Figure 2**. The occurrence of cilia in conventional *Bbs8 knockout is not altered.***

(A) Cilia staining with ARL13B showed no difference in ciliation between control and *Bbs8*$^{-/-}$ kidney; Scale bar: 50 µm; Zoom-in scale bar: 25 µm.

Supplementary Figure 3. ***Additional analyses based on the proteomic data***

(A) Principal component analysis (PCA) plots of the protein expression data of control and *Bbs8*$^{-/-}$ kidney samples. Depicted are the first two principal components for either whole proteome (WP) or phosphoproteome (PP). The axes represent the percentages of variation explained by the principal components. **(B)** Table of significantly up- and downregulated proteins of the WP. **(C)** Table of different expressed HDAC2 residues with their related phosphosites and regulation. **(D)** KEGG, GOCC and GOMF of WP **(E)** GOMF and GOCC of PP. All GO-terms based on 1D-enrichment, separated for up- (yellow) and downregulation (cyan). Ordered by p-values within the groups**.**

Supplementary Figure 4. **Additional analyses of the interactome data**

(A) Principal component analysis (PCA) plots of the protein expression data of F.GFP and F.hBBS8, shown with the first two principal components. The axes represent the percentages of variation explained by the principal components. **(B)** Scatter plot of different protein clusters expressed in the BBS8 interactome for different GO-terms: BBSome, chaperonin-containing T-complex, heat shock protein binding and Wnt signaling pathway. **(C)** Venn-Diagram of BBS8 interaction partners (986) with the significant candidates of the WP (26) showed an overlap of 4 proteins.

Supplementary Figure 5. **Original data: full-sized immunoblots.**

Original western blots only cropped to gel size **(A)** of Figure 4 A and **(B)** of Figure 4 E.

Acknowledgments

We extend our gratitude to Angelika Köser, Serena Greco-Torres and Stefanie Keller for their valuable technical assistance. We also wish to acknowledge the great support provided by the CECAD imaging facility and the CECAD proteomics facility. Furthermore, we want to convey our appreciation to all the individuals in our research group and numerous members of the SFB1403 for their meaningful discussions and support.

Funding: This study was supported by the German Research Foundation (DFG; SFB1403, project number 414786233, A09 to B.S. and T.B.; and FOR5547 to HMS, DW, and BS, project number 503306912, under Germany's Excellence Strategy – EXC2151 – Project-ID 390873048 (to D.W.), and WA 3382/8-1 – Project-ID 513767027 (to D.W.). B.S. was also supported by the German Federal Ministry of Research and Education (BMBF grant 01GM1515; NEOCYST consortium) and by the European Union (TheraCil). D.W. was also supported by the Else Kröner Fresenius Foundation (2021.EKFSE.53). P.M. was supported by the Studienstiftung des Deutschen Volkes. The CECAD proteomics facility was supported by the large instrument grant INST 1856/71-1 FUGG by the German Research Foundation (DFG Großgeräteantrag).

References

Ansley, S. J. *et al.* (2003) 'Basal body dysfunction is a likely cause of pleiotropic Bardet-Biedl syndrome', *Nature*, 425(6958), pp. 628–633. doi: 10.1038/NATURE02030.

Bankhead, P. *et al.* (2017) 'QuPath: Open source software for digital pathology image analysis', *Scientific Reports 2017 7:1*, 7(1), pp. 1–7. doi: 10.1038/s41598-017-17204-5.

Bardet, G. (1995) 'On congenital obesity syndrome with polydactyly and retinitis pigmentosa (a contribution to the study of clinical forms of hypophyseal obesity). 1920.', *Obesity research*, 3(4), pp. 387–99. Available at: http://www.ncbi.nlm.nih.gov/pubmed/8521156 (Accessed: 17 October 2019).

Beales, P. L. *et al.* (1999) 'New criteria for improved diagnosis of Bardet-Biedl syndrome: results of a population survey', *Journal of Medical Genetics*, 36(6), p. 437. doi: 10.1136/jmg.36.6.437.

Bentley-Ford, M. R. *et al.* (2021) 'A mouse model of BBS identifies developmental and homeostatic effects of BBS5 mutation and identifies novel pituitary abnormalities', *Human molecular genetics*, 30(3–4), pp. 234–246. doi: 10.1093/HMG/DDAB039.

Biedl, A. (1995) 'A pair of siblings with adiposo-genital dystrophy. 1922.', *Obesity research*, 3(4), p. 404. Available at: http://www.ncbi.nlm.nih.gov/pubmed/8521158 (Accessed: 17 October 2019).

Brücker, L. *et al.* (2023) 'The actin-bundling protein Fascin-1 modulates ciliary signalling', *Journal of Molecular Cell Biology*, 15(4), p. 22. doi: 10.1093/JMCB/MJAD022.

Cansever, H. N. *et al.* (2021) 'Serum uromodulin levels, MR imaging findings, and their relationship with eGFR-based CKD staging in ADPKD patients', *International urology and nephrology*, 53(7), pp. 1383–1389. doi: 10.1007/S11255-020-02730-5.

Cao, Y. *et al.* (2009) 'Chemical modifier screen identifies HDAC inhibitors as suppressors of PKD models', *Proceedings of the National Academy of Sciences of the United States of America*, 106(51), pp. 21819–21824. doi: 10.1073/PNAS.0911987106.

Cognard, N. *et al.* (2015) 'Comparing the Bbs10 complete knockout phenotype with a specific renal epithelial knockout one highlights the link between renal defects and systemic inactivation in mice', *Cilia*, 4. Available at: https://ciliajournal.biomedcentral.com/articles/10.1186/s13630-015-0019-8 (Accessed: 30 March 2021).

Dafinger, C. *et al.* (2021) 'Targeted deletion of Ruvbl1 results in severe defects of epidermal development and perinatal mortality', *Molecular and Cellular Pediatrics*, 8(1). doi: 10.1186/S40348-021-00111-1.

Van Dam, T. J. P. *et al.* (2019) 'CiliaCarta: An integrated and validated compendium of ciliary genes', *PLoS ONE*, 14(5). doi: 10.1371/JOURNAL.PONE.0216705.

Davis, R. E. *et al.* (2007) 'A knockin mouse model of the Bardet-Biedl syndrome 1 M390R mutation has cilia defects, ventriculomegaly, retinopathy, and obesity', *Proceedings of the National Academy of Sciences of the United States of America*, 104(49), pp. 19422–19427. doi: 10.1073/PNAS.0708571104.

Dilan, T. L. *et al.* (2018) 'Bardet-Biedl syndrome-8 (BBS8) protein is crucial for the development of outer segments in photoreceptor neurons.', *Human molecular genetics*, 27(2), pp. 283–294. doi: 10.1093/hmg/ddx399.

Elawad, O. A. M. A. *et al.* (2022) 'Bardet–Biedl syndrome: a case series', *Journal of Medical Case Reports*, 16(1), pp. 1–9. doi: 10.1186/S13256-022-03396-6/FIGURES/4.

Endicott, S. J. and Brueckner, M. (2018) 'NUP98 Sets the Size-Exclusion Diffusion Limit through the Ciliary Base', *Current biology : CB*, 28(10), pp. 1643-1650.e3. doi: 10.1016/J.CUB.2018.04.014.

Eom, G. H. and Kook, H. (2015) 'Role of histone deacetylase 2 and its posttranslational modificationsin cardiac hypertrophy', *BMB Reports*, 48(3), p. 131. doi: 10.5483/BMBREP.2015.48.3.242.

Fan, C.-M. and Tessier-Lavigne, M. (1994) 'Patterning of mammalian somites by surface ectoderm and notochord: Evidence for sclerotome induction by a hedgehog homolog', *Cell*, 79(7), pp. 1175–1186. doi: 10.1016/0092-8674(94)90009-4.

Fath, M. A. *et al.* (2005) 'Mkks-null mice have a phenotype resembling Bardet-Biedl syndrome', *Human molecular genetics*, 14(9), pp. 1109–1118. doi: 10.1093/HMG/DDI123.

Forsythe, E. and Beales, P. L. (2013) 'Bardet–Biedl syndrome', *European Journal of Human Genetics*, 21(1), pp. 8–13. doi: 10.1038/ejhg.2012.115.

Garcia-Gonzalo, F. R. and Reiter, J. F. (2017) 'Open Sesame: How Transition Fibers and the Transition Zone Control Ciliary Composition', *Cold Spring Harbor perspectives in biology*, 9(2). doi: 10.1101/CSHPERSPECT.A028134.

Gopalakrishnan, J. *et al.* (2023) 'Emerging principles of primary cilia dynamics in controlling tissue organization and function', *The EMBO Journal*, p. e113891. doi: 10.15252/EMBJ.2023113891.

Gresh, L. *et al.* (2004) 'A transcriptional network in polycystic kidney disease', *EMBO Journal*, 23(7), pp. 1657–1668. doi: 10.1038/SJ.EMBOJ.7600160/SUPPL_FILE/EMBJ7600160-SUP-0006.PDF.

Guo, D. F. *et al.* (2011) 'Inactivation of Bardet-Biedl syndrome genes causes kidney defects', *American Journal of Physiology - Renal Physiology*, 300(2), p. F574. doi: 10.1152/AJPRENAL.00150.2010.

Habbig, S. *et al.* (2011) 'NPHP4, a cilia-associated protein, negatively regulates the Hippo pathway', *The Journal of cell biology*, 193(4), pp. 633–642. doi: 10.1083/JCB.201009069.

Hildebrandt, F., Benzing, T. and Katsanis, N. (2011) 'Ciliopathies', *The New England journal of medicine*, 364(16), pp. 1533–1543. doi: 10.1056/NEJMRA1010172.

Hildebrandt, F. and Zhou, W. (2007) 'Nephronophthisis-associated ciliopathies.', *Journal of the American Society of Nephrology : JASN*, 18(6), pp. 1855–71. doi: 10.1681/ASN.2006121344.

Jensen, V. L. *et al.* (2018) 'Role for intraflagellar transport in building a functional transition zone', *EMBO reports*, 19(12). doi: 10.15252/EMBR.201845862.

Kobayashi, T. *et al.* (2017) 'HDAC2 promotes loss of primary cilia in pancreatic ductal adenocarcinoma', *EMBO reports*, 18(2), pp. 334–343. doi: 10.15252/EMBR.201541922.

Kretschmer, V. *et al.* (2019) 'Progressive Characterization of Visual Phenotype in Bardet-Biedl Syndrome Mutant Mice', *Investigative ophthalmology & visual science*, 60(4), pp. 1132–1143. doi: 10.1167/IOVS.18-25210.

Kretschmer, V. *et al.* (2023) 'Deletion of IFT20 exclusively in the RPE ablates primary cilia and leads to retinal degeneration', *PLoS biology*, 21(12). doi: 10.1371/JOURNAL.PBIO.3002402.

Kulaga, H. M. *et al.* (2004) 'Loss of BBS proteins causes anosmia in humans and defects in olfactory cilia structure and function in the mouse', *Nature genetics*, 36(9), pp. 994–998. doi: 10.1038/NG1418.

Laurence, J. Z. and Moon, R. C. (1995) 'Four cases of "retinitis pigmentosa" occurring in the same family, and accompanied by general imperfections of development. 1866.', *Obesity research*, 3(4), pp. 400–3. Available at: http://www.ncbi.nlm.nih.gov/pubmed/8521157 (Accessed: 17 October 2019).

Loktev, A. V. *et al.* (2008) 'A BBSome Subunit Links Ciliogenesis, Microtubule Stability, and Acetylation', *Developmental Cell*, 15(6), pp. 854–865. doi: 10.1016/j.devcel.2008.11.001.

May-Simera, H. L. *et al.* (2010) 'Bbs8, together with the planar cell polarity protein Vangl2, is required to establish left-right asymmetry in zebrafish', *Developmental biology*, 345(2), pp. 215–225. doi: 10.1016/J.YDBIO.2010.07.013.

May-Simera, H. L. *et al.* (2015) 'Ciliary proteins Bbs8 and Ift20 promote planar cell polarity in the cochlea', *Development (Cambridge, England)*, 142(3), pp. 555–566. doi: 10.1242/DEV.113696.

McConnachie, D. J., Stow, J. L. and Mallett, A. J. (2021) 'Ciliopathies and the Kidney: A Review', *American journal of kidney diseases : the official journal of the National Kidney Foundation*, 77(3), pp. 410–419. doi: 10.1053/J.AJKD.2020.08.012.

Monis, W. J., Faundez, V. and Pazour, G. J. (2017) 'BLOC-1 is required for selective membrane protein trafficking from endosomes to primary cilia', *The Journal of cell biology*, 216(7), pp. 2131–2150. doi: 10.1083/JCB.201611138.

Moser, J. J., Fritzler, M. J. and Rattner, J. B. (2011) 'Repression of GW/P body components and the RNAi microprocessor impacts primary ciliogenesis in human astrocytes', *BMC cell biology*, 12. doi: 10.1186/1471-2121-12-37.

Munsterberg, A. E. *et al.* (1995) 'Combinatorial signaling by Sonic hedgehog and Wnt family members induces myogenic bHLH gene expression in the somite.', *Genes & Development*, 9(23), pp. 2911–2922. doi: 10.1101/gad.9.23.2911.

Mykytyn, K. *et al.* (2004) 'Bardet-Biedl syndrome type 4 (BBS4)-null mice implicate Bbs4 in flagella formation but not global cilia assembly', *Proceedings of the National Academy of Sciences of the United States of America*, 101(23), pp. 8664–8669. doi: 10.1073/PNAS.0402354101.

Nachury, M. V. *et al.* (2007) 'A Core Complex of BBS Proteins Cooperates with the GTPase Rab8 to Promote Ciliary Membrane Biogenesis', *Cell*, 129(6), pp. 1201–1213. doi: 10.1016/j.cell.2007.03.053.

Nishimura, D. Y. *et al.* (2004) 'Bbs2-null mice have neurosensory deficits, a defect in social dominance, and retinopathy associated with mislocalization of rhodopsin', *Proceedings of the National Academy of Sciences of the United States of America*, 101(47), pp. 16588–16593. doi: 10.1073/PNAS.0405496101.

Patnaik, S. R. *et al.* (2019) 'Bardet–Biedl Syndrome proteins regulate cilia disassembly during tissue maturation', *Cellular and Molecular Life Sciences*, 76(4), pp. 757–775. doi: 10.1007/s00018-018-2966-x.

Pazour, G. J. and Bloodgood, R. A. (2008) 'Targeting Proteins to the Ciliary Membrane', *Current Topics in Developmental Biology*, 85, pp. 115–149. doi: 10.1016/S0070-2153(08)00805-3.

Postma, M. and Goedhartid, J. (2019) 'PlotsOfData-A web app for visualizing data together with their summaries'. doi: 10.1371/journal.pbio.3000202.

Pourquié, O. *et al.* (1996) 'Lateral and Axial Signals Involved in Avian Somite Patterning: A Role for BMP4', *Cell*, 84(3), pp. 461–471. doi: 10.1016/S0092-8674(00)81291-X.

Pugacheva, E. N. *et al.* (2007) 'HEF1-dependent Aurora A activation induces disassembly of the primary cilium', *Cell*, 129(7), pp. 1351–1363. doi: 10.1016/J.CELL.2007.04.035.

Putoux, A. *et al.* (2012) 'Phenotypic variability of Bardet-Biedl syndrome: focusing on the kidney', *Pediatric Nephrology*, 27(1), pp. 7–15. doi: 10.1007/s00467-010-1751-3.

Rahmouni, K. *et al.* (2008) 'Leptin resistance contributes to obesity and hypertension in mouse models of Bardet-Biedl syndrome', *The Journal of clinical investigation*, 118(4), pp. 1458–1467. doi: 10.1172/JCI32357.

Ran, J. *et al.* (2015) 'Deacetylation of α-tubulin and cortactin is required for HDAC6 to trigger ciliary

disassembly', *Scientific reports*, 5. doi: 10.1038/SREP12917.

Ratajczyk, K. *et al.* (2022) 'The Clinical Significance of Urinary Retinol-Binding Protein 4: A Review', *International Journal of Environmental Research and Public Health*, 19(16). doi: 10.3390/IJERPH19169878/S1.

Reiter, J. F., Blacque, O. E. and Leroux, M. R. (2012) 'The base of the cilium: roles for transition fibres and the transition zone in ciliary formation, maintenance and compartmentalization', *EMBO Reports*, 13(7), p. 608. doi: 10.1038/EMBOR.2012.73.

Reiter, J. F. and Leroux, M. R. (2017) 'Genes and molecular pathways underpinning ciliopathies', *Nature Reviews Molecular Cell Biology 2017 18:9*, 18(9), pp. 533–547. doi: 10.1038/nrm.2017.60.

Schneider, S. *et al.* (2021) 'Loss of Ciliary Gene Bbs8 Results in Physiological Defects in the Retinal Pigment Epithelium', *Frontiers in Cell and Developmental Biology*, 9, p. 607121. doi: 10.3389/FCELL.2021.607121/FULL.

Seo, S. *et al.* (2009) 'Requirement of Bardet-Biedl syndrome proteins for leptin receptor signaling', *Human molecular genetics*, 18(7), pp. 1323–1331. doi: 10.1093/HMG/DDP031.

Seo, S. *et al.* (2010) 'BBS6, BBS10, and BBS12 form a complex with CCT/TRiC family chaperonins and mediate BBSome assembly.', *Proceedings of the National Academy of Sciences of the United States of America*, 107(4), pp. 1488–93. doi: 10.1073/pnas.0910268107.

Stoetzel, C. *et al.* (2006) 'BBS8 is rarely mutated in a cohort of 128 Bardet-Biedl syndrome families', *Journal of human genetics*, 51(1), pp. 81–84. doi: 10.1007/S10038-005-0320-2.

Swa, H. L. F. *et al.* (2022) 'Evaluating Serum RBP4 as an Auxiliary Biomarker for CKDu Diagnosis', *Kidney and Dialysis 2022, Vol. 2, Pages 576-587*, 2(4), pp. 576–587. doi: 10.3390/KIDNEYDIAL2040052.

Tadenev, A. L. D. *et al.* (2011) 'Loss of Bardet-Biedl syndrome protein-8 (BBS8) perturbs olfactory function, protein localization, and axon targeting', *Proceedings of the National Academy of Sciences of the United States of America*, 108(25), pp. 10320–10325. doi: 10.1073/PNAS.1016531108.

Thielemans, R. *et al.* (2023) 'Unveiling the Hidden Power of Uromodulin: A Promising Potential Biomarker for Kidney Diseases', *Diagnostics (Basel, Switzerland)*, 13(19). doi: 10.3390/DIAGNOSTICS13193077.

Todaro, G. J. and Green, H. (1963) 'Quantitative studies of the growth of mouse embryo cells in culture and their development into established lines', *The Journal of cell biology*, 17(2), pp. 299–313. doi: 10.1083/JCB.17.2.299.

Tyanova, S. *et al.* (2016) 'The Perseus computational platform for comprehensive analysis of (prote)omics data', *Nature Methods 2016 13:9*, 13(9), pp. 731–740. doi: 10.1038/nmeth.3901.

Tyanova, S., Temu, T. and Cox, J. (2016) 'The MaxQuant computational platform for mass spectrometry–based shotgun proteomics', *Nature Protocols*, 11. doi: 10.1038/nprot.2016.136.

Vig, A. *et al.* (2020) 'DYNC2H1 hypomorphic or retina-predominant variants cause nonsyndromic retinal degeneration', *Genetics in Medicine*, 22(12), p. 2041. doi: 10.1038/S41436-020-0915-1.

Xun, C. *et al.* (2018) 'Circulating RBP4 Increase and Its Diagnosis of Chronic Kidney Disease', *Annals of clinical and laboratory science*, 48(2), pp. 205–207. Available at: https://pubmed.ncbi.nlm.nih.gov/29678848/ (Accessed: 20 February 2024).

Zaucke, F. *et al.* (2010) 'Uromodulin is expressed in renal primary cilia and UMOD mutations result in decreased ciliary uromodulin expression', *Human Molecular Genetics*, 19(10), p. 1985. doi: 10.1093/HMG/DDQ077.

Zhang, Q. *et al.* (2012) 'Intrinsic protein-protein interaction-mediated and chaperonin-assisted sequential assembly of stable bardet-biedl syndrome protein complex, the BBSome.', *The Journal of biological chemistry*, 287(24), pp. 20625–35. doi: 10.1074/jbc.M112.341487.

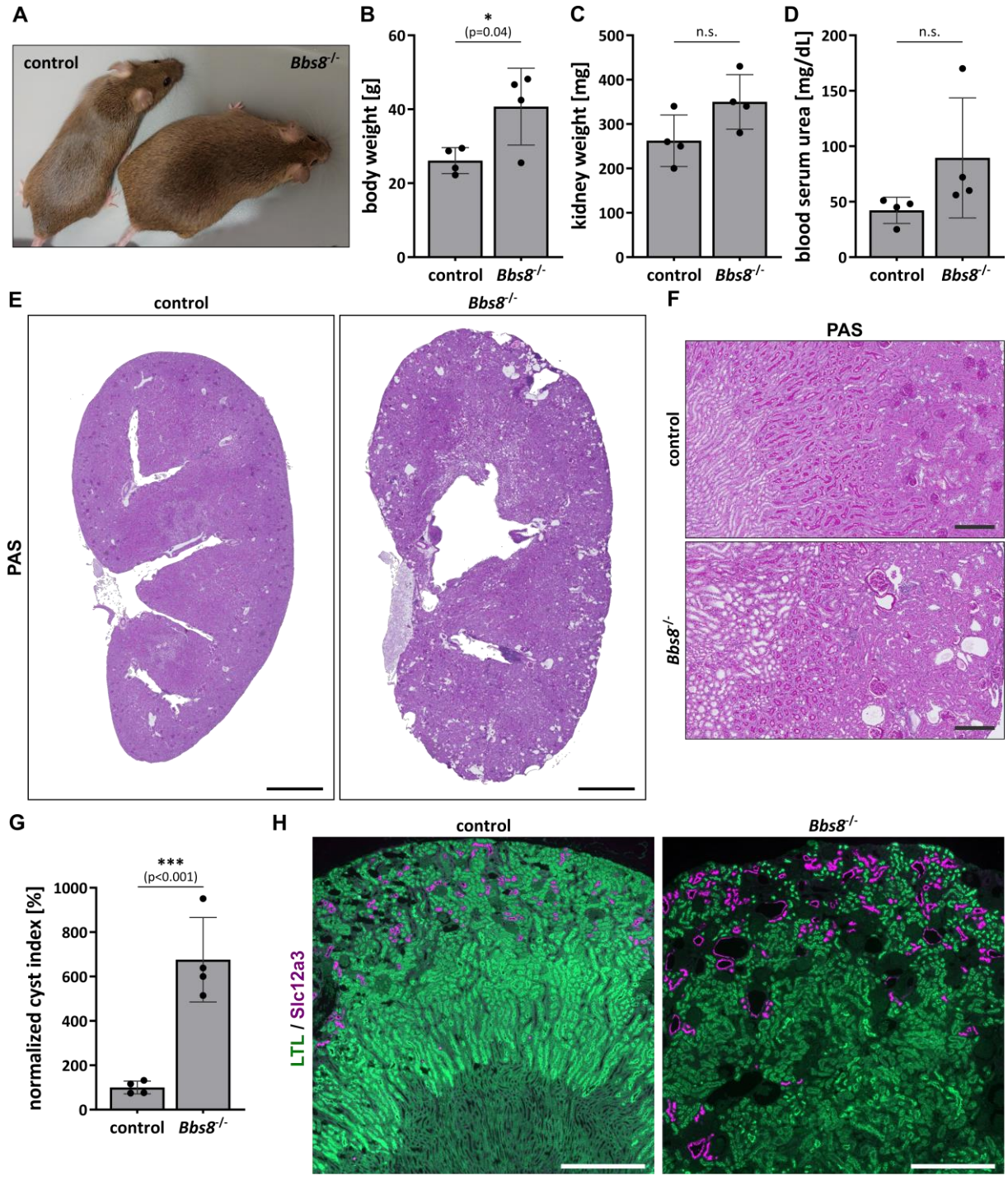
A
control
Bbs8-/-
B
*
(p=0.04)
body weight [g]
control
Bbs8-/-
C
n.s.
kidney weight [mg]
control
Bbs8-/-
D
n.s.
blood serum urea [mg/dL]
control
Bbs8-/-
E
control
Bbs8-/-
PAS
F
PAS
control
Bbs8-/-
G
***
(p<0.001)
normalized cyst index [%]
control
Bbs8-/-
H
control
Bbs8-/-
LTL / Slc12a3

Figure 1

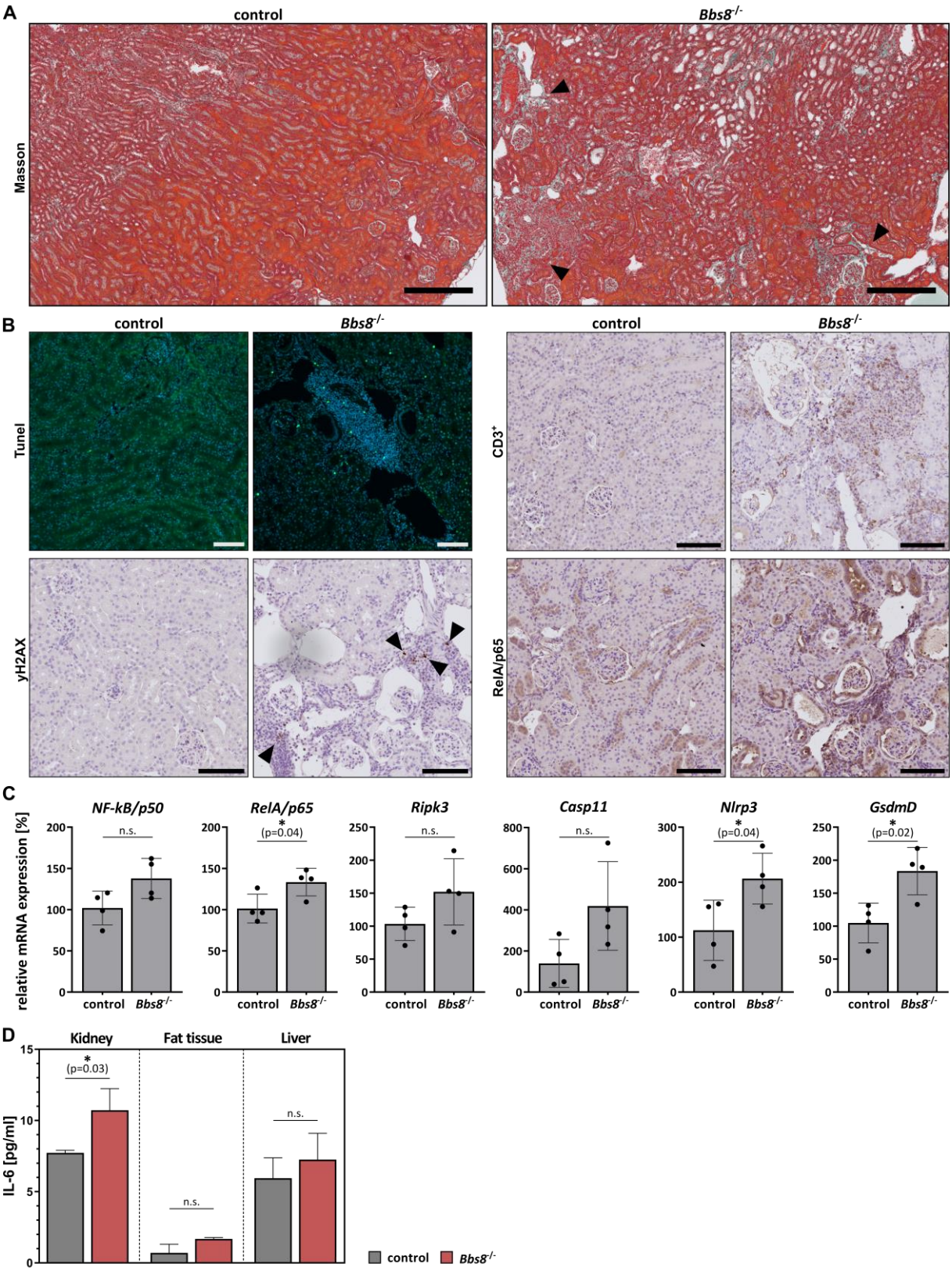
A
control
Bbs8-/-
Masson
B
control
Bbs8-/-
Tunel
yH2AX
control
Bbs8-/-
CD3+
RelA/p65
C
relative mRNA expression [%]
NF-kB/p50
RelA/p65
Ripk3
Casp11
Nlrp3
GsdmD
n.s.
*
(p=0.04)
(p=0.02)
control
Bbs8-/-
D
Kidney
Fat tissue
Liver
IL-6 [pg/ml]
*
(p=0.03)
n.s.
control
Bbs8-/-

Figure 2

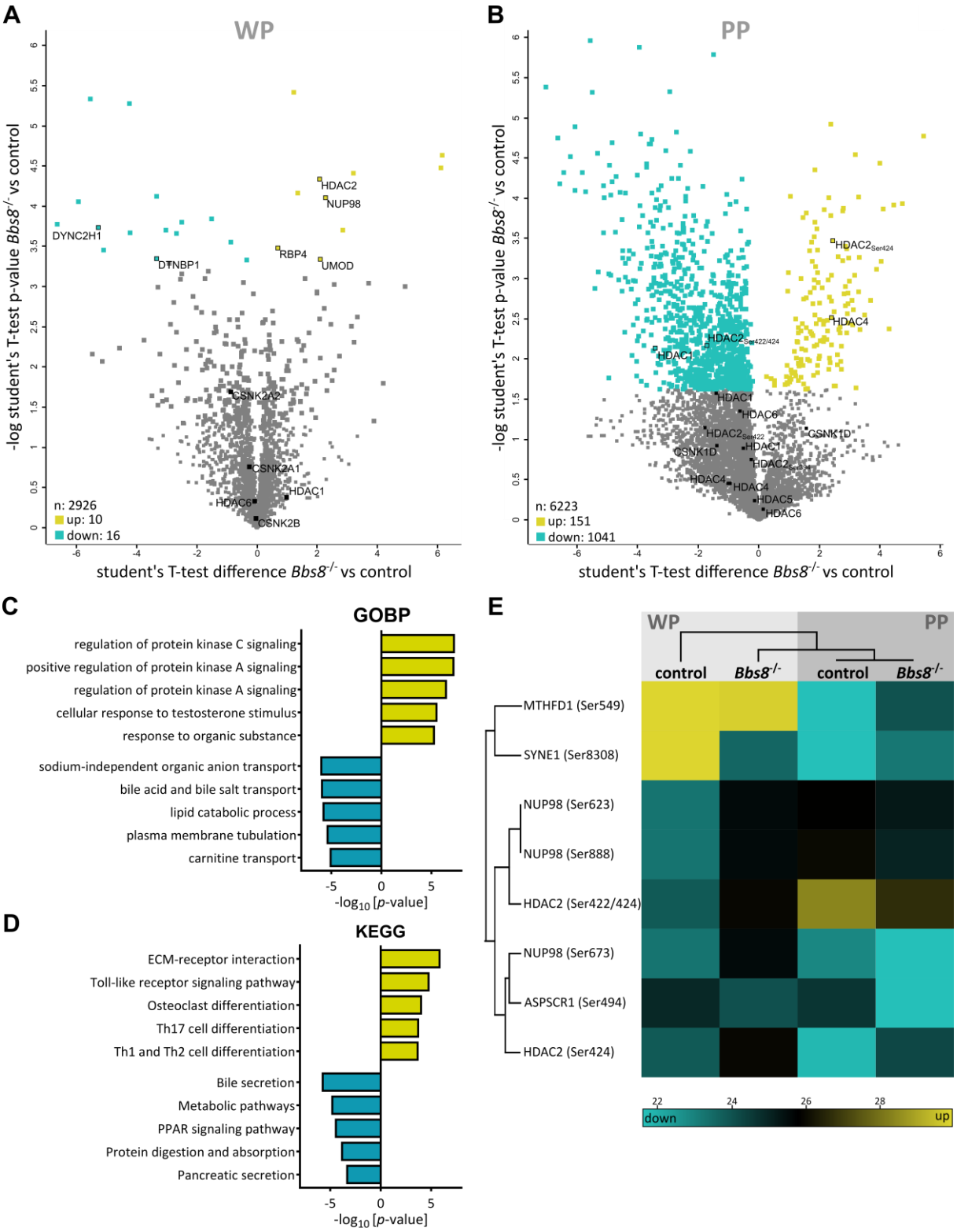
A
WP
-log student's T-test p-value Bbs8-/- vs control
student's T-test difference Bbs8-/- vs control
HDAC2
NUP98
DYNC2H1
RBP4
DTNBP1
UMOD
CSNK2A2
CSNK2A1
HDAC1
HDAC6
CSNK2B
n: 2926
up: 10
down: 16
B
PP
-log student's T-test p-value Bbs8-/- vs control
student's T-test difference Bbs8-/- vs control
HDAC2Ser424
HDAC4
HDAC2Ser422/424
HDAC1
HDAC1
HDAC6
HDAC2Ser422
CSNK1D
HDAC1
CSNK1D
HDAC2Ser424
HDAC4
HDAC4
HDAC5
HDAC6
n: 6223
up: 151
down: 1041
C
GOBP
regulation of protein kinase C signaling
positive regulation of protein kinase A signaling
regulation of protein kinase A signaling
cellular response to testosterone stimulus
response to organic substance
sodium-independent organic anion transport
bile acid and bile salt transport
lipid catabolic process
plasma membrane tubulation
carnitine transport
-log10 [p-value]
D
KEGG
ECM-receptor interaction
Toll-like receptor signaling pathway
Osteoclast differentiation
Th17 cell differentiation
Th1 and Th2 cell differentiation
Bile secretion
Metabolic pathways
PPAR signaling pathway
Protein digestion and absorption
Pancreatic secretion
-log10 [p-value]
E
WP
PP
control
Bbs8-/-
control
Bbs8-/-
MTHFD1 (Ser549)
SYNE1 (Ser8308)
NUP98 (Ser623)
NUP98 (Ser888)
HDAC2 (Ser422/424)
NUP98 (Ser673)
ASPSCR1 (Ser494)
HDAC2 (Ser424)
down
up

Figure 3

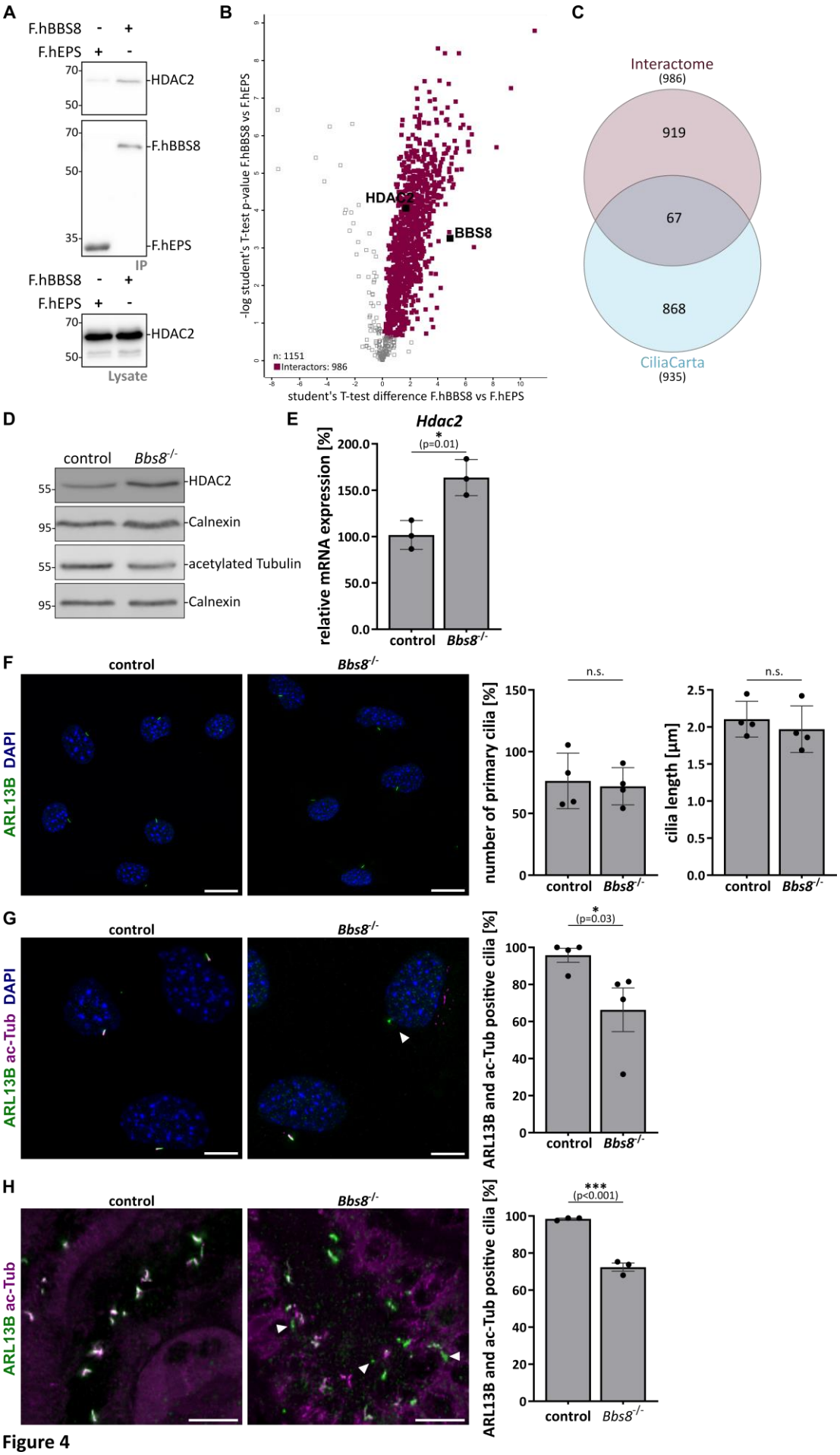
A
F.hBBS8 - +
F.hEPS + -
70
50
HDAC2
70
50
F.hBBS8
35
F.hEPS
IP
F.hBBS8 - +
F.hEPS + -
70
50
HDAC2
Lysate
B
-log student's T-test p-value F.hBBS8 vs F.hEPS
HDAC2
BBS8
n: 1151
Interactors: 986
student's T-test difference F.hBBS8 vs F.hEPS
C
Interactome
(986)
919
67
868
CiliaCarta
(935)
D
control
Bbs8-/-
55
HDAC2
95
Calnexin
55
acetylated Tubulin
95
Calnexin
E
Hdac2
*
(p=0.01)
relative mRNA expression [%]
200.0
150.0
100.0
50.0
0.0
control
Bbs8-/-
F
control
Bbs8-/-
ARL13B DAPI
n.s.
number of primary cilia [%]
150
100
50
0
control
Bbs8-/-
n.s.
cilia length [µm]
2.5
2.0
1.5
1.0
0.5
0.0
control
Bbs8-/-
G
control
Bbs8-/-
ARL13B ac-Tub DAPI
*
(p=0.03)
ARL13B and ac-Tub positive cilia [%]
100
80
60
40
20
0
control
Bbs8-/-
H
control
Bbs8-/-
ARL13B ac-Tub
***
(p<0.001)
ARL13B and ac-Tub positive cilia [%]
100
80
60
40
20
0
control
Bbs8-/-

Figure 4

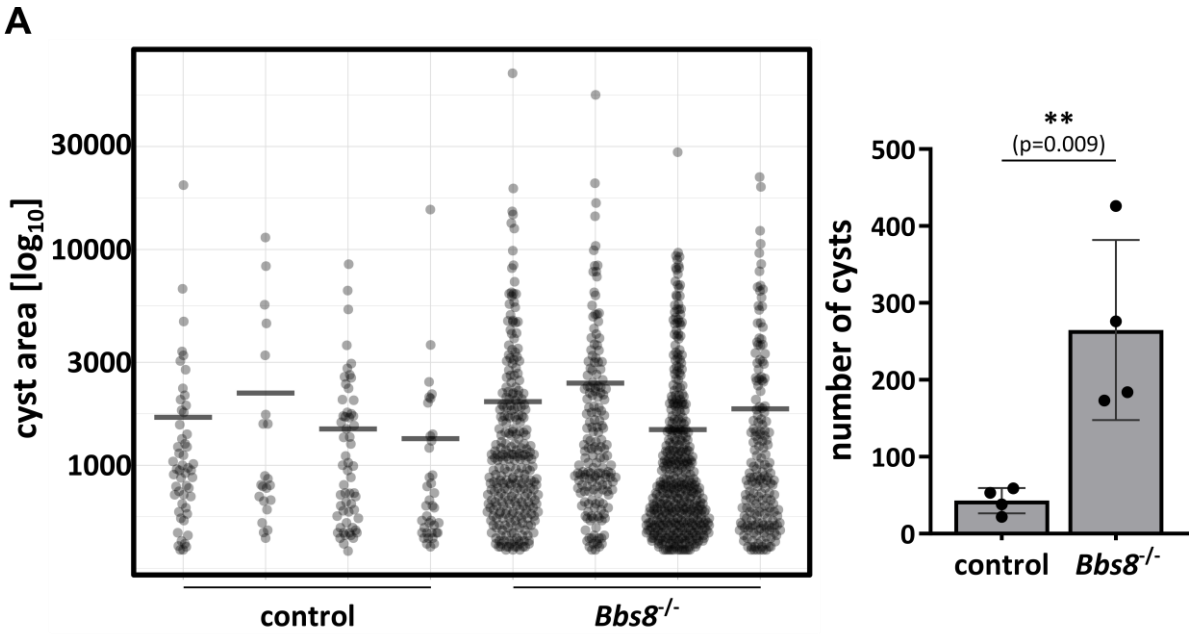

Supplementary figure 1

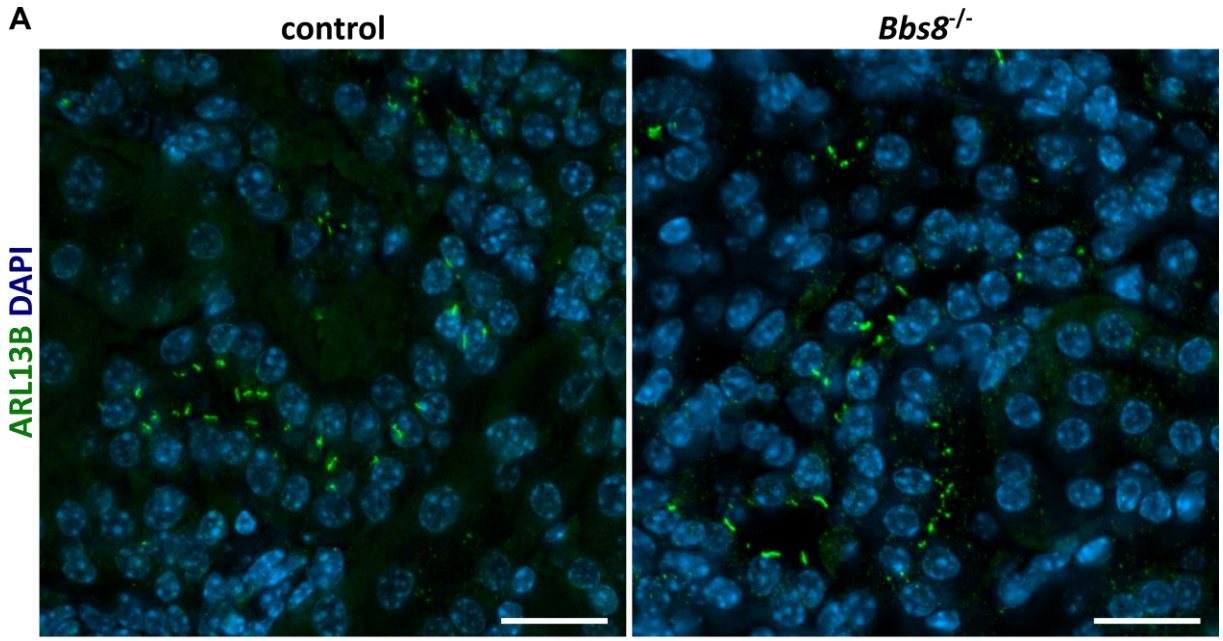

Supplementary figure 2

A

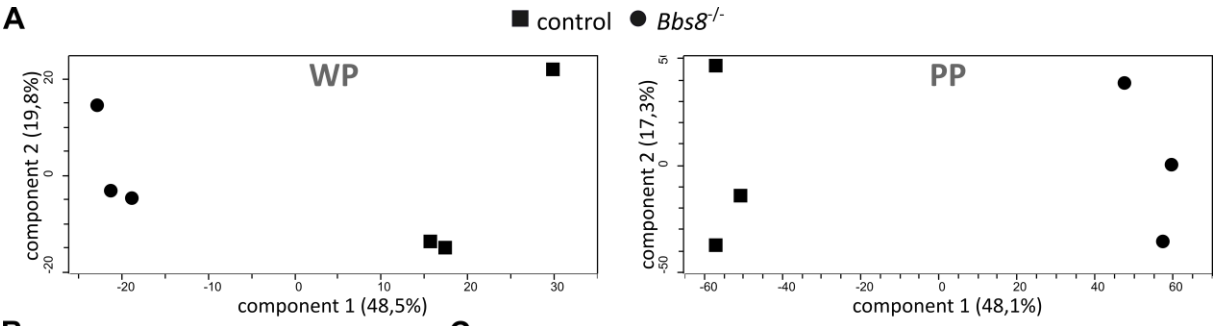

B

Up-Rregulated (-log p-value)		Down-Regulated (-log p-value)	
DCTN6	(5.41)	RBM22	(5.33)
THOC7	(4.63)	APOC1	(5.28)
AGO2	(4.47)	LYRM5	(4.92)
TTN	(4.41)	ACNAT2	(4.13)
HDAC2	(4.33)	GAR1	(4.05)
PARP3	(4.16)	ARHGAP18	(3.84)
NUP98	(4.10)	MRPL47	(3.80)
COPZ2	(3.70)	SYNE1	(3.77)
RBP4	(3.47)	DYNC2H1	(3.73)
UMOD	(3.33)	DAP	(3.70)
		UBE2V2	(3.67)
		NAA15	(3.66)
		ASPSCR1	(3.55)
		SUMO2	(3.46)
		DTNBP1	(3.35)
		MTHFD1	(3.33)

C

Residue	Sig. regulated	Phosphosite
HDAC2 Ser394	-	MLPHAPGVQMQAIPEDAVHED**S**GDEDGEDPDKR
HDAC2 Ser422	-	RIACDEEF**S**DSEDEGEGGRR
HDAC2 Ser424	up	RIACDEEFSD**S**EDEGEGGRR
HDAC2 Ser422/Ser424	down	RIACDEEF**S**D**S**EDEGEGGRR

D

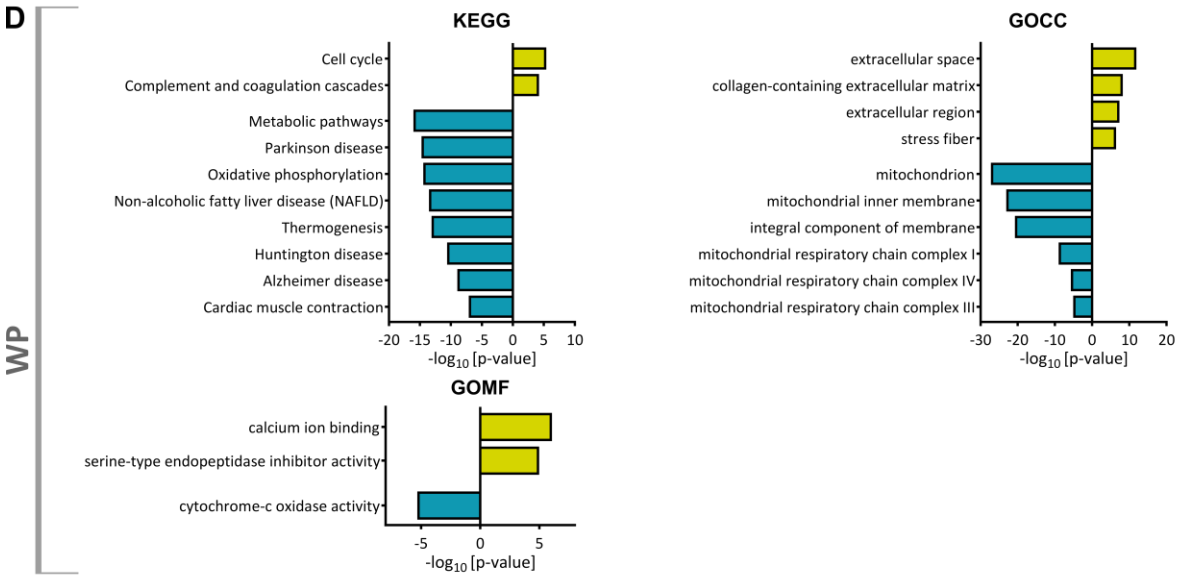

E

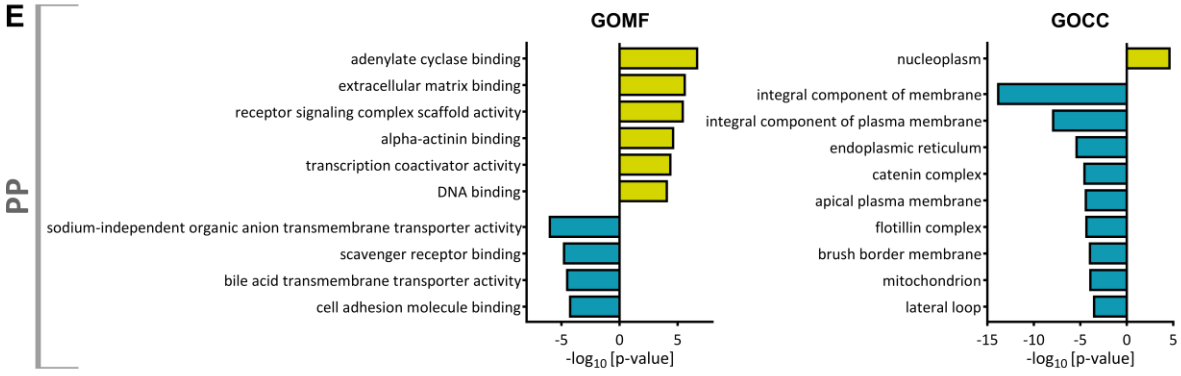

Supplementary figure 3

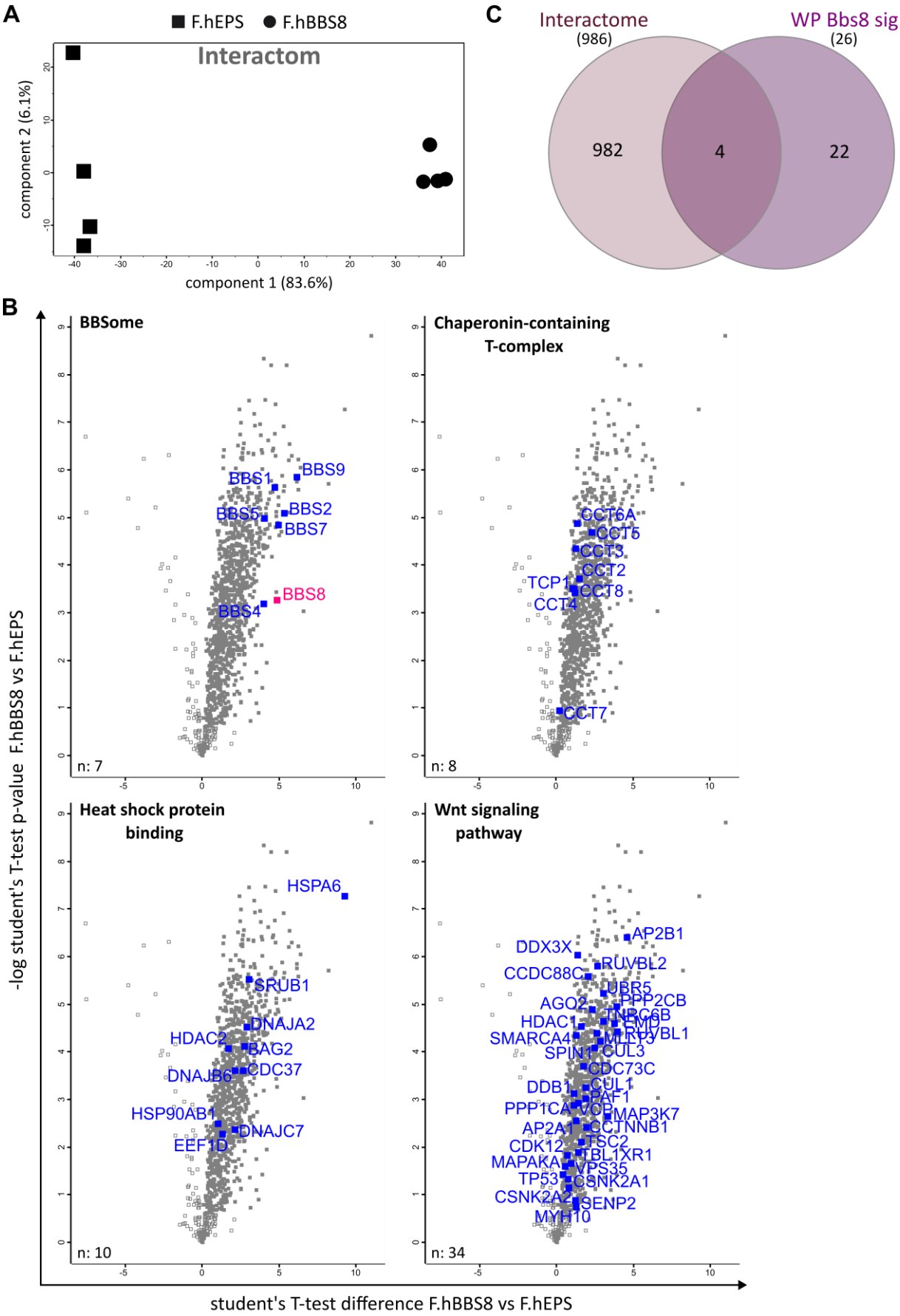

Supplementary figure 4

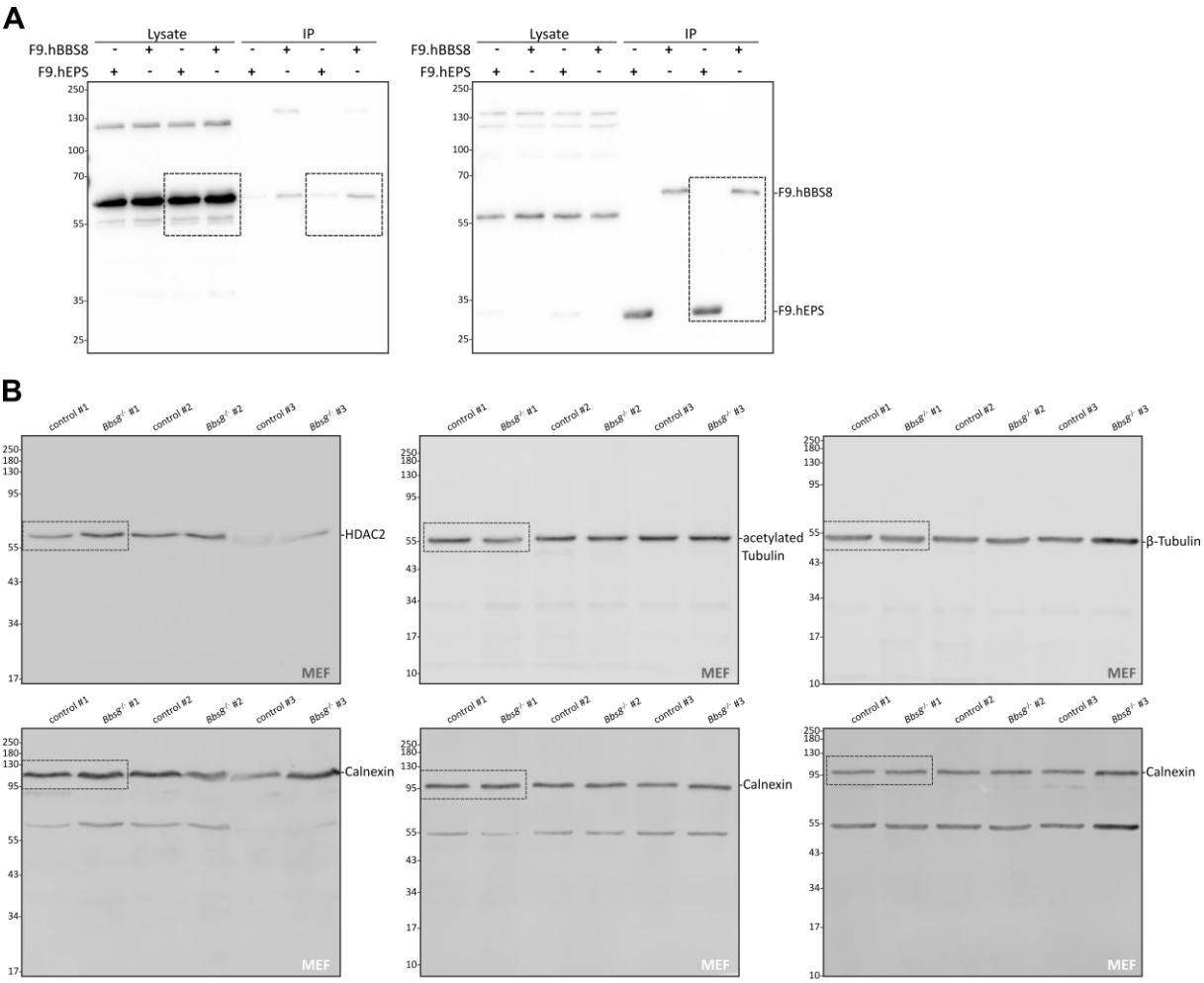

Supplementary figure 5

4. Discussion

Kidney pathologies in renal ciliopathies are characterized by loss of epithelial cells, cyst formation, growth, and, in some cases, interstitial fibrosis and inflammation [138,157]. This indicates that regulated cell death plays a role in the molecular mechanisms underlying kidney pathology. However, to date, the precise mechanisms and cell death pathways involved have remained unclear.

4.1 Primary cilia as a modulator for regulated cell death

Ciliopathies involving cystic kidney diseases are typically caused by pathogenic variants of ciliary genes leading to defects in the primary cilium or perturbation of ciliary signaling. To investigate if the primary cilium itself influences RCD signaling and pathway activation, mIMCD3 cells capable of forming primary cilia (=ciliated kidney cells (Ckc)) and mIMCD3 cells deficient in ciliogenesis (=non-ciliated kidney cells (Nckc)) were used to compare the outcome after induction of cell death. Through multiple cell death and viability assays, the RIPK3-dependent necroptosis pathway was found to be active in the absence of the primary cilium (Chapter 1). Upon RCD induction with a shift towards necroptosis, the presence of a primary cilium conferred protection. This effect could be rescued by RIPK1 inhibition. However, this does not explicitly confirm the activity of the necroptotic pathway, as there is also RIPK1-independent necroptosis [377] and RIPK1-dependent apoptosis [378]. Notably, RIPK3 inhibition led to the same rescue effect, confirming ongoing necroptosis.

It is important to point out that the investigation of ciliated cells and further examination of the role of the primary cilium *in vitro* is accompanied by the challenge that proliferating cells do not assemble a primary cilium [379]. Therefore, ciliogenesis in proliferating cell lines typically has to be induced by serum starvation, in order to stop proliferation and enhance the number of ciliated cells [28]. This might result in side effects due to both anti-proliferative signalling and the loss of factors normally present in FBS, which could affect multiple signalling pathways, including RCD. Therefore, experiments using serum starved and non-serum starved cells would not allow any conclusion about the role of cilia. Notably, in our study, viability assays were done in cells without serum starvation, since the selected subclones showed a significant difference in ciliation under these conditions. Nevertheless, this is not the only factor to influence the experimental outcome. *In vitro* cell culture experiments are always accompanied by a potential instability of the cell genotype. It is known that cell lines with high passage numbers are more prone to mutations and epigenetic changes and are further vulnerable to viral contamination [380,381]. Consequently, proliferation rate, metabolic capacity, or general cell health can change dramatically and, therefore, produce cross-contaminated and misidentified cell lines with a high heterogeneity [382]. It is feasible that these effects can be even more pronounced in transgenic cell lines. Keeping this in mind, we made use of the subclones Ckc and Nckc, which originate from the

same mIMCD3 parental cell line, however had a high passage number to begin with. Therefore, we cannot exclude the possibility of genetic drift. One additional lose end of the experimental data is that the molecular reasoning underlying the loss of Nckc ciliogenesis is unknown. Nowadays, there are methods to differentiate between changes due to single nucleotide polymorphisms within a CRISPR/Cas9 genetically mutated single-cell line [383]. For this reason, it would be interesting to perform karyotyping for chromosomal abnormalities to identify the acquired genetic mutations [384] or to perform deep sequencing of the cell lines. To control for unspecific clonal effects, additional experiments were performed in another cell line which displays significantly reduced ciliogenesis, namely the *Myo5a* knockout [365,385]. As expected, the *Myo5a*$^{-/-}$ cells were also partially protected from necroptosis in the cell viability assay as compared to their parental control line, showing the same trend as before with Nckc (Chapter 1). The milder effect observed in cells lacking *Myo5a* can be attributed to the fact that these cells do not exhibit a complete loss in ciliogenesis (5% remain ciliated) and only 40% of the control population used in this setting bear cilia. Therefore, the difference in cilia numbers is much less pronounced than in the Ckc and Nckc cells (>80% vs. <10% ciliated cells). To investigate cell death in relation to the primary cilium in more depth, further knockout cell lines for additional essential ciliary proteins could be generated, to shed light on whether all conditions respond in the same way. In addition, it would be striking to investigate, to what extent the observed effect is specific for renal epithelia cells and how other cell types with defective ciliogenesis react to the induction of cell death.

An additional limitation of the viability assays and work on cell death in cell culture is the absence of inflammation and other triggers from surrounding tissues. Consequently, it was crucial to use an *in vivo* model with defective ciliogenesis. Since the complete knockout of essential genes for ciliogenesis is embryonic lethal, we generated a conditional knockout model where the loss of ciliogenesis is restricted to cells of the distal tubule and collecting duct [386]. In principle, mouse models in which IFT is inhibited are suitable for such studies, either through the loss of individual IFT proteins or through the loss of motor proteins. We chose to focus on KIF3a, a kinesin subunit that is essential for anterograde IFT. To achieve a knockout in the renal epithelium, we used a floxed allele of Kif3a and a Ksp:Cre mouse line that expresses Cre in the distal tubules and the collecting ducts (=*Kif3a*^{tKO}). Experiments in the transgenic Kif3a^{tKO} confirmed a histological upregulation of RCD through multiple positive TUNEL events, as well as increased RNA transcription and protein expression of RIPK3 in 28-day-old animals (Chapter 1).

In summary, our study shows that the loss of the primary cilium *in vivo* closely mirrors observations *in vitro*, and influences RCD by increasing the susceptibility for necroptosis and, subsequently, inflammation. These *in vivo* results are consistent with additional studies, in which the deletion of primary cilia, by the knockout of either *Kif3a* or *IFT88* in the intestinal fibroblasts treated

with dextran sodium sulfate, a chemical colitogen to induced colitis, showed stimulation of inflammation and led to an increase of macrophages [387,388]. Furthermore, the level of IL-6 positive cells in these mice is upregulated, proving once more that the loss of the primary cilia increases the susceptibility to inflammation. This could also be shown in another animal model, namely the knockout of *Cdc42*, with a reduction in ciliogenesis, which showed an increase of apoptosis and cyst formation in embryonic kidneys [389]. Inflammatory signalling dependent on primary cilia was also confirmed in injected mice with bacterial-derived compound lipopolysaccharide (LPS),which mimics the entrance of microbial-derived products and therefore, induces inflammatory response [390,391]. This primarily led to a decrease in ciliary length, resulting in an increase of IL-1β-induced NF-κB signalling, revealing a role of primary cilia in the NF-κB pathway. Notably, extra ciliary functions of ciliary proteins have also been described to influence this pathway. RNA-sequencing (RNA-seq) analysis showed that IFT88 regulates the pro-inflammatory genes *Nos2*, *IL-6* and *Tnf*, modulating cytosolic NF-κB translocation dynamics [392].

Taken together, this data shows that primary cilia can act as a safeguard to protect the cells from undergoing regulated cell death. Hence, the role of the primary cilium in controlling RCD pathways and shaping the response upon cell death induction in renal epithelia cells is crucial and worthy of further investigation.

4.2 Ciliopathy mutations and complete loss of cilia in RCD regulation

Our *in vitro* data showed the influence of the total absence of the primary cilia on RCD. However, in most renal ciliopathies there are subtle changes in cilia morphology and function rather than a complete loss of the primary cilia. Under normal conditions, mice are not viable upon complete cilia deletion and die shortly before metanephric kidney development [43,45]. To overcome this issue and investigate the role of the primary cilium *in vivo*, the Cre-loxP system can be used to delete the target DNA sequences of the *Kif3a* gene in a tissue specific manner [393–395]. LoxP sites were placed at the 3' and 5' end of the *Kif3a* allele (floxed allele) and incorporated during homologue recombination into the germline. To generate kidney-specific deletion of the primary cilium, animals carrying the floxed *Kif3a* allele were crossed with Ksp:Cre [366] animals. This *Kif3a* transgenic knockout is characterized by the loss of the primary cilium specifically in distal tubules leading to activated necroptosis in the kidney and, therefore, to cystic kidneys. This mouse model is described as having normal primary cilia at birth (P0) with sustained cilia loss over time, with some tubule cells still ciliated at 4 weeks of age (Chapter 1) [45]. In this framework, it is important to note that loss of the primary cilium is not the actual process that induces cell death, but that it increases the susceptibility for RCD. This is also in line with studies in cisplatin-induced AKI in animals with an *Ift88* knockout in the proximal tubules [396]. Here, in the absence of *IFT88*, the apoptosis activity was increased; however, the level of autophagy marker LC3B was decreased. This is in contrast to our *in vitro* proteome data in which an upregulation of the

autophagy markers LC3 and SQSTM1/p62 was observed (Chapter 1). Nonetheless, it was shown that the SQSTM1/RIPK1 module connects the autophagosome with the necrosome and, therefore, it is involved in an active switch between apoptosis and necroptosis [288]. Therefore, the autophagosome seems to be more active in non-ciliated cells and through this it supports the susceptibility to necroptosis. Further investigations with *Kif3a*^{tKO} mice need to be done to gain insights into the role of the autophagosome *in vivo* in relation to the absence of the primary cilium.

In patients, subtle structural and functional defects typically occur with deregulated ciliary signalling, rather than a complete loss of this organelle. For example, in ADPKD the phenotype is described as ciliary length-dependent, highly influenced by the activity of polycystin. Elongation of primary cilia was found upon induced inactivation or by a conventional knockout of *Pkd1* or *Pkd2.* In addition, patients and mice display increased fibrosis, therefore, ADPKD was linked to apoptosis and inflammation [397,398]. Interestingly, the simultaneous knockout of *Ift88* and *Pkd2* inhibits cyst growth, by reducing the ciliary length and normalization of Wnt and mTOR pathway activation, [397]. It has also been shown, that the in the knockout of *Pkd1,* cyst formation is reduced, by the additional knockout of ciliary proteins like *Kif3a* [399]. This stresses the fact that a structurally intact primary cilium is required to promote cyst growth and therefore plays an intriguing role in cystogenesis.

It is important that the ciliary elongation was also found in ADPKD patients [397]. In contrast, many other ciliopathies are described with truncated primary cilia such as in NPH and NPH-RC: BBS, PKD and Alström Syndrome [400]. *Nphp9*/*Nek8*$^{jck/jck}$ mice show a recessive juvenile cystic kidney disease phenotype, therefore, resembling NPH and they harbour a point mutation in a known NPHP gene [401]. Surprisingly, *Nphp9*/*Nek8*$^{jck/jck}$ mice were also described to present longer primary cilia when compared to wildtype, contrasting to the ciliary expression in human NPH [402]. Nevertheless, this mouse model already develops a severe cystic kidney phenotype by the age of 2 weeks due to increased RCD (Chapter 2). Additionally, they exhibit an upregulation of fibrosis and pro-inflammatory cytokines, as well as the regulation of necroptosis. Remarkably, the pyroptotic cell death pathway seems to be dysregulated, as well. The question of whether *Nphp9*/*Nek8*$^{jck/jck}$ is a model for NPHP is not entirely clear. The affected gene, the early age of manifestation, and the recessive inheritance fit well with NPH, as does the interstitial fibrosis. However, the highly proliferative aspect of the cystic kidneys also shows parallels to ADPKD. Other NPH models often have a late onset phenotype, which can remain mild. In our facility, both NPHP7 and NPHP10 knockout animals only exhibited a subtle phenotype at one year of age. Therefore, we discontinued initial experiments and breeding with these animals and focused our efforts on other models such as *Nphp9*/*Nek8*$^{jck/jck}$.

In contrast to *Nphp9*/*Nek8*$^{jck/jck}$, ciliary length is not affected in the conventional knockout of *Bbs8* (Chapter 3). The *Bbs8*$^{-/-}$ model is characterized by a mild and slowly progressing renal phenotype, which correlates well with the NPH-RC ciliopathy BBS. Even though the ciliary length appears to be

unaffected, the loss of acetylated tubulin could destabilize primary cilia and, therefore, contribute to this mild phenotype. This destabilization might be caused by the upregulation of the deacetylase HDAC2 (Chapter 3). In the past, patients with pathogenic variants of *BBS8* have been described to suffer from retinopathy, obesity and other symptoms related to BBS [403]. Although, *Bbs2*, *Bbs4* and *Bbs10* knockouts, are described with a renal phenotype, which is more or less limited to the glomeruli and podocytes [404–406], the majority of investigations into this disease focused on the eye [108,407–409]. The retina of the eye contains photoreceptor cells of which the outer segments are regarded as highly specialized axonemes of primary cilia, which are essential for vision [410]. The outer segments are connected with the photoreceptor cells by connecting cilia, which are modified ciliary transition zones [411,412]. It has been already described that mice lacking *Bbs2* or *Bbs4* develop retinopathy with increased apoptotic activity, which led to retinal degeneration in the outer nuclear layer of the eye [405,413]. Interestingly, RIPK3-mediated necroptosis promotes neuroinflammation in diabetic retinopathy [414]. This shows that RCD in ciliopathies needs to be more widely examined, particularly in BBS. Indeed, it is not yet clear to which extent cell death in photoreceptor cells is comparable to, for example, the renal tubular cells. In our *Bbs8*$^{-/-}$ model, we were able to show an upregulation of pro-inflammatory cytokines, immune cells, and fibrosis, all together with an upregulation of pyroptosis marker (Chapter 3). This could indicate that the renal phenotype of this mouse model is more systemically affected with the inflammation pathway, pyroptosis, than by the local inflammation of necroptosis. Interestingly, such a border systemic influence has been shown for BBS10. The total knockout of BBS10 leads to obesity, retinal degeneration and polyuria [404]. However, these systemic effect in *Bbs10*$^{-/-}$ primarily affected the podocytes and glomeruli in the kidney. In the *Bbs8*$^{-/-}$ glomeruli, we did not prominently observed damage. Using a BBS8 floxed allele for a kidney tubule specific knockout could help to address the question, to what extent the knockout affects other organs and tissue, and if indeed due to systemic inflammation other symptoms might occur.

Overall, the data shows that the aberrant activity or the absence of primary cilia do both influence RCD in a similar fashion, potentially influenced by gene-specific mutations. In conclusion we have found evidence to support the hypothesis that the primary cilium is involved in shaping the cell death response and, additionally, in regulating the switch between different RCD pathways.

4.3 Extrarenal manifestations and systemic inflammatory signalling in ciliopathies: lessons from the BBS8 mice

To shed light on the environmental influences on RCD in the context of ciliopathies, we compared *Nphp9*/*Nek8*$^{jck/jck}$ with *Bbs8*$^{-/-}$ mice. The phenotype of *Nphp9*/*Nek8*$^{jck/jck}$ animals is regarded as severe kidney disease, typical for either NPH or ADPKD [101–105]. Fortunately, in mice, the development of cysts is described as a painless process, unlike in humans, as deduced by observing no aberrant behaviour

in affected animals [415]. In contrast to human ADPKD or NPH, the *Nphp9*/*Nek8*$^{jck/jck}$ model does not develop any symptoms in other organs. The *Bbs8*$^{-/-}$ mouse, on the other hand, mirrors nearly all the symptoms described in BBS8 patients, and, therefore, of the archetypical ciliopathy BBS. In 2003, the first patient family was described with a mutation in BBS8. The affected individuals presented with developmental delay, polydactyly, situs inversus, *retinitis pigmentosa,* obesity, and were additionally described to develop renal disease and display cognitive impairment, like other pathogenic variants of BBS [182,416]. In the *Bbs8*$^{-/-}$ mouse, previous studies revealed rapid onset of retinal degeneration, as well as significantly altered retina pigment epithelium homeostasis and function, essential for sustaining photoreceptor cells and visual function [108,109]. *Situs inversus* was not observed in our mouse model; however, work in zebrafish suggested that BBS8 is required for left-right asymmetry [417]. Polydactyly could be observed in very few of the investigated animals (data not shown). Both the visual phenotype as well as polydactyly is most likely associated with dysfunction of the primary cilium. Also, the observation that all of our *Bbs8*$^{-/-}$ mice were obese(Chapter 3), could be related to dysfunctional ciliary signalling in the brain, leading to hyperphagia [418]. Strikingly, we found a late-onset kidney phenotype, with a slow progression of cyst formation in the *Bbs8*$^{-/-}$ mice (Chapter 3). Cysts were mainly observed in the distal tubules and were accompanied with ongoing cell death and DNA damage. Positive TUNEL and γH2AX suggested involvement of RCD, but can also indicate genome instability and double-strand breaks [419–421]. Levels of specific cell death markers for necroptosis, like *Ripk3*, were not significantly increased as in the previous *in vitro* data of mIMCD3 cells, the *Kif3a*^{tko} or *Nphp9*/*Nek8*$^{jck/jck}$ mouse kidney samples (Chapters 1-3). Instead, the markers for pyroptosis genes like *Nlrp3*, *Casp11* and *GsdmD* were found to be upregulated in *Bbs8*$^{-/-}$ mice (Chapter 3). The only symptoms which might not have a direct link to ciliary dysfunction was the observed liver phenotype of non-alcoholic fatty liver disease. Therefore, this needs to be handled as a possible secondary symptom (Supp. Fig. 1). Interestingly, in BBS patients this liver phenotype is rare [422,423]. Since the majority of the symptoms are affected by the primary cilium, it cannot be excluded, that the observed inflammation only a contribute to severeness of the clinical picture.

The observed increase of IL-6 levels in the kidney of *Bbs8*$^{-/-}$ could indicate a potential systemic inflammation. IL-6 is important as a warning signal for the regulation of direct or indirect promotion of inflammation [424]. It is produced in response to infections and tissue injuries and is known to be disseminated to the liver through the blood stream [425], although the macrophages of the liver itself are one of the main sources of IL-6 release [426]. In CKD and ESRF patients, an increased IL-6 level is commonly observed, which accumulates alongside the further impairment of renal function [427–429]. However, our data does not indicate a higher expression of IL-6 in the liver, for this reason further analysis of the of the liver needs to be performed. In order to gain deeper insights into the potential role of IL-6 in *Bbs8*$^{-/-}$, a more thorough examination of blood plasma regarding IL-6 concentration levels

need to be performed. Additionally downstream of IL-6 activated acute phase proteins such as C-reactive protein (CRP), serum amyloid A (SAA), and fibrinogen could give further insights of the level of inflammation [430,431].

The correlation between obesity and IL-6 inflammation has already been shown in mice with a diet-induced obesity [432], as adipose tissue is overall described to release inflammatory signals [433]. This holds true as, in the adipose tissue, the macrophages polarize towards the M1 stage and neutrophils influx which leads to an activation of Th1 and Th17 cells and an increase of pro-inflammatory cytokines such as IL-1, IL-6, and TNFα [434]. GO-terms which we also found to be upregulated in the *Bbs8*$^{-/-}$ mouse (Chapter 3). However, the effect of diet-induced obesity could be reduced in mice deficient for IL-6 receptor, which attenuates the chemokine CC-chemokine-ligand-20 (CCL-20) expression and, therefore, shifts macrophage polarization towards tumour-promoting macrophages [432]. Additionally, it has already been observed that the central application of IL-6 in mice suppresses feeding and improves peripheral glucose homeostasis through IL-6 activated signal transducer and activator of transcription 3 (STAT3) signalling in hypothalamic neurons [435]. Furthermore, IL-6 knockout animals under a high-fat diet showed abnormalities in the phenotype and function of the kidney [436]. Through this, it is highly likely that the BBS phenotype is supported by systemic inflammation. To further prove this theory, a double knockout mouse for *Bbs8* and IL-6 could give insights into the role of IL-6, and thus inflammation, in the development of several BBS symptoms. The potential influence of obesity triggered inflammation to the clinical picture, as well as correlations between obesity and severity of other symptoms needs to be further investigated as BBS patients displaying obesity develop inflammation during early childhood, mainly caused by hyperphagia [437]. For example, if indeed *Bbs8*$^{-/-}$ mice also suffer from hyperphagia, a calorie restriction study could be performed in order to understand if the overall phenotype is reduced or limited through less systemic inflammation. It has already been shown that the depletion of *Bbs12* in pre-adipocytes promotes the development of adipose tissue which is driven by both hyperplasia and adipocyte hypertrophy [438,439]. This observation correlates with the clinical features of overall BBS patients [440]. Additionally, mice lacking BBS4 or BBS6, but not BBS2 show additional resistance to leptin, which is a known hormone expressed in fat cells that regulates energy balance by suppressing hunger [441,442]. Pair-feeding (matching the amount of food consumed) in these mice led to normalized body weight; however, the level of adiposity still increased [441]. Through this, one can suggest that the BBSome has additional effects in other tissues. Further, it would be interesting to determine if this effect only occurs in ciliopathies with the symptom of obesity. Therefore, the research could be extended to Almström syndrome, which is so far the only other ciliopathy accompanied by obesity [443]. This would provide more insights into the role of obesity in RCD and overall inflammation in ciliopathies. Nevertheless, calorie restriction is not an optimal therapeutic intervention in patients. Here, the first clinical trials using a medication with the melanocortin-4

receptor agonist, or with the drug setmelanotide, showed positive effects in BBS patients regarding obesity [444,445]. These treatments, besides calorie restrictions, in the BBS mouse models could help to investigate the influence of obesity to the overall phenotype, and if therapeutic interventions also affect other symptoms.

Even though we also found an upregulation of IL-6 in the *Nphp9*/*Nek8*$^{jck/jck}$ (Chapter 2), no additional symptoms were observed and the necroptotic cell death was potentially stronger regulated than the higher inflammatory pyroptosis pathway. Nevertheless, it cannot be stated that indeed systemic inflammation is occurring in BBS, although there is evidence for its contribution. In conclusion, these data support the notion that both renal and extrarenal symptoms in NPH-RC, specifically in the *Bbs8*$^{-/-}$ model, cannot be regarded as isolated phenomena restricted to specific organs. Instead, they both cause and respond to systemic influences and may thus be interconnected in a multidirectional fashion. This could include systemic effects of adipositas, kidney failure or liver disease or an overall increased inflammatory activity.

4.4 Inflammation in kidney disease as part of the phenotype in ciliopathies

In more than two decades of kidney ciliopathy research, the focus has primarily been on the primary cilium and the respective tubular epithelial cells. However, as mentioned before, renal ciliopathies, like NPH, exhibit not just cyst development, but massive interstitial fibrosis and inflammation which is part of the histological triad characterizing NPH. Therefore, it will be important to decipher the role of immune cells and inflammatory signalling in the pathogenesis of renal ciliopathies. Inflammation is a biological response of the immune system and, therefore, accompanied by an increased level of immune cells and immune mediators such as cytokines, and it is known to trigger fibrosis [446,447]. Thereby the inflammatory response is dependent on the encountered stimuli. These stimuli depend on different classes of germline-encoded pattern-recognition receptors families, like TLRs or NLRs, which detect pathogen-associated molecular patterns (PAMPs) or damage-associated molecular patterns (DAMPs) and trigger inflammation [448–450]. TLR signalling is primarily mediated by the adaptor protein myeloid differentiation factor-88, which controls the nuclear translocation of different transcription factors like NF-κB [448]. Cytokines such as IL-1β, IL-6 and TNF mediate inflammation by receptor activation (TLRs, IL-1R, IL-6R and TNFR), and trigger important intracellular signalling pathways like JAK/STAT, MAPK and NF-κB [451,452]. This promotes pro-inflammatory cytokine production and inflammatory cell recruitment.

Single-nucleus (sn) RNA-seq data of *Nphp9*/*Nek8*$^{jck/jck}$ mice generated in this thesis showed a relative increase of immune cells in the knockout mice compared to the control (Chapter 2). The increase of T-cells was further supported by the increased numbers of positive $CD3^+$ events, which was found in the *Nphp9*/*Nek8*$^{jck/jck}$ model but also in the *Bbs8*$^{-/-}$ mice (Chapters 2 and 3). In the case of the

Bbs8$^{-/-}$ mice, additionally activated NF-κB was observed. It has already been described that the NF-κB-regulator *NFκBiz*, member of the IκB family, is downregulated in AKI compared to the control [453]. Furthermore, the authors showed that *NFκBiz* regulates NF-κB-mediated response for example to the release of inflammatory cytokines, in a gene-specific manner. The investigation of cytokines revealed an upregulation of the inflammatory marker IL-6 in kidneys of the *Bbs8*$^{-/-}$ mice, and even more pronounced in *Nphp9*/*Nek8*$^{jck/jck}$ mice (Chapters 2 and 3). Therefore, similarly to the Bbs8 model, the NPH model *Nphp9*/*Nek8*$^{jck/jck}$ would be an ideal candidate for an additional knockout of IL-6 to understand the impact of IL-6 in disease progression. In addition, serum levels as well as the source of IL-6 should be investigated. The difference in the presence of pro-inflammatory cytokines could explain the milder renal phenotype of the *Bbs8*$^{-/-}$ mice. Nonetheless, both models showed renal fibrosis (Chapters 2 and 3). Moreover, inflammation has already recently been suggested to shape the phenotype in ADPKD [454]. Here, the authors investigated inflammation in the tubule-specific knockout of *Pkd1*. They could show increased $CD3^+$ as well as increased macrophages. Interestingly, the double knockout of *Pkd1* and of the transcription factor, STAT3 suppressed the expression of pro-inflammatory cytokines and further ameliorated the phenotype of the *Pkd1* knockout. Therefore, the authors suggested that STAT3 is not a driver of cyst formation but rather influences the crosstalk between immune and tubular cells. This is interesting as STAT3 is not only a general driver of pro- and anti-inflammatory crosstalk but also interacts with ciliary signalling [455,456]. *In vitro* data showed that the level of STAT3 is decreased in induced knockouts of either *Kif3a* or *IFT88,* which could indicate that the reduction of STAT3 *in vivo* would have a decreased ability to suppress cyst formation [454]. To resolve whether the level of STAT3 is also affected and pathophysiologically relevant in NPH or BBS, expression analysis followed by genetic experiments in mice, e.g. double knockouts, would be necessary. One way to further investigate chemo- and cytokines would be to perform a secretome analysis of various *Bbs8*$^{-/-}$ cells.

Nevertheless, we could show that inflammation has an important role within the pathogenesis of the kidney. Thereby, the pathogenesis is both initiated by RCD and concurrently further promoted by RCD. Therefore, the degree of inflammation could potentially serve as an indicator of the severity of the phenotype and the intensity of RCD in these situations.

4.5 The impact of Necroptosis in CKD

In the manuscript underlying the first part of this thesis, we found that the primary cilium influences cell death, specifically by inhibiting necroptosis. Cell death assays in murine Nckc cells showed that the induction of necroptosis could be rescued significantly by either inhibiting RIPK1 or RIPK3 (Chapter 1). *In vivo*, the impact of necroptosis in the kidney has been strongly investigated in AKI. Several studies showed a significantly increase of survival rates in mice lacking necroptosis players when AKI is induced

by IRI, compared to control mice [299,457,458]. As AKI increases the risk for CKD and *vice versa*, it could be assumed that the same RCD pathways in AKI play a role in CKD. Certainly, the kidney is an ideal organ for studying ischemia and cell death since, being a paired organ, it always presents the perfect control in experiments. Moreover, each kidney is typically supplied by a single artery without collaterals and their retroperitoneal location makes them easily accessible. Indeed, IRI experiments are relatively straightforward to conduct. Additionally, renal function can be assessed with relatively simple readout means. Consequently, numerous studies on RCD have utilized AKI in rodent kidney as a model. However, models for chronic, and particularly cystic, kidney diseases are more complex, and there is still a lack of extensive research in this field, even though experiments on AKI suggest an important role of RCD in CKD. It is still a challenge that the human phenotypes of renal ciliopathies are hardly reproducible in mice, even if the same mutation was induced or established 'disease genes' were deleted. One reason for these observations might be the sterile environment of animal housing, which influences the phenotypical development, but also the lack of genetic diversity in in-bred mouse strains or potential compensating mechanisms in the animals [459]. Another fact is the animal model's lifespan and age which might be crucial for the development of chronic diseases. For example, our self-made and validated CRISPR/Cas9-based knockouts of either *Nphp1* or *Nphp10* did not develop any obvious phenotype. In contrast, another *Nphp10* knockout mouse line was described to develop cortical cysts in the kidney already at P100 [169]. Notably, in our facility this mouse developed a much milder phenotype at a much later age (P548/1.5 years). Another mouse line, where we deleted *Nphp7/Glis2,* develops late-onset renal fibrosis with few cysts, in contrast to a previously described *Glis2* knockout mouse model with increased apoptosis and fibrosis starting at 8 weeks of age [167]. In conclusion, all of these models are not perfectly suitable for further investigations of RCD and potential therapeutic treatments. While previously working with the NPHP10 mice, we performed some experiments concerning RCD in which we only observed a weak effect of cell death in *Nphp10*$^{-/-}$ mIMCD3 cells and mice (data not shown). This limitation of standardized mouse models mimicking human disease prompted different approaches. We finally decided to primarily use the well characterized *Nphp9*/*Nek8*^{jck} mouse model. These mice carry a missense mutation in the *Nphp9* gene. Although this exact mutation has not been found in humans, these mice develop cystic kidney disease rather early on. In this mouse model, we were able to show that necroptosis plays an important role in the pathogenesis of the kidney. The expression of necroptosis markers was significantly increased in both mRNA and protein levels (Chapter 2). A simultaneous conventional knockout of *Ripk3*$^{-/-}$ in *Nphp9*/*Nek8*^{jck} showed an amelioration of the function and the cystic morphology of the kidney (Chapter 2), supporting the role of RIPK3 in the pathogenesis in *Nphp9*/*Nek8*$^{jck/jck}$. Surprisingly, these mice still presented a massive increase of inflammation (Chapter 2). Thus, the *Ripk3*$^{-/-}$ approach does not represent a total inhibition of cellular loss. At this stage, the activation of necroptosis as the prime

RCD pathway in this renal ciliopathy needed to be further ruled out by, for example, immunoblotting phosphorylated MLKL or RIPK3. As these antibodies do not work for these purposes, we are currently generating an additional knockout of *Mlkl* in the *Nphp9*/*Nek8*$^{jck/jck}$ mice. Using this specific model, we will be able to clarify whether in the knockout of *Ripk3*, the amelioration of renal function is caused by a necroptosis-independent function of RIPK3. Interestingly, an upregulation of key regulators of the pyroptosis were found in both in *Nphp9*/*Nek8*$^{jck/jck}$ mice as well as in *Nphp9*/*Nek8*$^{jck/jck}$ *lacking Ripk3* (Chapter 2). A transition towards pyroptosis, upon RIPK3 inhibition, could explain why the kidneys did not show a better outcome. It has already been shown that individual RCD pathways are tightly interconnected, in some contexts it was described as a linked regulation between necroptosis and pyroptosis: Casp3, Casp7 and Casp8 have a role in the activation of the NLRP3 inflammasome, and Casp8 can cleave GSDMD [460,461]. Furthermore, it was described that MLKL or RIPK3 could also activate NLRP3 and therefore, pyroptosis [462]. To investigate the potential role of pyroptosis in *Nphp9*/*Nek8*$^{jck/jck}$, we generated a knockout of *GsdmD*$^{-/-}$ in the *Nphp9*/*Nek8*$^{jck/jck}$ model. This mouse model showed a similar positive effect to the knockout of *Ripk3*$^{-/-}$ in *Nphp9*/*Nek8*$^{jck/jck}$, including the amelioration of the histological phenotype, as well as a significant improvement in the function of the kidney, however, to a slightly lesser extent than with the depletion of *Ripk3* (Chapter 2). Remarkably, even with the *GsdmD* knockout in *Nphp9*/*Nek8*$^{jck/jck}$, active pyroptosis could not be entirely ruled out as the RCD responsible for the *Nphp9*/*Nek8*$^{jck/jck}$ phenotype, as the increased transcription of *Nlrp3* and *Casp11* could still be observed. The same was observed for active necroptosis, as an upregulated transcription and increased protein levels of MLKL and RIPK3 were still detected (Chapter 2). This could indicate that the activation of NLRP3 inflammasome contributes to a GSDMD independent cell death or that the cell death is shifted towards necroptosis. This hypothesis could perhaps be addressed by the simultaneous knockout of *GsdmD* and *Ripk3* in the *Nphp9*/*Nek8*$^{jck/jck}$ mice. The crosstalk between necroptosis and pyroptosis was already shown in AKI in which a double knockout of *Mlkl* and *GsdmD* significantly improved the function of the kidney upon IRI compared to the single knockout of *GsdmD* [320]. An equal effect could be shown in cecal ligation and puncture induced sepsis. Here the single knockouts of *Ripk3* or *GsdmD* show an improved survival rate, however, the double knockout of *GsdmD* and *Ripk3* showed a much greater survival rate [321]. Additionally, in these animals the pro-inflammatory cytokine release of, for example, IL-6, IL-1β and TNF, were significantly further reduced compared to the single knockouts. In addition to genetic models of RCD, treatment studies with necroptosis (GSK872; Nec1s) or pyroptosis (CY-09; MCC950, VX-765) inhibitors could also be considered, as a future perspective for potential therapeutic approach [463]. Studies using Nec1 in AKI have already been executed, however, with on one hand mild improvements in renal damage and an increase in survival rates [299], and on the other a worsening of the phenotype in a *Pkd1* knockout [464]. Further, SNx induced cystic kidney disease in rats showed an amelioration of the phenotype upon treatment with Nec1; however, the effect was

even stronger in combination with zVAD [345]. This is in line with our *in vivo* results in which both apoptosis (Em) and necroptosis (Nec1s; GSK872) inhibitors are needed to show a prevention of cell death (Chapter 1).

In conclusion, we found clear evidence for increased necroptotic activity in *Nphp9*/*Nek8*$^{jck/jck}$, a model for cystic kidney disease with features of NPH. Necroptosis seems to be the prevalent cell death pathway which crosstalk's with pyroptosis and might represent a potential target for therapeutic interventions.

4.6 Cyst formation in distal tubules and loss of epithelial cells

The histological and functional analyses of our two ciliopathy models, NPH (*Nphp9*/*Nek8*$^{jck/jck}$) and BBS (*Bbs8*$^{-/-}$), revealed cyst formation, loss of epithelial cells as well as loss of function of the kidney (Chapter 2 and 3). Specifically, stainings for different cell types of the kidney unravelled that, in both models, the majority of cysts arise from the distal tubules, similar to what was observed in NPH or NPH-RC [465]. However, to date, there have been only limited studies addressing cystogenesis in such models. One study on an *Nphp1* mouse model described the renal cellular transcription landscape based on *Nphp1*$^{del2\text{-}20/del2\text{-}20}$ showing overrepresented distal convoluted tubule cells [466]. Within this cell population, the authors were able to detect the downregulation of genes associated with tubular development and kidney morphogenesis. Furthermore, similar to our results, they could also confirm that some of these distal convoluted cells become arrested at an early stage of differentiation and, therefore, proliferate to form cysts. Nevertheless, the exact mechanisms of cyst formation remain unclear. In ADPKD, cyst formation is influenced by many factors, known as the 'cyst probability landscape' [467]. Thereby, in combination with other factors of different biological processes, the PKD-protein level plays an important role. For example, in renal epithelial cells with a decreased level of functional PKD, cyst formation is significantly more likely. Single-cell (sc) RNA sequencing data from kidneys of control or ADPKD patients showed that besides the distal tubules, the proximal tubules, loop of Henle and collecting ducts also contributed to cyst formation [468]. This was identified in performed histology stainings, and later on by analysing the cell clusters of the snRNA-seq data for gene-expression signatures of PKD [468,469].

The renal phenotype of NPH and NPH-RC is, apart from cyst formation, characterized by loss of epithelial cells. Our first evidence of the loss of epithelial cells was found specifically on proximal tubule epithelial cells upon histology. Here, the amount of LTL-positive proximal tubules was reduced in *Nphp9*/*Nek8*$^{jck/jck}$ compared to controls (Chapter 2). Although we could not quantify the actual loss of proximal tubule epithelial cells, we found further evidence in the snRNA-seq data set from renal tissue of our *Nphp9*/*Nek8*$^{jck/jck}$ mice, with a reduced percentage of these cells compared to the control. Interestingly, in cells of the proximal tubule of *Nphp9*/*Nek8*$^{jck/jck}$, several damage markers were also

increased, like lipocalin 2 (*Lcn2*=NGAL), clusterin (*Clu*) and secreted phosphoprotein 1 (*Spp1*). *Lcn2* has already been previously described as a disease marker in FA-AKI [470], *Clu* modulates DNA damage triggered cell death [471], whereas *Spp1* is known to be present in the functions in tumour progression or modulating immune infiltration [472]. Nevertheless, even though we could show damaged or affected proximal tubule cells, this clustering is not sufficient to explain the real status of the cells. For example, damaged proximal tubule cells dedifferentiated for rapid proliferation and repair, thus losing some of the specific proximal tubule marker genes [473]. Therefore, these cells would potentially not be annotated as proximal tubules. For this reason, multiple annotation genes for cell types always need to be used. Additionally, the extension of these markers to differentiate between healthy, injured or aged in the different clusters could provide further in-depth information. Here, for example, the marker *Niban1* was identified as a specific molecular marker of cystic cells in both mice and humans [466] but also doublecortin domain containing 2 (*Dcdc2a*) was previously described as an injured proximal tubule marker additionally related to Wnt-signalling and regulation of the length of the cilium [474–476]. In NPH and PKD, the dysregulation of Wnt-signalling was described to play a role in the development of cysts through the involvement of β-catenin, which would make *Dcdc2a* also suitable as *a* potential cyst biomarker in proximal tubule cells [477]. In our data set, *Dcdc2a* is increased in the severely cystic *Nphp9*/*Nek8*$^{jck/jck}$ kidney, however, it is not proximal tubule specific (data not shown), whereas *Niban1* was not detected at all.

Remarkably, further knockout of *Ripk3* in *Nphp9*/*Nek8*$^{jck/jck}$ resulted in a great decrease in the level of *Lcn2* positive cells in proximal tubules. Notably, the amelioration of the kidney phenotype, which we observed in the cyst index of *Nphp9*/*Nek8*$^{jck/jck}$ *GsdmD*$^{-/-}$ mice, was not that clear in the snRNA-seq data. This weaker influence on transcription levels might be caused by the higher inflammatory impact of pyroptosis. It is known that the loss of pyroptosis could stimulate necroptosis [460–462], consistent with the upregulation of RIPK3 in these mice (Chapter 2). To ensure a restricted local effect, kidney-specific or, even more precisely, distal tubule-specific knockouts need to be generated. Together with this, future snRNA-seq data of isolated distal tubules may show cell death and ciliary signalling involved in the mechanism of cystogenesis.

In summary, our preliminary analyses of the snRNA-Seq data reveal a loss of proximal tubule cells and a significantly lower expression of damage markers in the knockouts of *Ripk3* and *GsdmD*. We now aim to develop and test hypotheses on the mechanisms leading to tubular damage as well as the distinct and common molecular and cellular details of how the loss of *Ripk3* and *GsdmD* ameliorates kidney pathology.

4.7 RCD as a therapeutic target in renal ciliopathies

Since primary cilia influence RCD, with necroptosis a predominant cell death pathway in cystic kidney disease, this leads to the question of to what extent RCD could be a potential target for therapeutic interventions. Our findings suggest that an early treatment focusing on the reduction of cell death and inflammation might be most beneficial. Certainly, this does not exclude the application of the same therapy at a later time point to decelerate its progression. Currently, almost all treatments in ciliopathies are designed to reduce symptoms and secondary complications. Thereby, most medications address symptoms like blood pressure, cholesterol and anaemia and patients require kidney replacement therapy, i.e. dialysis or transplantation, at later stages of the disease. Until now, there have been no clinical trials targeting RCD in either AKI or CKD patients. Our next steps, in the continuation of this project, would be to start preclinical studies in which we inhibit RCD pathway like for example necroptosis, i.e., Ripk3, in the mouse model. Since in renal ciliopathies inflammation and cell death occur in waves, this will influence our treatment strategy. For that reason, we believe it could be more effective to break the cycle of cystogenesis by applying 'stoss therapy', in which over a limited amount of time the treatment is performed before a longer break. This might additionally be advantageous as side effects would be reduced, eliminating the toxicity of longer treatments, and more convenient as it can reduce costs on the long run. In the longer perspective, it would be ideal to choose an application which specifically addresses the kidney, for example, by choosing a medication which could be efficiently filtered by the kidney, therefore reaching the target area, or manage to coat, for example, nanoparticles with specific agonists/antagonists of specific membrane proteins of tubular cells [478,479]. A pro-drug approach could also be of great value, due to the possibility of manipulating the drug release/activation characteristics, for example, only being active in the presence of acidic pH or by renal enzymes [480].

For many therapeutic strategies, an early diagnosis is essential and necessary for the best treatment efficiency. However, this is difficult as many renal ciliopathies develop insidious symptoms in the early onset of the disease, which are often not detected. Often, by the time of the diagnosis, the kidney function is already significantly altered. For this reason, it is of upmost importance to increase the knowledge of the early signs of disease and make doctors and patients aware of these signs, so that early treatment to prevent severe symptoms can be prescribed. The exact diagnosis can often be achieved more quickly through sequencing. Therefore, next-generation sequencing of patients with a certain symptomatic, or even in children from families with a known genetic disease, should be broadly available to identify specific mutations. Nevertheless, next-generation sequencing comes with a lot of technical challenges and ethical implications [481,482]. Another option, to improve early diagnosis and treatment, would be to develop molecular signatures for a variety of inherited disease and also cell

death, through which an adapted therapy could be applied. In fact, altered molecular signature might be of greater importance than the actual genetic diagnosis, due to the overlap between ciliopathies, both genetically and phenotypically. So far, one redeeming fact is that patients do not need to undergo a biopsy collection to be diagnosed with renal diseases like CKD. Almost all kidney defects are detectable via ultrasound and MRI imaging and, additionally, kidney function can be assessed biochemically from urine and serum [483]. This is a great advantage for patients; however, this does mean that researchers lack the opportunity to analyse patient material, for example, concerning RCD and inflammation and distinguish between so many nephropathies. There is still further non-invasive approach to investigate patient samples, which includes URECs (urine derived kidney epithelial cells), kidney tubuloids and kidney organoids, which can be cultured *in vitro*. These samples are derived from somatic cells, either cultured directly like URECs or reprogrammed to inducible pluripotent stem cells (iPSCs) [484,485]. These methods allow research in cells close to kidney physiology. Furthermore, it is also a good model to examine drug efficacy and toxicity in high-throughput screenings. With cells collected from patients with different mutations, it would also be possible to personalize therapeutic approaches. For this reason, therapeutic interventions against cell death could be tested in such models, although, without the factor of systemic inflammation. Therefore, there is still the need to investigate RCD *in vivo*. For example, *in vivo* experiments of *Ripk3*$^{-/-}$ mice with AKI revealed that RIPK3 promotes fibrosis; nevertheless, there is limited data for RIPK3 inhibition *in vivo* [347]. One *in vivo* study showed that in endotoxin-induced AKI, RIPK3 is upregulated, which could be attenuated by GSK872 [486]. The additional suppression of the proapoptotic protein Bax, by GSK872, further showed that Ripk3 is a potential target for prevention of endotoxin-induced AKI. Another study showed that GSK872 in LPS-induced acute lung injury and in rat spinal cord injury also reduces NLRP3 expression and inflammation [487,488]. For the other necroptosis marker, RIPK1, there are multiple studies in induced AKI which showed that the inhibition by Nec1s increases survival and reduces inflammation. In contrast, it has already been shown that a single dose of Nec1 did not prevent renal injury in FA-AKI at 48 h [312]. The daily injection of Nec1 reduced creatinine and urea levels in blood plasma but increased the expression of tubular cell injury marker LCN2 and cell death [470]. To date, the sole indication suggesting that this therapy could also mitigate effects in CKD has been observed in rat models. Following SNx surgery, levels of RIPK1 and RIPK3 rise eight weeks post-surgery [489]. Four weeks post-SNx surgery, the researchers administered a single dose of Nec1 to the rats, resulting in a significant improvement in kidney pathology and function, along with decreased expression of RIPK1, RIPK3, and MLKL.

This thesis provides compelling evidence that RCD is relevant to CKD. Specifically, necroptosis and pyroptosis were identified to contribute to renal ciliopathies, which can serve as mode for CKD. *In vitro* experiments demonstrated a significant rescue when necroptosis was inhibited using the RIPK3 inhibitor GSK872 upon simulated necroptosis (Chapter 1), and also *in vivo* an amelioration of the

function of the kidney was observed upon the knockout of *Ripk3* or *GsdmD*. However, further investigations need to be performed to understand the role of RCD more comprehensively. For instance, the developed phenotype could eventually be further improved by simultaneously knocking out *Ripk3* and *GsdmD*. According to my results, this joined deletion may also potentially prevent cystic kidney disease in the *Nek8*$^{jck/jck}$ mouse.

The acquired knowledge, coupled with the understanding that RCD is influenced by the primary cilium, prompts the question whether combined interventions targeting both ciliary signaling and RCD could be successful. However, further investigation into cyst development and cystogenesis as well as in the detailed function of primary cilia and RCD is required. Thus, this thesis might contribute to this growing body of evidence and encourages more research into this direction.

5. Conclusion

This thesis uncovers a novel and crucial role of the primary cilium in protecting renal epithelial cells from necroptosis. This establishes a connection between primary cilia and regulated cell death (RCD), thus shedding light on the complex interplay in renal ciliopathies between cyst formation, epithelial cell proliferation and hypersecretion on the one hand, and inflammation, cell death, and fibrosis on the other. Renal ciliopathies such as NPH or BBS still lack efficient treatments. A comprehensive understanding of these mechanisms is essential for the development of future therapeutic strategies and the research presented here lays the groundwork for understanding the underlying mechanisms that drive renal pathophysiology. Our findings in the *Nek8*$^{jck/jck}$ mouse, a model for NPH, demonstrated that cystic kidney disease is characterized by pronounced inflammation, increased cell death, and progressive renal fibrosis. It also revealed the increased expression of RIPK3. Strikingly, an amelioration of the kidney phenotype was observed upon concomitant deletion of *Ripk3*. Surprisingly, these animals showed an increase in inflammation by the upregulation of IL-6 and further evidence that pyroptosis might be activated, explaining the persistent though milder renal phenotype. Indeed, the deletion of *GsdmD* also ameliorated cystic kidney disease. This supports the fact that RCD pathways are tightly interconnected; thus, more knowledge of these interconnections in cystic kidney diseases is needed. Dysregulated RCD and inflammatory signalling were also observed in the BBS8 knockout mouse in the third part of this thesis. This mouse developed cystic kidney disease, with an upregulation of IL-6 and inflammation which might contribute to disease progression. Additionally, we found several key players known to cause cystic kidney disease significantly altered in the kidney tissue. In summary, all these findings hint towards an important role of RCD in the pathogenesis of cystic kidney disease and, as such, renal ciliopathies. RCD is certainly not the sole and primary cause of any of these diseases. This is also evident from the fact that loss of cilia itself does not cause increased cell death, rather it increases the susceptibility to cell death inducers. However, pharmacological inhibition of RCD in ciliopathies might be part of future therapeutic approaches. Such strategies involving the modulation of necroptosis or other RCD pathways hold promise for mitigating inflammation, cell death, and fibrosis. Bearing in mind that the extent of RCD is variable among different diseases, further in-depth analysis to define potential mechanisms needs to be performed. Thereby, particularly the BBS8 knockout model could be the foundation to investigate biomarkers for RCD and inflammation. For this reason, unbiased proteomic approaches and snRNA-Seq on these mice, but also in-depth analysis of treatment studies for ciliopathy models with specific antibodies (e.g. IL-6) or inhibition of necroptosis or pyroptosis, needs to be performed. Overall, it is exciting to see where research might lead, using meticulous fundamental biology research to understand the mechanisms of disease progression and to contribute to developing viable treatment options.

X. List of publications

Publications in Academic Journals

Emilia Kieckhöfer, Gisela G Slaats, Lena K Ebert, Marie-Christine Albert, Claudia Dafinger, Hamid Kashkar, Thomas Benzing, Bernhard Schermer. *Primary cilia suppress Ripk3-mediated necroptosis.* (2022) *Cell Death Discov* 2;8(1):477.

Seif El Din Abo Zed, Agnes Hackl, Katrin Bohl, Lena Ebert, **Emilia Kieckhöfer**, Carsten Müller, Kerstin Becker, Gregor Fink, Kai-Dietrich Nüsken, Eva Nüsken, Roman-Ulrich Müller, Bernhard Schermer, Lutz T Weber. *Mycophenolic acid directly protects podocytes by preserving the actin cytoskeleton and increasing cell survival.* (2023) *Sci Rep.* 15;13(1):4281.

Lioba Ester, Inês Cabrita, Michel Ventzke, **Emilia Kieckhöfer**, Marita Christodoulou, Amrei M Mandel, Paul Diefenhardt, Francesca Fabretti, Thomas Benzing, Sandra Habbig, Bernhard Schermer. *The role of the FSGS disease gene product and nuclear pore protein NUP205 in regulating nuclear localization and activity of transcriptional regulators YAP and TAZ.* (2023) *Hum Mol Genet*. ddad135

Preprint publications in academic journals

Emilia Kieckhöfer, Peter A Matthiessen, Lena K Ebert, Christina Klausen, Dagmar Wachten, Thomas Benzing, Helen May-Simera*, Bernhard Schermer*. *Loss of Bbs8 leads to cystic kidney disease in mice and affects tubulin acetylation through HDAC2*. (2024) BIORXIV/583949

Publications in International Academic Conferences

Oral presentation

Emilia Kieckhöfer, Gisela Slaats, Thomas Benzing, Bernhard Schermer. *Loss of primary cilia affects regulated cell death.* Embo Workshop, Dying in self-defense: Cell death Signaling in animals and plants (Crete, Greece May 2022), *flash talk*

Emilia Kieckhöfer, Thomas Benzing, Bernhard Schermer. *Primary cilia suppress Ripk3-mediated necroptosis.* Embo Workshop, Cilia 2022 (Cologne, Germany Oct 2022), *selected speaker*

Poster presentation

Emilia Kieckhöfer, Gisela Slaats, Thomas Benzing, Bernhard Schermer. *Loss of primary cilia affects regulated cell death.* Embo Workshop, Dying in self-defense: Cell death Signaling in animals and plants (Crete, Greece May 2022)

Emilia Kieckhöfer, Lena K. Ebert, Claudia Dafinger, Thomas Benzing, Bernhard Schermer. *Loss of Ripk3 ameliorates kidney architecture and function in the Jck model of cystic kidney disease.* Cologne Spring Meeting 2023 (Cologne, Germany Mar 2023)

Presentations and posters in the framework of the SFB1403

Oral presentation

Emilia Kieckhöfer, Gisela Slaats, Thomas Benzing, Bernhard Schermer. *Dissect the molecular pathways connecting nephronophthisis with RCD.* 1st PhD and Postdoc Retreat SFB1403 (Bad Honnef, Cologne Nov 2021)

Emilia Kieckhöfer, Thomas Benzing, Bernhard Schermer. *Primary cilia suppress Ripk3-mediated necroptosis.* 2nd PhD, Postdoc and PI Retreat SFB1403 22 (Mettmann, Germany Oct 2022)

Emilia Kieckhöfer, Thomas Benzing, Bernhard Schermer. *Regulated cell death and its role in ciliopathies*. SFB1403 Project presentation (Cologne, Germany Jun 2023)

Emilia Kieckhöfer, Lena Ebert, Thomas Benzing, Bernhard Schermer. *Regulated cell death in the pathogenesis of renal ciliopathies*. 3rd PhD, Postdoc and PI Retreat SFB1403 (Cologne, Germany Dec 2023)

Poster presentation

Emilia Kieckhöfer, Gisela Slaats, Thomas Benzing, Bernhard Schermer. *RCD as a consequence of mutation of cilia-associated genes.* 1st PhD, Postdoc and PI Retreat SFB1403 (Eitorf, Cologne Nov 2021)

Emilia Kieckhöfer, Gisela Slaats, Thomas Benzing, Bernhard Schermer. *Loss of primary cilia affects regulated cell death.* 2nd PhD, Postdoc and PI Retreat SFB1403 22 (Mettmann, Germany Oct 2022)

Emilia Kieckhöfer, Lena K. Ebert, Claudia Dafinger, Thomas Benzing, Bernhard Schermer. *Loss of Ripk3 ameliorates kidney architecture and function in the Jck model of cystic kidney disease.* 3rd PhD, Postdoc and PI Retreat SFB1403 (Cologne, Germany Dec 2023)

XI. Erklärung

Erklärung zur Dissertation

gemäß der Promotionsordnung vom 12. Marz 2020

Diese Erklärung muss in der Dissertation enthalten sein.

(This version must be included in the doctoral thesis)

„Hiermit versichere ich an Eides statt, dass ich die vorliegende Dissertation selbstständig und ohne die Benutzung anderer als der angegebenen Hilfsmittel und Literatur angefertigt habe. Alle Stellen, die wörtlich oder sinngemäß aus veröffentlichten und nicht veröffentlichten Werken dem Wortlaut oder dem Sinn nach entnommen wurden, sind als solche kenntlich gemacht. Ich versichere an Eides statt, dass diese Dissertation noch keiner anderen Fakultät oder Universität zur Prüfung vorgelegen hat; dass sie - abgesehen von unten angegebenen Teilpublikationen und eingebundenen Artikeln und Manuskripten - noch nicht veröffentlicht worden ist sowie, dass ich eine Veröffentlichung der Dissertation vor Abschluss der Promotion nicht ohne Genehmigung des Promotionsausschusses vornehmen werde. Die Bestimmungen dieser Ordnung sind mir bekannt. Darüber hinaus erkläre ich hiermit, dass ich die Ordnung zur Sicherung guter wissenschaftlicher Praxis und zum Umgang mit wissenschaftlichem Fehlverhalten der Universität zu Köln gelesen und sie bei der Durchführung der Dissertation zugrundeliegenden Arbeiten und der schriftlich verfassten Dissertation beachtet habe und verpflichte mich hiermit, die dort genannten Vorgaben bei allen wissenschaftlichen Tätigkeiten zu beachten und umzusetzen. Ich versichere, dass die eingereichte elektronische Fassung der eingereichten Druckfassung vollständig entspricht."

Teilpublikationen:

Emilia Kieckhöfer, Gisela G Slaats, Lena K Ebert, Marie-Christine Albert, Claudia Dafinger, Hamid Kashkar, Thomas Benzing, Bernhard Schermer. *Primary cilia suppress Ripk3-mediated necroptosis.* (2022) *Cell Death Discov* 2;8(1):477.

Emilia Kieckhöfer, Peter A Matthiessen, Lena K Ebert, Christina Klausen, Dagmar Wachten, Thomas Benzing, Helen May-Simera*, Bernhard Schermer*. *Loss of Bbs8 leads to cystic kidney disease in mice and affects tubulin acetylation through HDAC2.* (2024) BIORXIV/583949

Datum, Name und Unterschrift

11.03.2024 Emilia Kieckhöfer

XII. Acknowledgment

Foremost, I would like to express my deepest gratitude to Prof. Dr. Bernhard Schermer, my academic mentor and thesis advisor, whose invaluable guidance and expertise have been instrumental in shaping this research. His unwavering support, encouragement, and insightful feedback have been a constant source of inspiration throughout this journey. Thank you for giving me the opportunity to do my PhD in the Nephrolab.

I would also like to express my heartfelt thanks to my former supervisor (Master) and now collaborator, Prof. Dr. Helen May-Simera. She has always believed in me and was a great support for the first steps in my career. This thesis would also not be possible without Dr. Gisela Slaats, who originally brought me to the Nephrolab and supported the start of my PhD.

I extend my wholehearted gratitude to my esteemed colleagues of the Nephrolab for their shared commitment to advancing the field of biology. Your help and your support mean a lot to me. Moreover, I would like to express special thanks to Inês, Claudia and Lena for all your massive help, guidance and shared knowledge that enhanced the depth of my understanding and contributed significantly to the quality of this thesis. I also would like to thank the whole technician team separately for your overall support in the lab. Without you, it wouldn't have been possible for me to hand in my thesis. Just as importantly, I would like to thank my seatmate, Nelli, for being an integral part of this academic chapter and for making it a journey filled with both academic growth and delightful friendship.

To my dearest friend Lisa, who added a touch of joy to the academic rigours, creating lasting memories at conferences like in Crete, and also outside of biology research, all of which I will infinitely cherish: Thank you. Further, I have to express my sincere gratitude to Miriam, who supported me at all times and was always ready to listen if I needed someone. I also would like to thank Melanie, who took her time to correct my entire thesis and always had encouraging words for me during my PhD.

Lastly, but most importantly, I would like to express my profound thanks to, Peter. I deeply appreciate your unwavering support and motivation throughout this academic journey. I cannot express in words how grateful I am for your help and support!

This thesis is a culmination of collective efforts, and I am indebted to all those who have contributed to its realisation. Thank you!

Von ganzem Herzen möchte ich abschließend meiner Familie danken, für ihre unerschütterliche Unterstützung, ihr Verständnis in jeder Situation, ihre nicht endenden Aufmunterungen sowie Ermutigung. Ihre Liebe und ihr Glaube an meine Fähigkeiten waren einer der wichtigsten Grundsteine für meinen akademischen Erfolg!

Ich danke euch aus ganzem Herzen!

XIII. References

1. Singla V, Reiter JF. The primary cilium as the cell's antenna: Signaling at a sensory organelle. *Science (80-)*. 2006;313(5787):629-633. doi:10.1126/SCIENCE.1124534/ASSET/10A21FA3-88A5-4365-B96A-674444783FDA/ASSETS/GRAPHIC/313_629_F4.JPEG

2. Pazour GJ, Bloodgood RA. Targeting Proteins to the Ciliary Membrane. *Curr Top Dev Biol*. 2008;85:115-149. doi:10.1016/S0070-2153(08)00805-3

3. Cartwright JHE, Piro O, Tuval I. Chemosensing versus mechanosensing in nodal and Kupffer's vesicle cilia and in other left-right organizer organs. *Philos Trans R Soc B Biol Sci*. 2020;375(1792). doi:10.1098/rstb.2019.0566

4. Dobell C, Leeuwenhoek A van. *Antony van Leeuwenhoek and His "Little Animals"* Harcourt, Brace and company,; 1932. doi:10.5962/bhl.title.13354

5. Müller OF, Fabricius O. *Animalcula Infusoria Fluviatilia et Marina Que Detexit, Systematice Descripsit et Ad Vivum Delineari Curavit*. Typis N. Mölleri,; 1786. doi:10.5962/bhl.title.129933

6. Zimmermann KW. Beiträge zur Kenntniss einiger Drüsen und Epithelien. *Arch für mikroskopische Anat*. 1898;52(3):552-706. doi:10.1007/BF02975837

7. Barr MM, DeModena J, Braun D, Nguyen CQ, Hall DH, Sternberg PW. The Caenorhabditis elegans autosomal dominant polycystic kidney disease gene homologs lov-1 and pkd-2 act in the same pathway. *Curr Biol*. 2001;11(17):1341-1346. doi:10.1016/S0960-9822(01)00423-7

8. Pazour GJ, Dickert BL, Vucica Y, et al. Chlamydomonas IFT88 and its mouse homologue, polycystic kidney disease gene tg737, are required for assembly of cilia and flagella. *J Cell Biol*. 2000;151(3):709-718. doi:10.1083/JCB.151.3.709

9. Sorokin SP. Reconstructions of Centriole Formation and Ciliogenesis in Mammalian Lungs. *J Cell Sci*. 1968;3(2).

10. Oh EC, Katsanis N. Cilia in vertebrate development and disease. *Development*. 2012;139(3):443. doi:10.1242/DEV.050054

11. Kiesel P, Alvarez Viar G, Tsoy N, et al. The molecular structure of mammalian primary cilia revealed by cryo-electron tomography. *Nat Struct Mol Biol 2020 2712*. 2020;27(12):1115-1124. doi:10.1038/s41594-020-0507-4

12. Reiter JF, Blacque OE, Leroux MR. The base of the cilium: roles for transition fibres and the transition zone in ciliary formation, maintenance and compartmentalization. *EMBO Rep*. 2012;13(7):608. doi:10.1038/EMBOR.2012.73

13. O'Toole ET, Giddings TH, Dutcher SK. Understanding Microtubule Organizing Centers by Comparing Mutant and Wild-Type Structures with Electron Tomography. *Methods Cell Biol*. 2007;79(79):125-143. doi:10.1016/S0091-679X(06)79005-7

14. Mill P, Christensen ST, Pedersen LB. Primary cilia as dynamic and diverse signalling hubs in development and disease. *Nat Rev Genet 2023 247*. 2023;24(7):421-441. doi:10.1038/s41576-023-00587-9

15. Molla-Herman A, Ghossoub R, Blisnick T, et al. The ciliary pocket: an endocytic membrane domain at the base of primary and motile cilia. *J Cell Sci*. 2010;123(10):1785-1795. doi:10.1242/JCS.059519

16. Rattner JB, Sciore P, Ou Y, Van Der Hoorn FA, Lo IKY. Primary cilia in fibroblast-like type B synoviocytes lie within a cilium pit: a site of endocytosis. *Histol Histopathol*. 2010;25(7):865-

875. doi:10.14670/HH-25.865

17. Benmerah A. The ciliary pocket. *Curr Opin Cell Biol*. 2013;25(1):78-84. doi:10.1016/J.CEB.2012.10.011

18. Sorokin SP. Reconstructions of centriole formation and ciliogenesis in mammalian lungs. *J Cell Sci*. 1968;3(2):207-230. doi:10.1242/JCS.3.2.207

19. Latta H, Maunsbach AB, Madden SC. Cilia in different segments of the rat nephron. *J Biophys Biochem Cytol*. 1961;11(1):248-252. doi:10.1083/JCB.11.1.248

20. Bernabé-Rubio M, Andrés G, Casares-Arias J, et al. Novel role for the midbody in primary ciliogenesis by polarized epithelial cells. *J Cell Biol*. 2016;214(3):259-273. doi:10.1083/JCB.201601020/VIDEO-5

21. Garcia G, Raleigh DR, Reiter JF. How the ciliary membrane is organized inside-out to communicate outside-in. *Curr Biol*. 2018;28(8):R421. doi:10.1016/J.CUB.2018.03.010

22. Conduit PT, Wainman A, Raff JW. Centrosome function and assembly in animal cells. *Nat Rev Mol Cell Biol*. 2015;16(10):611-624. doi:10.1038/NRM4062

23. Tanos BE, Yang HJ, Soni R, et al. Centriole distal appendages promote membrane docking, leading to cilia initiation. *Genes Dev*. 2013;27(2):163-168. doi:10.1101/GAD.207043.112

24. Mazo G, Soplop N, Wang WJ, Uryu K, Tsou MFB. Spatial control of primary ciliogenesis by subdistal appendages alters sensation-associated properties of cilia. *Dev Cell*. 2016;39(4):424-437. doi:10.1016/J.DEVCEL.2016.10.006

25. Pazour GJ, Witman GB. The vertebrate primary cilium is a sensory organelle. *Curr Opin Cell Biol*. 2003;15(1):105-110. doi:10.1016/s0955-0674(02)00012-1

26. Sloboda RD, Rosenbaum JL. Making sense of cilia and flagella. *J Cell Biol*. 2007;179(4):575. doi:10.1083/JCB.200709039

27. Plotnikova O V., Golemis EA, Pugacheva EN. Cell Cycle-Dependent Ciliogenesis and Cancer. *Cancer Res*. 2008;68(7):2058. doi:10.1158/0008-5472.CAN-07-5838

28. Tucker RW, Pardee AB, Fujiwara K. Centriole ciliation is related to quiescence and DNA synthesis in 3T3 cells. *Cell*. 1979;17(3):527-535. doi:10.1016/0092-8674(79)90261-7

29. Dibella LM, Park A, Sun Z. Zebrafish Tsc1 reveals functional interactions between the cilium and the TOR pathway. *Hum Mol Genet*. 2009;18(4):595-606. doi:10.1093/HMG/DDN384

30. Bonnet CS, Aldred M, Von Ruhland C, Harris R, Sandford R, Cheadle JP. Defects in cell polarity underlie TSC and ADPKD-associated cystogenesis. *Hum Mol Genet*. 2009;18(12):2166-2176. doi:10.1093/HMG/DDP149

31. Omori Y, Chaya T, Katoh K, et al. Negative regulation of ciliary length by ciliary male germ cell-associated kinase (Mak) is required for retinal photoreceptor survival. *Proc Natl Acad Sci U S A*. 2010;107(52):22671-22676. doi:10.1073/PNAS.1009437108

32. Tammachote R, Hommerding CJ, Sinders RM, et al. Ciliary and centrosomal defects associated with mutation and depletion of the Meckel syndrome genes MKS1 and MKS3. *Hum Mol Genet*. 2009;18(17):3311-3323. doi:10.1093/HMG/DDP272

33. Williams CL, Masyukova S V., Yoder BK. Normal ciliogenesis requires synergy between the cystic kidney disease genes MKS-3 and NPHP-4. *J Am Soc Nephrol*. 2010;21(5):782-793. doi:10.1681/ASN.2009060597

34. Wheway G, Nazlamova L, Hancock JT. Signaling through the primary cilium. *Front Cell Dev Biol*.

2018;6(FEB):326557. doi:10.3389/FCELL.2018.00008/BIBTEX

35. Taschner M, Bhogaraju S, Lorentzen E. Architecture and function of IFT complex proteins in ciliogenesis. *Differentiation*. 2012;83(2):S12. doi:10.1016/J.DIFF.2011.11.001

36. Nakayama K, Katoh Y. Ciliary protein trafficking mediated by IFT and BBSome complexes with the aid of kinesin-2 and dynein-2 motors. *J Biochem*. 2018;163(3):155-164. doi:10.1093/jb/mvx087

37. Van den Hoek H, Klena N, Jordan MA, et al. In situ architecture of the ciliary base reveals the stepwise assembly of intraflagellar transport trains. *Science (80-)*. 2022;377(6605):543-548. doi:10.1126/SCIENCE.ABM6704/SUPPL_FILE/SCIENCE.ABM6704_MOVIES_S1_AND_S2.ZIP

38. Lacey SE, Foster HE, Pigino G. The molecular structure of IFT-A and IFT-B in anterograde intraflagellar transport trains. *Nat Struct Mol Biol*. 2023;30(5):584. doi:10.1038/S41594-022-00905-5

39. Liu P, Lechtreck KF. The Bardet-Biedl syndrome protein complex is an adapter expanding the cargo range of intraflagellar transport trains for ciliary export. *Proc Natl Acad Sci U S A*. 2018;115(5):E934-E943. doi:10.1073/pnas.1713226115

40. Qin H, Diener DR, Geimer S, Cole DG, Rosenbaum JL. Intraflagellar transport (IFT) cargo: IFT transports flagellar precursors to the tip and turnover products to the cell body. *J Cell Biol*. 2004;164(2):255-266. doi:10.1083/JCB.200308132

41. Hesketh SJ, Mukhopadhyay AG, Nakamura D, Toropova K, Roberts AJ. IFT-A structure reveals carriages for membrane protein transport into cilia. *Cell*. 2022;185(26):4971-4985.e16. doi:10.1016/J.CELL.2022.11.010

42. Cullen CL, O'Rourke M, Beasley SJ, et al. Kif3a deletion prevents primary cilia assembly on oligodendrocyte progenitor cells, reduces oligodendrogenesis and impairs fine motor function. *Glia*. 2021;69(5):1184. doi:10.1002/GLIA.23957

43. Takeda S, Yonekawa Y, Tanaka Y, Okada Y, Nonaka S, Hirokawa N. Left-Right Asymmetry and Kinesin Superfamily Protein KIF3A: New Insights in Determination of Laterality and Mesoderm Induction by kif3A−/− Mice Analysis. *J Cell Biol*. 1999;145(4):825. doi:10.1083/JCB.145.4.825

44. Marszalek JR, Ruiz-Lozano P, Roberts E, Chien KR, Goldstein LSB. Situs inversus and embryonic ciliary morphogenesis defects in mouse mutants lacking the KIF3A subunit of kinesin-II. *Proc Natl Acad Sci U S A*. 1999;96(9):5043. doi:10.1073/PNAS.96.9.5043

45. Lin F, Hiesberger T, Cordes K, et al. Kidney-specific inactivation of the KIF3A subunit of kinesin-II inhibits renal ciliogenesis and produces polycystic kidney disease. *Proc Natl Acad Sci U S A*. 2003;100(9):5286. doi:10.1073/PNAS.0836980100

46. Pan J, Snell WJ. Chlamydomonas shortens its flagella by activating axonemal disassembly, stimulating IFT particle trafficking, and blocking anterograde cargo loading. *Dev Cell*. 2005;9(3):431-438. doi:10.1016/J.DEVCEL.2005.07.010

47. Pan J, Wang Q, Snell WJ. An aurora kinase is essential for flagellar disassembly in Chlamydomonas. *Dev Cell*. 2004;6(3):445-451. doi:10.1016/S1534-5807(04)00064-4

48. Piao T, Luo M, Wang L, et al. A microtubule depolymerizing kinesin functions during both flagellar disassembly and flagellar assembly in Chlamydomonas. *Proc Natl Acad Sci U S A*. 2009;106(12):4713-4718. doi:10.1073/PNAS.0808671106

49. Wang L, Dynlacht BD. The regulation of cilium assembly and disassembly in development and disease. *Development*. 2018;145(18). doi:10.1242/DEV.151407

50. Wang G, Chen Q, Zhang X, et al. PCM1 recruits Plk1 to the pericentriolar matrix to promote primary cilia disassembly before mitotic entry. *J Cell Sci*. 2013;126(6):1355-1365. doi:10.1242/JCS.114918/263246/AM/PCM1-RECRUITS-PLK1-TO-PERICENTRIOLAR-MATRIX-TO

51. Kinzel D, Boldt K, Davis EE, et al. Pitchfork regulates primary cilia disassembly and left-right asymmetry. *Dev Cell*. 2010;19(1):66-77. doi:10.1016/J.DEVCEL.2010.06.005

52. Pugacheva EN, Jablonski SA, Hartman TR, Henske EP, Golemis EA. HEF1-dependent Aurora A activation induces disassembly of the primary cilium. *Cell*. 2007;129(7):1351-1363. doi:10.1016/J.CELL.2007.04.035

53. Hubbert C, Guardiola A, Shao R, et al. HDAC6 is a microtubule-associated deacetylase. *Nature*. 2002;417(6887):455-458. doi:10.1038/417455A

54. Ran J, Yang Y, Li D, Liu M, Zhou J. Deacetylation of α-tubulin and cortactin is required for HDAC6 to trigger ciliary disassembly. *Sci Rep*. 2015;5. doi:10.1038/SREP12917

55. Kobayashi T, Nakazono K, Tokuda M, Mashima Y, Dynlacht BD, Itoh H. HDAC2 promotes loss of primary cilia in pancreatic ductal adenocarcinoma. *EMBO Rep*. 2017;18(2):334-343. doi:10.15252/EMBR.201541922

56. Tsai SC, Seto E. Regulation of histone deacetylase 2 by protein kinase CK2. *J Biol Chem*. 2002;277(35):31826-31833. doi:10.1074/JBC.M204149200

57. Pan J, Seeger-Nukpezah T, Golemis EA. The role of the cilium in normal and abnormal cell cycles: emphasis on renal cystic pathologies. *Cell Mol Life Sci 2012 7011*. 2012;70(11):1849-1874. doi:10.1007/S00018-012-1052-Z

58. Nigg EA, Stearns T. The centrosome cycle: Centriole biogenesis, duplication and inherent asymmetries. *Nat Cell Biol*. 2011;13(10):1154-1160. doi:10.1038/NCB2345

59. Nager AR, Goldstein JS, Herranz-Pérez V, et al. An actin network dispatches ciliary GPCRs into extracellular vesicles to modulate signaling. *Cell*. 2017;168(1-2):252. doi:10.1016/J.CELL.2016.11.036

60. Nigg EA, Raff JW. Centrioles, centrosomes, and cilia in health and disease. *Cell*. 2009;139(4):663-678. doi:10.1016/J.CELL.2009.10.036

61. Fliegauf M, Benzing T, Omran H. When cilia go bad: cilia defects and ciliopathies. *Nat Rev Mol Cell Biol 2007 811*. 2007;8(11):880-893. doi:10.1038/nrm2278

62. Gerdes JM, Davis EE, Katsanis N. The vertebrate primary cilium in development, homeostasis, and disease. *Cell*. 2009;137(1):32-45. doi:10.1016/J.CELL.2009.03.023

63. Satir P, Pedersen LB, Christensen ST. The primary cilium at a glance. *J Cell Sci*. 2010;123(4):499-503. doi:10.1242/jcs.050377

64. Otto EA, Hurd TW, Airik R, et al. Candidate exome capture identifies mutation of SDCCAG8 as the cause of a retinal-renal ciliopathy. *Nat Genet*. 2010;42(10):840-850. doi:10.1038/NG.662

65. Dong C, Filipeanu CM, Duvernay MT, Wu G. Regulation of G protein-coupled receptor export trafficking. *Biochim Biophys Acta - Biomembr*. 2007;1768(4):853-870. doi:10.1016/J.BBAMEM.2006.09.008

66. Händel M, Schulz S, Stanarius A, et al. Selective targeting of somatostatin receptor 3 to neuronal cilia. *Neuroscience*. 1999;89(3):909-926. doi:10.1016/S0306-4522(98)00354-6

67. Berbari NF, Lewis JS, Bishop GA, Askwith CC, Mykytyn K. Bardet-Biedl syndrome proteins are required for the localization of G protein-coupled receptors to primary cilia. *Proc Natl Acad Sci*

U S A. 2008;105(11):4242-4246. doi:10.1073/pnas.0711027105

68. Brailov I, Bancila M, Brisorgueil MJ, Miquel MC, Hamon M, Vergé D. Localization of 5-HT6 receptors at the plasma membrane of neuronal cilia in the rat brain. *Brain Res*. 2000;872(1-2):271-275. doi:10.1016/S0006-8993(00)02519-1

69. Koemeter-Cox AI, Sherwood TW, Green JA, et al. Primary cilia enhance kisspeptin receptor signaling on gonadotropin- releasing hormone neurons. *Proc Natl Acad Sci U S A*. 2014;111(28):10335-10340. doi:10.1073/PNAS.1403286111/SUPPL_FILE/PNAS.1403286111.SM05.MOV

70. Wheway G, Schmidts M, Mans DA, et al. An siRNA-based functional genomics screen for the identification of regulators of ciliogenesis and ciliopathy genes. *Nat Cell Biol 2014 178*. 2015;17(8):1074-1087. doi:10.1038/ncb3201

71. Fan C-M, Tessier-Lavigne M. Patterning of mammalian somites by surface ectoderm and notochord: Evidence for sclerotome induction by a hedgehog homolog. *Cell*. 1994;79(7):1175-1186. doi:10.1016/0092-8674(94)90009-4

72. Du SJ, Devoto SH, Westerfield M, Moon RT. Positive and negative regulation of muscle cell identity by members of the hedgehog and TGF-beta gene families. *J Cell Biol*. 1997;139(1):145-156. doi:10.1083/jcb.139.1.145

73. Schneider L, Cammer M, Lehman J, et al. Directional Cell Migration and Chemotaxis in Wound Healing Response to PDGF-AA are Coordinated by the Primary Cilium in Fibroblasts. *Cell Physiol Biochem*. 2010;25(2-3):279-292. doi:10.1159/000276562

74. Munsterberg AE, Kitajewski J, Bumcrot DA, McMahon AP, Lassar AB. Combinatorial signaling by Sonic hedgehog and Wnt family members induces myogenic bHLH gene expression in the somite. *Genes Dev*. 1995;9(23):2911-2922. doi:10.1101/gad.9.23.2911

75. Beachy PA, Karhadkar SS, Berman DM. Tissue repair and stem cell renewal in carcinogenesis. *Nature*. 2004;432(7015):324-331. doi:10.1038/NATURE03100

76. Echelard Y, Epstein DJ, St-Jacques B, et al. Sonic hedgehog, a member of a family of putative signaling molecules, is implicated in the regulation of CNS polarity. *Cell*. 1993;75(7):1417-1430. doi:10.1016/0092-8674(93)90627-3

77. Krauss S, Concordet JP, Ingham PW. A functionally conserved homolog of the Drosophila segment polarity gene hh is expressed in tissues with polarizing activity in zebrafish embryos. *Cell*. 1993;75(7):1431-1444. doi:10.1016/0092-8674(93)90628-4

78. Mehta P, Singh P, Gupta NJ, et al. Mutations in the desert hedgehog (DHH) gene in the disorders of sexual differentiation and male infertility. *J Assist Reprod Genet*. 2021;38(7):1871. doi:10.1007/S10815-021-02140-1

79. Nakano Y, Guerrero I, Hidalgo A, Taylor A, Whittle JRS, Ingham PW. A protein with several possible membrane-spanning domains encoded by the Drosophila segment polarity gene patched. *Nature*. 1989;341(6242):508-513. doi:10.1038/341508A0

80. Niewiadomski P, Niedziółka SM, Markiewicz Ł, Uśpieński T, Baran B, Chojnowska K. Gli Proteins: Regulation in Development and Cancer. *Cells*. 2019;8(2). doi:10.3390/CELLS8020147

81. Briscoe J, Thérond PP. The mechanisms of Hedgehog signalling and its roles in development and disease. *Nat Rev Mol Cell Biol 2013 147*. 2013;14(7):416-429. doi:10.1038/nrm3598

82. Schneider L, Clement CA, Teilmann SC, et al. PDGFRαα Signaling Is Regulated through the Primary Cilium in Fibroblasts. *Curr Biol*. 2005;15(20):1861-1866.

doi:10.1016/J.CUB.2005.09.012

83. Fredriksson L, Li H, Eriksson U. The PDGF family: four gene products form five dimeric isoforms. *Cytokine Growth Factor Rev*. 2004;15(4):197-204. doi:10.1016/J.CYTOGFR.2004.03.007

84. Suizu F, Hirata N, Kimura K, et al. Phosphorylation-dependent Akt–Inversin interaction at the basal body of primary cilia. *EMBO J*. 2016;35(12):1346-1363. doi:10.15252/EMBJ.201593003

85. Pulkkinen K, Murugan S, Vainio S. Wnt signaling in kidney development and disease. *Organogenesis*. 2008;4(2):55. doi:10.4161/ORG.4.2.5849

86. Whyte JL, Smith AA, Helms JA. Wnt Signaling and Injury Repair. *Cold Spring Harb Perspect Biol*. 2012;4(8). doi:10.1101/CSHPERSPECT.A008078

87. Habas R, Dawid IB. Dishevelled and Wnt signaling: is the nucleus the final frontier? *J Biol*. 2005;4(1). doi:10.1186/JBIOL22

88. Pereira CP, Bachli EB, Schoedon G. The wnt pathway: a macrophage effector molecule that triggers inflammation. *Curr Atheroscler Rep*. 2009;11(3):236-242. doi:10.1007/S11883-009-0036-4

89. Staal FJT, Arens R. Wnt Signaling as Master Regulator of T-Lymphocyte Responses: Implications for Transplant Therapy. *Transplantation*. 2016;100(12):2584-2592. doi:10.1097/TP.0000000000001393

90. De Herreros AG, Duñach M. Intracellular Signals Activated by Canonical Wnt Ligands Independent of GSK3 Inhibition and β-Catenin Stabilization. *Cells*. 2019;8(10). doi:10.3390/CELLS8101148

91. Sun J, Robert ME, Duan Y, et al. Crosstalk between NF-kappaB and beta-catenin pathways in bacterial-colonized intestinal epithelial cells. *Am J Physiol Gastrointest Liver Physiol*. 2005;289(1). doi:10.1152/AJPGI.00515.2004

92. Duan Y, Liao AP, Kuppireddi S, Ye Z, Ciancio MJ, Sun J. beta-Catenin activity negatively regulates bacteria-induced inflammation. *Lab Invest*. 2007;87(6):613-624. doi:10.1038/LABINVEST.3700545

93. Ljungberg JK, Kling JC, Tran TT, Blumenthal A. Functions of the WNT Signaling Network in Shaping Host Responses to Infection. *Front Immunol*. 2019;10. doi:10.3389/FIMMU.2019.02521

94. Meyer IS, Leuschner F. The role of Wnt signaling in the healing myocardium: a focus on cell specificity. *Basic Res Cardiol*. 2018;113(6). doi:10.1007/S00395-018-0705-Y

95. Houschyar KS, Chelliah MP, Rein S, et al. Role of Wnt signaling during inflammation and sepsis: A review of the literature. *Int J Artif Organs*. 2018;41(5):247-253. doi:10.1177/0391398818762357

96. Aamir K, Khan HU, Sethi G, Hossain MA, Arya A. Wnt signaling mediates TLR pathway and promote unrestrained adipogenesis and metaflammation: Therapeutic targets for obesity and type 2 diabetes. *Pharmacol Res*. 2020;152. doi:10.1016/J.PHRS.2019.104602

97. Pietilä I, Prunskaite-Hyyryläinen R, Kaisto S, et al. Wnt5a Deficiency Leads to Anomalies in Ureteric Tree Development, Tubular Epithelial Cell Organization and Basement Membrane Integrity Pointing to a Role in Kidney Collecting Duct Patterning. *PLoS One*. 2016;11(1). doi:10.1371/JOURNAL.PONE.0147171

98. Guay-Woodford LM. Renal cystic diseases: diverse phenotypes converge on the

cilium/centrosome complex. *Pediatr Nephrol*. 2006;21(10):1369-1376. doi:10.1007/s00467-006-0164-9

99. Quinlan RJ, Tobin JL, Beales PL. Modeling ciliopathies: Primary cilia in development and disease. *Curr Top Dev Biol*. 2008;84:249-310. doi:10.1016/S0070-2153(08)00605-4

100. Stokman MF, Saunier S, Benmerah A. Renal Ciliopathies: Sorting Out Therapeutic Approaches for Nephronophthisis. *Front Cell Dev Biol*. 2021;9:653138. doi:10.3389/FCELL.2021.653138/BIBTEX

101. Forsythe E, Beales PL. Bardet–Biedl syndrome. *Eur J Hum Genet*. 2013;21(1):8-13. doi:10.1038/ejhg.2012.115

102. Badano JL, Mitsuma N, Beales PL, Katsanis N. The ciliopathies: an emerging class of human genetic disorders. *Annu Rev Genomics Hum Genet*. 2006;7:125-148. doi:10.1146/ANNUREV.GENOM.7.080505.115610

103. Davis EE, Katsanis N. The ciliopathies: a transitional model into systems biology of human genetic disease. *Curr Opin Genet Dev*. 2012;22(3):290-303. doi:10.1016/J.GDE.2012.04.006

104. Basten SG, Giles RH. Functional aspects of primary cilia in signaling, cell cycle and tumorigenesis. *Cilia*. 2013;2(1):1-23. doi:10.1186/2046-2530-2-6/FIGURES/3

105. Baker K, Beales PL. Making sense of cilia in disease: the human ciliopathies. *Am J Med Genet C Semin Med Genet*. 2009;151C(4):281-295. doi:10.1002/AJMG.C.30231

106. May-Simera H, Nagel-Wolfrum K, Wolfrum U. Cilia - The sensory antennae in the eye. *Prog Retin Eye Res*. 2017;60:144-180. doi:10.1016/J.PRETEYERES.2017.05.001

107. May-Simera HL, Wan Q, Jha BS, et al. Primary Cilium-Mediated Retinal Pigment Epithelium Maturation Is Disrupted in Ciliopathy Patient Cells. *Cell Rep*. 2018;22(1):189. doi:10.1016/J.CELREP.2017.12.038

108. Schneider S, De Cegli R, Nagarajan J, et al. Loss of Ciliary Gene Bbs8 Results in Physiological Defects in the Retinal Pigment Epithelium. *Front Cell Dev Biol*. 2021;9:607121. doi:10.3389/FCELL.2021.607121/FULL

109. Kretschmer V, Patnaik SR, Kretschmer F, Chawda MM, Hernandez-Hernandez V, May-Simera HL. Progressive Characterization of Visual Phenotype in Bardet-Biedl Syndrome Mutant Mice. *Invest Ophthalmol Vis Sci*. 2019;60(4):1132-1143. doi:10.1167/IOVS.18-25210

110. Mitchison HM, Valente EM. Motile and non-motile cilia in human pathology: from function to phenotypes. *J Pathol*. 2017;241(2):294-309. doi:10.1002/PATH.4843

111. Haycraft CJ, Banizs B, Aydin-Son Y, Zhang Q, Michaud EJ, Yoder BK. Gli2 and Gli3 localize to cilia and require the intraflagellar transport protein polaris for processing and function. *PLoS Genet*. 2005;1(4):0480-0488. doi:10.1371/JOURNAL.PGEN.0010053

112. Vetrini F, D'Alessandro LCA, Akdemir ZC, et al. Bi-allelic Mutations in PKD1L1 Are Associated with Laterality Defects in Humans. *Am J Hum Genet*. 2016;99(4):886. doi:10.1016/J.AJHG.2016.07.011

113. Grimes DT, Keynton JL, Buenavista MT, et al. Genetic Analysis Reveals a Hierarchy of Interactions between Polycystin-Encoding Genes and Genes Controlling Cilia Function during Left-Right Determination. *PLoS Genet*. 2016;12(6). doi:10.1371/JOURNAL.PGEN.1006070

114. Zhuo JL, Li XC. Proximal nephron. *Compr Physiol*. 2013;3(3):1079-1123. doi:10.1002/CPHY.C110061

115. Hickling DR, Sun T-T, Wu X-R. Anatomy and Physiology of the Urinary Tract: Relation to Host Defense and Microbial Infection. *Microbiol Spectr*. 2015;3(4). doi:10.1128/MICROBIOLSPEC.UTI-0016-2012

116. Heilmann M, Neudecker S, Wolf I, et al. Quantification of glomerular number and size distribution in normal rat kidneys using magnetic resonance imaging. *Nephrol Dial Transplant*. 2012;27(1):100-107. doi:10.1093/NDT/GFR273

117. Beeman SC, Zhang M, Gubhaju L, et al. Measuring glomerular number and size in perfused kidneys using MRI. *Am J Physiol Renal Physiol*. 2011;300(6). doi:10.1152/AJPRENAL.00044.2011

118. Haberle DA, Von Baeyer H. Characteristics of glomerulotubular balance. *Am J Physiol*. 1983;244(4). doi:10.1152/AJPRENAL.1983.244.4.F355

119. Alpern RJ. Cell mechanisms of proximal tubule acidification. *Physiol Rev*. 1990;70(1):79-114. doi:10.1152/PHYSREV.1990.70.1.79

120. Feraille E, Sassi A, Olivier V, Arnoux G, Martin PY. Renal water transport in health and disease. *Pflugers Arch*. 2022;474(8):841-852. doi:10.1007/S00424-022-02712-9

121. Wang K, Kestenbaum B. Proximal Tubular Secretory Clearance: A Neglected Partner of Kidney Function. *Clin J Am Soc Nephrol*. 2018;13(8):1291. doi:10.2215/CJN.12001017

122. Zacchia M, Capolongo G, Rinaldi L, Capasso G. The importance of the thick ascending limb of Henle's loop in renal physiology and pathophysiology. *Int J Nephrol Renovasc Dis*. 2018;11:81-92. doi:10.2147/IJNRD.S154000

123. Reilly RF, Ellison DH. Mammalian distal tubule: physiology, pathophysiology, and molecular anatomy. *Physiol Rev*. 2000;80(1):277-313. doi:10.1152/PHYSREV.2000.80.1.277

124. Subramanya AR, Ellison DH. Distal convoluted tubule. *Clin J Am Soc Nephrol*. 2014;9(12):2147-2163. doi:10.2215/CJN.05920613

125. Rao R, Bhalla V, Pastor-Soler NM. Intercalated Cells of the Kidney Collecting Duct in Kidney Physiology. *Semin Nephrol*. 2019;39(4):353-367. doi:10.1016/J.SEMNEPHROL.2019.04.005

126. Leiz J, Schmidt-Ott KM. Claudins in the Renal Collecting Duct. *Int J Mol Sci*. 2019;21(1). doi:10.3390/IJMS21010221

127. Pearce D, Soundararajan R, Trimpert C, Kashlan OB, Deen PMT, Kohan DE. Collecting Duct Principal Cell Transport Processes and Their Regulation. *Clin J Am Soc Nephrol*. 2015;10(1):135. doi:10.2215/CJN.05760513

128. Fountain JH, Kaur J, Lappin SL. Physiology, Renin Angiotensin System. *StatPearls*. Published online March 12, 2023. Accessed December 6, 2023. https://www.ncbi.nlm.nih.gov/books/NBK470410/

129. Lee Hamm L, Nakhoul N, Hering-Smith KS. Acid-Base Homeostasis. *Clin J Am Soc Nephrol*. 2015;10(12):2232-2242. doi:10.2215/CJN.07400715

130. Kagan KO, Dufke A, Gembruch U. Renal cystic disease and associated ciliopathies. *Curr Opin Obstet Gynecol*. 2017;29(2):85-94. doi:10.1097/GCO.0000000000000348

131. Barr MM, Sternberg PW. A polycystic kidney-disease gene homologue required for male mating behaviour in C. elegans. *Nature*. 1999;401(6751):386-389. doi:10.1038/43913

132. Watnick T, Germino G. From cilia to cyst. *Nat Genet 2003 344*. 2003;34(4):355-356. doi:10.1038/ng0803-355

133. Bergmann C, Guay-Woodford LM, Harris PC, Horie S, Peters DJM, Torres VE. Polycystic kidney disease. *Nat Rev Dis Prim*. 2018;4(1). doi:10.1038/S41572-018-0047-Y

134. Bergmann C. ARPKD and early manifestations of ADPKD: the original polycystic kidney disease and phenocopies. *Pediatr Nephrol*. 2015;30(1):15-30. doi:10.1007/S00467-013-2706-2

135. Ibraghimov-Beskrovnaya O, Bukanov N. Polycystic kidney diseases: From molecular discoveries to targeted therapeutic strategies. *Cell Mol Life Sci 2007 654*. 2007;65(4):605-619. doi:10.1007/S00018-007-7362-X

136. Torres VE, Harris PC. Autosomal dominant polycystic kidney disease: the last 3 years. *Kidney Int*. 2009;76(2):149. doi:10.1038/KI.2009.128

137. Gall EC Le, Audrézet MP, Chen JM, et al. Type of PKD1 mutation influences renal outcome in ADPKD. *J Am Soc Nephrol*. 2013;24(6):1006-1013. doi:10.1681/ASN.2012070650

138. Grantham JJ, Torres VE, Chapman AB, et al. Volume progression in polycystic kidney disease. *N Engl J Med*. 2006;354(20):2122-2130. doi:10.1056/NEJMOA054341

139. Wilson PD. Polycystic Kidney Disease. *https://doi.org/101056/NEJMra022161*. 2004;350(2):151-164. doi:10.1056/NEJMRA022161

140. Müller RU, Schermer B. Hippo signaling-a central player in cystic kidney disease? *Pediatr Nephrol*. 2020;35(7):1143-1152. doi:10.1007/S00467-019-04299-3

141. Nauli SM, Alenghat FJ, Luo Y, et al. Polycystins 1 and 2 mediate mechanosensation in the primary cilium of kidney cells. *Nat Genet*. 2003;33(2):129-137. doi:10.1038/NG1076

142. Gargalionis AN, Papavassiliou KA, Basdra EK, Papavassiliou AG. Polycystins: Mechanosensors with Diagnostic and Prognostic Potential in Cancer. *Trends Mol Med*. 2016;22(1):7-9. doi:10.1016/J.MOLMED.2015.11.002

143. Delling M, Indzhykulian AA, Liu X, et al. Primary cilia are not calcium-responsive mechanosensors. *Nature*. 2016;531(7596):656-660. doi:10.1038/NATURE17426

144. Malekshahabi T, Khoshdel Rad N, Serra AL, Moghadasali R. Autosomal dominant polycystic kidney disease: Disrupted pathways and potential therapeutic interventions. *J Cell Physiol*. 2019;234(8):12451-12470. doi:10.1002/JCP.28094

145. Fick GM, Gabow PA. Hereditary and acquired cystic disease of the kidney. *Kidney Int*. 1994;46(4):951-964. doi:10.1038/KI.1994.354

146. Wilson PD, Falkenstein D. The pathology of human renal cystic disease. *Curr Top Pathol*. 1995;88:1-50. doi:10.1007/978-3-642-79517-6_1/COVER

147. Hoyer PF. Clinical manifestations of autosomal recessive polycystic kidney disease. *Curr Opin Pediatr*. 2015;27(2):186-192. doi:10.1097/MOP.0000000000000196

148. Onuchic LF, Furu L, Nagasawa Y, et al. PKHD1, the polycystic kidney and hepatic disease 1 gene, encodes a novel large protein containing multiple immunoglobulin-like plexin-transcription-factor domains and parallel beta-helix 1 repeats. *Am J Hum Genet*. 2002;70(5):1305-1317. doi:10.1086/340448

149. Ward CJ, Hogan MC, Rossetti S, et al. The gene mutated in autosomal recessive polycystic kidney disease encodes a large, receptor-like protein. *Nat Genet*. 2002;30(3):259-269. doi:10.1038/NG833

150. Ward CJ, Yuan D, Masyuk T V., et al. Cellular and subcellular localization of the ARPKD protein; fibrocystin is expressed on primary cilia. *Hum Mol Genet*. 2003;12(20):2703-2710.

doi:10.1093/HMG/DDG274

151. Wolf MTF, Hildebrandt F. Nephronophthisis. *Pediatr Nephrol*. 2011;26(2):181-194. doi:10.1007/S00467-010-1585-Z

152. Fanconi G, Hanhart E, von Albertini A, Uhlinger E, Dolivo G, Prader A. Familial Juvenile Nephronophthisis (idiopathic parenchymal contracted kidney). *Helv pædiatrica acta*. 1951;6(1):1-49. doi:10.1111/j.1651-2227.1962.tb06582.x

153. Renkema KY, Stokman MF, Giles RH, Knoers NVAM. Next-generation sequencing for research and diagnostics in kidney disease. *Nat Rev Nephrol*. 2014;10(8):433-444. doi:10.1038/NRNEPH.2014.95

154. Waldherr R, Lennert T, Weber HP, Födisch HJ, Schärer K. The nephronophthisis complex. A clinicopathologic study in children. *Virchows Arch A Pathol Anat Histol*. 1982;394(3):235-254. doi:10.1007/BF00430668

155. Ala-Mello S, Koskimies O, Rapola J, Kääriäinen H. Nephronophthisis in Finland: epidemiology and comparison of genetically classified subgroups. *Eur J Hum Genet*. 1999;7(2):205-211. doi:10.1038/SJ.EJHG.5200268

156. König J, Kranz B, König S, et al. Phenotypic Spectrum of Children with Nephronophthisis and Related Ciliopathies. *Clin J Am Soc Nephrol*. 2017;12(12):1974-1983. doi:10.2215/CJN.01280217

157. Konrad M. Nephronophthise. *Pädiatrische Nephrol*. Published online 2002:103-107. doi:10.1007/978-3-642-56378-2_14

158. Srivastava S, Molinari E, Raman S, Sayer JA. Many Genes-One Disease? Genetics of Nephronophthisis (NPHP) and NPHP-Associated Disorders. *Front Pediatr*. 2018;5. doi:10.3389/FPED.2017.00287

159. Gonçalves J, Pelletier L. The Ciliary Transition Zone: Finding the Pieces and Assembling the Gate. *Mol Cells*. 2017;40(4):243. doi:10.14348/MOLCELLS.2017.0054

160. Sang L, Miller JJ, Corbit KC, et al. Mapping the NPHP-JBTS-MKS protein network reveals ciliopathy disease genes and pathways. *Cell*. 2011;145(4):513-528. doi:10.1016/J.CELL.2011.04.019

161. Hurd TW, Otto EA, Mishima E, et al. Mutation of the Mg2+ transporter SLC41A1 results in a nephronophthisis-like phenotype. *J Am Soc Nephrol*. 2013;24(6):967-977. doi:10.1681/ASN.2012101034

162. O'Toole JF, Liu Y, Davis EE, et al. Individuals with mutations in XPNPEP3, which encodes a mitochondrial protein, develop a nephronophthisis-like nephropathy. *J Clin Invest*. 2010;120(3):791-802. doi:10.1172/JCI40076

163. Halbritter J, Porath JD, Diaz KA, et al. Identification of 99 novel mutations in a worldwide cohort of 1,056 patients with a nephronophthisis-related ciliopathy. *Hum Genet*. 2013;132(8):865. doi:10.1007/S00439-013-1297-0

164. Olbrich H, Fliegauf M, Hoefele J, et al. Mutations in a novel gene, NPHP3, cause adolescent nephronophthisis, tapeto-retinal degeneration and hepatic fibrosis. *Nat Genet*. 2003;34(4):455-459. doi:10.1038/NG1216

165. Hildebrandt F, Attanasio M, Otto E. Nephronophthisis: Disease Mechanisms of a Ciliopathy. *J Am Soc Nephrol*. 2009;20(1):23. doi:10.1681/ASN.2008050456

166. Gagnadoux MF, Bacri JL, Broyer M, Habib R. Infantile chronic tubulo-interstitial nephritis with

cortical microcysts: variant of nephronophthisis or new disease entity? *Pediatr Nephrol*. 1989;3(1):50-55. doi:10.1007/BF00859626

167. Attanasio M, Uhlenhaut NH, Sousa VH, et al. Loss of GLIS2 causes nephronophthisis in humans and mice by increased apoptosis and fibrosis. *Nat Genet*. 2007;39(8):1018-1024. doi:10.1038/NG2072

168. Kim Y-S, Kang HS, Herbert R, et al. Krüppel-Like Zinc Finger Protein Glis2 Is Essential for the Maintenance of Normal Renal Functions. *Mol Cell Biol*. 2008;28(7):2358. doi:10.1128/MCB.01722-07

169. Airik R, Slaats GG, Guo Z, et al. Renal-retinal ciliopathy gene Sdccag8 regulates DNA damage response signaling. *J Am Soc Nephrol*. 2014;25(11):2573-2583. doi:10.1681/ASN.2013050565

170. Omran H, Häffner K, Burth S, et al. Human adolescent nephronophthisis: gene locus synteny with polycystic kidney disease in pcy mice. *J Am Soc Nephrol*. 2001;12(1):107-113. doi:10.1681/ASN.V121107

171. Cook SA, Collin GB, Bronson RT, et al. A mouse model for Meckel syndrome type 3. *J Am Soc Nephrol*. 2009;20(4):753-764. doi:10.1681/ASN.2008040412

172. Atala A, Freeman MR, Mandell J, Beier DR. Juvenile cystic kidneys (jck): a new mouse mutation which causes polycystic kidneys. *Kidney Int*. 1993;43(5):1081-1085. doi:10.1038/KI.1993.151

173. Liu S, Lu W, Obara T, et al. A defect in a novel Nek-family kinase causes cystic kidney disease in the mouse and in zebrafish. *Development*. 2002;129(24):5839-5846. doi:10.1242/DEV.00173

174. Manning DK, Sergeev M, Van Heesbeen RG, et al. Loss of the ciliary kinase Nek8 causes left-right asymmetry defects. *J Am Soc Nephrol*. 2013;24(1):100-112. doi:10.1681/ASN.2012050490

175. Hildebrandt F, Zhou W. Nephronophthisis-associated ciliopathies. *J Am Soc Nephrol*. 2007;18(6):1855-1871. doi:10.1681/ASN.2006121344

176. Hildebrandt F, Benzing T, Katsanis N. Ciliopathies. *N Engl J Med*. 2011;364(16):1533-1543. doi:10.1056/NEJMRA1010172

177. Laurence JZ, Moon RC. Four cases of "retinitis pigmentosa" occurring in the same family, and accompanied by general imperfections of development. 1866. *Obes Res*. 1995;3(4):400-403. Accessed October 17, 2019. http://www.ncbi.nlm.nih.gov/pubmed/8521157

178. Bardet G. On congenital obesity syndrome with polydactyly and retinitis pigmentosa (a contribution to the study of clinical forms of hypophyseal obesity). 1920. *Obes Res*. 1995;3(4):387-399. Accessed October 17, 2019. http://www.ncbi.nlm.nih.gov/pubmed/8521156

179. Biedl A. A pair of siblings with adiposo-genital dystrophy. 1922. *Obes Res*. 1995;3(4):404. Accessed October 17, 2019. http://www.ncbi.nlm.nih.gov/pubmed/8521158

180. Wheway G, Lord J, Baralle D. Splicing in the pathogenesis, diagnosis and treatment of ciliopathies. *Biochim Biophys Acta - Gene Regul Mech*. 2019;1862(11-12):194433. doi:10.1016/J.BBAGRM.2019.194433

181. Putoux A, Attie-Bitach T, Martinovic J, Gubler M-C. Phenotypic variability of Bardet-Biedl syndrome: focusing on the kidney. *Pediatr Nephrol*. 2012;27(1):7-15. doi:10.1007/s00467-010-1751-3

182. Ansley SJ, Badano JL, Blacque OE, et al. Basal body dysfunction is a likely cause of pleiotropic

Bardet-Biedl syndrome. *Nature*. 2003;425(6958):628-633. doi:10.1038/nature02030

183. Ece Solmaz A, Onay H, Atik T, et al. Targeted multi-gene panel testing for the diagnosis of Bardet Biedl syndrome: Identification of nine novel mutations across BBS1, BBS2, BBS4, BBS7, BBS9, BBS10 genes. *Eur J Med Genet*. 2015;58(12):689-694. doi:10.1016/j.ejmg.2015.10.011

184. Clarke PGH, Clarke S. Nineteenth century research on naturally occurring cell death and related phenomena. *Anat Embryol (Berl)*. 1996;193(2):81-99. doi:10.1007/BF00214700

185. Vogt C. Untersuchungen über die Entwicklungsgeschichte der Geburtshelferkröte (Alytes obstetricans) . - Solothurn : Jent u. Gassmann, 1842 / [rezensiert von:] Theile - JPortal.https://zs.thulb.uni-jena.de/receive/jportal_jparticle_00306280. Published 1842. Accessed July 22, 2019.

186. Yokouchi Y, Sakiyama JI, Kameda T, et al. BMP-2/-4 mediate programmed cell death in chicken limb buds. *Development*. 1996;122(12):3725-3734. doi:10.1242/DEV.122.12.3725

187. Glücksmann A. Cell deaths in normal vertebrate ontogeny. *Biol Rev Camb Philos Soc*. 1951;26(1):59-86. doi:10.1111/J.1469-185X.1951.TB00774.X

188. Saunders JW. Death in embryonic systems. *Science*. 1966;154(3749):604-612. doi:10.1126/SCIENCE.154.3749.604

189. Hinchliffe JR. Cell death in embryogenesis. *Cell death Biol Pathol*. Published online 1981:35-78. doi:10.1007/978-94-011-6921-9_3

190. Schwartz LM. The role of cell death genes during development. *Bioessays*. 1991;13(8):389-395. doi:10.1002/BIES.950130805

191. Jorgensen I, Rayamajhi M, Miao EA. Programmed cell death as a defence against infection. *Nat Rev Immunol*. 2017;17(3):151-164. doi:10.1038/NRI.2016.147

192. Nagata S, Tanaka M. Programmed cell death and the immune system. *Nat Rev Immunol*. 2017;17(5):333-340. doi:10.1038/NRI.2016.153

193. Fuchs Y, Steller H. Programmed cell death in animal development and disease. *Cell*. 2011;147(4):742-758. doi:10.1016/J.CELL.2011.10.033

194. Weerasinghe P, Buja LM. Oncosis: an important non-apoptotic mode of cell death. *Exp Mol Pathol*. 2012;93(3):302-308. doi:10.1016/J.YEXMP.2012.09.018

195. Galluzzi L, Bravo-San Pedro JM, Kepp O, Kroemer G. Regulated cell death and adaptive stress responses. *Cell Mol Life Sci*. 2016;73(11-12):2405-2410. doi:10.1007/S00018-016-2209-Y

196. Galluzzi L, Vitale I, Aaronson SA, et al. Molecular mechanisms of cell death: recommendations of the Nomenclature Committee on Cell Death 2018. *Cell Death Differ*. 2018;25(3):486-541. doi:10.1038/s41418-017-0012-4

197. Krysko D V., Garg AD, Kaczmarek A, Krysko O, Agostinis P, Vandenabeele P. Immunogenic cell death and DAMPs in cancer therapy. *Nat Rev Cancer*. 2012;12(12):860-875. doi:10.1038/NRC3380

198. Galluzzi L, Kepp O, Kroemer G. Mitochondria: master regulators of danger signalling. *Nat Rev Mol Cell Biol*. 2012;13(12):780-788. doi:10.1038/NRM3479

199. Sarhan M, Land WG, Tonnus W, Hugo CP, Linkermann A. Origin and Consequences of Necroinflammation. *Physiol Rev*. 2018;98(2):727-780. doi:10.1152/PHYSREV.00041.2016

200. Bejoy J, Qian ES, Woodard LE. Tissue Culture Models of AKI: From Tubule Cells to Human Kidney Organoids. *J Am Soc Nephrol*. 2022;33(3):487-501. doi:10.1681/ASN.2021050693

201. Pop C, Salvesen GS. Human caspases: activation, specificity, and regulation. *J Biol Chem*. 2009;284(33):21777-21781. doi:10.1074/jbc.R800084200

202. Kerr JFR, Wyllie AH, Currie AR. Apoptosis: a basic biological phenomenon with wide-ranging implications in tissue kinetics. *Br J Cancer*. 1972;26(4):239-257. doi:10.1038/BJC.1972.33

203. Fink SL, Cookson BT. Apoptosis, pyroptosis, and necrosis: mechanistic description of dead and dying eukaryotic cells. *Infect Immun*. 2005;73(4):1907-1916. doi:10.1128/IAI.73.4.1907-1916.2005

204. Rai NK, Tripathi K, Sharma D, Shukla VK. Apoptosis: a basic physiologic process in wound healing. *Int J Low Extrem Wounds*. 2005;4(3):138-144. doi:10.1177/1534734605280018

205. Cohen GM. Caspases: the executioners of apoptosis. *Biochem J*. 1997;326 (Pt 1)(Pt 1):1-16. doi:10.1042/BJ3260001

206. Kang SJ, Wang S, Kuida K, Yuan J. Distinct downstream pathways of caspase-11 in regulating apoptosis and cytokine maturation during septic shock response. *Cell Death Differ*. 2002;9(10):1115-1125. doi:10.1038/SJ.CDD.4401087

207. Koenig U, Eckhart L, Tschachler E. Evidence that caspase-13 is not a human but a bovine gene. *Biochem Biophys Res Commun*. 2001;285(5):1150-1154. doi:10.1006/BBRC.2001.5315

208. Nakagawa T, Zhu H, Morishima N, et al. Caspase-12 mediates endoplasmic-reticulum-specific apoptosis and cytotoxicity by amyloid-beta. *Nature*. 2000;403(6765):98-103. doi:10.1038/47513

209. Hu S, Snipas SJ, Vincenz C, Salvesen G, Dixit VM. Caspase-14 is a novel developmentally regulated protease. *J Biol Chem*. 1998;273(45):29648-29653. doi:10.1074/JBC.273.45.29648

210. Hengartner MO. The biochemistry of apoptosis. *Nature*. 2000;407(6805):770-776. doi:10.1038/35037710

211. Saelens X, Festjens N, Walle L Vande, Gurp M van, Loo G van, Vandenabeele P. Toxic proteins released from mitochondria in cell death. *Oncogene*. 2004;23(16):2861-2874. doi:10.1038/sj.onc.1207523

212. Hill MM, Adrain C, Duriez PJ, Creagh EM, Martin SJ. Analysis of the composition, assembly kinetics and activity of native Apaf-1 apoptosomes. *EMBO J*. 2004;23(10):2134-2145. doi:10.1038/SJ.EMBOJ.7600210

213. Schimmer AD. Inhibitor of apoptosis proteins: translating basic knowledge into clinical practice. *Cancer Res*. 2004;64(20):7183-7190. doi:10.1158/0008-5472.CAN-04-1918

214. Cory S, Adams JM. The Bcl2 family: regulators of the cellular life-or-death switch. *Nat Rev Cancer*. 2002;2(9):647-656. doi:10.1038/nrc883

215. Enari M, Sakahira H, Yokoyama H, Okawa K, Iwamatsu A, Nagata S. A caspase-activated DNase that degrades DNA during apoptosis, and its inhibitor ICAD. *Nature*. 1998;391(6662):43-50. doi:10.1038/34112

216. Marie Hardwick J, Soane L. Multiple Functions of BCL-2 Family Proteins. *Cold Spring Harb Perspect Biol*. 2013;5(2). doi:10.1101/CSHPERSPECT.A008722

217. Joza N, Susin SA, Daugas E, et al. Essential role of the mitochondrial apoptosis-inducing factor in programmed cell death. *Nature*. 2001;410(6828):549-554. doi:10.1038/35069004

218. Susin SA, Daugas E, Ravagnan L, et al. Two distinct pathways leading to nuclear apoptosis. *J Exp Med*. 2000;192(4):571-579. doi:10.1084/JEM.192.4.571

219. Elmore S. Apoptosis: a review of programmed cell death. *Toxicol Pathol*. 2007;35(4):495-516. doi:10.1080/01926230701320337

220. Kischkel FC, Hellbardt S, Behrmann I, et al. Cytotoxicity-dependent APO-1 (Fas/CD95)-associated proteins form a death-inducing signaling complex (DISC) with the receptor. *EMBO J*. 1995;14(22):5579-5588. Accessed October 18, 2019. http://www.ncbi.nlm.nih.gov/pubmed/8521815

221. Kataoka T, Schröter M, Hahne M, et al. FLIP Prevents Apoptosis Induced by Death Receptors But Not by Perforin/Granzyme B, Chemotherapeutic Drugs, and Gamma Irradiation. *J Immunol*. 1998;161(8):3936-3942. doi:10.4049/JIMMUNOL.161.8.3936

222. Holler N, Zaru R, Micheau O, et al. Fas triggers an alternative, caspase-8-independent cell death pathway using the kinase RIP as effector molecule. *Nat Immunol*. 2000;1(6):489-495. doi:10.1038/82732

223. Zhang DW, Shao J, Lin J, et al. RIP3, an energy metabolism regulator that switches TNF-induced cell death from apoptosis to necrosis. *Science*. 2009;325(5938):332-336. doi:10.1126/SCIENCE.1172308

224. Sun L, Wang H, Wang Z, et al. Mixed lineage kinase domain-like protein mediates necrosis signaling downstream of RIP3 kinase. *Cell*. 2012;148(1-2):213-227. doi:10.1016/J.CELL.2011.11.031

225. Zhao J, Jitkaew S, Cai Z, et al. Mixed lineage kinase domain-like is a key receptor interacting protein 3 downstream component of TNF-induced necrosis. *Proc Natl Acad Sci U S A*. 2012;109(14):5322-5327. doi:10.1073/PNAS.1200012109/SUPPL_FILE/PNAS.201200012SI.PDF

226. Wilson NS, Dixit V, Ashkenazi A. Death receptor signal transducers: nodes of coordination in immune signaling networks. *Nat Immunol 2009 104*. 2009;10(4):348-355. doi:10.1038/ni.1714

227. Berghe T Vanden, Linkermann A, Jouan-Lanhouet S, Walczak H, Vandenabeele P. Regulated necrosis: the expanding network of non-apoptotic cell death pathways. *Nat Rev Mol Cell Biol*. 2014;15(2):135-147. doi:10.1038/NRM3737

228. Newton K, Dugger DL, Wickliffe KE, et al. Activity of protein kinase RIPK3 determines whether cells die by necroptosis or apoptosis. *Science*. 2014;343(6177):1357-1360. doi:10.1126/SCIENCE.1249361

229. Bertrand MJM, Milutinovic S, Dickson KM, et al. cIAP1 and cIAP2 facilitate cancer cell survival by functioning as E3 ligases that promote RIP1 ubiquitination. *Mol Cell*. 2008;30(6):689-700. doi:10.1016/J.MOLCEL.2008.05.014

230. Kreuz S, Siegmund D, Scheurich P, Wajant H. NF-kappaB inducers upregulate cFLIP, a cycloheximide-sensitive inhibitor of death receptor signaling. *Mol Cell Biol*. 2001;21(12):3964-3973. doi:10.1128/MCB.21.12.3964-3973.2001

231. O'Donnell MA, Perez-Jimenez E, Oberst A, et al. Caspase 8 inhibits programmed necrosis by processing CYLD. *Nat Cell Biol*. 2011;13(12):1437-1442. doi:10.1038/NCB2362

232. Chen X, Zhu R, Zhong J, et al. Mosaic composition of RIP1–RIP3 signalling hub and its role in regulating cell death. *Nat Cell Biol 2022 244*. 2022;24(4):471-482. doi:10.1038/s41556-022-00854-7

233. Chen W, Zhou Z, Li S, et al. Diverse Sequence Determinants Control Human and Mouse Receptor Interacting Protein 3 (RIP3) and Mixed Lineage Kinase domain-Like (MLKL) Interaction in Necroptotic Signaling. *J Biol Chem*. 2013;288(23):16247-16261. doi:10.1074/JBC.M112.435545

234. Guo X, Chen Y, Liu Q. Necroptosis in heart disease: Molecular mechanisms and therapeutic implications. *J Mol Cell Cardiol*. 2022;169:74. doi:10.1016/J.YJMCC.2022.05.006

235. Hitomi J, Christofferson DE, Ng A, et al. Identification of a Molecular Signaling Network that Regulates a Cellular Necrotic Cell Death Pathway. *Cell*. 2008;135(7):1311-1323. doi:10.1016/J.CELL.2008.10.044

236. Hildebrand JM, Tanzer MC, Lucet IS, et al. Activation of the pseudokinase MLKL unleashes the four-helix bundle domain to induce membrane localization and necroptotic cell death. *Proc Natl Acad Sci U S A*. 2014;111(42):15072-15077. doi:10.1073/PNAS.1408987111

237. Morgan MJ, Liu ZG. Programmed cell death with a necrotic-like phenotype. *Biomol Concepts*. 2013;4(3):259-275. doi:10.1515/BMC-2012-0056

238. Wang W, Prokopec JS, Zhang Y, et al. Sensing plasma membrane pore formation induces chemokine production in survivors of regulated necrosis. *Dev Cell*. 2022;57(2):228-245.e6. doi:10.1016/J.DEVCEL.2021.12.015

239. Dixon SJ, Lemberg KM, Lamprecht MR, et al. Ferroptosis: an iron-dependent form of nonapoptotic cell death. *Cell*. 2012;149(5):1060-1072. doi:10.1016/J.CELL.2012.03.042

240. Tang D, Kroemer G. Ferroptosis. *Curr Biol*. 2020;30(21):R1292-R1297. doi:10.1016/J.CUB.2020.09.068

241. Chen X, Li J, Kang R, Klionsky DJ, Tang D. Ferroptosis: machinery and regulation. *Autophagy*. 2021;17(9):2054. doi:10.1080/15548627.2020.1810918

242. Brigelius-Flohé R, Maiorino M. Glutathione peroxidases. *Biochim Biophys Acta - Gen Subj*. 2013;1830(5):3289-3303. doi:10.1016/J.BBAGEN.2012.11.020

243. Zhang C, Liu X, Jin S, Chen Y, Guo R. Ferroptosis in cancer therapy: a novel approach to reversing drug resistance. *Mol Cancer*. 2022;21(1):1-12. doi:10.1186/S12943-022-01530-Y/FIGURES/3

244. Brennan MA, Cookson BT. Salmonella induces macrophage death by caspase-1-dependent necrosis. *Mol Microbiol*. 2000;38(1):31-40. doi:10.1046/J.1365-2958.2000.02103.X

245. Friedlander AM. Macrophages Are Sensitive to Anthrax Lethal Toxin through an Acid-dependent Process*. *J Biol Chem*. 1986;261(16):7123-7126. doi:10.1016/S0021-9258(17)38364-3

246. D'Souza CA, Heitman J. Dismantling the Cryptococcus coat. *Trends Microbiol*. 2001;9(3):112-113. doi:10.1016/S0966-842X(00)01945-4

247. Fernandes-Alnemri T, Yu JW, Juliana C, et al. The AIM2 inflammasome is critical for innate immunity to Francisella tularensis. *Nat Immunol*. 2010;11(5):385-393. doi:10.1038/NI.1859

248. Fink SL, Bergsbaken T, Cookson BT. Anthrax lethal toxin and Salmonella elicit the common cell death pathway of caspase-1-dependent pyroptosis via distinct mechanisms. *Proc Natl Acad Sci U S A*. 2008;105(11):4312-4317. doi:10.1073/PNAS.0707370105

249. Cervantes J, Nagata T, Uchijima M, Shibata K, Koide Y. Intracytosolic Listeria monocytogenes induces cell death through caspase-1 activation in murine macrophages. *Cell Microbiol*. 2008;10(1):41-52. doi:10.1111/J.1462-5822.2007.01012.X

250. Fink SL, Cookson BT. Pyroptosis and host cell death responses during Salmonella infection. *Cell Microbiol*. 2007;9(11):2562-2570. doi:10.1111/J.1462-5822.2007.01036.X

251. Yu P, Zhang X, Liu N, Tang L, Peng C, Chen X. Pyroptosis: mechanisms and diseases. *Signal*

Transduct Target Ther 2021 61. 2021;6(1):1-21. doi:10.1038/s41392-021-00507-5

252. Hersh D, Monack DM, Smith MR, Ghori N, Falkow S, Zychlinsky A. The Salmonella invasin SipB induces macrophage apoptosis by binding to caspase-1. *Proc Natl Acad Sci U S A*. 1999;96(5):2396-2401. doi:10.1073/PNAS.96.5.2396

253. Franchi L, Eigenbrod T, Muñoz-Planillo R, Nuñez G. The inflammasome: a caspase-1-activation platform that regulates immune responses and disease pathogenesis. *Nat Immunol*. 2009;10(3):241-247. doi:10.1038/NI.1703

254. Broz P, Ruby T, Belhocine K, et al. Caspase-11 increases susceptibility to Salmonella infection in the absence of caspase-1. *Nature*. 2012;490(7419):288-291. doi:10.1038/NATURE11419

255. Wicherska-pawłowska K, Wróbel T, Rybka J. Toll-Like Receptors (TLRs), NOD-Like Receptors (NLRs), and RIG-I-Like Receptors (RLRs) in Innate Immunity. TLRs, NLRs, and RLRs Ligands as Immunotherapeutic Agents for Hematopoietic Diseases. *Int J Mol Sci*. 2021;22(24). doi:10.3390/IJMS222413397

256. Kayagaki N, Warming S, Lamkanfi M, et al. Non-canonical inflammasome activation targets caspase-11. *Nature*. 2011;479(7371):117-121. doi:10.1038/NATURE10558

257. Wang S, Miura M, Jung YK, et al. Identification and Characterization of Ich-3, a Member of the Interleukin-1β Converting Enzyme (ICE)/Ced-3 Family and an Upstream Regulator of ICE. *J Biol Chem*. 1996;271(34):20580-20587. doi:10.1074/JBC.271.34.20580

258. Faucheu C, Diu A, Chan AWE, et al. A novel human protease similar to the interleukin-1 beta converting enzyme induces apoptosis in transfected cells. *EMBO J*. 1995;14(9):1914-1922. doi:10.1002/J.1460-2075.1995.TB07183.X

259. Sansonetti PJ, Phalipon A, Arondel J, et al. Caspase-1 activation of IL-1beta and IL-18 are essential for Shigella flexneri-induced inflammation. *Immunity*. 2000;12(5):581-590. doi:10.1016/S1074-7613(00)80209-5

260. Kovacs SB, Miao EA. Gasdermins: Effectors of pyroptosis. *Trends Cell Biol*. 2017;27(9):673. doi:10.1016/J.TCB.2017.05.005

261. Elias EE, Lyons B, Muruve DA. Gasdermins and pyroptosis in the kidney. *Nat Rev Nephrol 2023 195*. 2023;19(5):337-350. doi:10.1038/s41581-022-00662-0

262. Shi J, Zhao Y, Wang K, et al. Cleavage of GSDMD by inflammatory caspases determines pyroptotic cell death. *Nature*. 2015;526(7575):660-665. doi:10.1038/NATURE15514

263. Fritsch M, Günther SD, Schwarzer R, et al. Caspase-8 is the molecular switch for apoptosis, necroptosis and pyroptosis. *Nat 2019 5757784*. 2019;575(7784):683-687. doi:10.1038/s41586-019-1770-6

264. Taabazuing CY, Okondo MC, Bachovchin DA. Pyroptosis and Apoptosis Pathways Engage in Bidirectional Crosstalk in Monocytes and Macrophages. *Cell Chem Biol*. 2017;24(4):507-514.e4. doi:10.1016/J.CHEMBIOL.2017.03.009

265. Ding J, Wang K, Liu W, et al. Pore-forming activity and structural autoinhibition of the gasdermin family. *Nature*. 2016;535(7610):111-116. doi:10.1038/NATURE18590

266. Verzella D, Pescatore A, Capece D, et al. Life, death, and autophagy in cancer: NF-κB turns up everywhere. *Cell Death Dis*. 2020;11(3). doi:10.1038/S41419-020-2399-Y

267. Oeckinghaus A, Ghosh S. The NF-κB Family of Transcription Factors and Its Regulation. *Cold Spring Harb Perspect Biol*. 2009;1(4). doi:10.1101/CSHPERSPECT.A000034

268. Hayden MS, Ghosh S. Shared principles in NF-kappaB signaling. *Cell*. 2008;132(3):344-362. doi:10.1016/J.CELL.2008.01.020

269. Karin M. How NF-kappaB is activated: the role of the IkappaB kinase (IKK) complex. *Oncogene*. 1999;18(49):6867-6874. doi:10.1038/SJ.ONC.1203219

270. Sun SC, Ley SC. New insights into NF-kappaB regulation and function. *Trends Immunol*. 2008;29(10):469-478. doi:10.1016/J.IT.2008.07.003

271. Rahighi S, Ikeda F, Kawasaki M, et al. Specific recognition of linear ubiquitin chains by NEMO is important for NF-kappaB activation. *Cell*. 2009;136(6):1098-1109. doi:10.1016/J.CELL.2009.03.007

272. Beinke S, Ley SC. Functions of NF-κB1 and NF-κB2 in immune cell biology. *Biochem J*. 2004;382(Pt 2):393. doi:10.1042/BJ20040544

273. Schmid JA, Birbach A. IkappaB kinase beta (IKKbeta/IKK2/IKBKB)--a key molecule in signaling to the transcription factor NF-kappaB. *Cytokine Growth Factor Rev*. 2008;19(2):157-165. doi:10.1016/J.CYTOGFR.2008.01.006

274. Wang N, Liang H, Zen K. Molecular mechanisms that influence the macrophage m1-m2 polarization balance. *Front Immunol*. 2014;5(NOV). doi:10.3389/FIMMU.2014.00614

275. Zank DC, Bueno M, Mora AL, Rojas M. Idiopathic Pulmonary Fibrosis: Aging, Mitochondrial Dysfunction, and Cellular Bioenergetics. *Front Med*. 2018;5(FEB):1. doi:10.3389/FMED.2018.00010

276. Karin M, Lin A. NF-κB at the crossroads of life and death. *Nat Immunol 2002 33*. 2002;3(3):221-227. doi:10.1038/ni0302-221

277. Pasparakis M. Role of NF-κB in epithelial biology. *Immunol Rev*. 2012;246(1):346-358. doi:10.1111/J.1600-065X.2012.01109.X

278. Liu T, Zhang L, Joo D, Sun SC. NF-κB signaling in inflammation. *Signal Transduct Target Ther 2017 21*. 2017;2(1):1-9. doi:10.1038/sigtrans.2017.23

279. Deter RL, De Duve C. Influence of glucagon, an inducer of cellular autophagy, on some physical properties of rat liver lysosomes. *J Cell Biol*. 1967;33(2):437-449. doi:10.1083/JCB.33.2.437

280. Yang Z, Klionsky DJ. Mammalian autophagy: core molecular machinery and signaling regulation. *Curr Opin Cell Biol*. 2010;22(2):124-131. doi:10.1016/J.CEB.2009.11.014

281. Suzuki K, Kubota Y, Sekito T, Ohsumi Y. Hierarchy of Atg proteins in pre-autophagosomal structure organization. *Genes to Cells*. 2007;12(2):209-218. doi:10.1111/J.1365-2443.2007.01050.X

282. Kabeya Y, Mizushima N, Yamamoto A, Oshitani-Okamoto S, Ohsumi Y, Yoshimori T. LC3, GABARAP and GATE16 localize to autophagosomal membrane depending on form-II formation. *J Cell Sci*. 2004;117(Pt 13):2805-2812. doi:10.1242/JCS.01131

283. Bjørkøy G, Lamark T, Brech A, et al. p62/SQSTM1 forms protein aggregates degraded by autophagy and has a protective effect on huntingtin-induced cell death. *J Cell Biol*. 2005;171(4):603-614. doi:10.1083/JCB.200507002/VIDEO-3

284. Hubert V, Peschel A, Langer B, Gröger M, Rees A, Kain R. LAMP-2 is required for incorporating syntaxin-17 into autophagosomes and for their fusion with lysosomes. *Biol Open*. 2016;5(10):1516-1529. doi:10.1242/BIO.018648

285. Díaz-Troya S, Pérez-Pérez ME, Florencio FJ, Crespo JL. The role of TOR in autophagy regulation from yeast to plants and mammals. *Autophagy*. 2008;4(7):851-865. doi:10.4161/AUTO.6555

286. Ito Y, Ofengeim D, Najafov A, et al. RIPK1 mediates axonal degeneration by promoting inflammation and necroptosis in ALS. *Science*. 2016;353(6299):603-608. doi:10.1126/SCIENCE.AAF6803

287. Huang Y, Feng Y, Cui L, et al. Autophagy-Related LC3 Accumulation Interacted Directly With LIR Containing RIPK1 and RIPK3, Stimulating Necroptosis in Hypoxic Cardiomyocytes. *Front Cell Dev Biol*. 2021;9:679637. doi:10.3389/FCELL.2021.679637/BIBTEX

288. Goodall ML, Fitzwalter BE, Zahedi S, et al. The Autophagy Machinery Controls Cell Death Switching between Apoptosis and Necroptosis. *Dev Cell*. 2016;37(4):337. doi:10.1016/J.DEVCEL.2016.04.018

289. Bard JBL. Growth and death in the developing mammalian kidney: signals, receptors and conversations. *Bioessays*. 2002;24(1):72-82. doi:10.1002/BIES.10024

290. Schumer M, Colombel MC, Sawczuk IS, et al. Morphologic, biochemical, and molecular evidence of apoptosis during the reperfusion phase after brief periods of renal ischemia. *Am J Pathol*. 1992;140(4):831. Accessed September 14, 2023. /pmc/articles/PMC1886381/?report=abstract

291. Havasi A, Borkan SC. Apoptosis and acute kidney injury. *Kidney Int*. 2011;80(1):29-40. doi:10.1038/ki.2011.120

292. Priante G, Gianesello L, Ceol M, Del Prete D, Anglani F. Cell Death in the Kidney. *Int J Mol Sci*. 2019;20(14). doi:10.3390/IJMS20143598

293. Servais H, Ortiz A, Devuyst O, Denamur S, Tulkens PM, Mingeot-Leclercq MP. Renal cell apoptosis induced by nephrotoxic drugs: cellular and molecular mechanisms and potential approaches to modulation. *Apoptosis*. 2008;13(1):11-32. doi:10.1007/S10495-007-0151-Z

294. Homsi E, Janino P, De Faria JBL. Role of caspases on cell death, inflammation, and cell cycle in glycerol-induced acute renal failure. *Kidney Int*. 2006;69(8):1385-1392. doi:10.1038/SJ.KI.5000315

295. Wu X, Guo R, Chen P, Wang Q, Cunningham PN. TNF induces caspase-dependent inflammation in renal endothelial cells through a Rho- and myosin light chain kinase-dependent mechanism. *Am J Physiol Renal Physiol*. 2009;297(2). doi:10.1152/AJPRENAL.00089.2009

296. Bonventre J V., Weinberg JM. Recent advances in the pathophysiology of ischemic acute renal failure. *J Am Soc Nephrol*. 2003;14(8):2199-2210. doi:10.1097/01.ASN.0000079785.13922.F6

297. Linkermann A, Bräsen JH, Himmerkus N, et al. Rip1 (receptor-interacting protein kinase 1) mediates necroptosis and contributes to renal ischemia/reperfusion injury. *Kidney Int*. 2012;81(8):751-761. doi:10.1038/KI.2011.450

298. Takahashi N, Duprez L, Grootjans S, et al. Necrostatin-1 analogues: critical issues on the specificity, activity and in vivo use in experimental disease models. *Cell Death Dis*. 2012;3(11):e437. doi:10.1038/CDDIS.2012.176

299. Linkermann A, Bräsen JH, Darding M, et al. Two independent pathways of regulated necrosis mediate ischemia-reperfusion injury. *Proc Natl Acad Sci U S A*. 2013;110(29):12024-12029. doi:10.1073/PNAS.1305538110/-/DCSUPPLEMENTAL

300. Luedde M, Lutz M, Carter N, et al. RIP3, a kinase promoting necroptotic cell death, mediates

adverse remodelling after myocardial infarction. *Cardiovasc Res*. 2014;103(2):206-216. doi:10.1093/CVR/CVU146

301. Xu Y, Ma H, Shao J, et al. A role for tubular necroptosis in cisplatin-induced AKI. *J Am Soc Nephrol*. 2015;26(11):2647-2658. doi:10.1681/ASN.2014080741

302. Ramesh G, Reeves WB. TNF-α mediates chemokine and cytokine expression and renal injury in cisplatin nephrotoxicity. *J Clin Invest*. 2002;110(6):835-842. doi:10.1172/JCI15606

303. Newton K, Dugger DL, Maltzman A, et al. RIPK3 deficiency or catalytically inactive RIPK1 provides greater benefit than MLKL deficiency in mouse models of inflammation and tissue injury. *Cell Death Differ*. 2016;23(9):1565. doi:10.1038/CDD.2016.46

304. Varfolomeev EE, Schuchmann M, Luria V, et al. Targeted Disruption of the Mouse Caspase 8 Gene Ablates Cell Death Induction by the TNF Receptors, Fas/Apo1, and DR3 and Is Lethal Prenatally. *Immunity*. 1998;9(2):267-276. doi:10.1016/S1074-7613(00)80609-3

305. Kaiser WJ, Upton JW, Long AB, et al. RIP3 mediates the embryonic lethality of caspase-8-deficient mice. *Nat 2011 4717338*. 2011;471(7338):368-372. doi:10.1038/nature09857

306. Linkermann A, Skouta R, Himmerkus N, et al. Synchronized renal tubular cell death involves ferroptosis. *Proc Natl Acad Sci U S A*. 2014;111(47):16836-16841. doi:10.1073/PNAS.1415518111

307. Maremonti F, Meyer C, Linkermann A. Mechanisms and Models of Kidney Tubular Necrosis and Nephron Loss. *J Am Soc Nephrol*. 2022;33(3):472. doi:10.1681/ASN.2021101293

308. Poyan Mehr A, Tran MT, Ralto KM, et al. De novo NAD+ biosynthetic impairment in acute kidney injury in humans. *Nat Med*. 2018;24(9):1351-1359. doi:10.1038/S41591-018-0138-Z

309. Dolma S, Lessnick SL, Hahn WC, Stockwell BR. Identification of genotype-selective antitumor agents using synthetic lethal chemical screening in engineered human tumor cells. *Cancer Cell*. 2003;3(3):285-296. doi:10.1016/S1535-6108(03)00050-3

310. Choi N, Whitlock R, Klassen J, et al. Early intraoperative iron-binding proteins are associated with acute kidney injury after cardiac surgery. *J Thorac Cardiovasc Surg*. 2019;157(1):287-297.e2. doi:10.1016/J.JTCVS.2018.06.091

311. Baliga R, Zhang Z, Baliga M, Ueda N, Shah S V. In vitro and in vivo evidence suggesting a role for iron in cisplatin-induced nephrotoxicity. *Kidney Int*. 1998;53(2):394-401. doi:10.1046/J.1523-1755.1998.00767.X

312. Martin-Sanchez D, Ruiz-Andres O, Poveda J, et al. Ferroptosis, but Not Necroptosis, Is Important in Nephrotoxic Folic Acid-Induced AKI. *J Am Soc Nephrol*. 2017;28(1):218-229. doi:10.1681/ASN.2015121376

313. Ni L, Yuan C, Wu X. Targeting ferroptosis in acute kidney injury. *Cell Death Dis 2022 132*. 2022;13(2):1-11. doi:10.1038/s41419-022-04628-9

314. Lau A, Chung H, Komada T, et al. Renal immune surveillance and dipeptidase-1 contribute to contrast-induced acute kidney injury. *J Clin Invest*. 2018;128(7):2894-2913. doi:10.1172/JCI96640

315. Zhang Z, Shao X, Jiang N, et al. Caspase-11-mediated tubular epithelial pyroptosis underlies contrast-induced acute kidney injury. *Cell Death Dis*. 2018;9(10). doi:10.1038/S41419-018-1023-X

316. Miao N, Yin F, Xie H, et al. The cleavage of gasdermin D by caspase-11 promotes tubular epithelial cell pyroptosis and urinary IL-18 excretion in acute kidney injury. *Kidney Int*.

2019;96(5):1105-1120. doi:10.1016/J.KINT.2019.04.035

317. Shen X, Wang H, Weng C, Jiang H, Chen J. Caspase 3/GSDME-dependent pyroptosis contributes to chemotherapy drug-induced nephrotoxicity. *Cell Death Dis*. 2021;12(2). doi:10.1038/S41419-021-03458-5

318. Wang Y, Gao W, Shi X, et al. Chemotherapy drugs induce pyroptosis through caspase-3 cleavage of a gasdermin. *Nature*. 2017;547(7661):99-103. doi:10.1038/NATURE22393

319. Xia W, Li Y, Wu M, et al. Gasdermin E deficiency attenuates acute kidney injury by inhibiting pyroptosis and inflammation. *Cell Death Dis*. 2021;12(2). doi:10.1038/S41419-021-03431-2

320. Tonnus W, Maremonti F, Belavgeni A, et al. Gasdermin D-deficient mice are hypersensitive to acute kidney injury. *Cell Death Dis*. 2022;13(9). doi:10.1038/S41419-022-05230-9

321. Chen H, Li Y, Wu J, et al. RIPK3 collaborates with GSDMD to drive tissue injury in lethal polymicrobial sepsis. *Cell Death Differ*. 2020;27(9):2568-2585. doi:10.1038/S41418-020-0524-1

322. Kahlenberg JM, Kaplan MJ. The inflammasome and lupus: another innate immune mechanism contributing to disease pathogenesis? *Curr Opin Rheumatol*. 2014;26(5):475-481. doi:10.1097/BOR.0000000000000088

323. Su X, Liu B, Wang S, et al. NLRP3 inflammasome: A potential therapeutic target to minimize renal ischemia/reperfusion injury during transplantation. *Transpl Immunol*. 2022;75. doi:10.1016/J.TRIM.2022.101718

324. Wada J, Makino H. Innate immunity in diabetes and diabetic nephropathy. *Nat Rev Nephrol*. 2016;12(1):13-26. doi:10.1038/NRNEPH.2015.175

325. Zhang H, Sun SC. NF-κB in inflammation and renal diseases. *Cell Biosci*. 2015;5(1):63. doi:10.1186/S13578-015-0056-4

326. Yaribeygi H, Atkin SL, Simental-Mendía LE, Barreto GE, Sahebkar A. Anti-inflammatory effects of resolvins in diabetic nephropathy: Mechanistic pathways. *J Cell Physiol*. 2019;234(9):14873-14882. doi:10.1002/JCP.28315

327. Kiryluk K, Novak J. The genetics and immunobiology of IgA nephropathy. *J Clin Invest*. 2014;124(6):2325-2332. doi:10.1172/JCI74475

328. Volpini RA, Costa RS, Da Silva CGA, Coimbra TM. Inhibition of nuclear factor-kappaB activation attenuates tubulointerstitial nephritis induced by gentamicin. *Nephron Physiol*. 2004;98(4). doi:10.1159/000081558

329. Kumar D, Singla SK, Puri V, Puri S. The Restrained Expression of NF-kB in Renal Tissue Ameliorates Folic Acid Induced Acute Kidney Injury in Mice. *PLoS One*. 2015;10(1). doi:10.1371/JOURNAL.PONE.0115947

330. Gerondakis S, Grumont R, Gugasyan R, et al. Unravelling the complexities of the NF-kappaB signalling pathway using mouse knockout and transgenic models. *Oncogene*. 2006;25(51):6781-6799. doi:10.1038/SJ.ONC.1209944

331. Tang C, Livingston MJ, Liu Z, Dong Z. Autophagy in kidney homeostasis and disease. *Nat Rev Nephrol 2020 169*. 2020;16(9):489-508. doi:10.1038/s41581-020-0309-2

332. He L, Livingston MJ, Dong Z. Autophagy in acute kidney injury and repair. *Nephron Clin Pract*. 2014;127(1-4):56-60. doi:10.1159/000363677

333. Melk A, Baisantry A, Schmitt R. The yin and yang of autophagy in acute kidney injury.

Autophagy. 2016;12(3):596-597. doi:10.1080/15548627.2015.1135284

334. Wang Y, Nartiss Y, Steipe B, McQuibban GA, Kim PK. ROS-induced mitochondrial depolarization initiates PARK2/PARKIN-dependent mitochondrial degradation by autophagy. *Autophagy*. 2012;8(10):1462-1476. doi:10.4161/AUTO.21211

335. Martin JL, Gruszczyk A V., Beach TE, Murphy MP, Saeb-Parsy K. Mitochondrial mechanisms and therapeutics in ischaemia reperfusion injury. *Pediatr Nephrol*. 2019;34(7):1167-1174. doi:10.1007/S00467-018-3984-5

336. Duann P, Lianos EA, Ma J, Lin PH. Autophagy, Innate Immunity and Tissue Repair in Acute Kidney Injury. *Int J Mol Sci*. 2016;17(5). doi:10.3390/IJMS17050662

337. Decuypere JP, Ceulemans LJ, Agostinis P, et al. Autophagy and the Kidney: Implications for Ischemia-Reperfusion Injury and Therapy. *Am J Kidney Dis*. 2015;66(4):699-709. doi:10.1053/J.AJKD.2015.05.021

338. Jiang M, Liu K, Luo J, Dong Z. Autophagy is a renoprotective mechanism during in vitro hypoxia and in vivo ischemia-reperfusion injury. *Am J Pathol*. 2010;176(3):1181-1192. doi:10.2353/AJPATH.2010.090594

339. Kimura T, Takahashi A, Takabatake Y, et al. Autophagy protects kidney proximal tubule epithelial cells from mitochondrial metabolic stress. *Autophagy*. 2013;9(11):1876-1886. doi:10.4161/AUTO.25418

340. Kimura T, Takabatake Y, Takahashi A, et al. Autophagy protects the proximal tubule from degeneration and acute ischemic injury. *J Am Soc Nephrol*. 2011;22(5):902-913. doi:10.1681/ASN.2010070705

341. Jiang M, Wei Q, Dong G, Komatsu M, Su Y, Dong Z. Autophagy in proximal tubules protects against acute kidney injury. *Kidney Int*. 2012;82(12):1271-1283. doi:10.1038/KI.2012.261

342. Levey AS, Coresh J. Chronic kidney disease. *Lancet (London, England)*. 2012;379(9811):165-180. doi:10.1016/S0140-6736(11)60178-5

343. Hill NR, Fatoba ST, Oke JL, et al. Global Prevalence of Chronic Kidney Disease - A Systematic Review and Meta-Analysis. *PLoS One*. 2016;11(7). doi:10.1371/JOURNAL.PONE.0158765

344. Webster AC, Nagler E V., Morton RL, Masson P. Chronic Kidney Disease. *Lancet (London, England)*. 2017;389(10075):1238-1252. doi:10.1016/S0140-6736(16)32064-5

345. Zhu Y, Cui H, Xia Y, Gan H. RIPK3-Mediated Necroptosis and Apoptosis Contributes to Renal Tubular Cell Progressive Loss and Chronic Kidney Disease Progression in Rats. *PLoS One*. 2016;11(6):156729. doi:10.1371/JOURNAL.PONE.0156729

346. Xiao X, Du C, Yan Z, Shi Y, Duan H, Ren Y. Inhibition of Necroptosis Attenuates Kidney Inflammation and Interstitial Fibrosis Induced By Unilateral Ureteral Obstruction. *Am J Nephrol*. 2017;46(2):131-138. doi:10.1159/000478746

347. Imamura M, Moon JS, Chung KP, et al. RIPK3 promotes kidney fibrosis via AKT-dependent ATP citrate lyase. *JCI Insight*. 2018;3(3). doi:10.1172/JCI.INSIGHT.94979

348. Shi Y, Huang C, Zhao Y, et al. RIPK3 blockade attenuates tubulointerstitial fibrosis in a mouse model of diabetic nephropathy. *Sci Rep*. 2020;10(1). doi:10.1038/S41598-020-67054-X

349. Li Y, Yuan Y, Huang Z xing, et al. GSDME-mediated pyroptosis promotes inflammation and fibrosis in obstructive nephropathy. *Cell Death Differ*. 2021;28(8):2333-2350. doi:10.1038/S41418-021-00755-6

350. Wang Y, Li Y, Chen Z, et al. GSDMD-dependent neutrophil extracellular traps promote macrophage-to-myofibroblast transition and renal fibrosis in obstructive nephropathy. *Cell Death Dis*. 2022;13(8). doi:10.1038/S41419-022-05138-4

351. Wu M, Xia W, Jin Q, et al. Gasdermin E Deletion Attenuates Ureteral Obstruction- and 5/6 Nephrectomy-Induced Renal Fibrosis and Kidney Dysfunction. *Front cell Dev Biol*. 2021;9. doi:10.3389/FCELL.2021.754134

352. Wu J, Raman A, Coffey NJ, et al. The key role of NLRP3 and STING in APOL1-associated podocytopathy. *J Clin Invest*. 2021;131(20). doi:10.1172/JCI136329

353. Coll RC, Robertson AAB, Chae JJ, et al. A small-molecule inhibitor of the NLRP3 inflammasome for the treatment of inflammatory diseases. *Nat Med*. 2015;21(3):248-257. doi:10.1038/NM.3806

354. Guan Y, Liang X, Ma Z, et al. A single genetic locus controls both expression of DPEP1/CHMP1A and kidney disease development via ferroptosis. *Nat Commun*. 2021;12(1). doi:10.1038/S41467-021-25377-X

355. Kim S, Kang SW, Joo J, et al. Characterization of ferroptosis in kidney tubular cell death under diabetic conditions. *Cell Death Dis*. 2021;12(2). doi:10.1038/S41419-021-03452-X

356. Fang X, Wang H, Han D, et al. Ferroptosis as a target for protection against cardiomyopathy. *Proc Natl Acad Sci U S A*. 2019;116(7):2672-2680. doi:10.1073/PNAS.1821022116

357. Zhang X, Li LX, Ding H, Torres VE, Yu C, Li X. Ferroptosis Promotes Cyst Growth in Autosomal Dominant Polycystic Kidney Disease Mouse Models. *J Am Soc Nephrol*. 2021;32(11):2759-2776. doi:10.1681/ASN.2021040460

358. Yang B, Fu L, Privratsky JR, et al. Interleukin-1 receptor activation aggravates autosomal dominant polycystic kidney disease by modulating regulated necrosis. *Am J Physiol - Ren Physiol*. 2019;317(2):F221-F228. doi:10.1152/AJPRENAL.00104.2019/ASSET/IMAGES/LARGE/ZH20071988250006.JPEG

359. Lin TA, Wu VCC, Wang CY. Autophagy in Chronic Kidney Diseases. *Cells*. 2019;8(1). doi:10.3390/CELLS8010061

360. Kieckhöfer E, Slaats GG, Ebert LK, et al. Primary cilia suppress Ripk3-mediated necroptosis. *Cell Death Discov 2022 81*. 2022;8(1):1-12. doi:10.1038/s41420-022-01272-2

361. Borgal L, Habbig S, Hatzold J, et al. The Ciliary Protein Nephrocystin-4 Translocates the Canonical Wnt Regulator Jade-1 to the Nucleus to Negatively Regulate β-Catenin Signaling. *J Biol Chem*. 2012;287(30):25370. doi:10.1074/JBC.M112.385658

362. Borgal L, Rinschen MM, Dafinger C, et al. Jade-1S phosphorylation induced by CK1α contributes to cell cycle progression. *Cell Cycle*. 2016;15(8):1034. doi:10.1080/15384101.2016.1152429

363. Brody JR, Kern SE. History and principles of conductive media for standard DNA electrophoresis. *Anal Biochem*. 2004;333(1):1-13. doi:10.1016/j.ab.2004.05.054

364. Miller JH. *Experiments in Molecular Genetics*. Cold Spring Harbor Laboratory; 1972. Accessed September 30, 2019. https://openlibrary.org/books/OL5298363M/Experiments_in_molecular_genetics

365. Kohli P, Höhne M, Jüngst C, et al. The ciliary membrane-associated proteome reveals actin-binding proteins as key components of cilia. *EMBO Rep*. 2017;18(9):1521-1535. doi:10.15252/EMBR.201643846

366. Shao X, Somlo S, Igarashi P. Epithelial-specific Cre/lox recombination in the developing kidney and genitourinary tract. *J Am Soc Nephrol*. 2002;13(7):1837-1846. doi:10.1097/01.ASN.0000016444.90348.50

367. Tadenev ALD, Kulaga HM, May-Simera HL, Kelley MW, Katsanis N, Reed RR. Loss of Bardet-Biedl syndrome protein-8 (BBS8) perturbs olfactory function, protein localization, and axon targeting. *Proc Natl Acad Sci U S A*. 2011;108(25):10320-10325. doi:10.1073/PNAS.1016531108

368. Truett GE, Heeger P, Mynatt RL, Truett AA, Walker JA, Warman ML. Preparation of PCR-quality mouse genomic DNA with hot sodium hydroxide and tris (HotSHOT). *Biotechniques*. 2000;29(1):52-54. doi:10.2144/00291BM09

369. Bankhead P, Loughrey MB, Fernández JA, et al. QuPath: Open source software for digital pathology image analysis. *Sci Reports 2017 71*. 2017;7(1):1-7. doi:10.1038/s41598-017-17204-5

370. Breyne K, Cool SK, Demon D, Demeyere K, Vandenberghe T. Non-Classical ProIL-1beta Activation during Mammary Gland Infection Is Pathogen-Dependent but Caspase-1 Independent. *PLoS One*. 2014;9(8):105680. doi:10.1371/journal.pone.0105680

371. Wu H, Kirita Y, Donnelly EL, Humphreys BD. Advantages of single-nucleus over single-cell RNA sequencing of adult kidney: Rare cell types and novel cell states revealed in fibrosis. *J Am Soc Nephrol*. 2019;30(1):23-32. doi:10.1681/ASN.2018090912/-/DCSUPPLEMENTAL

372. Liu YC, Chen CJ. Online 2D High-pH and Low-pH Reversed-Phase Nano-LC-MS/MS System for Deep Proteome Analysis. *Anal Chem*. 2023;95(14):5850-5857. doi:10.1021/ACS.ANALCHEM.2C02455

373. Demichev V, Messner CB, Vernardis SI, Lilley KS, Ralser M. DIA-NN: neural networks and interference correction enable deep proteome coverage in high throughput. *Nat Methods 2019 171*. 2019;17(1):41-44. doi:10.1038/s41592-019-0638-x

374. Tyanova S, Temu T, Sinitcyn P, et al. The Perseus computational platform for comprehensive analysis of (prote)omics data. *Nat Methods 2016 139*. 2016;13(9):731-740. doi:10.1038/nmeth.3901

375. Tyanova S, Temu T, Cox J. The MaxQuant computational platform for mass spectrometry–based shotgun proteomics. *Nat Protoc*. 2016;11. doi:10.1038/nprot.2016.136

376. Perez-Riverol Y, Csordas A, Bai J, et al. The PRIDE database and related tools and resources in 2019: improving support for quantification data. *Nucleic Acids Res*. 2019;47(D1):D442-D450. doi:10.1093/NAR/GKY1106

377. Wang L, Chang X, Feng J, Yu J, Chen G. TRADD Mediates RIPK1-Independent Necroptosis Induced by Tumor Necrosis Factor. *Front Cell Dev Biol*. 2020;7:506019. doi:10.3389/FCELL.2019.00393/BIBTEX

378. Ju E, Park KA, Shen HM, Hur GM. The resurrection of RIP kinase 1 as an early cell death checkpoint regulator—a potential target for therapy in the necroptosis era. *Exp Mol Med 2022 549*. 2022;54(9):1401-1411. doi:10.1038/s12276-022-00847-4

379. Bettencourt-Dias M, Hildebrandt F, Pellman D, Woods G, Godinho SA. Centrosomes and cilia in human disease. *Trends Genet*. 2011;27(8):307-315. doi:10.1016/J.TIG.2011.05.004

380. Cao J, Wu X, Qin X, Li Z. Uncovering the Effect of Passage Number on HT29 Cell Line Based on the Cell Metabolomic Approach. *J Proteome Res*. 2021;20(3):1582-1590.

doi:10.1021/ACS.JPROTEOME.0C00806

381. Jensen HL, Norrild B. The effects of cell passages on the cell morphology and the outcome of herpes simplex virus type 1 infection. *J Virol Methods*. 2000;84(2):139-152. doi:10.1016/S0166-0934(99)00129-9

382. Hughes P, Marshall D, Reid Y, Parkes H, Gelber C. The costs of using unauthenticated, over-passaged cell lines: how much more data do we need? *Biotechniques*. 2007;43(5):575-586. doi:10.2144/000112598

383. Tian R, Pan Y, Etheridge THA, et al. Pitfalls in Single Clone CRISPR-Cas9 Mutagenesis to Fine-Map Regulatory Intervals. *Genes (Basel)*. 2020;11(5). doi:10.3390/GENES11050504

384. Ozkan E, Lacerda MP. Genetics, Cytogenetic Testing And Conventional Karyotype. *StatPearls*. Published online August 8, 2023. Accessed February 8, 2024. https://www.ncbi.nlm.nih.gov/books/NBK563293/

385. Wu CT, Chen HY, Tang TK. Myosin-Va is required for preciliary vesicle transportation to the mother centriole during ciliogenesis. *Nat Cell Biol*. 2018;20(2):175-185. doi:10.1038/S41556-017-0018-7

386. Pfirrmann T, Gerhardt C. Life-Saver or Undertaker: The Relationship between Primary Cilia and Cell Death in Vertebrate Embryonic Development. *J Dev Biol 2022, Vol 10, Page 52*. 2022;10(4):52. doi:10.3390/JDB10040052

387. Paul C, Tang R, Longobardi C, et al. Loss of primary cilia promotes inflammation and carcinogenesis. *EMBO Rep*. 2022;23(12):e55687. doi:10.15252/EMBR.202255687

388. Chassaing B, Aitken JD, Malleshappa M, Vijay-Kumar M. Dextran Sulfate Sodium (DSS)-Induced Colitis in Mice. *Curr Protoc Immunol*. 2014;104(SUPPL.104):Unit. doi:10.1002/0471142735.IM1525S104

389. Choi SY, Chacon-Heszele MF, Huang L, et al. Cdc42 deficiency causes ciliary abnormalities and cystic kidneys. *J Am Soc Nephrol*. 2013;24(9):1435-1450. doi:10.1681/ASN.2012121236/-/DCSUPPLEMENTAL

390. Baek H, Shin HJ, Kim JJ, et al. Primary cilia modulate TLR4-mediated inflammatory responses in hippocampal neurons. *J Neuroinflammation*. 2017;14(1):1-10. doi:10.1186/S12974-017-0958-7/FIGURES/5

391. Raduolovic K, Mak'Anyengo R, Kaya B, Steinert A, Niess JH. Injections of Lipopolysaccharide into Mice to Mimic Entrance of Microbial-derived Products After Intestinal Barrier Breach. *J Vis Exp*. 2018;2018(135):57610. doi:10.3791/57610

392. Fie MM, Koneva L, Collins I, et al. Ciliary proteins specify the cell inflammatory response by tuning NFκB signalling, independently of primary cilia. *J Cell Sci*. 2020;133(13). doi:10.1242/JCS.239871

393. Sauer B, Henderson N. Site-specific DNA recombination in mammalian cells by the Cre recombinase of bacteriophage P1. *Proc Natl Acad Sci U S A*. 1988;85(14):5166-5170. doi:10.1073/PNAS.85.14.5166

394. Sternberg N, Hamilton D. Bacteriophage P1 site-specific recombination. I. Recombination between loxP sites. *J Mol Biol*. 1981;150(4):467-486. doi:10.1016/0022-2836(81)90375-2

395. Araki K, Imaizumi T, Okuyama K, Oike Y, Yamamura KI. Efficiency of recombination by Cre transient expression in embryonic stem cells: comparison of various promoters. *J Biochem*. 1997;122(5):977-982. doi:10.1093/OXFORDJOURNALS.JBCHEM.A021860

396. Wang S, Zhuang S, Dong Z. IFT88 deficiency in proximal tubular cells exaggerates cisplatin-induced injury by suppressing autophagy. *Am J Physiol - Ren Physiol*. 2021;321(3):F269-F277. doi:10.1152/AJPRENAL.00672.2020/ASSET/IMAGES/LARGE/AJPRENAL.00672.2020_F007.JPEG

397. Shao L, El-Jouni W, Kong F, et al. Genetic reduction of cilium length by targeting intraflagellar transport 88 protein impedes kidney and liver cyst formation in mouse models of autosomal polycystic kidney disease. *Kidney Int*. 2020;98(5):1225-1241. doi:10.1016/J.KINT.2020.05.049

398. Wu G, D'Agati V, Cai Y, et al. Somatic Inactivation of Pkd2 Results in Polycystic Kidney Disease. *Cell*. 1998;93(2):177-188. doi:10.1016/S0092-8674(00)81570-6

399. Ma M, Tian X, Igarashi P, Pazour GJ, Somlo S. Loss of cilia suppresses cyst growth in genetic models of autosomal dominant polycystic kidney disease. *Nat Genet*. 2013;45(9):1004. doi:10.1038/NG.2715

400. Avasthi P, Marshall WF. Stages of Ciliogenesis and Regulation of Ciliary Length. *Differentiation*. 2012;83(2):S30. doi:10.1016/J.DIFF.2011.11.015

401. Otto EA, Trapp ML, Schultheiss UT, Helou J, Quarmby LM, Hildebrandt F. NEK8 mutations affect ciliary and centrosomal localization and may cause nephronophthisis. *J Am Soc Nephrol*. 2008;19(3):587-592. doi:10.1681/ASN.2007040490

402. Smith LA, Bukanov NO, Husson H, et al. Development of Polycystic Kidney Disease in Juvenile Cystic Kidney Mice: Insights into Pathogenesis, Ciliary Abnormalities, and Common Features with Human Disease. *J Am Soc Nephrol*. 2006;17(10):2821-2831. doi:10.1681/ASN.2006020136

403. Sheffield VC. Use of isolated populations in the study of a human obesity syndrome, the Bardet-Biedl syndrome. *Pediatr Res*. 2004;55(6):908-911. doi:10.1203/01.PDR.0000127013.14444.9C

404. Cognard N, Scerbo MJ, Obringer C, et al. Comparing the Bbs10 complete knockout phenotype with a specific renal epithelial knockout one highlights the link between renal defects and systemic inactivation in mice. *Cilia*. 2015;4. Accessed March 30, 2021. https://ciliajournal.biomedcentral.com/articles/10.1186/s13630-015-0019-8

405. Nishimura DY, Fath M, Mullins RF, et al. Bbs2-null mice have neurosensory deficits, a defect in social dominance, and retinopathy associated with mislocalization of rhodopsin. *Proc Natl Acad Sci U S A*. 2004;101(47):16588-16593. doi:10.1073/PNAS.0405496101

406. Guo DF, Beyer AM, Yang B, Nishimura DY, Sheffield VC, Rahmouni K. Inactivation of Bardet-Biedl syndrome genes causes kidney defects. *Am J Physiol - Ren Physiol*. 2011;300(2):F574. doi:10.1152/AJPRENAL.00150.2010

407. Hsu Y, Seo S, Sheffield VC. Photoreceptor cilia, in contrast to primary cilia, grant entry to a partially assembled BBSome. *Hum Mol Genet*. 2021;30(1):87-102. doi:10.1093/HMG/DDAA284

408. Mäkeläinen S, Hellsand M, van der Heiden AD, et al. Deletion in the Bardet-Biedl Syndrome Gene TTC8 Results in a Syndromic Retinal Degeneration in Dogs. *Genes (Basel)*. 2020;11(9):1-27. doi:10.3390/GENES11091090

409. Hsu Y, Garrison JE, Seo S, Sheffield VC. The absence of BBSome function decreases synaptogenesis and causes ectopic synapse formation in the retina. *Sci Reports 2020 101*. 2020;10(1):1-19. doi:10.1038/s41598-020-65233-4

410. Wheway G, Parry DA, Johnson CA. The role of primary cilia in the development and disease of the retina. *Organogenesis*. 2014;10(1):69. doi:10.4161/ORG.26710

411. Mercey O, Kostic C, Bertiaux E, et al. The connecting cilium inner scaffold provides a structural foundation that protects against retinal degeneration. *PLoS Biol*. 2022;20(6). doi:10.1371/JOURNAL.PBIO.3001649

412. Röhlich P. The sensory cilium of retinal rods is analogous to the transitional zone of motile cilia. *Cell Tissue Res*. 1975;161(3):421-430. doi:10.1007/BF00220009

413. Swiderski RE, Nishimura DY, Mullins RF, et al. Gene expression analysis of photoreceptor cell loss in bbs4-knockout mice reveals an early stress gene response and photoreceptor cell damage. *Invest Ophthalmol Vis Sci*. 2007;48(7):3329-3340. doi:10.1167/IOVS.06-1477

414. Huang Z, Liang J, Chen S, et al. RIP3-mediated microglial necroptosis promotes neuroinflammation and neurodegeneration in the early stages of diabetic retinopathy. *Cell Death Dis 2023 143*. 2023;14(3):1-11. doi:10.1038/s41419-023-05660-z

415. Bajwa ZH, Sial KA, Malik AB, Steinman TI. Pain patterns in patients with polycystic kidney disease. *Kidney Int*. 2004;66(4):1561-1569. doi:10.1111/J.1523-1755.2004.00921.X

416. Hichri H, Stoetzel C, Laurier V, et al. Testing for triallelism: analysis of six BBS genes in a Bardet-Biedl syndrome family cohort. *Eur J Hum Genet*. 2005;13(5):607-616. doi:10.1038/SJ.EJHG.5201372

417. May-Simera HL, Kai M, Hernandez V, Osborn DPS, Tada M, Beales PL. Bbs8, together with the planar cell polarity protein Vangl2, is required to establish left-right asymmetry in zebrafish. *Dev Biol*. 2010;345(2):215-225. doi:10.1016/J.YDBIO.2010.07.013

418. Wu Y, Zhou J, Yang Y. Peripheral and central control of obesity by primary cilia. *J Genet Genomics*. 2023;50(5):295-304. doi:10.1016/J.JGG.2022.12.006

419. Harn HJ, Shen KL, Yueh KC, et al. Apoptosis occurs more frequently in intraductal carcinoma than in infiltrating duct carcinoma of human breast cancer and correlates with altered p53 expression: detected by terminal-deoxynucleotidyl-transferase-mediated dUTP-FITC nick end labelling (TUNEL). *Histopathology*. 1997;31(6):534-539. doi:10.1046/J.1365-2559.1997.3270906.X

420. Lemke G. How macrophages deal with death. *Nat Rev Immunol*. 2019;19(9):539-549. doi:10.1038/S41577-019-0167-Y

421. Bekeschus S, Schütz CS, Nießner F, et al. Elevated H2AX Phosphorylation Observed with kINPen Plasma Treatment Is Not Caused by ROS-Mediated DNA Damage but Is the Consequence of Apoptosis. *Oxid Med Cell Longev*. 2019;2019. doi:10.1155/2019/8535163

422. Bezerra, Renata Nogueira; Falcao, Lydia Teófilo De Moraes; Lavor, Caio Vieira de Oliveira; Kerstenetzky MS. Bardet-Biedl syndrome and hepatosplenomegaly: A case report of a rare presentation. *J Clin Images Med Case Reports*. 2023;4(1). doi:10.52768/2766-7820/2256

423. Shrinkhal, Singh A, Agrawal A, Mittal S, Udenia H, Bandu G. A rare case of Bardet–Biedl syndrome. *Taiwan J Ophthalmol*. 2020;10(2):138. doi:10.4103/TJO.TJO_62_19

424. Nishimoto N, Yoshizaki K, Tagoh H, et al. Elevation of serum interleukin 6 prior to acute phase proteins on the inflammation by surgical operation. *Clin Immunol Immunopathol*. 1989;50(3):399-401. doi:10.1016/0090-1229(89)90147-5

425. Tanaka T, Narazaki M, Kishimoto T. IL-6 in Inflammation, Immunity, and Disease. *Cold Spring Harb Perspect Biol*. 2014;6(10):16295-16296. doi:10.1101/CSHPERSPECT.A016295

426. Norris CA, He M, Kang LI, et al. Synthesis of IL-6 by Hepatocytes Is a Normal Response to Common Hepatic Stimuli. *PLoS One*. 2014;9(4):96053. doi:10.1371/JOURNAL.PONE.0096053

427. Pecoits-Filho R, Heimbürger O, Bárány P, et al. Associations between circulating inflammatory markers and residual renal function in CRF patients. *Am J Kidney Dis*. 2003;41(6):1212-1218. doi:10.1016/S0272-6386(03)00353-6

428. Takahashi T, Kubota M, Nakamura T, Ebihara I, Koide H. Interleukin-6 gene expression in peripheral blood mononuclear cells from patients undergoing hemodialysis or continuous ambulatory peritoneal dialysis. *Ren Fail*. 2000;22(3):345-354. doi:10.1081/JDI-100100878

429. Su H, Lei CT, Zhang C. Interleukin-6 signaling pathway and its role in kidney disease: An update. *Front Immunol*. 2017;8(APR). doi:10.3389/FIMMU.2017.00405/FULL

430. Heinrich PC, Castell J V., Andus T. Interleukin-6 and the acute phase response. *Biochem J*. 1990;265(3):621-636. doi:10.1042/BJ2650621

431. Jain S, Gautam V, Naseem S. Acute-phase proteins: As diagnostic tool. *J Pharm Bioallied Sci*. 2011;3(1):118. doi:10.4103/0975-7406.76489

432. Wunderlich CM, Ackermann PJ, Ostermann AL, et al. Obesity exacerbates colitis-associated cancer via IL-6-regulated macrophage polarisation and CCL-20/CCR-6-mediated lymphocyte recruitment. *Nat Commun*. 2018;9(1). doi:10.1038/S41467-018-03773-0

433. Ellulu MS, Patimah I, Khaza'ai H, Rahmat A, Abed Y. Obesity and inflammation: the linking mechanism and the complications. *Arch Med Sci*. 2017;13(4):851. doi:10.5114/AOMS.2016.58928

434. Artemniak-Wojtowicz D, Pyrżak B, Kucharska AM. Obesity and chronic inflammation crosslinking. *Cent J Immunol*. 2020;45(4):461. doi:10.5114/CEJI.2020.103418

435. Timper K, Denson JL, Steculorum SM, Rose-John S, Wunderlich FT, Br€ Uning Correspondence JC. IL-6 Improves Energy and Glucose Homeostasis in Obesity via Enhanced Central IL-6 trans-Signaling. *Cell Rep*. 2017;19:267-280. doi:10.1016/j.celrep.2017.03.043

436. Harcourt BE, Forbes JM, Matthews VB. Obesity-induced renal impairment is exacerbated in interleukin-6-knockout mice. *Nephrology*. 2012;17(3):257-262. doi:10.1111/J.1440-1797.2011.01547.X

437. Forsythe E, Mallya UG, Yang M, et al. Burden of hyperphagia and obesity in Bardet–Biedl syndrome: a multicountry survey. *Orphanet J Rare Dis*. 2023;18(1):182. doi:10.1186/S13023-023-02723-4

438. Marion V, Stoetzel C, Schlicht D, et al. Transient ciliogenesis involving Bardet-Biedl syndrome proteins is a fundamental characteristic of adipogenic differentiation. *Proc Natl Acad Sci U S A*. 2009;106(6):1820-1825. doi:10.1073/PNAS.0812518106

439. Marion V, Mockel A, De Melo C, et al. BBS-induced ciliary defect enhances adipogenesis, causing paradoxical higher-insulin sensitivity, glucose usage, and decreased inflammatory response. *Cell Metab*. 2012;16(3):363-377. doi:10.1016/J.CMET.2012.08.005

440. Grace C, Beales P, Summerbell C, et al. Energy metabolism in Bardet-Biedl syndrome. *Int J Obes Relat Metab Disord*. 2003;27(11):1319-1324. doi:10.1038/SJ.IJO.0802420

441. Rahmouni K, Fath MA, Seo S, et al. Leptin resistance contributes to obesity and hypertension in mouse models of Bardet-Biedl syndrome. *J Clin Invest*. 2008;118(4):1458-1467. doi:10.1172/JCI32357

442. Al-Hussaniy HA, Alburghaif AH, Naji MA. Leptin hormone and its effectiveness in reproduction, metabolism, immunity, diabetes, hopes and ambitions. *J Med Life*. 2021;14(5):600. doi:10.25122/JML-2021-0153

443. Vaisse C, Reiter JF, Berbari NF. Cilia and Obesity. *Cold Spring Harb Perspect Biol*. 2017;9(7). doi:10.1101/CSHPERSPECT.A028217

444. Tauber M. Setmelanotide for controlling weight and hunger in Bardet-Biedl syndrome. *lancet Diabetes Endocrinol*. 2022;10(12):829-830. doi:10.1016/S2213-8587(22)00309-6

445. Haqq AM, Chung WK, Dollfus H, et al. Efficacy and safety of setmelanotide, a melanocortin-4 receptor agonist, in patients with Bardet-Biedl syndrome and Alström syndrome: a multicentre, randomised, double-blind, placebo-controlled, phase 3 trial with an open-label period. *lancet Diabetes Endocrinol*. 2022;10(12):859. doi:10.1016/S2213-8587(22)00277-7

446. Chen L, Deng H, Cui H, et al. Inflammatory responses and inflammation-associated diseases in organs. *Oncotarget*. 2018;9(6):7204. doi:10.18632/ONCOTARGET.23208

447. Wynn TA. Cellular and molecular mechanisms of fibrosis. *J Pathol*. 2008;214(2):199. doi:10.1002/PATH.2277

448. Brusselle G, Bracke K. Targeting immune pathways for therapy in asthma and chronic obstructive pulmonary disease. *Ann Am Thorac Soc*. 2014;11 Suppl 5:S322-S328. doi:10.1513/ANNALSATS.201403-118AW

449. Gudkov A V., Komarova EA. p53 and the Carcinogenicity of Chronic Inflammation. *Cold Spring Harb Perspect Med*. 2016;6(11). doi:10.1101/CSHPERSPECT.A026161

450. Takeuchi O, Akira S. Pattern recognition receptors and inflammation. *Cell*. 2010;140(6):805-820. doi:10.1016/J.CELL.2010.01.022

451. Hendrayani SF, Al-Harbi B, Al-Ansari MM, Silva G, Aboussekhra A. The inflammatory/cancer-related IL-6/STAT3/NF-κB positive feedback loop includes AUF1 and maintains the active state of breast myofibroblasts. *Oncotarget*. 2016;7(27):41974-41985. doi:10.18632/ONCOTARGET.9633

452. Kaminska B. MAPK signalling pathways as molecular targets for anti-inflammatory therapy--from molecular mechanisms to therapeutic benefits. *Biochim Biophys Acta*. 2005;1754(1-2):253-262. doi:10.1016/J.BBAPAP.2005.08.017

453. Poveda J, Sanz AB, Rayego-Mateos S, et al. NFκBiz protein downregulation in acute kidney injury: Modulation of inflammation and survival in tubular cells. *Biochim Biophys Acta - Mol Basis Dis*. 2016;1862(4):635-646. doi:10.1016/J.BBADIS.2016.01.006

454. Viau A, Baaziz M, Aka A, et al. Tubular STAT3 Limits Renal Inflammation in Autosomal Dominant Polycystic Kidney Disease. *J Am Soc Nephrol*. 2020;31(5):1035-1049. doi:10.1681/ASN.2019090959

455. Willson TA, Jurickova I, Collins M, Denson LA. Deletion of intestinal epithelial cell STAT3 promotes T-lymphocyte STAT3 activation and chronic colitis following acute dextran sodium sulfate injury in mice. *Inflamm Bowel Dis*. 2013;19(3):512-525. doi:10.1097/MIB.0B013E31828028AD

456. Jarnicki A, Putoczki T, Ernst M. Stat3: linking inflammation to epithelial cancer - more than a “gut” feeling? *Cell Div*. 2010;5. doi:10.1186/1747-1028-5-14

457. Newton K, Dugger DL, Maltzman A, et al. RIPK3 deficiency or catalytically inactive RIPK1 provides greater benefit than MLKL deficiency in mouse models of inflammation and tissue injury. *Cell Death Differ*. 2016;23(9):1565-1576. doi:10.1038/CDD.2016.46

458. Von Mässenhausen A, Tonnus W, Himmerkus N, et al. Phenytoin inhibits necroptosis. *Cell Death Dis 2018 93*. 2018;9(3):1-15. doi:10.1038/s41419-018-0394-3

459. Jaric I, Voelkl B, Clerc M, et al. The rearing environment persistently modulates mouse phenotypes from the molecular to the behavioural level. *PLOS Biol*. 2022;20(10):e3001837. doi:10.1371/JOURNAL.PBIO.3001837

460. Vince JE, De Nardo D, Gao W, et al. The Mitochondrial Apoptotic Effectors BAX/BAK Activate Caspase-3 and -7 to Trigger NLRP3 Inflammasome and Caspase-8 Driven IL-1β Activation. *Cell Rep*. 2018;25(9):2339-2353.e4. doi:10.1016/J.CELREP.2018.10.103

461. Orning P, Weng D, Starheim K, et al. Pathogen blockade of TAK1 triggers caspase-8-dependent cleavage of gasdermin D and cell death. *Science*. 2018;362(6418):1064-1069. doi:10.1126/SCIENCE.AAU2818

462. Bertheloot D, Latz E, Franklin BS. Necroptosis, pyroptosis and apoptosis: an intricate game of cell death. *Cell Mol Immunol 2021 185*. 2021;18(5):1106-1121. doi:10.1038/s41423-020-00630-3

463. Wei S, Feng M, Zhang S. Molecular Characteristics of Cell Pyroptosis and Its Inhibitors: A Review of Activation, Regulation, and Inhibitors. *Int J Mol Sci*. 2022;23(24). doi:10.3390/IJMS232416115

464. Yang B, Fu L, Privratsky JR, et al. Interleukin-1 receptor activation aggravates autosomal dominant polycystic kidney disease by modulating regulated necrosis. *Am J Physiol - Ren Physiol*. 2019;317(2):F221. doi:10.1152/AJPRENAL.00104.2019

465. Braun DA, Hildebrandt F. Nephronophthisis and Related Ciliopathies. *Pediatr Nephrol*. Published online 2021:1-28. doi:10.1007/978-3-642-27843-3_119-1

466. Wang Q, Zou B, Wei X, et al. Identification of renal cyst cells of type I Nephronophthisis by single-nucleus RNA sequencing. *Front Cell Dev Biol*. 2023;11:1192935. doi:10.3389/FCELL.2023.1192935/BIBTEX

467. Leonhard WN, Happe H, Peters DJM. Variable Cyst Development in Autosomal Dominant Polycystic Kidney Disease: The Biologic Context. *J Am Soc Nephrol*. 2016;27(12):3530. doi:10.1681/ASN.2016040425

468. Li Q, Wang Y, Deng W, et al. Heterogeneity of cell composition and origin identified by single-cell transcriptomics in renal cysts of patients with autosomal dominant polycystic kidney disease. *Theranostics*. 2021;11(20):10064. doi:10.7150/THNO.57220

469. Malas TB, Formica C, Leonhard WN, et al. Meta-analysis of polycystic kidney disease expression profiles defines strong involvement of injury repair processes. *Am J Physiol Renal Physiol*. 2017;312(4):F806-F817. doi:10.1152/AJPRENAL.00653.2016

470. Martin-Sanchez D, Fontecha-Barriuso M, Carrasco S, et al. TWEAK and RIPK1 mediate a second wave of cell death during AKI. *Proc Natl Acad Sci U S A*. 2018;115(16):4182-4187. doi:10.1073/PNAS.1716578115/-/DCSUPPLEMENTAL

471. Ming X, Bao C, Hong T, et al. Clusterin, a Novel DEC1 Target, Modulates DNA Damage-Mediated Cell Death. *Mol Cancer Res*. 2018;16(11):1641-1651. doi:10.1158/1541-7786.MCR-18-0070

472. Gao W, Liu D, Sun H, et al. SPP1 is a prognostic related biomarker and correlated with tumor-infiltrating immune cells in ovarian cancer. *BMC Cancer*. 2022;22(1):1367. doi:10.1186/S12885-022-10485-8

473. Kusaba T, Lalli M, Kramann R, Kobayashi A, Humphreys BD. Differentiated kidney epithelial cells repair injured proximal tubule. *Proc Natl Acad Sci U S A*. 2014;111(4):1527-1532. doi:10.1073/PNAS.1310653110/SUPPL_FILE/PNAS.201310653SI.PDF

474. Schueler M, Braun DA, Chandrasekar G, et al. DCDC2 mutations cause a renal-hepatic ciliopathy by disrupting Wnt signaling. *Am J Hum Genet*. 2015;96(1):81-92. doi:10.1016/J.AJHG.2014.12.002

475. Massinen S, Hokkanen ME, Matsson H, et al. Increased expression of the dyslexia candidate gene DCDC2 affects length and signaling of primary cilia in neurons. *PLoS One*. 2011;6(6). doi:10.1371/JOURNAL.PONE.0020580

476. Balzer MS, Rohacs T, Susztak K. How Many Cell Types Are in the Kidney and What Do They Do? *https://doi.org/101146/annurev-physiol-052521-121841*. 2022;84:507-531. doi:10.1146/ANNUREV-PHYSIOL-052521-121841

477. Malik SA, Modarage K, Goggolidou P. The Role of Wnt Signalling in Chronic Kidney Disease (CKD). *Genes 2020, Vol 11, Page 496*. 2020;11(5):496. doi:10.3390/GENES11050496

478. Yang K, Shang Y, Yang N, Pan S, Jin J, He Q. Application of nanoparticles in the diagnosis and treatment of chronic kidney disease. *Front Med*. 2023;10:1132355. doi:10.3389/FMED.2023.1132355/BIBTEX

479. Du B, Yu M, Zheng J. Transport and interactions of nanoparticles in the kidneys. *Nat Rev Mater 2018 310*. 2018;3(10):358-374. doi:10.1038/s41578-018-0038-3

480. Liu D, Shu G, Jin F, et al. ROS-responsive chitosan-SS31 prodrug for AKI therapy via rapid distribution in the kidney and long-term retention in the renal tubule. *Sci Adv*. 2020;6(41). doi:10.1126/SCIADV.ABB7422/SUPPL_FILE/ABB7422_SM.PDF

481. Tabor HK, Stock J, Brazg T, et al. Informed consent for whole genome sequencing: a qualitative analysis of participant expectations and perceptions of risks, benefits, and harms. *Am J Med Genet A*. 2012;158A(6):1310-1319. doi:10.1002/AJMG.A.35328

482. Tabor HK, Berkman BE, Hull SC, Bamshad MJ. Genomics really gets personal: how exome and whole genome sequencing challenge the ethical framework of human genetics research. *Am J Med Genet A*. 2011;155A(12):2916-2924. doi:10.1002/AJMG.A.34357

483. Arts HH, Knoers NVAM. Current insights into renal ciliopathies: what can genetics teach us? *Pediatr Nephrol*. 2013;28(6):863-874. doi:10.1007/s00467-012-2259-9

484. Chitrangi S, Vaity P, Jamdar A, Bhatt S. Patient-derived organoids for precision oncology: a platform to facilitate clinical decision making. *BMC Cancer*. 2023;23(1). doi:10.1186/S12885-023-11078-9

485. Yousef Yengej FA, Jansen J, Rookmaaker MB, Verhaar MC, Clevers H. Kidney Organoids and Tubuloids. *Cells*. 2020;9(6). doi:10.3390/CELLS9061326

486. Zhang S, Li R, Dong W, et al. RIPK3 mediates renal tubular epithelial cell apoptosis in endotoxin-induced acute kidney injury. *Mol Med Rep*. 2019;20(2):1613. doi:10.3892/MMR.2019.10416

487. Xue S, Cao ZX, Wang JN, et al. Receptor-Interacting Protein Kinase 3 Inhibition Relieves Mechanical Allodynia and Suppresses NLRP3 Inflammasome and NF-κB in a Rat Model of Spinal Cord Injury. *Front Mol Neurosci*. 2022;15:861312. doi:10.3389/FNMOL.2022.861312/BIBTEX

488. Chen J, Chen H, Yang H, Dai H. SPC25 upregulation increases cancer stem cell properties in non-small cell lung adenocarcinoma cells and independently predicts poor survival. *Biomed Pharmacother*. 2018;100:233-239. doi:10.1016/J.BIOPHA.2018.02.015

489. Zhu Y, Cui H, Gan H, et al. Necroptosis mediated by receptor interaction protein kinase 1 and

3 aggravates chronic kidney injury of subtotal nephrectomised rats. *Biochem Biophys Res Commun*. 2015;461(4):575-581. doi:10.1016/J.BBRC.2015.03.164

XIV. Supplements

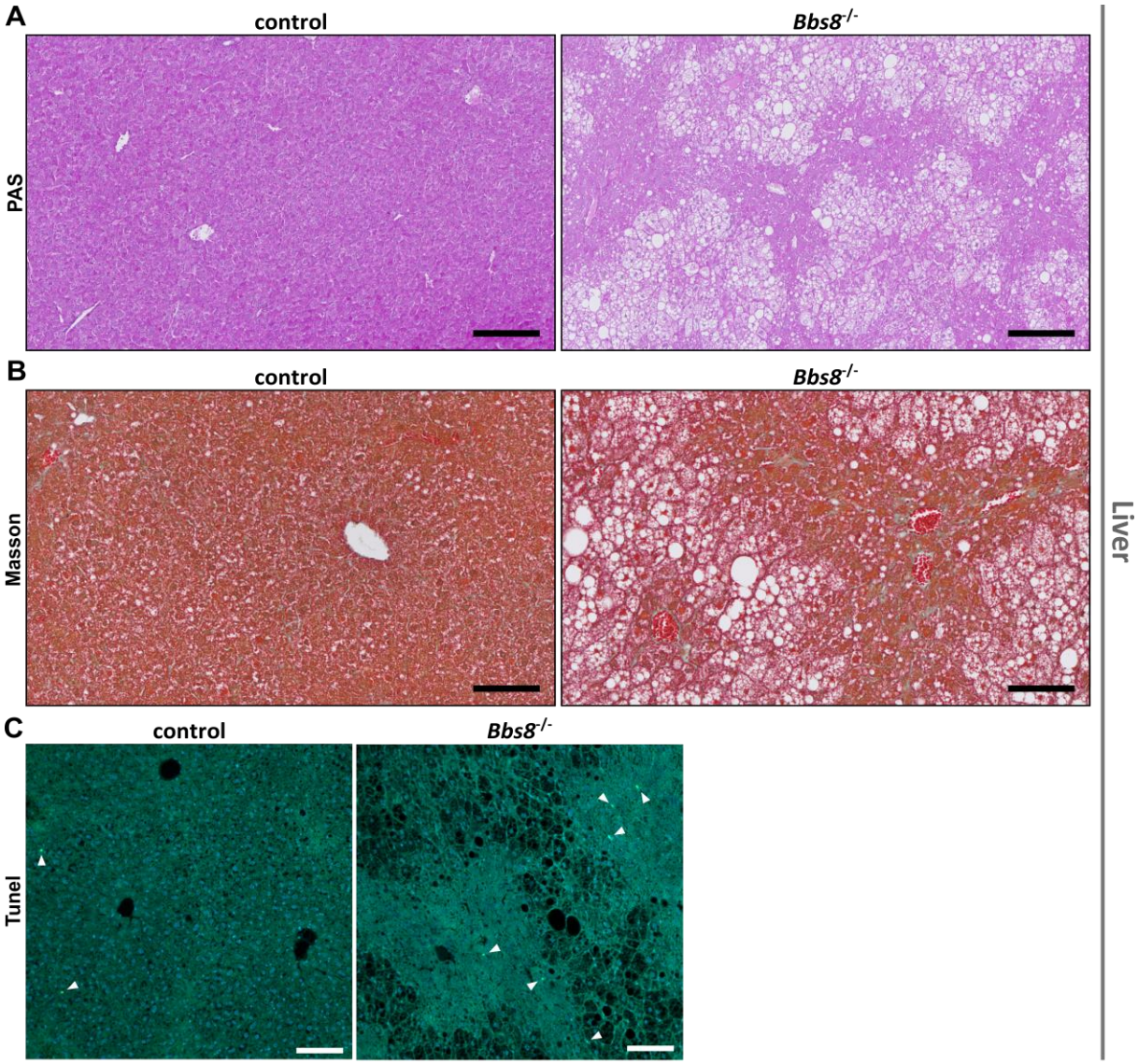

Supplementary Figure 1 ***Bbs8 knockout mice do not develop cystic liver but fatty liver disease.***

Pathology of liver tissue of 46-week-old control and Bbs8 deficient mice: ***(A)*** *PAS staining, scale bar: 200 µm,* ***(B)*** *Masson's trichrome stain, scale bar: 100 µm,* ***(C)*** *TUNEL staining, scale bar: 50 µm.*

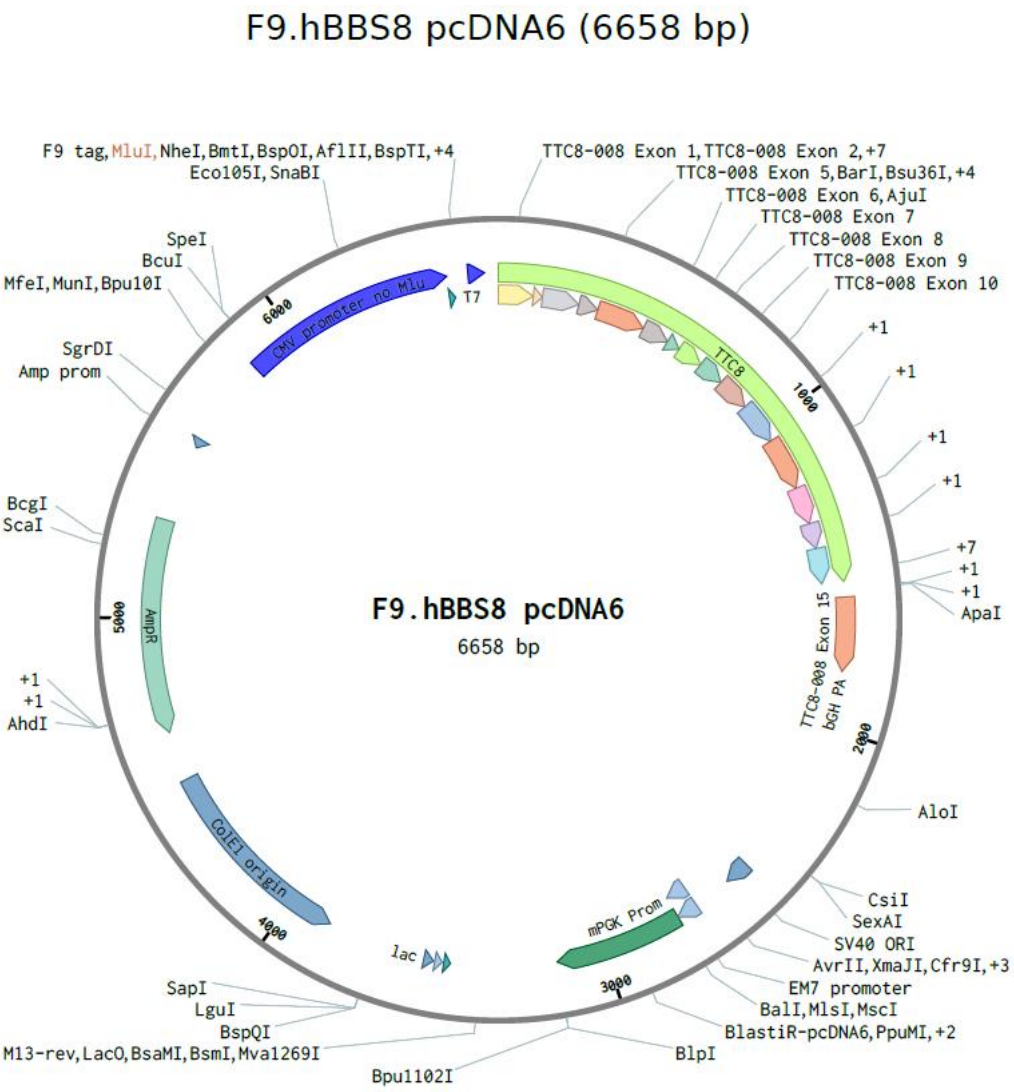

Supplementary Figure 2 ***Vector map of Flag-tagged human BBS8.***